UNIVERSITÄT ZU LÜBECK

From the Institute of Anatomy

of the University of Lübeck

Director: Prof. Dr. Dr. Tobias Lange

CD4+ T Cell Receptor Sequences During Progression Towards Experimental Pemphigoid

for the Fulfillment of

Requirements

for the Doctoral Degree

of the University of Lübeck

from the Institute of Anatomy

Submitted by

Farbod Bahreini

from Tehran, Iran

Lübeck 2025

First referee: Prof. Dr. Kathrin Kalies

Second referee: Prof. Dr. Christian Karsten

Chairperson: Prof. Dr. Lars Redecke

Date of oral examination: April 2nd, 2026

Approved for printing: April 7th, 2026

Dedication

To my father, Farshad, whose love now lives beyond this world:

Dad, I write these words with the weight of missing you. You are no longer here to see this moment, but your presence fills every line of it. Every success of mine carries your soul. You were my strength, my quiet teacher, my unspoken courage. All my life, I tried to make you proud, and I hope, somehow, that you can see me now. I dedicate this work to your soul, to the love that will never fade, to the man whose voice still guides me when I lose my way. You are not gone, because you live in everything I am. Love you, Daddy!

To my mother, Sousan:

Mom, your love has been the constant light that never dimmed, even in the darkest times. You have carried me through every distance, every silence, every storm. Your sacrifices are beyond words, your prayers beyond measure. You raised me with faith that never broke. This achievement, every word of it, belongs as much to you as it does to me. If I have come this far, it is because you never let me fall. Thanks for being on Dad's side and Mamani's side in the worst situations. Thanks for being so patient. Thanks for being my mom. Love you so much, Mommy!

To Hasti, my wife:

My love, my home, my patient heart. You have endured every absence, every night apart, with a grace that humbles me. Your faith in me gave meaning to my struggle, and your voice gave me strength when I had none. This thesis is not my achievement; it is ours. You carried the weight of distance so that I could carry my dreams. And know this, nothing in life, no distance, no hardship, could ever lessen what you are to me. Thanks for being on Dad's side while we just got married. Love you from the deepest corners of my soul!

To Fartash, my brother:

You became the strength of our family when I could not be there. You stood beside Mom and Dad, protecting them, comforting them, being the son I could not be. You carried more than

your share, and I will forever be in your debt. You are not only my brother, you are the piece of me that stayed home when I left. Without you, none of this would have been possible. Thanks for being on Dad's side and Mamani's side in the situations I could not tolerate.

To my grandmother, whose soul still surrounds me:

Mamani, I grew up in the warmth of your prayers, and though you are gone, I still feel you nearby. Your love shaped my heart, and your memory guides me still. This work is also yours, because everything good in me began with you.

To Ghazal, my cousin:

The sister I never had. You have been my comfort in loneliness, my support in hardship, and my wife's companion in my absence. You filled the distance with love and care that words can never repay.

Special Thanks:

To Neda, for being the daughter my mother needed when I was far away, and for standing beside our family in our hardest times.

To Nesa, whose love and connection make the miles between us feel shorter.

To my father-in-law and mother-in-law, Mahmood and Zhale, for caring for their daughter, Hasti, during and after our marriage, giving me peace of mind across the miles.

To Fariba, for her kindness and constant friendship.

To Foujan, whose smile brings light to our family.

To Sami, whose warmth brings us all closer together.

And to my dear friends: Makan, Alireza, Amin, Ali B, Forouzan, Negar, Shiva T., Shiva K., Leyli, Javad, Pouria, Zana, Vahab, Tina, Soroush, Sadegh, Shirin, Afsaneh, Hanie, Vahid, Ali N, and Omid; thank you for your laughter, your faith, and your presence when I felt alone.

I would also like to thank my professors and mentors in Iran who gave me the confidence and courage to follow science: Dr. Shirin Shahangian, Prof. Dr. Khosro Khajeh, Dr. Bahareh

Dabirmanesh, Prof. Dr. Nima Rezaei, Dr. Fahimeh Ghavami, Dr. Fatemeh Rashno, and Dr. Parisa Nasrollahi.

This is not just my thesis.

It is the story of a father's soul that still protects me,

a mother's prayers whispered across oceans,

a wife's faith that never broke,

a brother's strength,

a family's love that distance could not weaken.

And this is the story of a young boy who carried his dreams across oceans, a boy whose heart beat for science, yet whose soul never left home. He came to Germany with hope and determination, chasing knowledge through sleepless nights and silent prayers. But no matter how far he went, his heart stayed with the people he loved; the voices, the memories, the warmth that made him who he is. This work is not just the story of research and discovery; it is the story of love, distance, loss, and faith; of a heart divided by borders, yet held together by purpose.

Acknowledgments

I would like to express my deepest and most heartfelt gratitude to my supervisor, Prof. Dr. Kathrin Kalies, whose guidance, patience, and unwavering support have shaped not only this thesis but also the person I have become through it. Her scientific insight, kindness, and belief in me gave me the confidence to move forward even when the path felt uncertain. She has been more than a supervisor: a true mentor who inspired me with her integrity, compassion, and dedication to science. I will always be grateful for the trust she placed in me, the time she devoted to my growth, and the strength she gave me when I needed it most.

I would also like to sincerely thank Prof. Dr. Jürgen Westermann, the former Head of the Institute of Anatomy, for his leadership and support during the early years of my doctoral studies, and Prof. Dr. Peter König and Prof. Dr. Dr. Tobias Lange, the current Heads of the Institute, for providing an inspiring and collaborative scientific environment and for their encouragement and interest in my research and for their incredible support.

I am thankful to Dr. Christoph Hammers and Dr. Katja Bieber for their support as members of my Thesis Advisory Committee, who helped me develop my ideas during this time.

My heartfelt thanks go to our wonderful technicians: Petra Lau, Nina Schneider, Daniela Rieck, René Pagel, and Susanne Allan, for their outstanding technical assistance, precision, and kindness. Their dedication and care have been indispensable to the completion of this work, and I could never have finished my Ph.D. without their help.

I am also deeply thankful to Dr. Kai Kalies for his generous help, insightful advice, and constructive discussions that enriched my work at every stage.

I am thankful to Prof. Dr. Christian Karsten and Prof. Dr. Lars Redecke for reviewing my Ph.D. dissertation and providing their valuable comments.

Many thanks to the RTG2633, especially to its spokesperson, Prof. Dr. Ralf Ludwig, and the Co-Spokesperson, Prof. Dr. Jennifer Hundt, for their support.

Finally, I extend my warmest thanks to all colleagues, collaborators, and friends who supported me throughout this journey; for their encouragement, understanding, and companionship that made this long path not only possible but truly meaningful.

Table of Contents

Table of Figures and Tables

List of Abbreviations

Abbreviation	Full Form
AIBDs	Autoimmune Blistering Diseases
Bcl6	B Cell Lymphoma 6
BP180	Bullous Pemphigoid Antigen 180
BP230	Bullous Pemphigoid Antigen 230
CD11b	Cluster of Differentiation 11b
CD154	Cluster of Differentiation 154 (CD40 Ligand)
CD28	Cluster of Differentiation 28
CD4+	Cluster of Differentiation 4 Positive
CD40L	CD40 Ligand
CD80	Cluster of Differentiation 80
CD86	Cluster of Differentiation 86
CDNPs	Cell-Derived Nanoparticles
CDR	Complementarity-Determining Region
CDR1	Complementarity-Determining Region 1
CDR2	Complementarity-Determining Region 2
CDR3	Complementarity-Determining Region 3
Col7	Type VII Collagen
CXCL12	C-X-C Motif Chemokine Ligand 12
CXCL13	C-X-C Motif Chemokine Ligand 13
CXCR5	C-X-C Chemokine Receptor Type 5
DAMPs	Damage-Associated Molecular Patterns
DAB	3,3′-Diaminobenzidine
DEJ	Dermal-Epidermal Junction
DMEM	Dulbecco's Modified Eagle Medium
DTT	dithiothreitol
EBA	Epidermolysis Bullosa Acquisita
FBS	Fetal Bovine Serum
FcγRIV	Fc Gamma Receptor IV
FcγRs	Fc Gamma Receptors
FOXP3	Forkhead Box P3
Gata3	GATA Binding Protein 3
GC	Germinal Center
GCs	Germinal Centers
ICOS	Inducible T Cell Costimulator
IFN-γ	Interferon Gamma
IgE	Immunoglobulin E
IgG	Immunoglobulin G
IgG1	Immunoglobulin G1

Abbreviation	Full Form
IgG2a	Immunoglobulin G2a
IgG2b	Immunoglobulin G2b
IgG2c	Immunoglobulin G2c
IL-10	Interleukin-10
IL-1β	Interleukin-1 Beta
IL-21	Interleukin-21
IL-4	Interleukin-4
IL-6	Interleukin-6
Ingln	Inguinal Lymph Node
Ki67	Marker of Proliferation Ki-67
LAL	Limulus Amebocyte Lysate
LN	Lymph Node
LPS	Lipopolysaccharide
mCol7c	Murine Type VII Collagen C-Terminal Fragment
MEM	Minimum Essential Medium
MHC	Major Histocompatibility Complex
MS	Multiple Sclerosis
NETosis	Neutrophil Extracellular Trap Formation
OAT	Ovalbumin in Combination with Alum and TiterMax
OVA	Ovalbumin
PAT	PBS in Alum and TiterMax
PBS	Phosphate-Buffered Saline
PD-1	Programmed Cell Death Protein 1
Pln	Popliteal Lymph Node
pMHC	Peptide-Major Histocompatibility Complex
PMSF	phenylmethylsulfonyl fluoride
RAG1	Recombination Activating Gene 1
RAG2	Recombination Activating Gene 2
RAMPs	Resolution-Associated Molecular Patterns
ROS	Reactive Oxygen Species
RSS	Recombination Signal Sequences
SDS-PAGE	sodium dodecyl sulfate–polyacrylamide gel electrophoresis
SLE	Systemic Lupus Erythematosus
T1DM	Type 1 Diabetes Mellitus
TCR	T Cell Receptor
TCRα	T Cell Receptor Alpha
TCRαβ	T Cell Receptor Alpha Beta
TCRβ	T Cell Receptor Beta
TCRR	T Cell Receptor Repertoire
TCZ	T Cell Zone

Abbreviation	Full Form
TdT	Terminal Deoxynucleotidyl Transferase
Tfh	T Follicular Helper
TGF-β	Transforming Growth Factor Beta
Th1	T Helper 1
Th17	T Helper 17
Th2	T Helper 2
TNF-α	Tumor Necrosis Factor Alpha
Tregs	Regulatory T Cells
TSH	Thyroid-Stimulating Hormone

Zusammenfassung

Autoantikörpervermittelte Erkrankungen wie die Epidermolysis bullosa acquisita (EBA) entstehen durch einen Zusammenbruch der Immuntoleranz, der sich häufig in einem eingeschränkten T-Zell-Rezeptor-Repertoire (TCRR) widerspiegelt. Diese Arbeit untersucht zwei komplementäre Strategien zur Wiederherstellung der Toleranz, die beide auf eine Umgestaltung des TCRR abzielen. Im EBA-Modell hat sich gezeigt, dass eine Vorbehandlung mit Ovalbumin in Kombination mit Alum und TiterMax (OAT) die Erkrankung vollständig verhindert. Auf der Grundlage dieses Modells zeigen wir hier, dass die OAT-Vorbehandlung das Repertoire der follikulären T-Helferzellen signifikant umgestaltet hat. OAT erhöhte die Diversität, reduzierte die klonale Dominanz und führte neue Sequenzmerkmale ein. Die Transkriptomanalyse ergab knotspezifische Programme, wobei sich der Leistenlymphknoten in Richtung regulatorischer und metabolischer Signalwege verschob, was mit einer tolerogenen Umgebung übereinstimmt. Eine zweite Strategie untersuchte die Auswirkungen von Cell-Derived Nanoparticles (CDNPs), multi-epitopischen Proteinaggregaten von ~150 nm, die reproduzierbar mit Annexin A5 markiert wurden. CDNPs reduzierten die IL-6-Sekretion aus Makrophagen geringfügig und erweiterten das TCRβ-Repertoire innerhalb der T-Zell-Zonen der Milz, indem sie die klonale Dominanz einschränkten. CDNPs erhöhten auch die *Tcrb*- und *Gata3*-Expression, was auf eine verstärkte T-Zell-Aktivität mit einer Th2-assoziierten Tendenz hindeutet. Zusammengenommen unterstreichen diese Ergebnisse zwei unterschiedliche, aber sich ergänzende Ansätze: OAT veranschaulicht, wie eine antigenspezifische Immunabweichung das Repertoire umgestalten und die Toleranz unterstützen kann, während CDNPs als antigenunabhängige Modulatoren wirken, die sowohl die angeborene als auch die adaptive Immunität umprogrammieren können. Aus translationaler Sicht bietet OAT ein Modell für tolerogene Impfungen bei Krankheiten mit bekannten Antigenen, während CDNPs eine potenzielle Therapie für Fälle bieten, in denen Autoantigene vielfältig oder undefiniert sind.

Beide Ansätze unterstreichen die Bedeutung des TCRR als zentraler Determinant der Toleranz und vielversprechendes therapeutisches Ziel bei Autoantikörper-bedingten Erkrankungen.

Abstract

Autoantibody-mediated diseases, such as epidermolysis bullosa acquisita (EBA), arise from a breakdown in immune tolerance, often reflected in restricted T-cell receptor repertoires (TCRRs). This thesis examines two complementary strategies for restoring tolerance, both of which converge on reshaping the TCRR. In the EBA model, pretreatment with ovalbumin in combination with Alum and TiterMax (OAT) has been shown to completely prevent disease. Building on this model, herein, we demonstrate that OAT pretreatment significantly reshaped the T follicular helper repertoire. OAT increased diversity, reduced clonal dominance, and introduced novel sequence features. Transcriptomic analysis revealed node-specific programs, with the inguinal lymph node (Ingln) shifting toward regulatory and metabolic pathways, consistent with a tolerogenic environment. A second strategy examined the effects of cell-derived nanoparticles (CDNPs), which are multi-epitopic protein aggregates of ~150 nm, reproducibly marked by Annexin A5. CDNPs modestly reduced IL-6 secretion from macrophages and broadened TCRβ repertoires within splenic T-cell zones by limiting clonal dominance. CDNPs also increased *Tcrb* and *Gata3* expression, indicating enhanced T-cell activity with a Th2-associated bias. Together, these findings highlight two distinct but complementary approaches: OAT illustrates how antigen-specific immune deviation can reshape repertoires and support tolerance, whereas CDNPs act as multi-epitope modulators capable of reprogramming both innate and adaptive immunity. From a translational perspective, OAT suggests a model for tolerogenic vaccination in diseases with known antigens, while CDNPs provide a potential therapy where autoantigens are diverse or undefined. Both approaches underscore the TCRR as a central determinant of tolerance and a promising therapeutic target in autoantibody-driven disease.

1. Introduction

1.1. The immunological architecture of autoimmunity

The vertebrate immune system has developed a complex structure that maintains a balance between defending against pathogens and tolerating the body's own tissues. The key concept here is immunological self-tolerance, which prevents self-reactive lymphocytes from causing harm by eliminating or inactivating them (Shirafkan et al., 2024). When these tolerance mechanisms fail, it can result in autoimmune diseases, where the immune system mistakenly attacks self-tissues (Yasmeen et al., 2024).

1.1.1. Central and peripheral tolerance mechanisms

Self-tolerance is achieved through both central and peripheral mechanisms. In the thymus, immature T cells (thymocytes) undergo strict selection processes. During positive selection, thymocytes must recognize self–major histocompatibility complex (MHC) molecules with enough affinity to receive survival signals (Hogquist et al., 2005). Negative selection then eliminates thymocytes with T cell receptors (TCRs) that bind too strongly to self-peptides, mainly involving thymic epithelial cells and dendritic cells (Klein et al., 2014). This process prevents most autoreactive T cells from entering the periphery. Nevertheless, negative selection is not perfect, and some autoreactive T cells escape deletion (Hogquist et al., 2005). To handle these, multiple layers of peripheral tolerance come into play. Autoreactive T cells that encounter antigens without proper costimulatory signals (like CD28–CD80/CD86) may become anergic; they survive but are inactive (Podojil & Miller, 2009; Schwartz, 2003). Repeated stimulation without inflammatory cues can also cause activation-induced cell death, removing autoreactive clones. Additionally, regulatory T cells (Tregs), marked by FOXP3 expression, suppress autoreactive responses through cytokines such as interleukin-10 (IL-10 and transforming growth factor-β (TGF-β), and via cell–cell contact mechanisms. Together, central and

peripheral tolerance preserve immune balance and prevent autoimmunity under normal conditions (Sakaguchi et al., 2008).

1.1.2. Breakdown of tolerance and the emergence of autoimmunity

When these tolerance mechanisms break down, autoreactive T cells can become activated, resulting in harmful immune responses against the body's own antigens (Ujiie & Shimizu, 2012). One important mechanism contributing to this loss of tolerance is molecular mimicry, in which structural similarities between self-antigens and microbial epitopes lead to the activation of cross-reactive autoreactive T or B cells.

The specific outcome varies based on genetic factors, environmental influences, and the type of autoantigen involved. In systemic autoimmune conditions like systemic lupus erythematosus (SLE), a wide range of nuclear autoantigens are targeted, causing extensive inflammation and tissue damage (Pisetsky, 2024). Conversely, organ-specific autoimmune diseases such as type 1 diabetes or multiple sclerosis involve focused attacks on pancreatic β cells or central nervous system myelin, respectively. Despite these differences, a common feature is the central role of autoreactive $CD4^+$ T cells, which coordinate inflammatory responses and assist autoreactive B cells (Bieber et al., 2016; Ujiie & Shimizu, 2012). A key characteristic of many autoimmune diseases is the production of autoantibodies, which can cause damage through several mechanisms: (i) forming immune complexes that deposit in tissues and activate complement, (ii) binding Fc gamma receptors (FcγRs) on neutrophils and macrophages to recruit cells and release inflammatory mediators, and (iii) directly disrupting the function of their target proteins (Giltiay et al., 2012; Hampe, 2012). Examples include pemphigus vulgaris (autoantibodies to desmogleins), myasthenia gravis (anti-AChR antibodies), and Graves' disease (TSH receptor-stimulating antibodies), all of which illustrate how autoantibodies can directly impair or overactivate their target tissues.

Therefore, the generation of autoantibodies illustrates the convergence of abnormal T and B cell responses, with autoreactive $CD4^+$ T cells playing an essential role. These effector mechanisms are central to the pathology of epidermolysis bullosa acquisita (EBA), in which autoreactive $CD4^+$ T cells drive the production of pathogenic autoantibodies. Thus, EBA provides a powerful context to investigate how tolerance breakdown at the T cell level translates into autoantibody-mediated tissue injury (Bieber et al., 2016; Ludwig, 2013).

1.1.3. Epidermolysis Bullosa Acquisita as a model

EBA is a classic example of autoantibody-related pathology, a blistering autoimmune skin disorder caused by autoantibodies targeting type VII collagen (Col7), a key structural protein of anchoring fibrils at the dermal–epidermal junction (DEJ) (Ludwig, 2013). Clinically, EBA presents with skin fragility, subepidermal blistering, and scarring (Vorobyev et al., 2017). Patients show disease heterogeneity, including inflammatory and mechanobullous variants, which reflect different immunopathological mechanisms (Ludwig, 2013). The generation of anti-Col7 autoantibodies relies on autoreactive $CD4^+$ T cells, which help B cells and promote germinal center (GC) formation (Iwata et al., 2013). Notably, murine models of immunization-induced EBA reveal that disease severity is heavily influenced by the MHC haplotype, highlighting the importance of antigen presentation in disease susceptibility (Hammers et al., 2011). These models further confirm that EBA is driven by a Th1 immune response, evidenced by increased expression of the Th1 cytokine interferon-γ (IFN-γ) in draining LNs and lesional skin, along with the presence of complement-activating IgG2b and IgG2c autoantibodies in the blood and at the DEJ (Gross et al., 2024).

1.1.4. Relevance of EBA to mechanistic studies of autoimmunity

EBA provides a unique experimental platform for studying autoreactive T and B cell interactions. The disease relies heavily on $CD4^+$ T cell help. It provides measurable indicators

at various levels, such as circulating and tissue-bound autoantibodies, IgG deposition at the DEJ, infiltration of inflammatory cells in affected skin, and cytokine expression changes in draining lymphoid tissues (Kridin et al., 2019). Additionally, identifying Col7 as the autoantigen is a significant advantage in autoimmunity research; it is a well-defined molecular target that can be used precisely for experimental immunization. This clarity enables controlled manipulation of antigen exposure and consistent disease induction in mouse models (Koga et al., 2019).

The mouse model of immunization-induced EBA is now well-established and widely used. It accurately mimics the immunopathological features of human EBA, including dependence on Col7-specific autoantibodies, complement activation, and Fcγ receptor–mediated neutrophil recruitment at the DEJ (Kovacs et al., 2020; Zillikens et al., 2021). Importantly, the model is reproducible across labs and provides insight into the cellular and molecular processes leading to tissue damage mediated by autoantibodies (Kovacs et al., 2020). Unlike many autoimmune models with undefined autoantigens, EBA provides a manageable framework to trace the timeline from antigen exposure to T cell activation, GC formation, autoantibody production, and clinical pathology (Koga et al., 2019).

Consequently, EBA is valuable not only as a disease model but also as a paradigmatic system for studying autoimmunity and specifically autoantibody-mediated autoimmunity (Tešanović Perković et al., 2023). It facilitates understanding how immune tolerance is broken, how autoreactive $CD4^+$ T cells are activated, and how they influence B cell responses to produce autoantibodies continuously (Iwata et al., 2013). Notably, EBA allows investigation into the role of T follicular helper (Tfh) cells, a specialized $CD4^+$ subset essential for GC dynamics and autoantibody generation (Niebuhr et al., 2021). The availability of defined antigens, robust mouse models, and clear immunopathological readouts makes EBA a powerful tool to explore fundamental questions about T cell–B cell interactions in autoimmunity (Tešanović Perković et

al., 2023). Among the $CD4^+$ T cell subsets involved in EBA, Tfh cells are of particular importance. As the only T cells capable of sustaining GC reactions, they represent a critical bridge between autoreactive T cells and pathogenic B cell responses. The following section, therefore, outlines the biology of Tfh cells, their spatial dynamics within LNs, and their contribution to autoimmune pathology.

1.2. Tfh Cells, the T cell zone, and germinal center dynamics

This section will describe the biology of T cells and Tfh cells specifically, how Tfh cells are differentiated in the LN, the role of this T cell subset in GC formation, and its contribution to autoimmunity.

1.2.1. Biology of Tfh cells

Tfh cells, a specific subset of $CD4^+$ T cells, are uniquely designed to assist B cells. Their development is controlled by the transcription factor B cell lymphoma 6 (Bcl-6), which inhibits other lineage pathways, such as Th1, Th2, and Th17, while promoting genes necessary for follicular localization and B cell support. Additional key regulators include Ascl2 and c-Maf, which work alongside Bcl6 to define the Tfh transcriptional profile (Crotty, 2019).

Phenotypically, Tfh cells are identified by the expression of the chemokine receptor CXCR5, which facilitates their migration from the T cell zone into CXCL13-rich B cell follicles. They also express high levels of programmed cell death protein 1 (PD-1) and inducible costimulator (ICOS), both of which are crucial for maintaining Tfh–B cell interactions. A key functional marker is the expression of CD154 (CD40L), a costimulatory molecule unique to antigen-activated T cells that is essential for B cell activation and survival within GCs (Vinuesa et al., 2016).

Cytokine secretion is another defining aspect of Tfh cells. They produce abundant interleukin-21 (IL-21), a cytokine vital for B cell proliferation, class-switch recombination, and affinity

maturation. Depending on the context, Tfh cells may also secrete IL-4, supporting class switching to IgG1 and IgE, or IFN-γ, which promotes switching to IgG2a/c subclasses (Niebuhr et al., 2021). These cytokine profiles demonstrate the ability of Tfh cells to tailor B cell responses based on the nature of the antigen and the local inflammatory milieu (Crotty, 2019).

1.2.2. The T cell zone as the origin of Tfh differentiation

Within secondary lymphoid organs like the LN, the T cell zone (paracortex) serves as the main area where naïve T cells first encounter antigens. Dendritic cells, mainly antigen-presenting cells, migrate into this region with antigens from peripheral tissues and display peptide–MHC class II complexes to $CD4^+$ T cells. When T cells recognize their specific antigen, they receive additional signals such as CD28–CD80/86 and ICOS–ICOSL, along with cytokines like IL-6 and IL-21. These signals trigger clonal expansion and differentiation (Crotty, 2014, 2019). Some activated $CD4^+$ T cells develop into Tfh cells, marked by Bcl6, CXCR5, PD-1, and ICOS expression (Vinuesa et al., 2016). These early Tfh precursors then migrate toward the boundary between the T and B cell zones, guided by chemokines, and eventually move into the B cell zone follicles (Kim et al., 2024).

Beyond initiating normal immune responses, the T cell zone also represents a critical checkpoint in tolerance. Autoreactive $CD4^+$ T cells that escape thymic deletion can become activated here and, if not suppressed by regulatory mechanisms, may differentiate into Tfh precursors (Walker, 2022). Because only Tfh cells can enter B cell follicles and drive GC responses, the events that occur in the T cell zone strongly influence whether an immune response remains protective or becomes autoreactive. This is particularly relevant in autoantibody-mediated diseases such as EBA, where Tfh differentiation in the paracortex seeds GC reactions that sustain pathogenic B cell help (Niebuhr et al., 2021; Niebuhr et al., 2020).

The LN is divided into anatomical compartments that can be seen under a microscope. B cell follicles, found in the cortex beneath the capsule, are rich in $B220^+$ cells and serve as the

environment where B cells grow and are tested. When the immune system is activated, B cells in these follicles multiply and create GCs (Takeuchi et al., 2018; Victora & Nussenzweig, 2012). The nuclear protein Ki67 is commonly used to detect these dividing B cells, making it a good marker for active GC activity (Playoust et al., 2023). In contrast, the T cell zone is located in the paracortex between follicles and is mainly made up of T cells. This organization keeps T cells first active in the paracortex before they move into the follicles to assist B cells (Daniel et al., 2022).

GC formation represents a key transition point in the adaptive immune response. Following antigen exposure, B cells that capture and process antigen migrate toward the T–B border, where they present peptide–MHC class II complexes to newly activated $CD4^+$ T cells (Syeda et al., 2024). These interactions lead to the establishment of GCs, which are structurally divided into a dark zone of proliferating centroblasts undergoing somatic hypermutation and a light zone where centrocytes compete for selection (Allen et al., 2007; Gatto & Brink, 2010). The high proliferation rate of GC B cells explains the strong Ki67 staining typically observed in these structures (Allen et al., 2007; Victora & Nussenzweig, 2012). These structural events establish the GC microenvironment in which Tfh cells exert their specialized functions. How mature Tfh cells guide B cell selection, survival, and affinity maturation within GCs is discussed in the following section.

The compartmentalization of these zones is illustrated in Figure 1, showing a murine LN stained for B220 (blue, B cell follicles), Ki67 (brown/red, proliferating GC B cells), and TCRβ (beige, T cell-rich paracortex). $B220^+$ follicles are evident in the cortex, $Ki67^+$ clusters mark GCs within follicles, and the T cell zone is seen as the central paracortex between follicles. Together, these structural compartments establish the framework for Tfh differentiation and the initiation of GC responses, which ultimately drive high-affinity antibody production (Bahreini, Niebuhr, Belde, Bieber, et al., 2022; Bahreini, Niebuhr, Belde, Westermann, et al., 2022; Niebuhr, 2019).

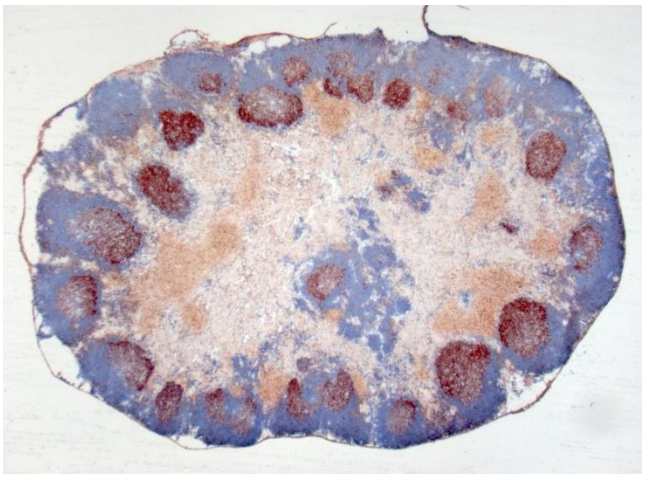

Figure 1. Structural compartmentalization of a murine lymph node. Immunohistology for B220 (B cells, blue), Ki67 (proliferating GC B cells, brown/red), and TCRβ (T cells, beige) reveals distinct anatomical zones: B cell follicles in the cortex, proliferating GCs within follicles, the T cell zone (paracortex) in the central area, and the medulla extending toward the hilum. Tfh cells differentiate in the T cell zone before migrating into GCs to support B cell responses.

1.2.3. Tfh cells in germinal center function

Once Tfh cells enter follicles and establish GCs, they play their specialized role in guiding B cell selection and differentiation. In the light zone of the GC, Tfh cells communicate with B cells via CD40L–CD40 interactions, ICOS–ICOSL engagement, and cytokines like IL-21 and IL-4 (Crotty, 2019; Kim et al., 2024; Yang et al., 2024). These signals collectively influence B cell survival, additional mutation rounds, or differentiation into plasma or memory B cells (Crotty, 2019; Kim et al., 2024). By selectively assisting B cells that present high-affinity peptide–MHC complexes, Tfh cells promote affinity maturation, helping expand only the most effective antibody clones (Petersone & Walker, 2024).

This phase of the GC reaction is crucial for producing long-lasting plasma cells and memory B cells, which support durable humoral immunity. Notably, the assistance from Tfh cells is specific and closely linked to antigen recognition. Since only $CD4^+$ T cells that have encountered an antigen can become Tfh cells, their presence in GCs inherently indicates antigen-specific activation. Consequently, the Tfh TCR repertoire (TCRR) provides a direct

molecular indicator of the antigens that influence humoral immunity (Niebuhr et al., 2021; Song & Craft, 2024).

In autoimmunity, this targeted assistance can turn harmful. Supporting autoreactive B cells, abnormal Tfh responses promote the production of high-affinity autoantibodies that can cause tissue damage. Therefore, although Tfh cells are essential for protective immunity, they also play a central role in driving autoantibody-mediated autoimmune diseases like systemic lupus erythematosus, pemphigus vulgaris, and EBA (Christodoulou et al., 2025).

1.2.4. Pathogenic potential of Tfh cells in autoimmunity

Growing evidence suggests that Tfh cells are key players in autoantibody-related diseases. This concept is covered by both human disease and murine models, which consistently demonstrate an expanded or dysregulated Tfh compartment in autoantibody-driven conditions. In systemic lupus erythematosus (SLE), higher levels of circulating Tfh-like cells are linked to disease activity and autoantibody levels (Kim et al., 2018). In pemphigus vulgaris, Tfh cells have been shown to encourage autoreactive B cell responses against desmogleins (Holstein et al., 2021). In mouse models of EBA, Tfh cells display limited TCRR, indicating clonal expansion of autoreactive Tfh clones (Niebuhr et al., 2021). These findings support the idea that abnormal Tfh responses directly contribute to breaking immune tolerance and boosting autoreactive B cell activity.

Overall, Tfh cell biology emphasizes their dual role as key regulators of protective antibody responses and as potent contributors to autoantibody-related disease when immune tolerance breaks down. Since Tfh cells are inherently antigen-specific, examining their TCRR offers a direct molecular insight into the clonotypes responsible for protective versus autoreactive

responses. The following section will concentrate on developing and analyzing TCR diversity and its significance for autoimmunity.

1.3. Understanding TCRR

This section will aim to describe the current understanding of the area of TCRR by explaining the structure and generation of TCRR and its diversity, the up-to-date approaches to analyze TCRR, TCRR alterations in autoimmunity and autoimmune blistering diseases, and last but not least, why it is pivotal to analyze Tfh and T cell zone repertoires.

1.3.1. Structure and generation of TCR diversity

TCR is the key factor in antigen recognition within adaptive immunity. Most traditional T cells have a heterodimeric TCR made up of an α and a β chain, each with variable and constant regions. Among these, the β chain is most commonly studied in repertoire analyses because it greatly influences diversity by including D gene segments, which are not present in the α chain, and it often offers more detailed clonotype information (Rosati et al., 2017).

Each TCR chain contacts peptide–MHC (pMHC) complexes through three complementarity-determining regions (CDRs). CDR1 and CDR2 are encoded within the germline V segment and primarily interact with the α-helices of the MHC molecule. By contrast, CDR3 spans the junction of V, D, and J segments in the β chain and incorporates both germline-encoded and non-templated nucleotides added during recombination. This region lies at the center of the antigen-binding site and makes direct contact with the presented peptide, thereby acting as the principal determinant of antigen specificity. Because of its high degree of variability, CDR3 is the focus of nearly all repertoire sequencing studies and defines the clonotype of individual T cells (Vujovic et al., 2020; Wong et al., 2019).

Diversity in the TCRR develops during T cell maturation in the thymus through V(D)J recombination. During this process, RAG1 and RAG2 enzymes facilitate precise cleavage at recombination signal sequences (RSS), allowing for the random assembly of one variable (V), one diversity (D), and one joining (J) segment (Braams et al., 2023; Fugmann, 2001). These segments are then joined to a constant (C) region to form a full exon that encodes the TCRβ chain. In mice, the TCRβ locus includes approximately 35 V segments, 2 D segments, and 13 J segments, resulting in hundreds of possible combinations (Migalska et al., 2018). This diversity is further enhanced by junctional diversity, which results from the imperfect joining of segments and the random addition or deletion of nucleotides by terminal deoxynucleotidyl transferase (TdT). Junctional diversity mainly contributes to variability in the CDR3 region and greatly expands the potential TCRR, reaching over 10^15 unique sequences (Zarnitsyna et al., 2013).

After recombination, the rearranged DNA is transcribed, undergoes RNA splicing, and is translated into a functional TCRβ chain. This chain pairs with a rearranged TCRα chain to create the αβ heterodimer present on the T cell surface (Rosati et al., 2017). Structurally, CDR1 and CDR2 play a role in stabilizing interactions with MHC molecules, while the highly variable CDR3 loop determines peptide specificity (Croce et al., 2024; Wong et al., 2019). Therefore, the TCR's organization forms a precisely calibrated system where germline-encoded regions are crucial, regions provide stability, and somatically diversified junctional regions confer specificity.

Figure 2 (adopted and redesigned from Migalska et al. (Migalska et al., 2018)) illustrates the process, showing the germline TCRβ locus, V, D, and J gene segment recombination, and the formation of the CDR3 region. It also emphasizes the subsequent molecular steps, transcription, splicing, and translation, that lead to the assembly of the αβ TCR heterodimer on the T cell surface. The figure highlights why CDR3β is the main target of high-throughput sequencing: it

reflects the highest diversity and offers a direct molecular indicator of antigen-specific T cell responses.

The diversity generated does not happen without limits. T cells undergo strict selection in the thymus, which shapes their pool before they migrate to the rest of the body. Positive selection allows thymocytes with TCRs that can weakly bind self–MHC molecules to survive, while negative selection removes those with TCRs that bind too strongly to self-peptide-MHC complexes (Kim et al., 2021; Klein et al., 2014). This two-step process greatly narrows the potential repertoire, creating a group of T cells that are MHC-restricted but mostly self-tolerant. However, thymic selection is not perfect, and some autoreactive clones can escape into the periphery, serving as the foundation for autoimmune diseases (Parish & Heath, 2008).

These structural and developmental principles have a significant impact on repertoire analysis. First, the CDR3β region, being the most diverse part of the TCR, serves as the best target for sequencing-based methods (Turner et al., 2006). Second, the equilibrium between diversity and clonality indicates the immune system's functional status: a diverse and evenly spread repertoire signifies health, while oligoclonal expansions are typical in infections, cancer, or autoimmunity (N. Li et al., 2020). Lastly, since thymic selection does not eliminate all autoreactive TCRs, repertoire analysis is uniquely capable of revealing the clonal dynamics involved in diseases like EBA (Niebuhr et al., 2021; Yates, 2014).

In autoimmunity research, analyzing the TCRR offers valuable insights into both the diversity of the T cell population and the development of dominant clonotypes that could contribute to disease progression (Niebuhr et al., 2021). This reasoning forms the basis for the analyses in this thesis, where the TCRβ repertoire of Tfh cells in GCs and T cells in the paracortical T cell zone was studied to explore different aspects of autoreactive T cell behavior.

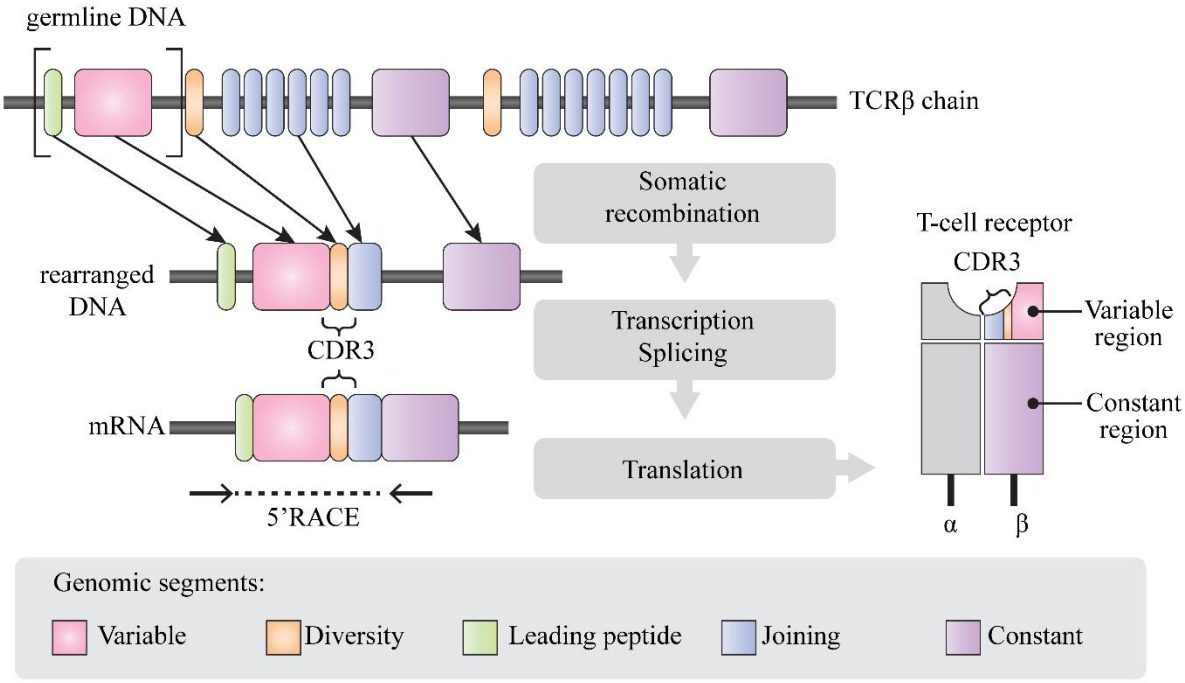

Figure 2. Generation of TCRβ diversity through V(D)J recombination. The germline TCRβ locus contains multiple variable (V), diversity (D), joining (J), and constant (C) gene segments, together with a leading peptide sequence. During T cell development, somatic recombination randomly joins one V, one D, and one J segment to form a rearranged locus. Junctional diversity is introduced at the V–D and D–J junctions by random nucleotide insertion and deletion, creating a highly variable third complementarity-determining region (CDR3). The rearranged DNA is transcribed, spliced, and translated into a functional TCRβ chain, which pairs with a rearranged TCRα chain to form the αβ TCR expressed on the cell surface. While CDR1 and CDR2 are germline-encoded and primarily contact the MHC molecule, CDR3 lies at the center of the antigen-binding site and provides the major determinant of peptide specificity. *The figure was adopted and redesigned from Migalska et al. (Harrell et al., 2008; Migalska et al., 2018)*

1.3.2. Approaches to analyze the TCRR

Advancements in high-throughput sequencing have enabled detailed quantitative and qualitative analysis of TCRR at an unprecedented level of detail (Heather et al., 2018). Current repertoire analyses mainly focus on the TCRβ chain, as the presence of D segments and

extensive junctional modifications offers sensitive insights into clonal selection (Rosati et al., 2017). In this context, individual clonotypes are usually identified by unique combinations of V gene, J gene, and CDR3 amino acid sequences (Farmanbar et al., 2019). The complete set of clonotypes in a sample forms the TCRR, with their relative frequencies serving as a fingerprint of current or past antigen-induced immune responses (Fu et al., 2021).

To analyze and compare repertoires, several metrics are commonly used. Richness indicates the total number of unique clonotypes in a sample, representing the repertoire's breadth, while clonality measures how evenly these clonotypes are distributed throughout the sample. Polyclonal repertoires have many small clones, whereas oligoclonal repertoires are dominated by a few expanded clones, often signifying strong antigen-driven expansion (Chiffelle et al., 2020). Diversity indices, like Shannon entropy and Simpson’s diversity index, merge richness and evenness into a single value, reflecting overall repertoire complexity (Mahdy et al., 2024; Seay et al., 2016; Simpson, 1949). In autoimmune or chronic inflammatory conditions, decreased diversity and increased clonality are often seen, indicating the selective growth of autoreactive or persistent T cell clones (Tuong et al., 2024).

Beyond overall diversity within a sample, comparing repertoires across different groups or anatomical sites requires measures of overlap. Jaccard indices evaluate the proportion of shared clonotypes between two repertoires, ignoring their abundance (Kang et al., 2015; Magurran, 2013). Conversely, the Morisita–Horn index considers clonotype frequencies, highlighting the impact of dominant clones that may significantly influence immune responses (Horn, 1966; Venturi et al., 2008). Jensen–Shannon divergence extends this by comparing probability distributions, providing values that indicate whether repertoires are nearly identical or markedly different (Yokota et al., 2017). In practical terms, Jaccard focuses on repertoire breadth, while Morisita–Horn and Jensen–Shannon more directly reflect the effects of clonal dominance and selection pressures.

Structural features of the repertoire offer additional insights. The distribution of CDR3 lengths results from recombination and thymic selection, with shifts reflecting constraints imposed by specific antigens or MHC haplotypes (Lu et al., 2019). Amino acid k-mer analysis breaks down short sequence motifs within CDR3 loops, linking biochemical properties like charge, polarity, and hydrophobicity to peptide–MHC binding preferences (Yohannes et al., 2021). Finding recurrent motifs across different clones is often seen as evidence of convergent selection, where distinct T cells develop similar structural solutions to recognize the same antigen. Likewise, V and J gene usage profiles can reveal recombination biases inherent to the gene locus or non-random selection of specific segments during immune responses (Mark et al., 2022).

Repertoire analysis is significantly affected by technical and experimental factors. Sequencing depth influences diversity estimates, as detecting rare clonotypes requires adequate coverage (Laydon et al., 2015; Rosati et al., 2017). Normalization methods, such as down-sampling to equal read depths, are often used to make comparisons between samples fair (Wang et al., 2019). Additionally, bioinformatics pipelines need careful definition of clonotypes since minor sequence errors or PCR artifacts can artificially increase perceived diversity (Smirnova et al., 2023; Wang et al., 2021). Despite these issues, reliable frameworks now facilitate meaningful comparisons of repertoires across biological replicates, treatment groups, and anatomical compartments (Seo & Choi, 2025).

These approaches, when combined, create a comprehensive toolkit for studying TCRR. Quantitative measures determine breadth and dominance, overlap metrics evaluate similarity, and sequence-based analyses identify structural features related to antigen specificity. In autoimmune disease research, these techniques are beneficial for detecting skewed repertoires, autoreactive clonal expansions, and convergent motifs that may contribute to disease. In this study, we applied these methods to analyze Tfh cells in GCs and T cells in the paracortical zone,

providing a detailed view of how tolerance loss and immune modulation reshape repertoire architecture across different lymphoid tissues.

1.3.3. TCRR alterations in autoimmunity and autoimmune blistering diseases

The TCRR's structure directly reflects how the immune system balances tolerance and reactivity (Zhang et al., 2025). In healthy people, peripheral T cell pools display wide diversity and polyclonality, with no single clonotype dominating. This even spread allows for effective immunity against various pathogens while reducing the risk of autoreactive clones gaining an advantage. In this setting, diversity acts as a protective buffer: the greater the clonotype variety, the less likely autoreactive clones will expand uncontrollably (Emerson et al., 2017).

In contrast, autoimmunity often shows evidence of TCR restriction. Multiple studies across various diseases reveal a decreased repertoire diversity, biased gene usage, and oligoclonal expansions, which suggest antigen-driven selection. For instance, in systemic lupus erythematosus (SLE), circulating and tissue-resident T cells tend to have limited repertoires with convergent CDR3 motifs, indicating shared autoreactive specificities (Hou et al., 2023; Zeng et al., 2025). Tfh cells in SLE have been shown to support autoreactive B cells that produce anti-nuclear antibodies, with restricted TCRR closely linked to disease activity (Blanco et al., 2016). In type 1 diabetes mellitus (T1DM), pancreatic islets are infiltrated by $CD4^+$ T cells with narrowed TCR usage, reflecting clonal expansion against β-cell antigens (Kent et al., 2005). Similarly, in multiple sclerosis (MS), CNS-infiltrating T cells display biased Vβ usage and oligoclonal dominance, indicating selective expansion in response to myelin antigens (Oksenberg et al., 1990). These findings highlight a common pattern: healthy immune repertoires are diverse and balanced, whereas autoimmunity is characterized by clonal skewing, reduced diversity, and the persistence of autoreactive clones.

Autoimmune blistering diseases (AIBDs) offer a valuable model for studying these principles because their pathology is closely tied to autoreactive B cells and their $CD4^+$ T cell helpers. For instance, in pemphigus vulgaris, Tfh cells are increased and aid B cell responses against desmogleins, which are the key adhesion molecules targeted by autoantibodies (Hennerici et al., 2016). Changes in the Tfh cell repertoire have been linked to heightened GC activity and continuous production of high-affinity IgG autoantibodies (Crotty, 2014; Merkenschlager et al., 2021). Similarly, in bullous pemphigoid, higher levels of circulating Tfh-like cells are associated with more severe disease and increased IgG autoantibodies against BP180 and BP230, indicating that skewed Tfh activity is a common feature of blistering autoimmune conditions (Li et al., 2013; Pérals et al., 2025).

EBA provides a particularly accessible system for studying repertoire dynamics in AIBDs. Earlier research using murine models of immunization-induced EBA showed that Tfh repertoires in draining LNs become clonally restricted as the disease progresses (Niebuhr et al., 2021). This restriction suggests the selective growth of dominant autoreactive $CD4^+$ T cell clones that are specific for Col7, the autoantigen involved in EBA. These expanded Tfh clones inhabit GCs, where they assist autoreactive B cells, promoting the production of Col7-specific autoantibodies. These antibodies deposit at the DEJ, causing tissue damage. Therefore, repertoire restriction in EBA is not just a consequence of immune activation but a key mechanism driving the disease, indicating a failure of tolerance at the Tfh level during selection and expansion.

From a mechanistic perspective, the limited TCRR in AIBDs highlights the antigen-driven nature of these diseases. While infections often produce diverse repertoires with many clonotypes, autoimmunity tends to involve the expansion of a few autoreactive clonotypes that repeatedly encounter their specific self-antigen in secondary lymphoid organs (Mitchell & Michels, 2020). This results in decreased diversity, increased clonality, and shared motifs in

CDR3 regions (Zou et al., 2023). The detection of these features in Tfh repertoires strongly indicates that autoreactive $CD4^+$ T cells actively support GC responses and the production of pathogenic autoantibodies.

Repertoire studies across autoimmune diseases consistently show limited diversity and clonal dominance, indicating autoreactive selection (Mitchell & Michels, 2020; Terhaar et al., 2024). In autoimmune blistering diseases (AIBDs) such as pemphigus, bullous pemphigoid, and EBA, these changes are especially significant because Tfh cells play a key role in driving autoreactive B cell responses (Fang et al., 2020; Lee et al., 2023). Consequently, the TCRR offers a molecular perspective to observe how immune tolerance breaks down and autoreactive T cell clones emerge (Mitchell & Michels, 2020). These findings underpin the analyses in this thesis, where the TCRβ repertoires of Tfh cells and T cell zone populations were examined to understand how tolerance failure and immune regulation influence clonal architecture in blistering autoimmunity.

1.3.4. Why analyze Tfh and T cell zone repertoires?

Tfh cells serve as the effector component of humoral immunity, because only antigen-activated $CD4^+$ T cells can enter GCs and assist B cells. Their repertoires therefore reflect the specific clonotypes involved in antibody responses, including those that are autoreactive in blistering diseases. In contrast, the T cell zone (paracortex) is the initial site of priming, where naïve $CD4^+$ T cells first meet antigen-presenting dendritic cells and undergo tolerance checks. Examining repertoires in both areas offers complementary insights: T cell zone repertoires show the initiation and potential failure of tolerance, while Tfh repertoires demonstrate the results of clonal selection and effector differentiation (Allen et al., 2011; Niebuhr et al., 2021; Seay et al., 2016). This dual approach provides a more comprehensive understanding of how autoreactive T cells arise and support harmful B cell responses in autoimmunity.

1.4. Ovalbumin in adjuvants pretreatment as a model of antigen-specific immune reprogramming in EBA

Previous research showed that in immunization-induced EBA, the TCRR of Tfh cells in draining LNs becomes clonally restricted (Niebuhr et al., 2021). It was found that in the disease, Tfh repertoires are dominated by a few expanded clonotypes, with significant overlap between contralateral LNs. This pattern indicates that a small pool of autoreactive $CD4^+$ T cells undergoes clonal expansion and migrates across lymphoid tissues to sustain GC activity. Such repertoire restriction is characteristic of antigen-driven autoreactivity and highlights Tfh cells' key role in aiding pathogenic B cells during EBA. The study also suggested that TCRR restriction plays a part in EBA development. A later study by Niebuhr and colleagues, published in The Journal of Investigative Dermatology, examined whether prior antigen exposure could influence these autoreactive responses (Niebuhr et al., 2020). In this experiment, mice were pretreated with ovalbumin (OVA), a highly immunogenic xenogeneic protein for mice due to a lack of previous tolerance, combined with adjuvants Alum and Titermax (OVA+Alum+Titermax: OAT). OVA served as a strong but irrelevant stimulus, Alum promotes Th2 responses, and Titermax enhances innate activation as a potent emulsifying adjuvant and is also reported as a Th1 adjuvant (Baumjohann et al., 2013; Fan et al., 2022; McKee & Marrack, 2017). Collectively, this approach aimed to condition the LN environment before murine type VII collagen C-terminal fragment (mCol7c) immunization. It was demonstrated that OAT pretreatment completely prevented the clinical development of EBA, whereas pretreatment with PBS in Alum and Titermax (PAT) did not interfere with disease (Figure 3A) (Niebuhr et al., 2020). Protection was observed despite the ongoing presence of Col7-specific autoantibodies and GCs, which shows that B-cell activation and autoantibody production continued. The key difference was in the cytokine profile of the T cell population. In mice pretreated with OAT, T cell zones showed significantly lower levels of *IFN-γ*, resulting in a reduced *IFN-γ/IL-4* ratio and a shift from Th1 to Th2 responses. These findings suggest

that OAT does not prevent Tfh cell differentiation or GC formation but instead shifts the functional polarization of $CD4^+$ T cells away from harmful Th1 responses.

The pretreatment protocol aimed to target the LNs that would later drain the autoantigen challenge (see Figure 3B). Injections into the hind footpads drain directly to the popliteal lymph node (Pln), while injections at the tail base drain to Ingln (Harrell et al., 2008). By administering OAT sequentially into both footpads and the tail base, antigen exposure was distributed across these key draining sites prior to mCol7c immunization. Previous studies showed that this approach reduced *IFN-γ/IL-4* expression and shifted the immune response toward a Th2 profile in the draining LNs, creating a preconditioned environment for autoreactive priming (Niebuhr et al., 2020). Overall, these findings indicate that (i) Tfh repertoires in EBA typically become clonally restricted, reflecting autoreactive T cell expansion, and (ii) OAT prevents disease by modulating cytokine balance in T cell zones and changing T cell help quality (Niebuhr et al., 2021; Niebuhr et al., 2020). The main insight is that protection does not stem from the absence of autoreactive B cells or autoantibodies, but from reprogramming the T cell compartment toward a less pathogenic, Th2-biased state. OAT serves as a model of antigen-specific immune deviation, where a xenogeneic protein combined with Th2-biasing adjuvants imparts tolerance-like properties to LN immunity before autoimmune challenge. While these results highlight cytokine reprogramming, they also suggest that OAT might counteract Tfh repertoire restriction in EBA, preventing autoreactive T cell clonal dominance in LNs that initiate the disease.

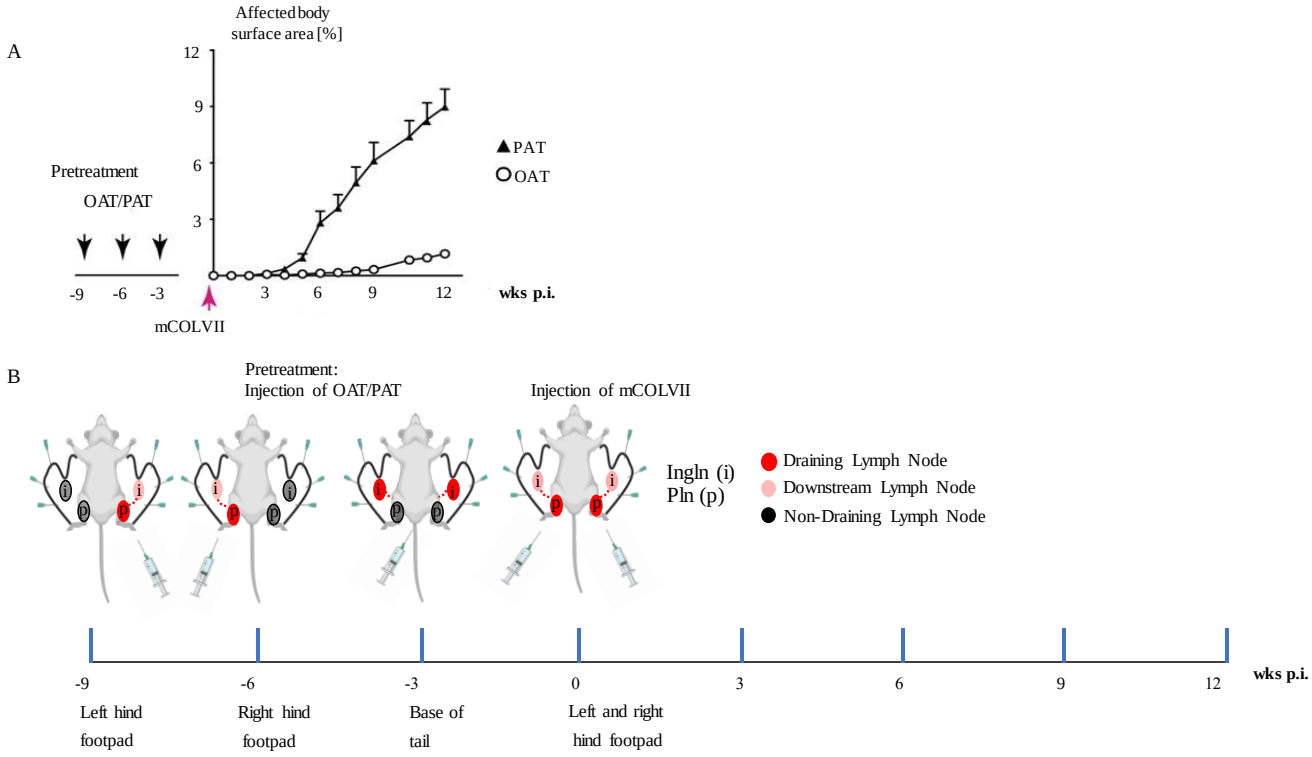

Figure 3. Experimental design and disease severity in the OAT-pretreated EBA mouse model. A) Affected body surface area (%) over time in OAT-pretreated and PAT-only groups. OAT pretreatment completely inhibited EBA development compared to the PAT control group.

B) Timeline of pretreatment and immunization protocol. Mice received OAT/PAT injections in the left hind footpad (week –9; draining to the left popliteal lymph node, Pln), right hind footpad (week –6; draining to the right Pln), and base of the tail (week –3; draining to the inguinal lymph nodes, Ingln), followed by mColVIIc immunization in both hind footpads at week 0. Disease progression was monitored for 12 weeks post-immunization (p.i.). The photo was adopted from *Niebuhr et. al., JID 2020.* And *Harreell et al., J Immunol*

From a mechanistic standpoint, OAT illustrates the concept of immune deviation. Unlike deletion or anergy, which silence or remove autoreactive clones, OAT permits GCs and autoantibody production to persist but shifts $CD4^+$ T cell responses toward a Th2-biased profile. Since EBA exhibits limited Tfh repertoires, it is likely that OAT's protection results not only from a cytokine shift from Th1 to Th2 but also from expanding the TCRR, thus reducing the dominance of autoreactive T cell clones. Although OVA pretreatment effectively prevents disease development in experimental models, its protective effect is not strictly antigen-specific. Rather than inducing tolerance only toward OVA epitopes, it promotes a broader, bystander-type immune modulation that suppresses autoreactive responses. In contrast, cell-derived

nanoparticles (CDNPs) represent a multiepitopic mixture of intracellular proteins, offering a diverse repertoire of naturally processed self-antigens that can engage multiple immune pathways simultaneously. This composition suggests that CDNPs may mimic and even enhance the immunomodulatory effects of OAT pretreatment, providing a more versatile strategy for controlling autoimmune inflammation. The following section will focus on CDNPs and their potential as a broadly applicable approach for immune modulation in autoimmunity.

1.5. CDNPs as multiepitopic immune modulators

The antigen-specific immune deviation induced by OAT demonstrates that autoreactive pathology in EBA can be prevented by conditioning the lymph node (LN) environment prior to disease onset. However, a major limitation of this method is its reliance on a specific antigen (OVA), which limits its relevance to human autoimmunity, where the triggering autoantigens are often unknown, diverse, or multiple. To address this issue, alternative strategies have been developed that do not depend on a single defined antigen but instead expose the immune system to a wide range of antigens with multiple epitopes. One such method uses CDNPs, which serve as versatile regulators of both innate and adaptive immune responses through their complex and physiologically relevant protein composition.

1.5.1. Composition and structural features of CDNPs

CDNPs are protein-based nanoparticles isolated from mammalian cells under nutrient deprivation and stress (Kunz, Xia, et al., 2017). Kunz and colleagues showed that stressed cells release non-vesicular nanoparticles about 100–200 nm in size, which differ structurally from extracellular vesicles like exosomes (Kunz, Xia, et al., 2017; Osteikoetxea et al., 2015). Proteomic analysis indicates that CDNPs contain abundant intracellular proteins such as annexins, actin, histones, and heat shock proteins, along with small amounts of ribonucleotides (Kunz, Xia, et al., 2017). Their composition features a broad multi-epitope

protein profile, distinguishing them from the single-antigen stimulus of OVA used in OAT pretreatment. This diverse molecular cargo likely explains their ability to influence immune responses in a more generalized, multi-epitope manner.

1.5.2. Cellular uptake and innate immune reprogramming

CDNPs are mainly taken up by myeloid cells, especially macrophages and neutrophils, where they modulate innate immune responses to become less pro-inflammatory. In macrophages, CDNPs uptake increases IL-10 and decreases IL-1β, both at baseline and after zymosan stimulation, with a tendency for reduced TNF-α, while IL-6 levels stay stable (Kunz, Hauenschild, et al., 2017). Neutrophils also acquire a regulatory phenotype after internalizing CDNP. They display a temporary increase in CD11b, sustained CD80 expression, and higher IL-10 secretion. However, they do not activate typical effector responses, such as ROS production, NETosis, or TNF-α release. Instead, they become less responsive to LPS, migrate less effectively toward CXCL12, and are strongly inclined toward apoptosis (Raudszus et al., 2025). Overall, these findings indicate that CDNP uptake alters innate immune cells into states that result in less tissue damage, thereby creating an anti-inflammatory environment that supports healing and recovery. These changes in innate immunity set the stage for subsequent regulation of adaptive immune responses.

1.5.3. Effects on adaptive immunity

In addition to affecting innate cells, CDNPs also influence adaptive immune responses. In an antibody-induced EBA model, treating with CDNPs markedly elevated IL-4 levels in draining LNs, pointing to a Th2 skewing, while preserving lymphoid structure and germinal centers (Kunz, Hauenschild, et al., 2017). This indicates that CDNPs modify the quality of T-cell assistance and effector differentiation without disturbing the overall organization or activation of adaptive immunity.

1.5.4. Disease models and functional outcomes

Research has shown that CDNPs affect autoimmune and infectious disease models, as well as *in vitro* systems. In antibody-induced EBA, Kunz et al. showed that administering porcine CDNP decreased dermal inflammation and enhanced clinical scores. This protection coincided with a significant increase in IL-4 mRNA in draining LN, while IL-10 and IFN-γ remained unchanged, and IL-1β and FcγRIV showed a downward trend. Importantly, CDNP treatment preserved lymphoid structures and GCs while modifying T-cell help and effector responses. The study also demonstrated that CDNPs promote epithelial regeneration in human skin explants, indicating a potential role in wound healing through a combination of immunomodulation and tissue repair. In a Leishmania major infection model, Kunz et al. reported that CDNP treatment elevated IL-4 production and shifted parasite-specific antibody responses toward IgG1, although lesion size was unchanged (Kunz, Hauenschild, et al., 2017).

In a polymicrobial sepsis model induced by cecal ligation and puncture, Kunz et al. observed in a separate study that CDNPs accumulated at the infection site, decreased peritoneal IL-6 and IL-10 levels, reduced the bacterial load by approximately two logs, and exhibited direct bacterial killing. These nanoparticles were primarily taken up by F4/80^{+} macrophages, with some uptake also observed in inflammatory monocytes and neutrophils, resulting in increased expression of CD11b and MHC II in these cells. Overall, these results indicate that CDNPs boost phagocyte activation and bacterial clearance, while also preventing excessive inflammation (Kunz, Xia, et al., 2017).

Additional *in vitro* studies reinforce these findings, indicating that some neutrophils take up CDNPs and experience functional changes, shifting to less harmful phenotypes (Raudszus et al., 2025). Overall, the findings suggest that CDNPs do not broadly suppress immunity but instead reprogram innate and adaptive responses into less harmful, more regulatory states. They decrease skin inflammation and promote Th2 responses in EBA, improve bacterial clearance in

sepsis, support epithelial regeneration, induce IL-4 and IgG1 in parasitic infections, and reprogram neutrophils into less damaging phenotypes *in vitro*. This evidence presents CDNPs as multi-component immunomodulators with potential applications in autoimmune blistering diseases, sepsis, and other conditions.

1.5.5. Conceptual positioning relative to OAT

The results of OAT pretreatment and CDNP administration can be seen as two complementary approaches for reprogramming the immune system. OAT, which combines a xenogeneic protein (OVA) with adjuvants that encourage Th1 and Th2 responses (Alum and Titermax), illustrates the concept of antigen-specific immune deviation. It shows that autoreactive damage in EBA can be avoided even when GC activity and circulating autoantibodies are ongoing. Mechanistically, OAT modifies the cytokine balance in T cell zones, reducing the *IFN-γ/IL-4* ratio and disconnecting autoantibody production from tissue-damaging immunity (Niebuhr et al., 2020). Additionally, considering the limited Tfh repertoires in EBA, it is likely that OAT also works by expanding the clonotypic diversity of Tfh cells, preventing autoreactive clonal dominance.

In contrast, CDNPs do not rely on a single defined antigen but instead function as multiepitopic immune modulators. Instead of depending on a specific epitope, they carry a diverse and multi-epitope protein cargo that can activate a wide range of immune receptors (Kunz, Xia, et al., 2017). This molecular diversity enables them to reprogram both innate and adaptive immune responses simultaneously. Functionally, CDNPs produce outcomes similar to OAT, such as decreased inflammatory activity, increased IL-4 production, and possible relief from clonal restriction without needing prior knowledge of the relevant autoantigen. Significantly, the antigen-agnostic property of CDNPs makes them more suitable for application in complex autoimmune diseases where the autoantigens initiating the condition may be unknown or differ among patients.

Thus, although OAT demonstrates proof of principle for antigen-specific deviation, CDNPs expand on this idea by providing a versatile platform for inducing tolerance. Both approaches suggest that immune reprogramming can be accomplished either through targeted antigen conditioning or by modulating cellular pathways independently of antigens. This thesis examines both strategies concurrently, focusing on how they change the Tfh receptor repertoire and influence the cytokine environment in autoimmune blistering disease.

1.6. Objectives and conceptual framework

Despite progress in modeling autoimmune blistering diseases like EBA, several questions remain open: why do Tfh repertoires become clonally restricted, how can pretreatments such as OAT prevent disease despite ongoing GCs and autoantibodies, and whether multiepitopic approaches such as CDNPs can replicate or enhance these protective effects? Addressing these gaps is crucial for understanding how local LN conditioning and systemic immune shifts interact to influence autoimmune outcomes.

The main goals of this thesis are threefold:

(i) to explore how OAT pretreatment reshapes Tfh clonality and transcriptional profiles in draining LNs,

(ii) to isolate and study CDNPs as multiepitope immune modulators, and

(iii) to assess how CDNPs influence TCRβ repertoire structure *in vivo*. These objectives connect antigen-specific and multiepitopic approaches for managing autoreactive T cell responses.

The thesis begins with an analysis of OAT pretreatment, examining repertoire changes and transcriptional shifts in the Pln and Ingln. It then moves to CDNPs, where molecular profiling,

in vivo repertoire analysis, and transcriptional markers (*Tcrb, Gata3*) are used to test their capacity to promote diversification and induce tolerogenic immune deviation.

Ultimately, this work aims to demonstrate that both xenogeneic antigen conditioning and multiepitopic nanoparticle treatment converge on a common goal: diversifying the T cell repertoire and mitigating Th1-driven pathology. By integrating these strategies, the thesis not only advances the understanding of tolerance induction in EBA but also highlights new possibilities for broadly applicable, multiepitopic therapies in autoimmune diseases.

2. Materials and Methods

2.1. Materials

2.1.1. Laboratory animals

Female C57BL/6J mice, aged 8–10 weeks (Charles River Laboratory, Sulzfeld, Germany), were maintained under specific pathogen-free conditions, with free access to food and water. All procedures involving animals received approval from the Schleswig-Holstein state authority (Ministerium für Energiewende, Landwirtschaft, Umwelt, Natur und Digitalisierung; MELUND) and were conducted in accordance with institutional and national ethical standards.

2.1.2. Reagents and kits

Experiments were conducted using the reagents and kits mentioned in Table 1.

Table 1: Reagents and kits used in the process.

Item	Company
0.1 µm polystyrene beads (NanoStandards)	Particle Metrix GmbH, Germany
1,4-Dithiothreitol (DTT)	Sigma-Aldrich Inc., USA
2-Mercaptoethanol (98%)	Sigma-Aldrich Inc., USA
4’,6-Diamidino-2-Phenylindole (DAPI)	Thermo Fisher Scientific, USA
5× DNA Loading Buffer Blue	Bioline Reagents, UK
Acetic acid 100%	Carl Roth GmbH & Co. KG, Germany
Acetone 99.8%	Carl Roth GmbH & Co. KG, Germany
Agarose peqGOLD	VWR International GmbH, Germany
Alum adjuvant	Thermo Fisher Scientific
Annexin V (Annexin A5) antibody, GTX103250 (Lot 39890)	GeneTex, USA
Aquatex	Merck KGaA, Germany
aqueous mounting medium	Merck, Germany
Bepanthen Augen- und Nasensalbe	Bayer AG, Germany
Bovine Serum Albumin (BSA, IgG-free)	Sigma-Aldrich Inc., USA

Bromophenol Blue	Sigma-Aldrich Inc., USA
Benzonase	Sigma-Aldrich Inc., USA
Chloroform 99%	Carl Roth GmbH & Co. KG, Germany
Coomassie Brilliant Blue	Sigma-Aldrich Inc., USA
DMEM high glucose	Sigma-Aldrich Chemie GmbH, München, Germany
DNase I	Thermo Fisher Scientific, USA
dNTP Mix 10 mM each	Thermo Fisher Scientific, USA
(D)PBS (1×)	Gibco, Thermo Fisher Scientific, USA
PBS with MgCl2 and CaCl2	Sigma-Aldrich Inc., USA
Ethanol 99.8%	Carl Roth GmbH & Co. KG, Germany
ExtrAvidin Alkaline Phosphatase	Sigma-Aldrich
ExtrAvidin Alkaline Phosphatase	Sigma-Aldrich Inc., USA
ExtrAvidin Peroxidase	Sigma-Aldrich Inc., USA
Fast Blue RR Salt	Sigma-Aldrich Inc., USA
Formaldehyde 37%	Merck KGaA, Germany
Formamide 99%	Sigma-Aldrich Inc., USA
GlutaMAX™ Supplement	Gibco, Thermo Fisher Scientific, USA
Goat anti-rabbit IgG–FITC	Jackson ImmunoResearch, USA
Hematoxylin Solution (Mayer's)	Merck KGaA, Germany
Hydrochloric acid 37%	Sigma-Aldrich Inc., USA
HyperLadder 100 bp	Bioline Reagents, UK
innuPREP RNA Mini Kit 2.0	Analytik Jena
Isopropanol 99.95%	Carl Roth GmbH & Co. KG, Germany
Liquid DAB+ Substrate	Agilent Technologies, Inc., USA
MEM Non-essential Amino Acid Solution 100x	Sigma-Aldrich Inc., USA
Methanol 99.9%	Carl Roth GmbH & Co. KG, Germany
Midi Gel Adapter	Thermo Fisher Scientific, USA
MiSeq Reagent Kit v2 (300 cycle)	Illumina Inc., USA
Mouse anti-FITC–Alkaline Phosphatase	Jackson ImmunoResearch, USA
Mouse IL-6 ELISA Kit	Invitrogen GmbH, Germany
Mounting Medium	Sigma-Aldrich Inc., USA
MTBIvc reagent system (i1-18)	iRepertoire Inc., USA
Multiplex PCR Kit	QIAGEN N.V., Netherlands
N, N-Dimethylformamide	Sigma-Aldrich Inc., USA
NuPAGE 4–12% Bis-Tris Protein Gel	Thermo Fisher Scientific, USA
NuPAGE Antioxidant	Thermo Fisher Scientific, USA
NuPAGE MES SDS Running Buffer	Thermo Fisher Scientific, USA
OneStep RT-PCR Kit	QIAGEN N.V., Netherlands
Ovalbumin (OVA)	Sigma-Aldrich Chemie GmbH, München, Germany
PageRuler Prestained Protein Ladder	Thermo Fisher Scientific, USA

Pam3CSK4 (PAM) (TLR2/1 ligand)	EMC Microcollections GmbH, Tübingen, Germany
Paraformaldehyde	Carl Roth GmbH & Co. KG, Germany
Penicillin–Streptomycin	Thermo Fisher Scientific, USA
PerfeCTa NGS Quantification Kit	Quantabio, USA
PhiX Control v3	Illumina Inc., USA
Pierce™ BCA Protein Assay Kit	Thermo Fisher Scientific, USA
Pierce™ Chromogenic Endotoxin Quant Kit (LAL)	Thermo Fisher Scientific, USA
PMSF (phenylmethylsulfonyl fluoride)	Sigma-Aldrich Inc., USA
QIAquick Gel Extraction Kit	Qiagen, Netherlands
QuantiFluor RNA System	Promega Corporation, USA
RevertAid H^- Reverse Transcriptase (EPO 452)	Thermo Fisher Scientific
Rompun (20 mg/mL Xylazine)	Bayer Vital GmbH, Germany
Roti® Fluoro PVDF Membrane	Carl Roth GmbH & Co. KG, Germany
RNase-free water	QIAGEN N.V., Netherlands
Roti-GelStain	Carl Roth GmbH & Co. KG, Germany
Sodium azide (NaN_3)	Sigma-Aldrich Inc., USA
Sodium chloride (NaCl)	Merck KGaA, Germany
Sodium dodecyl sulfate (SDS)	Thermo Fisher Scientific, USA
Sodium hydroxide (NaOH)	Carl Roth GmbH & Co. KG, Germany
Sodium pyruvate	Sigma-Aldrich Inc., USA
SYBR Green PCR Master Mix	Thermo Fisher Scientific, USA
Toluidine blue	Merck, Germany
Tissue freezing medium	Leica Instruments GmbH, Germany
TiterMax	Sigma-Aldrich
Tris base	Sigma-Aldrich Inc., USA
Triton X-114	Sigma-Aldrich Inc., USA
Trypan blue 0.4%	Thermo Fisher Scientific, USA
Tween 20	Serva Electrophoresis GmbH, Germany
Xylene 99%	Merck, Germany
α-MEM medium	Bio & Sell GmbH, Germany

2.1.3. Solutions and buffer

The solutions and buffer mentioned in Table 2 were experimentally used.

Table 2: Solutions and buffers used in the process.

Solution / Buffer	Composition / Description
IHC antibody dilution buffer	1% w/v BSA (IgG-free), 0.5% w/v NaN_3, PBS
Immunofluorescence blocking solution	0.5% w/v BSA (IgG-free), PBS
Laemmli buffer	25 mM Tris, 192 mM glycine, 0.1% w/v SDS, 0.01% w/v Bromophenol blue, H_2O
NaOH (1 M)	1 M NaOH, H_2O
PAGE sample dilution buffer	15 mM DTT, 20% v/v Glycerol, 2.5% v/v 2-Mercaptoethanol, 1× Laemmli buffer
PBS	2.5 mM KCl, 1.5 mM KH_2PO_4, 140 mM NaCl, 6.5 mM Na_2HPO_4, H_2O, pH 7.25
TAE buffer	40 mM Tris base, 20 mM acetic acid, one mM EDTA, H_2O, pH 7.6
TBS-Tween	50 mM Tris base, 0.05% Tween 20, 0.8% NaCl, H_2O, pH 7.6
Tris buffer (0.1 M)	0.1 M Tris base, H_2O, pH 8.2
Coomassie Blue staining solution	0.2% w/v Coomassie Brilliant Blue, 10% v/v acetic acid, 40% v/v methanol, H_2O
Coomassie Blue destaining solution	10% v/v acetic acid, 40% v/v methanol, H_2O
DAPI staining solution	3.5 mM DAPI, PBS
Fast Blue staining solution	3 mM Fast Blue RR Salt, APAAP substrate
Fast Red staining solution	1.5 mM Fast Red RR Salt, APAAP substrate
Culture medium J774A.1	10 % FBS, 1% mM Glutamax, 1% streptomycin-penicillin.
Culture medium EFN-R	10 % FBS, 1% mM Glutamax, 1% streptomycin-penicillin, 1% Sodium Pyruvate, 1% non-essential amino acids
Washing buffer	500 mL PBS 0.05% Tween 20

2.1.4. Cell lines

Cell lines listed in Table 3 were used for the experimental trials.

Table 3: Cell lines used in the process.

Cell line	Species / Cell type	Supplier / Source
EFN-R	Porcine kidney epithelial cells	Friedrich-Loeffler-Institut, Insel Riems, Germany
J774A.1	Murine macrophage-like cell line	Cell Lines Service GmbH, Eppelheim, Germany

2.1.5. Consumables

Consumables listed in Table 4 were used for the experimental trials.

Table 4: Consumables used in the process.

Item	Manufacturer / Supplier
50 µm / 70 µm Cell Strainer	Greiner Bio-One GmbH, Austria
96-Well Plates (polypropylene, v-bottom)	Greiner Bio-One GmbH, Austria
Cell Culture Flasks (25, 75, 175 cm^2)	Sigma-Aldrich Chemie GmbH, Germany
Cell Scraper	Sarstedt AG & Co. KG, Germany
Centrifugation Tubes (15 mL, 50 mL)	Sarstedt AG & Co. KG, Germany
Cover Slips, 13 mm	Glaswarenfabrik Karl Hecht GmbH, Germany
CryoPure Tube 1.6 mL	Sarstedt AG & Co. KG, Germany
Cell Master Roller Flasche steril	Greiner, Germany
Eppendorf Combitips® (12.5 mL)	Eppendorf AG, Germany
ELISA microtest plate, 96-well, flat-bottom	Sarstedt, Germany

Glass Slides and Coverslips	Gerhard Menzel GmbH, Germany
MembraneSlide 1.0 PEN NF	Carl Zeiss Microscopy GmbH, Germany
MicroFine Insulin Syringes, 1 mL	Becton, Dickinson and Company, USA
Mini Cell Scraper	Biotium Inc., USA
Omnifix® 1 mL Syringes	B. Braun AG, Germany
Parafilm M®	Sigma-Aldrich Inc., USA
PCR Optical Adhesive Cover	Life Technologies, USA
PCR Plate Half Skirt (LP)	Sarstedt AG & Co. KG, Germany
Pipet-Jet	nerbe plus GmbH, Germany
Pipette Filter Tips (10 µL, 200 µL, 1000 µL)	nerbe plus GmbH, Germany
Pipette Tips (10 µL, 20 µL, 100 µL, 200 µL, 1000 µL)	nerbe plus GmbH, Germany
Pipette Tips (20–300 µL)	Eppendorf AG, Germany
Reaction Tubes (0.2 mL, 0.5 mL, 1.5 mL, 2 mL, 5 mL)	Sarstedt AG & Co. KG, Germany
Reaction Tubes (15 mL, 50 mL)	nerbe plus GmbH, Germany
Safe-Lock Tubes 1.5 mL	Eppendorf AG, Germany
Serological Pipette (25 mL)	Th. Geyer GmbH & Co KG, Germany
Serological Pipette (5 mL, 10 mL)	nerbe plus GmbH, Germany
Superfrost Plus Microscope Slides	Thermo Fisher Scientific, USA
Thermanox™ Coverslips	Thermo Fisher Scientific, USA

2.1.6. Primers

The primers listed in Table 5 were used in the experimental trials.

Table 5: Primers used in the process.

Gene / Target	Primer Sequence (5′ → 3′)	Supplier
Tcrb (T-cell receptor β chain)	F: CTT CAA AGA GAC CAA CGC CAC R: CTT TCA GCA GGA GGA TTC GGA G	Invitrogen, USA)
Gata3 (GATA binding protein 3)	F: GGT AAT GGG GAC TAC CTT TT R: TGG TGG TGG TCT GAC AGT TC	Invitrogen, USA)
Gapdh (Glyceraldehyde-3-phosphate dehydrogenase)	F: GAC GGC CGC ATC TTG T R: CAC ACC GAC CCA TTT T	Biomers, Germany

2.1.7. Devices and instruments

The devices and instruments listed in Table 6 were used in the experimental trials.

Table 6: Devices and instruments used in the process.

Device / Instrument	Manufacturer / Model
MiSeq System	Illumina Inc., USA
Cryostat	Leica CM3050S, Leica Microsystems, Germany
Laser Microdissection System	PALM MicroBeam / Microlaser-System SYS63TE/PA7, Carl Zeiss Microscopy GmbH, Germany
Thermal Cycler	Primus 96 Plus Thermal Cycler, Eurofins Genomics GmbH, Germany
Real-Time PCR System	StepOnePlus™ Real-Time PCR, Thermo Fisher Scientific, USA
Centrifuge	Centrifuge 5417R, 5247R, Thermomixer comfort, Eppendorf AG, Germany
Mini Centrifuge	MiniSpin Plus (Rotor F-45-12-11), Eppendorf AG, Germany

Vacuum Concentrator (SpeedVac)	Vacuum Centrifuge Concentrator 5301 (Rotor F-45-48-11), Eppendorf AG, Germany
Sonicator	Bandelin Sonopuls HD4100 with TS106 sonotrode, Bandelin Electronic, Germany
Ultracentrifuge	Beckman Coulter, USA
ELISA Plate Reader	Multiskan FC, Thermo Fisher Scientific, USA
Gel Documentation System	EBOX VX 5, VILBER LOURMAT GmbH, Germany
Electrophoresis Apparatus	Criterion Cell + PowerPac Basic, Bio-Rad Laboratories Inc., USA
Western Blot Imaging System	Odyssey® Infrared Imaging System, LI-COR Biosciences, USA
Nanoparticle Tracking Analyzer	ZetaView® NTA System (EV_488C), Particle Metrix GmbH, Germany
Optical Microscope	Olympus BX53 with DP74 Digital Camera, Olympus Europe, Germany
Additional Microscopes	Axiophot, Axioskop 2 plus, Axiovert 200, Carl Zeiss Microscopy GmbH, Germany
Thermomixer / Shaker	Thermomixer comfort, Eppendorf AG, Germany
Vortexer	Vortex-Genie 2, Scientific Industries Inc., USA
Mini Shaker titramax 1000	Heidolph, Germany

Quantus™ Fluorometer	Promega, USA
Water Bath	Phoenix, Germany
Class 2 biosafety cabinet	LabGard, USA
INCUDRIVE D-I, CM bottle incubator	Schuett Biotec, Germany
Power Supply	Heinzinger LNG 350-6 Economy Line, Germany
Pipettes	Eppendorf Research Plus, Eppendorf AG, Germany
Battery-powered pipetting aid accu-jet® S with power supply unit, berry	Brand, Germany
-80 °C Freezer	Panasonic, Japan
Scale 120g-0.0001 g	Sartorius, Germany
Scale 300g-0.1 g	Kern, Germany
Scale 300g-0.01 g	Kern, Germany
pH meter	Hanna Instruments, Germany

2.1.8. Antibodies

The antibodies used in the experimental trials are listed in Table 7.

Table 7: Antibodies used in the process.

Antibody	Clone / Catalog No.	Supplier
Anti-Ki-67	Clone 16A8	BioLegend, San Diego, USA
Anti-B220 / CD45R	Clone RA3-6B2	BioLegend, San Diego, USA
Anti-TCRβ	Clone H57-597	BD Pharmingen / Becton Dickinson and Company, USA
Annexin V (A5)	Cat. #GTX103250	GeneTex, Irvine, CA, USA
Goat Anti-Rabbit IgG (H&L) Antibody DyLight™ 800 Conjugated	Cat. #611-145-122	Rockland, USA
ExtrAvidin Alkaline Phosphatase	Cat. #E2636	Sigma-Aldrich Inc., USA
ExtrAvidin Peroxidase	Cat. #E2886	Sigma-Aldrich Inc., USA

2.1.9. Software and packages

Software and packages used for the experimental trials are listed in Tables 8 and 9, respectively.

Table 8: Software used in the process.

Software	Version	Developer / Publisher
MiSeq System Control Software	v4.1.0	Illumina Inc., USA
Leica LMD Software	v8.4	Leica Microsystems, Germany
ZetaView® Nanoparticle Tracking Software	ZetaView v8.05.16 SP7	Particle Metrix GmbH, Germany
Odyssey® Software	v3.0	LI-COR Biosciences, USA
GainData® ELISA Data Analysis	Online software	Arigo Biolaboratories, Taiwan, ROC
GraphPad Prism	v10	Dotmatics, USA
Microsoft Excel	Microsoft 365	Microsoft Corporation, USA
Aida image analyzer	v3.21	Elysia-Raytest, Germany
RStudio	2024.09.1 Build 394	Posit Software, USA
ClonoCalc	v2.1	Fraunhofer Institute for Cell Therapy and Immunology, Germany
MiXCR	v4.7	MiLaboratory, Russia
Endnote	21	Clarivate, USA
Grammarly	Online software	Grammarly, Inc
ChatGPT	4.5	OpenAI, USA
Grok	3	xAI
Palm Robo software	4.8.0.1	Carl Zeiss, Germany

Table 9: R and Bioinformatics Packages.

R Package / Library	Version	Developer / Publisher
R	v4.4.0 (2024-04-24 ucrt)	R Core Team, Vienna, Austria
Immunarch	v0.9.1	ImmunoMind, Russia
DESeq2	v1.46.0	Love et al., USA
clusterProfiler	v4.14.4	Yu et al., China
org.Mm.eg.db	v3.18.0	Bioconductor, USA
biomaRt	v2.60.0	Bioconductor, USA
EnhancedVolcano	v1.20.0	Bioconductor / Blighe, UK
ggplot2	v3.5.1	Wickham, USA
dplyr	v1.1.4	Wickham, USA
openxlsx	v4.2.5.2	Schauberger et al., USA
writexl	v1.5.0	Ooms, USA
pathview	v1.42.0	Bioconductor, USA
tidyverse	V2.0.0	tidyverse / RStudio, USA

2.2. Methods

2.2.1. OAT pretreatment, GC isolation, and TCRβ/RNA-Seq analyses

2.2.1.1 Mice and experimental design

Our research group previously established and carried out the animal experiments and induction of experimental EBA, as detailed by Niebuhr (Niebuhr et al., 2020; Niebuhr, 2019). Mice were divided into two groups: OAT-pretreat and PAT-control. The pretreatment involved sequential subcutaneous injections of 50 µl of 0.8 mg/ml OVA (42.8 kDa) emulsified in Alum and TiterMax every three weeks. The initial and second injections were given into the left and right

hind footpads, respectively, while the third was administered at the tail base, aiming for the draining LNs: Pln and Ingln. Control animals received PBS instead of Ova (PAT).

Three weeks after the final pretreatment, mice were immunized subcutaneously in both hind footpads with 60 µg mCol7c emulsified 1:1 (v/v) in TiterMax to induce experimental EBA. Following immunization, mice were monitored for clinical disease progression over 12 weeks. At day +21 post immunization. Plns and Inglns were harvested for immunohistology, Tfh cell isolation, and TCRR analysis.

2.2.1.2. Lymph node collection and immunohistochemistry

LN processing and staining were performed according to previously established protocols in our laboratory (Bahreini, Niebuhr, Belde, Westermann, et al., 2022; Niebuhr et al., 2020; Niebuhr, 2019). Briefly, Pln and Inglns were carefully excised, freed of surrounding adipose tissue, embedded in Optimal Cutting Temperature compound, and snap-frozen in liquid nitrogen to preserve tissue morphology and RNA integrity. Frozen specimens were stored at −80 °C until cryosectioning.

Cryosections (6–8 µm) were prepared on Superfrost Plus glass slides using a cryostat at −20 °C. Sections were fixed in acetone (−20 °C, 10 min), air-dried, and rehydrated in PBS. Slides were blocked with 1% BSA in PBS to minimize nonspecific binding before antibody incubation.

Immunohistochemical staining was performed sequentially using the following primary antibodies:

1- Anti-Ki-67 to detect proliferating germinal-center (GC) B cells,
2- Anti-B220/CD45R to delineate B cell follicles.

Bound antibodies were visualized using a biotin–ExtrAvidin detection system: ExtrAvidin Alkaline Phosphatase with Fast Red or Fast Blue substrates for Ki-67 and B220 staining, and

Slides were counterstained lightly with hematoxylin, rinsed, and mounted in mounting medium. GCs were identified as dense Ki-67^{+} regions within B220^{+} follicles. All staining steps were performed under RNase-free conditions to allow subsequent RNA-based analyses.

2.2.1.3. Laser microdissection of GC–Tfh cells

Laser microdissection of GCs was performed as previously described (Bahreini, Niebuhr, Belde, Westermann, et al., 2022), allowing the isolation of GC-enriched regions containing antigen-activated B and Tfh cells while preserving tissue architecture and RNA integrity.

Following immunohistochemical identification of GC regions on reference slides, serial sections from the same LNs were prepared on membrane slides and subjected to a short toluidine blue staining protocol optimized for RNA preservation (Bahreini, Niebuhr, Belde, Westermann, et al., 2022). Sections were fixed in 75% ethanol (10 min), rinsed in RNase-free water, stained with 0.1% toluidine blue for 2 min, washed twice (2 min each), and dehydrated in 96% ethanol (15 s). All steps were carried out under RNase-free conditions to minimize RNA degradation.

GC areas were identified by correlating toluidine-blue–stained sections with adjacent immunostained slides, where GCs appeared as Ki-67^{+} clusters within B220^{+} follicles. The corresponding GC regions were excised using a PALM MicroBeam Laser Microdissection System operated with PALM RoboSoftware. Isolated GC fragments (2×10^{6}–10×10^{6} μm² per sample) were catapulted directly into sterile adhesive microtubes pre-coated with mineral oil to facilitate capture. The collected tissue was immediately lysed in lysis solution, vortexed, and stored at −20 °C until RNA isolation.

2.2.1.4. RNA extraction and quality control

Total RNA from laser microdissected GCs was isolated using the innuPREP RNA Mini Kit 2.0 following the manufacturer's instructions with minor adaptations optimized for microdissected and cryopreserved samples.

For microdissected GC samples, tissue was collected in 500 µL microtubes containing 350 µL Lysis Solution RL, while cryopreserved LN samples were lysed in 1.5 mL tubes with 700 µL Lysis Solution RL.

After thawing, samples were vortexed for 1 min and briefly centrifuged at maximum speed (10 s, short spin). For microdissected samples, the lysate was transferred into a 1.5 mL microtube using a 1 mL syringe and the volume adjusted to 700 µL with additional Lysis Solution RL.

Lysates were homogenized by drawing the solution through the syringe ten times (the syringe and needle were disposed of as biohazardous waste). Subsequently, 700 µL of 70% ethanol was added and mixed gently by pipetting five times.

The total 1.4 mL lysate was then applied to a Spin Filter R in two steps (700 µL each), centrifuging for 1 min at 12,000 rpm per step. The flow-through and used receiver tubes were discarded after each spin. The bound RNA was washed sequentially with: 500 µL Washing Solution HS, centrifuged for 1 min at 12,000 rpm, and, 700 µL Washing Solution LS, centrifuged for 1 min at 12,000 rpm. After each wash, the spin filter was transferred to a new receiver tube, and the filtrate was discarded. The membrane was then dried by centrifugation for 2 min at 13,000 rpm to remove residual ethanol. For elution, the spin filter was placed in a 1.5 mL Elution Tube, and 60 µL RNase-free water was applied directly onto the membrane, incubated for 1 min, and centrifuged at 10,000 rpm for 1 min. To maximize RNA yield (by approximately 15–30%), the eluate was reapplied to the same filter, incubated for 1 min, and centrifuged again under identical conditions. The final eluate was collected, and the filter was

discarded. RNA was then concentrated in a SpeedVac concentrator (60 °C for ~25 min) until a final volume of approximately 8 µL was reached for downstream DNA digestion and library preparation.

RNA concentration and quality were determined using a Quantus™ Fluorometer with the QuantiFluor RNA System, following the manufacturer's protocol. Briefly, a 1× TE buffer was prepared by diluting 50 µL of 20× TE in 950 µL PCR-grade water. RNA dye working solutions were prepared according to the concentration range of the samples:

1- Low-concentration RNA dye: 999 µL 1× TE + 1 µL dye (photosensitive)
2- High-concentration RNA dye: 796 µL 1× TE + 4 µL dye (photosensitive)

For each measurement, 1 µL of the RNA sample was diluted in 99 µL of 1× TE buffer. Then, 100 µL of the appropriate dye working solution was added to 100 µL of the diluted RNA, gently mixed, briefly centrifuged, and incubated in the dark for 5 min. Fluorescence was measured using the Quantus™ Fluorometer, and RNA concentrations were automatically calculated based on the instrument's calibration curve. If measurements fell outside the standard range (displayed as higher than standard or lower than standard), samples were re-measured using the corresponding high- or low-range protocol. Only RNA samples within the linear detection range and of sufficient purity were used for downstream cDNA synthesis and TCRβ library preparation.

2.2.1.5. Next-generation sequencing of TCRβ libraries

2.2.1.5.1. Amplicon-rescued multiplex PCR (arm-PCR)

Gene-specific amplification of TCRβ transcripts was achieved using an amplicon-rescued multiplex PCR (arm-PCR), consisting of two consecutive PCR steps as described by Han et al. and Wang et al. (Han et al., 2006; Wang et al., 2010). The MTB IVc reagent system was

employed, containing 24 forward and reverse primers targeting murine TCRβ V- and C-segments, respectively.

In the first PCR step, reverse transcription and multiplex-nested PCR were performed successively in a 25 µL reaction containing:

1) 10 µL of DNase-digested RNA (from Section 2.2.1.4),
2) 5 µL 5× OneStep RT-PCR buffer,
3) 1 µL 10 mM dNTP mix,
4) 3 µL MTBIvc primer (including a sample-specific index sequence),
5) 1 µL OneStep RT-PCR enzyme mix,
6) 5 µL RNase-free water.

The total RNA input was limited to 500 ng, with volume adjustments made using RNase-free water. A No Template Control (NTC) was included in all runs. Thermal cycling was performed using the following conditions:

Step	Temperature	Time	Cycles
Reverse transcription	50 °C	40 min	1
Initial denaturation	95 °C	15 min	1
Denaturation	94 °C	30 s	15
Annealing	60 °C	2 min	15
Elongation	72 °C	30 s	15
Denaturation	94 °C	30 s	10
Elongation	72 °C	2 min	10
Final elongation	72 °C	10 min	1

The second PCR step was used for exponential amplification with Illumina-compatible universal primers (PE PCR Primer 1.0 and PCR Primer 2.0).

The reaction (25 µL total volume) contained:

1) 1 µL of the first-step PCR product,

2) 12.5 µL Multiplex PCR Master Mix,

3) 2.5 µL communal Illumina primers,

4) 9 µL nuclease-free water.

Cycling conditions were as follows:

Step	Temperature	Time	Cycles
Initial denaturation	95 °C	15 min	1
Denaturation	94 °C	30 s	40
Annealing	60 °C	30 s	40
Elongation	72 °C	30 s	40
Final elongation	72 °C	5 min	1

Amplified products were stored at −20 °C until verification by gel electrophoresis.

2.2.1.5.2 Agarose gel electrophoresis

Amplification success was verified by 2% (w/v) agarose gel electrophoresis in 1× TAE buffer. Agarose was dissolved at 95 °C, cooled to 65 °C, and supplemented with Roti-GelStain (1:10,000 v/v) before casting. Each reaction (25 µL of second-round arm-PCR product) was mixed with 5 µL 5× DNA loading buffer and loaded onto the gel.

A 5 µL HyperLadder 100 bp marker was run in parallel.

Electrophoresis was performed at 110 V for 30 min. Gels were visualized under UV illumination using the Gel Doc system with a fixed exposure of 64 ms. Single, distinct product bands at 280–300 bp indicated successful amplification. NTCs showed no product at this range, displaying only nonspecific bands at 140–150 bp. Positive product bands (250–330 bp) were excised and stored at −20 °C until purification.

2.2.1.5.3 DNA gel extraction

Purification of PCR products was performed using the QIAquick Gel Extraction Kit according to the manufacturer's protocol. Gel slices were weighed, and 3 volumes of Buffer QG were added per gel volume (1 mg = 1 mL). Samples were incubated at 50 °C for 10 min (extended as needed until complete dissolution). After adding 1 volume of isopropanol, up to 700 µL of the mixture was applied to a QIAquick spin column and centrifuged at 12,000 × g for 1 min. The flow-through was discarded, and the binding step was repeated if necessary. The column was washed with 500 µL Buffer QG, centrifuged, and then washed with 750 µL Buffer PE for 3 min at 12,000 × g. After drying (1 min at 12,000 × g), DNA was eluted with 10 µL Buffer EB, incubated for 1 min, and centrifuged again (12,000 × g, 1 min). Purified libraries were stored at −20 °C until quantification.

2.2.1.5.4 Library quantification

Sequencing library concentrations were determined using the PerfeCTa NGS Quantification Kit following the manufacturer's protocol. Libraries were diluted 1:10,000 with 1× Library Dilution Buffer. For each measurement, 4 µL of diluted library, 4 µL of amplification standards (0.0005–5 pM, 426 bp), or 4 µL H_2O (NTC) were pipetted into a 96-well PCR plate. A 16 µL master mix was prepared per well, containing:

1) 10 µL 2× PerfeCTa SYBR Green SuperMix,
2) 0.6 µL Illumina Primer Mix,
3) 5.4 µL nuclease-free water.

qPCR reactions were performed in technical duplicates on an ABI PRISM system using the following conditions:

Step	Temperature	Time	Cycles
Initial denaturation	95 °C	5 min	1
Denaturation	95 °C	20 s	35
Annealing	60 °C	30 s	35
Elongation	72 °C	45 s	35
Melt curve	95 °C (15 s), 60–95 °C ramp (0.5 °C/s)	-	1

Baseline settings (3–8) and a fluorescence threshold of 0.2 were applied for all reactions.

Based on standard amplification curves, Ct values were converted into raw concentrations.

Absolute concentrations were calculated as:

Size-corrected conc. (pM)=Raw conc. (pM)×280426=Raw conc. (pM)×1.52

Accounting for dilution, the final library concentration was calculated as:

Library conc. (nM)=Size-corrected conc. (pM)×10,000

2.2.1.5.5 Illumina MiSeq sequencing

TCRβ sequencing libraries were analyzed using the Illumina MiSeq platform with the MiSeq Reagent Kit v2 (300 cycles). 6-8 individually indexed libraries were processed in parallel.

Each library was normalized to 2 nM and pooled by combining 5 µL of each normalized sample.

The pooled 2 nM library (5 µL) was denatured with 5 µL 0.2 M NaOH for 5 min at 20 °C, then diluted with 990 µL HT1 buffer to obtain a 10 pM library pool.

Subsequently, 450 µL of the 10 pM pool was mixed with 150 µL HT1 buffer to yield a 7.5 pM sequencing pool.

As internal control, PhiX Control v3 (Illumina) was prepared by combining 2 µL 10 nM PhiX library, 3 µL library dilution buffer, and 5 µL 0.2 M NaOH, followed by incubation for 5 min at 20 °C. The mixture was filled up with 990 µL HT1 buffer to create a 20 pM PhiX library, which was then diluted with HT1 (375 µL + 225 µL) to obtain a 12.5 pM PhiX control.

For sequencing, 510 µL of the 7.5 pM sample pool was combined with 90 µL of the 12.5 pM PhiX control and loaded into the MiSeq reagent cartridge. The flow cell was rinsed with molecular-grade water to remove residual particles before sequencing. Paired-end sequencing (2 × 150 bp) was performed using Illumina PE Read 1 and Read 2 primers. Sequencing output was generated in FASTQ format. Run quality was evaluated based on PhiX control metrics, cluster density, and cluster pass filter rate. Runs with a cluster density of 750 ± 150 K/mm² and > 90% pass filter were considered successful and used for downstream bioinformatic analysis.

2.2.1.6 Data processing and TCRβ clonotype assembly

Raw paired-end FASTQ files obtained from Illumina MiSeq sequencing were processed using a combined ClonoCalc–MiXCR workflow, as established previously in our (Niebuhr et al., 2022; Niebuhr et al., 2021).

2.2.1.6.1 Preprocessing with ClonoCalc

Initial processing of raw sequencing data was performed using ClonoCalc v2.1. This included demultiplexing, read pairing, and quality filtering.

FASTQ files were split according to individual sample barcodes using the FASTX Barcode Splitter module. Reads with barcode mismatches or insufficient quality (Phred score < 30) were excluded. Corresponding read pairs were matched and merged using the PEAR algorithm (v0.9.6) to generate high-quality, full-length read assemblies.

Merged reads were subsequently filtered by length (250–330 bp) and exported as processed FASTQ files for downstream analysis in MiXCR.

2.2.1.6.2 Clonotype identification with MiXCR

The high-quality processed reads were analyzed using the MiXCR software package (v4.7) (Bolotin et al., 2017; Bolotin et al., 2015). MiXCR performs alignment, assembly, error correction, and clonotype assignment based on the IMGT murine TCRβ reference. Reads were aligned to V, D, and J gene segments, and clonotypes were defined as unique combinations of V gene, J gene, and CDR3 amino acid sequence. Only productive, in-frame rearrangements were retained.

PCR and sequencing errors were corrected using the built-in assemblePartial and extendAlignments algorithms. Singleton clonotypes (n = 1) were excluded to minimize background noise. For each sample, MiXCR output tables contained V(D)J usage, CDR3 nucleotide and amino acid sequences, read counts, and relative frequencies. The processed clonotype repertoires were exported in .txt format. All the coding needed for this analysis is provided in Supplementary Code 1.

2.2.1.6.3 Downstream repertoire analysis

Processed clonotype tables were imported into the R environment 4.4.0 (2024-04-24 ucrt) using the Immunarch package (v0.9.1) (Team, 2019). Data normalization was performed based on the number of productive clonotypes per sample.

Processed MiXCR clonotype tables were loaded into R using Immunarch (repLoad). Analyses were performed on productive rearrangements; where indicated, datasets were additionally filtered to retain above-median clones by readCount per sample, generating an "Koll47_Abovemedian" panel used for subset analyses and tracking. Overall clonotype structure was quantified with repExplore: CDR3 length distributions were computed on amino-

acid sequences (.method="len", .col="aa") and converted to relative frequencies within each sample; total and unique clonotype counts were obtained (.method="volume") and, when needed, verified by spectratype counts on nt CDR3s. V and J gene usage was derived with geneUsage (human TRBV/TRBJ dictionaries as implemented in Immunarch: "hs.trbv", "hs.trbj") with normalization enabled, and exported as percentage matrices for groupwise comparison. To characterize clonal expansion, clonotype abundance distributions were computed with repExplore(.method="count"). Public repertoire sharing was evaluated by pubRep both pairwise (e.g., combined popliteal PBS vs OVA) and within groups.

For cross-sample similarity, pairwise repertoire overlap was calculated with repOverlap using Jaccard (presence/absence) and Morisita–Horn (abundance-weighted) indices. These metrics were computed on whole repertoires and on frequency-defined subsets produced by deterministic filters in R: the top 100 clones, the top 10%, the 10–20% strata, and the last 50% (tail) after sorting by Clones. Grouped overlap summaries (mean ± SD) were generated for popliteal/inguinal and OVA/PBS partitions defined in a tab-delimited metadata file, and exported to Excel. Clonotype tracking across tissues used trackClonotypes on CDR3aa+V keys to follow either the top 20 or top 100 clones from a reference repertoire into the paired repertoire; when tracking was scripted manually, left/right nodes were aggregated, relative frequencies were computed per repertoire, the top set in the reference was selected, and the matched CDR3aa list was left-joined to the counterpart, assigning 0 to missing clonotypes to quantify complete losses. Additional relative clone count tables were produced by normalizing cloneCount to each sample's total.

Sequence-feature analyses included k-mer profiling of CDR3 amino acid 3-mers using getKmers. For inguinal OVA vs. PBS, k-mer counts were summed per group, converted to percent relative frequency, and an enrichment score (OVA% − PBS%) was computed for each k-mer. Analogous pipelines were run after combining left/right nodes per mouse and exporting

per-sample k-mer profiles. Repertoire clustering on CDR3aa was performed using seqDist followed by seqCluster with a 0.9 sequence-similarity threshold to enumerate unique clusters per sample. CDR3 length distributions were converted to percentages within the sample. 3-mer profiles were converted to percent and contrasted, retaining the union of top-10 k-mers from each time point per mouse. All data wrangling was performed using dplyr, and outputs were saved with openxlsx/writexl. Exploratory visualizations utilized Immunarch vis() and ggplot2, while final figures were prepared downstream from the exported tables. In supplementary code 2, the coding detail is described.

2.2.1.7. RNA-Seq and transcriptional analysis

GC-enriched RNA (Section 2.3) was processed for mRNA-Seq by Biomarker Technologies (BMK) GmbH (Technologiepark Münster, Johann-Krane-Weg 42, 48149 Münster, Germany). Poly(A)+ RNA was isolated, fragmented, and reverse-transcribed to cDNA; Illumina-compatible libraries were constructed according to standard protocols and sequenced as paired-end 150-bp (PE150) reads on an Illumina platform. Per-library output averaged ~6 Gb, with >94% bases at Q30, yielding high-quality data for downstream analysis.

Raw reads were aligned to the mouse reference genome (GRCm38/mm10) using HISAT2, and gene-level counts were generated from the aligned BAM files (feature summarization as in the BMK pipeline). The resulting gene × sample count matrix ("Kathrin_hisat2_out.txt") and a curated sample sheet were imported to R. Analyses were performed in DESeq2 with the design formula set to the combined experimental factor (group = tissue_adjuvant), after prefiltering genes with total counts < 10 across all samples. For the primary comparison, the reference level was set to plk_OVA_Alum_TM, and differential expression was computed for ingLK_OVA_Alum_TM vs plk_OVA_Alum_TM. In addition, a subset analysis restricted to Alum_Titermax samples was run with design = ~ tissue to contrast ingLK vs plk. LFC shrinkage used ashr. Unless otherwise stated, transcripts were considered differentially expressed at

adjusted p (Benjamini–Hochberg) < 0.05 with an effect-size filter of |log2FC| ≥ 0.5; exploratory tables were also generated at padj < 0.1 (as in the code). Variance stabilization used VST, and unsupervised PCA was performed on VST data (DESeq2), with additional labeling and plotting in ggplot2. Volcano plots were produced with EnhancedVolcano (pCutoff = 0.05; FCcutoff = 0.5) using a custom color key.

For functional interpretation, mouse gene identifiers were annotated via biomaRt, and enrichment analyses were performed in clusterProfiler. GO gene set enrichment (GSEA) used gseGO (ontology = ALL, OrgDb = org.Mm.eg.db, pAdjustMethod = FDR, minGSSize = 3, maxGSSize = 1000). KEGG over-representation and GSEA used mmu (mouse) with enrichKEGG/gseKEGG; pathway views were rendered with pathview. Where required, gene symbols were mapped to Entrez IDs prior to enrichment. All computations used R with DESeq2, ashr, clusterProfiler, org.Mm.eg.db, biomaRt, ggplot2, EnhancedVolcano, and standard tidyverse utilities; intermediate and final result tables (DE lists, PCA coordinates, enrichment outputs) were exported to CSV/Excel for figure generation. In supplementary code 3, the coding detail is described.

2.2.1. Production and quality assessment of cell-derived nanoparticles with endotoxin control and *in Vitro* immunomodulatory assays

2.2.2.1. Generation of CDNPs

To generate CDNPs, porcine kidney epithelial cells (EFN-R) were cultured under sterile conditions. Cells were maintained in α-MEM medium with or without ribonucleosides supplemented with 10% Fetal bovine serum (FBS), 1% penicillin-streptomycin, 1% GlutaMAX™ supplement, 1% sodium pyruvate, and 1% MEM non-essential amino acids. Cultures were incubated at 37 °C in a humidified atmosphere containing 5% CO_2 and passaged twice weekly at 80–90% confluence.

After culture expansion, EFN-R cells were harvested from Cell Master™ roller bottles under sterile conditions. Growth medium was first decanted, and each bottle was rinsed once with PBS to remove residual serum components. Cells were detached by adding 7.5 mL (3,5 ng/µl) trypsin–EDTA and incubating the bottles at 37 °C for approximately 2 min in a roller incubator. The detached cell suspension was then collected into six 50 mL Falcon tubes, each pre-filled with 42 mL of PBS.

The culture bottles were subsequently rinsed again with the PBS from the Falcon tubes to ensure maximal recovery of cells, and the combined suspension was gently returned to the Falcon tubes. To inhibit proteolytic degradation, 250 µL phenylmethylsulfonyl fluoride (PMSF, 0.5 mM final concentration) was added to each tube, followed by gentle inversion. Samples were centrifuged at 400 × g for 8 min, and the resulting supernatant was discarded. The pellets were loosened by gentle tapping, resuspended in 50 mL PBS containing 0.5 mM PMSF, and centrifuged again under identical conditions.

Following the second wash, pellets were resuspended in 20 mL PBS supplemented with Ca^{2+} and Mg^{2+} and again stabilized with 100 µL PMSF. Pellets were then stored at −20 °C until further processing or transfer for nanoparticle isolation.

Harvested EFN-R suspensions (8-12 × 20 mL; total ≈ 160-240 mL) were thawed overnight at 4 °C and homogenized by vigorous vortexing. For mechanical disruption, the suspensions were sonicated on ice using a Bandelin Sonopuls equipped with a TS106 sonotrode. The probe was placed centrally in each tube, and sonication was performed at 15% amplitude for 8 s per aliquot, without pulsation, to ensure uniform cell disruption while preventing overheating.

The sonicated suspensions were then divided into up to eight 50 mL Falcon tubes and centrifuged for 30 min at ≈ approximately 5000 × g and 4 °C to remove coarse debris. Supernatants were carefully decanted into Beckman Type 45 Ti ultracentrifuge tubes, while the

pellets were resuspended in 1 mL of PBS per 20 mL of the starting suspension and retained for subsequent SDS-PAGE analysis.

For nanoparticle isolation, the supernatants were subjected to ultracentrifugation at 25,000 rpm (Ti 45 Rotor, 72000 × g) for 150 min at 4 °C using a Beckman ultracentrifuge. The resulting supernatant, corresponding to the cytosolic fraction, was stored for later protein analysis. In contrast, the pellet, representing the crude CDNP fraction, was resuspended in 1 mL PBS per 20 mL starting suspension using a Dounce homogenizer until no visible clumps remained.

Samples were digested for any nucleic acid contamination using Benzonase. For this, 5 mL of the homogenized sample was treated with 7 µL of Benzonase and incubated for 30 min at room temperature. A chloroform purification step was performed to remove residual lipids and protein contaminants. The CDNP suspension was diluted with PBS to a final volume of 95 mL, split into two 47.5 mL Falcon tubes, and supplemented with water-saturated chloroform to a final concentration of 5% (v/v) (47.5 mL sample + 2.5 mL chloroform). Samples were gently inverted 3–4 times until the solution appeared finely pearled, then centrifuged for 15 min at 9384 × g, 4 °C. The aqueous supernatant, containing purified CDNPs, was carefully collected without disturbing the interphase or chloroform layer and stored overnight at 4 °C.

CDNPs were concentrated by a second ultracentrifugation step using a Beckman MLA-80 rotor (6 mL tubes, maximum 6.5 mL). Samples were centrifuged for 160 min at 60,000 rpm (370,000 Xg, 4 °C using a Ti70 rotor). Supernatants from both runs were pooled and reserved for SDS-PAGE. The resulting pellets were resuspended in the residual supernatant (≈ 100–150 µL per tube) and combined using a Dounce homogenizer to ensure complete dispersion.

For removal of membrane-associated proteins, aliquots of the final CDNP suspension (≤ 500 µL each) were treated with 2% Triton X-114 and mixed thoroughly. The samples were incubated sequentially for 30 min on ice (0 °C), 30 min at 4 °C with gentle shaking (800 rpm), and 30 min at 37 °C without agitation. After incubation, the samples were centrifuged for 20

min at 14,000 rpm (21000 xg, using a FA-45-30-11 rotor) and 27 °C. The aqueous supernatant, representing the detergent-free CDNP fraction, was then transferred to new tubes, ensuring that no detergent phase was carried over. The final CDNP preparations were stored at 4 °C for short-term use or at −20 °C for long-term storage until they were used in experiments.

2.2.2.2. Quantification and quality control of CDNP preparations

The protein content and purity of CDNP preparations were evaluated by sodium dodecyl sulfate–polyacrylamide gel electrophoresis (SDS-PAGE) under reducing conditions. Protein concentration was determined using the Pierce™ BCA Protein Assay Kit to ensure equal loading between samples.

Electrophoretic separation was performed on NuPAGE 4–12% Bis-Tris Protein Gels (Thermo Fisher Scientific, USA) using NuPAGE MES SDS Running Buffer and NuPAGE Antioxidant. The cathodic chamber contained 5% (v/v) MES SDS Running Buffer supplemented with 0.25% NuPAGE Antioxidant, and the anodic chamber was filled with standard running buffer in laboratory-grade H_2O. Samples were prepared in Laemmli buffer containing 15 mM dithiothreitol (DTT), 20% (v/v) glycerol, and 2.5% (v/v) 2-mercaptoethanol, and heated at 95 °C for 5 min before loading. The PageRuler™ Prestained Protein Ladder served as a molecular weight reference. Gels were run at a constant voltage of 120 V until the dye front reached the bottom of the gel.

After electrophoresis, gels were either stained with Coomassie Blue or transferred to PVDF membranes for Western blotting. The Coomassie Blue staining solution consisted of 40% (v/v) methanol, 10% (v/v) acetic acid, 0.025% (w/v) Coomassie Brilliant Blue R, and 0.025% (w/v) Coomassie Brilliant Blue G. Following staining and destaining, gels were washed overnight in laboratory-grade H_2O. A quantitative assessment was performed relative to a bovine serum

albumin standard, and visualization of the protein bands was achieved using the Odyssey Infrared Imaging System (LI-COR Biosciences).

For Western blot analysis, proteins were transferred to Roti® Fluoro PVDF membranes (for 36 min at 2 mA/Cm^2. Membranes were blocked for 60 min at room temperature with 3% BSA in PBS, and antibody incubations were carried out in the same blocking solution. The primary Annexin V antibody was used at a 1:300 dilution and incubated overnight at 4 °C. After washing with PBS containing 0.05% Tween-20 (PBST), membranes were incubated with an IRDye 800 in the dark for 60 min at room temperature, followed by a tertiary alkaline phosphatase–conjugated mouse antibody for 60 min at room temperature.

Recombinant Annexin A5 standards (0.285–1.14 µg) were loaded alongside experimental CDNP batches, with or without ribonucleoside supplementation, to calibrate detection sensitivity and confirm specificity. Protein transfer and probing were followed by fluorescent detection using an IRDye 800 in the dark. The PageRuler prestained molecular weight ladder (red channel) served as a reference, with markers indicated in kilodaltons (kDa). Distinct fluorescent bands in the 35–40 kDa range corresponded to the expected molecular weight of Annexin A5.

. Signal acquisition and quantitative analysis were performed using the Odyssey Infrared Imaging System, ensuring consistent detection of Annexin A5 as a molecular marker and confirming batch-to-batch reproducibility of CDNP preparations.

2.2.2.3. Characterization of CDNP size, distribution, and protein–particle correlation

The particle size, concentration, and distribution of isolated CDNPs were analyzed by nanoparticle tracking analysis (NTA) using the ZetaView® system equipped with a 488 nm laser. Measurements were conducted at 25 °C under standardized instrument parameters (EV_488C SOP defined by the manufacturer :Temperature: 25 °C; pH: 7.0; Conductivity:

12,217 µS/cm; Max area: 1000; Min area: 10; Min brightness: 30; nm/class: 10; Analysis: 1 cycle, 11 positions; Mode: Electrophoresis & Brownian Motion via Laser Scattering Microscopy). Before each run, the system was calibrated using 0.1 µm polystyrene beads and rinsed with 0.2 µm-filtered DPBS. To minimize aggregation, CDNP samples were gently mixed and diluted 1:100,000 in filtered PBS immediately before measurement. For each sample, videos were recorded at 11 positions and analyzed automatically using the ZetaView software to obtain the mean particle size (nm), size distribution, and particle concentration (particles/mL). Each analysis was performed on four independent CDNP batches to assess reproducibility. The average particle radius and distribution were compared across batches.

To examine the relationship between particle number and protein content, total protein concentrations, as determined by the Pierce™ BCA Protein Assay, were correlated with NTA-derived particle counts.

2.2.2.4. Endotoxin detection

Endotoxin levels in CDNP preparations were quantified using the Pierce™ Chromogenic Endotoxin Quant Kit following the manufacturer's High Standard Protocol (0.1–1.0 EU/mL range). The assay is based on the Limulus Amebocyte Lysate (LAL) reaction, in which endotoxin-activated serine proteases release p-nitroaniline (pNA) from a chromogenic substrate, resulting in a yellow color that is proportional to the endotoxin concentration.

A standard curve was generated using serial dilutions of the E. coli (O111:B4) endotoxin standard, ranging from 0.1 to 1.0 EU/mL, with endotoxin-free water as a blank. All reagents, tips, and microplates were certified endotoxin-free, and all samples were assayed in duplicates. Fifty microliters (50 µL) of each standard or CDNP sample were added per well, followed by 50 µL of reconstituted Amebocyte Lysate reagent. The plate was gently mixed and incubated at 37 ± 1 °C for the period indicated on the lysate vial. Subsequently, 100 µL of pre-warmed

chromogenic substrate was added to each well and incubated for 6 min at 37 °C. The reaction was stopped by adding 50 µL of 25% acetic acid, and absorbance was immediately measured at 405 nm using a microplate reader.

Endotoxin concentrations were calculated from the linear regression of the standard curve ($R^2 \geq 0.98$) and expressed as endotoxin units per milliliter (EU/mL). CDNP batches exceeding the acceptable level of 0.1 EU/mL were treated with Triton X-114 for phase separation as described in Section 2.2.1. Post-treatment samples were re-evaluated using the same LAL protocol to confirm that the endotoxin level was reduced to below 0.1 EU/mL, ensuring the suitability of CDNPs for subsequent *in vivo* and *in vitro* use.

2.2.2.5. *in Vitro* analysis of CDNP-mediated modulation of IL-6 secretion

To evaluate the immunomodulatory properties of CDNPs under endotoxin-free conditions, murine macrophage-like J774A.1 cells were used. Cells were cultured in DMEM supplemented with 10% FBS, 1% penicillin-streptomycin, and 1% GlutaMAX™. Cultures were maintained at 37 °C in a humidified 5% CO_2 atmosphere.

For stimulation assays, 5×10^5 cells per well were seeded into 48-well plates and allowed to adhere for 24 h. The medium was then replaced with fresh DMEM containing either PBS (negative control), Ova (5 µg/mL), CDNPs (0.5, 1, 2.5, or 5 µg/mL), PAM (100 ng/mL), or combinations of PAM with CDNPs or OVA in a total volume of 500 µL per well.

After 5 h of incubation at 37 °C, supernatants were collected, centrifuged (500 × g, 5 min, RT) to remove cell debris, and stored at −20 °C until cytokine quantification. IL-6 secretion was measured using the Mouse IL-6 ELISA Kit according to the manufacturer's protocol. Washing steps were performed with PBS containing 0.05% (v/v) Tween-20, and all samples were analyzed in duplicate. Absorbance was measured at 450 nm using a plate reader. Cytokine concentrations were calculated from the standard curve and expressed in picograms per

milliliter (pg/mL). Data analysis was performed with GainData® ELISA Data Analysis Software (Arigo Biolaboratories, Taiwan, ROC).

2.2.3. *in Vivo* CDNP treatment, T cell zone isolation, and TCRβ repertoire analysis

2.2.3.1 *in Vivo* CDNP treatment and sample collection

The in vivo CDNP experiment aimed to determine whether repeated CDNP administration can alter TCRR dynamics without the use of any adjuvant or sensitizing agent. Originally designed and executed by Christina Bomholt at the Institute of Anatomy, University of Lübeck, the study spanned five weeks (day −28 to +7). It involved two groups of female C57BL/6J mice: one treated with CDNPs and a control group receiving PBS. After a 1–2 week acclimatization to reduce stress-related immune variability, the mice followed a modified DTH-like schedule that simulates a typical delayed-type hypersensitivity protocol, but without using a hapten or sensitizer.

Beginning on day −28, mice in the treatment group received intraperitoneal injections of CDNPs (10 µg in PBS, 200 µL per injection) and control animals received an equal volume of PBS. Injections were administered every second day for a total of 16 injections over the five weeks, ensuring sustained systemic exposure throughout both the sensitization and challenge phases.

To mimic the DTH structure while avoiding any exogenous sensitization, acetone was applied as a neutral vehicle to the abdomen on day 0 and to the ears on day 5. Ear thickness was measured to evaluate potential contact reactivity; however, no significant differences were detected between the CDNP- and PBS-treated groups (data not shown).

On day 7, mice were euthanized using terminal anesthesia, and lymphoid organs, including the spleen and LNs, were collected for immunological analysis. Two T-cell zones (TCZs) per

spleen were isolated via laser microdissection, followed by high-throughput TCRβ sequencing to assess clonotype diversity, frequency, and repertoire composition.

This modified DTH-like design provided a controlled, adjuvant-free framework for assessing the baseline immunomodulatory effects of CDNPs in vivo, minimizing external immune triggers while ensuring reproducible systemic exposure.

2.2.3.2. Immunohistochemistry of lymph node sections

LN processing and staining were performed according to previously established protocols in our laboratory (Niebuhr et al., 2020). Briefly, Plns and Inglns were removed, cleared of surrounding adipose tissue, embedded in OCT compound (Tissue-Tek®, Sakura Finetek), and snap-frozen in liquid nitrogen to preserve tissue morphology and RNA integrity. Frozen samples were stored at −80 °C until they were cryosectioned. Cryosections (6–8 µm) were prepared using a Leica CM3050S cryostat (Leica Microsystems) at −20 °C and mounted on Superfrost Plus™ glass slides (Thermo Fisher Scientific). Sections were fixed in acetone (−20 °C, 10 min), air-dried, and rehydrated in PBS. To minimize nonspecific binding, slides were blocked with 1% BSA in PBS before antibody incubation.

Sequential immunohistochemical staining was performed under RNase-free conditions. Primary antibodies used included Ki-67 (clone 16A8, BioLegend) for proliferating GC B cells, B220/CD45R to outline B-cell follicles, and TCRβ for detection of the T cell zone (TCZ). Bound antibodies were visualized with a biotin–ExtrAvidin detection system (Sigma-Aldrich). For B220 and Ki-67, ExtrAvidin–Alkaline Phosphatase (1:100) was used, with Fast Blue and Fast Red substrates, respectively. TCRβ staining was developed using ExtrAvidin–Peroxidase (1:100) and DAB.

After each staining step, the slides were rinsed twice with TBS-Tween (0.05%), lightly counterstained with hematoxylin, and then mounted using mounting medium. TCZs were visualized by the distribution pattern of $TCR\beta^+$.

2.2.3.3 Laser microdissection of T cell zone

Laser microdissection of TCZs was performed following the standard procedure used for GC (Section 2.1.3), with slight modifications for identifying and isolating T-cell–enriched regions. After immunohistochemically localizing the TCZ on reference slides ($TCR\beta^+$ areas next to $B220^+$ follicles), serial cryosections from LNs were prepared on polyethylene naphthalate (PEN) membrane slides (1.0 µm; Carl Zeiss). Sections were briefly fixed in 75% ethanol for 10 min, rinsed in RNase-free water, and stained with 0.1% toluidine blue for 2 min to preserve structural orientation and RNA integrity. Following two quick rinses in water (2 min each), sections were dehydrated in 96% ethanol for 15 s and air-dried under RNase-free conditions. TCZ regions were identified by correlating toluidine-blue–stained sections with immunostained reference slides, ensuring precise anatomical localization. The Leica LMD7000 Laser Microdissection System was used for dissection and collection, operated with Leica LMD software v8.4. Isolated TCZ fragments (roughly $2 \times 10^6 – 1 \times 10^7$ µm² per sample) were catapulted into sterile microtubes pre-coated with mineral oil to prevent sample loss. The tissue was immediately lysed in 350 µL of lysis solution containing β-mercaptoethanol, vortexed, and stored at −80 °C until RNA extraction was performed.

2.2.3.4. RNA extraction and quality control

RNA extraction from laser-microdissected TCZ samples was performed as described in Section 2.1.4, using the innuPREP RNA Mini Kit 2.0 according to the manufacturer's protocol. RNA quantity and integrity were assessed using a Quantus Fluorometer.

2.2.3.5. Next-generation sequencing of TCRβ libraries

Next-generation sequencing of TCRβ libraries was carried out on the Illumina MiSeq platform using the MiSeq Reagent Kit v2 (300 cycles), as described in Section 2.1.5. Library normalization, pooling, PhiX control preparation, and sequencing conditions followed the same protocol, and sequencing output was generated in FASTQ format for subsequent analysis.

2.2.3.6. Data processing and TCRβ clonotype assembly

Raw FASTQ files from MiSeq runs were processed using MiXCR to assemble clonotypes based on unique CDR3 amino acid (aa) and nucleotide (nt) sequences. Productive TCRβ rearrangements were exported as tab-delimited tables and further analyzed in R (v4.3.1) using the Immunarch package. All repertoires were imported with repLoad(), normalized, and annotated according to V and J gene usage. Basic repertoire statistics, including the number of unique clonotypes, CDR3 length distribution, and gene segment frequency, were obtained using repExplore() and geneUsage().

Subsequent analyses included pairwise repertoire overlap using Jaccard and Morisita–Horn similarity indices (repOverlap()), quantification of public clonotypes (pubRep()), and diversity assessment by Shannon entropy. To control for sequencing depth variation, only clonotypes with read counts above the sample-specific median were retained for comparison.

For intra-mouse comparisons, clonotypes from left and right draining LNs were merged and tracked across anatomical sites using trackClonotypes() based on shared CDR3 aa + V-gene combinations. Top 50–100 dominant clonotypes, as well as rare (< 0.01%) and abundant (> 1%) subsets, were separately evaluated. K-mer composition (3- to 5-mers) was profiled with getKmers() to assess structural diversity and amino acid motif enrichment between treatment groups. All quantitative results were exported in CSV/Excel format and visualized in R using the ggplot2 package. In supplementary code 4, the coding detail is described.

2.2.3.7. Quantitative real-time PCR (qPCR) analysis of *Tcrb* and *Gata3* expression

RNA extraction from laser-microdissected TCZ samples was performed as described in Section 2.1.4, using the innuPREP RNA Mini Kit 2.0 according to the manufacturer's protocol. RNA quantity and integrity were assessed using a Quantus Fluorometer.

Before reverse transcription, residual genomic DNA was eliminated using DNase I. For each sample, the RNA volume was adjusted to 8 µL with RNase-free water, then 1 µL of 10× DNase reaction buffer and 1 µL of DNase I enzyme were added. The mixture was incubated for 15 minutes at 20 °C, then inactivated by adding 1 µL of Stop Solution and heating at 70 °C for 10 minutes. Immediately after, samples were kept on ice.

cDNA synthesis was carried out using the RevertAid H^- Reverse Transcriptase kit. Each 20 µL reaction included 10 µL of DNase-treated RNA and 10 µL of master mix, which contained 5× reaction buffer, dNTPs, and random hexamer primers. The mixtures were gently combined and incubated sequentially at 25 °C for 10 minutes, then at 42 °C for 60 minutes for reverse transcription, and finally at 70 °C for 10 minutes to terminate the reaction. The resulting cDNA was stored at −20°C until it was used for quantitative PCR.

Transcribed cDNA obtained as described in Section 2.3.8 was diluted 1:2 in nuclease-free water. For each reaction, 1 µL of diluted cDNA was added per well of a 96-well plate. A 19 µL master mix was then added, consisting of 10 µL SYBR Green PCR Master Mix (Thermo Fisher Scientific, USA), 7 µL nuclease-free water, and 2 µL primer mix.

All qRT-PCR reactions were performed in technical duplicates on a StepOnePlus™ Real-Time PCR System. Amplification was carried out under the following cycling conditions:

Step	Temperature	Time	Cycles
Initial denaturation	95 °C	10 min	1
Denaturation	95 °C	45 s	50
Annealing and elongation	60 °C	60 s	50

2.3. Statistical analysis and software

Data analysis was conducted using GraphPad Prism and R. Results are shown as mean ± standard deviation (SD). Data integrity was visually checked following Tukey's guidelines (Tukey, 1977). Normality was evaluated with the D'Agostino–Pearson omnibus test (D'agostino & Pearson, 1973). For two-group comparisons, either the unpaired t-test (parametric) or the Mann-Whitney U test (non-parametric) was used. For three or more groups, data were analyzed using one-way ANOVA with Dunnett's post-hoc or the Kruskal–Wallis test with Dunn's multiple comparison test for non-parametric data. When two independent factors were involved, two-way ANOVA with Dunnett's correction was applied. Significance levels were $p < 0.05$, ** $p < 0.01$, and *** $p < 0.001$.

ChatGPT 4.5 and Grammarly were used to refine the language of this manuscript.

Grok 3 was used to refine the code that was used in this dissertation.

3. Results

Autoimmune blistering diseases, such as EBA, are initiated by autoreactive $CD4^+$ T cells that drive pathogenic B-cell responses (Koga et al., 2019). Previous studies showed that Tfh receptor repertoires in draining LNs become clonally restricted during disease, and that pretreatment with OAT prevents clinical EBA despite the persistence of autoantibodies (Niebuhr et al., 2021). This indicates that protection may be linked to altered T-cell responses rather than the absence of autoreactive B cells. In particular, OAT pretreatment has been associated with a reduced *IFN-γ/IL-4* ratio, reflecting a Th1-to-Th2 deviation in $CD4^+$ T-cell polarization (Niebuhr et al., 2020). To examine this further, we analyzed the Tfh TCRβ repertoire and transcriptional profiles in OAT- versus PAT mice to determine how OAT modulates clonal architecture and gene expression in secondary lymphoid organs.

Simultaneously, we explored whether a similar shift could be achieved through a multiepitope modulation with CDNPs. These particles are known to have broad anti-inflammatory effects by increasing IL-10 levels and suppressing pro-inflammatory cytokines like IL-1β, IL-6, and TNF-α (Kunz, Hauenschild, et al., 2017). They are internalized by macrophages and neutrophils, where they boost CD11b and CD80 expression, promote Th2 polarization of $CD4^+$ T cells, and reduce tissue inflammation (Raudszus et al., 2025). In EBA models, CDNP treatment has been associated with higher IL-4 production, less tissue damage, and faster wound healing (Kunz, Hauenschild, et al., 2017). We then investigated whether CDNPs, similar to OAT, could modify the TCRR and induce a Th1-to-Th2 shift, thus decreasing autoreactive T-cell activity. This was assessed by measuring *Gata3* and *Tcrb* transcripts; *Gata3* as an indicator of Th2 differentiation and *Tcrb* as an indicator of overall TCR transcript levels.

3.1. OAT pretreatment reprograms LN immunity

To assess how OAT pretreatment affects LN immunity in experimental EBA, mice were given sequential OAT or PAT injections at different lymphatic drainage sites (left hind footpad, right hind footpad, and tail base). This was followed by mCol7c immunization in both hind footpads (Figure 3). GC–Tfh cells were isolated via laser microdissection for TCRβ repertoire sequencing and RNA-seq analysis. We hypothesized that OAT pretreatment would decrease the clonal dominance of autoreactive Tfh cells. These experiments aimed to see if OAT alters the clonal structure and transcriptional profile of Tfh cells within draining LNs.

3.1.1. OAT pretreatment influences the Tfh receptor repertoire

We first analyzed the Tfh TCRβ repertoire, as it represents a direct measure of clonal selection and expansion within GCs. Changes in repertoire diversity and dominance serve as sensitive indicators of how OAT pretreatment modulates autoreactive $CD4^+$ T-cell dynamics in LNs. In the following sections, we therefore examine these repertoire features in detail, focusing on sequencing output, clonotype abundance, overlap patterns, directional sharing, and qualitative characteristics.

3.1.1.1 No difference in GC–Tfh cell sequencing output between PAT and OAT groups

Our initial step to test the hypothesis involved analyzing the TCRβ repertoire of GC–Tfh cells obtained from draining LNs (Ingln and Pln) collected at week +3 of the experiment. We identified GC regions through prior immunohistochemical staining for B220 and Ki67, and isolated GC–Tfh cells using laser microdissection for high-throughput TCRβ sequencing (Illumina).

Table 10 summarizes the sequencing output and clonotype counts across experimental groups. The total number of TCRβ sequences obtained per sample ranged between ~0.05–2.2 × 10^6 reads, with mean values of 0.69 × 10^6 for PAT Ingln, 0.72 × 10^6 for OAT Ingln, 1.00 × 10^6 for PAT Pln, and 0.78 × 10^6 for OAT Pln. Similarly, the number of unique clonotypes was comparable between groups, averaging ~3,700–5,500 per condition. No statistically significant differences were observed in either the total number of sequencing reads or the number of unique clonotypes between OAT- and PAT-pretreated mice (Figure 4).

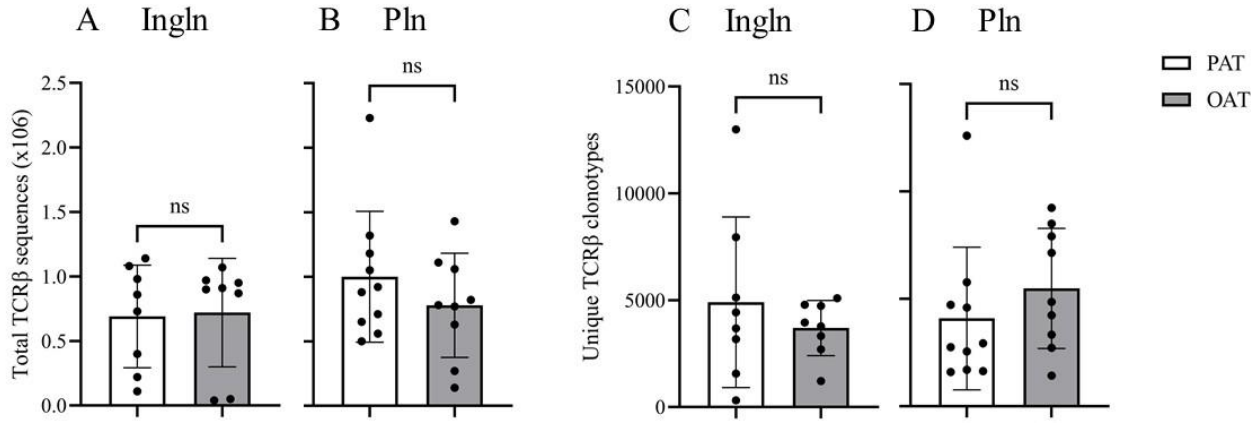

Figure 4. Sequencing output and clonotype counts of GC–Tfh cells in OAT- and PAT-pretreated mice. A–B) Total number of TCRβ sequences obtained from Ingln and popliteal Pln at week +3 post-immunization. C–D) Number of unique TCRβ clonotypes identified in Ingln and Pln. Data are shown as mean ± SD. No significant differences (ns) were observed between OAT and PAT groups in either sequencing depth or clonotype counts.

These findings show that OAT pretreatment has no impact on sequencing reads or overall clonotype numbers in both LN compartments. Thus, differences in repertoire characteristics, including clonal dominance, overlap, and diversity indices, cannot be attributed to technical sequencing variations. Instead, they represent actual biological changes in the Tfh cell repertoire.

Table 10. Comparative Analysis of Tfh-TCRβ Clonality and Sequencing Output in Pln and Inglns Across Treatment Groups

Treatment	Lymph node	Mouse	Position	Total TCRβ sequences ($x10^6$)	unique TCRβ clonotypes	number of Tfh-clonotypes subjected to analysis >median
PAT	Ingln	1	Right	0.22	4434	2180
		1	Left	0.4	310	155
		2	Right	0.98	5128	2550
		2	Left	1.08	7943	3927
		3	Right	1.14	12997	6351
		4	Right	0.11	3682	1786
		5	Right	0.86	3176	1585
		5	Left	0.73	1568	784
		Mean+SD		0.69 ± 0.40	4904.75 ± 3994.93	2414.75 ± 1953.17
OAT	Ingln	1	Right	0.05	1215	598
		1	Left	0.97	3781	1890
		2	Right	0.9	3320	1650
		2	Left	0.95	5098	2534
		3	Right	0.04	4737	2349
		4	Right	0.87	4790	2385
		4	Left	1.07	3951	1974
		5	Right	0.91	2700	1347
		Mean+SD		0.72 ± 0.42	3699.00 ± 1287.69	1840.88 ± 641.42
PAT	Pln	1	Right	1.32	4728	2357
		1	Left	0.56	1592	795
		2	Right	1.05	2754	1377
		2	Left	0.5	1643	820
		3	Right	0.88	2935	1466
		3	Left	0.71	5776	2858
		4	Right	2.23	4602	2301
		4	Left	0.65	1703	851
		5	Right	1.18	2552	1269
		5	Left	0.92	12608	6204
		Mean+SD		1.00 ± 0.51	4089.30 ± 3324.62	2029.80 ± 1632.69
OAT	Pln	1	Right	1.11	4866	2426
		1	Left	0.77	7149	3526
		2	Right	1.43	7911	3946
		2	Left	0.78	8503	4235
		3	Right	1.06	9248	4615
		3	Left	0.27	1431	715
		4	Right	0.14	3337	1661
		4	Left	0.63	4238	2101
		5	Left	0.82	2722	1360
		Mean+SD		0.78 ± 0.40	5489.44 ± 2796.07	2731.67 ± 1391.87

For downstream analyses, only clonotypes with frequencies above the median were considered. This filtering step minimizes the impact of low-abundance, potentially artifactual sequences and allows for a more robust comparison of repertoire characteristics by enriching for biologically relevant clonotypes. For selected analyses, clonotypes from the Pln and Ingln were combined to minimize sampling bias and enhance the overall representation of Tfh cell diversity. This methodological approach allowed us to precisely evaluate whether OAT-induced immune conditioning reshapes the GC-Tfh cell repertoire, and whether such clonal remodeling correlates with the observed protection against autoimmune pathology. The subsequent sections will detail specific changes observed in clonotype abundance, overlap between LNs, and qualitative characteristics of the Tfh receptor repertoire associated with OAT pretreatment.

3.1.1.2. Increased frequency of low-abundance Tfh clonotypes in OAT-pretreated in draining lymph nodes

The total and unique Tfh clonotypes obtained from GC–Tfh cells showed no significant differences between OAT- and PAT-pretreated groups (Figure 4). This finding confirmed that sequencing depth and clonotype yield were comparable, excluding technical artifacts as a confounding factor. However, the absolute numbers of clonotypes do not accurately reflect the frequency with which individual clonotypes are represented within the repertoire. Since autoreactive immune responses are often characterized by the expansion of dominant, high-frequency clonotypes, we next asked whether clonotypes were distributed at similar frequencies in the draining LNs of both groups. Given that the initial OAT injections targeted the footpads (draining to the Pln) and the final OAT boost was administered at the base of the tail (draining to the Ingln), we hypothesized that these differences in antigen exposure history might shape the abundance patterns of Tfh clonotypes within each LN compartment.

In the Pln, clonotypes were categorized as small ($0 < X \leq 1$), medium ($1 < X \leq 10$), or large ($10 < X \leq 100$). In PAT mice, the proportions of small (~44%) and medium (~40%) clonotypes were comparable, with no significant difference between these two categories, while large clonotypes accounted for a smaller fraction (~16%) (Figure 5A, 5C). In OAT-pretreated mice, however, the distribution shifted markedly: small clonotypes increased to ~58% and became significantly more frequent than medium clonotypes (~28%, $p = 0.006$). In contrast, both medium and large clonotypes were reduced compared with PAT controls (Figure 5B, 5C). Cumulative frequency plots further supported this observation, with an exemplary comparison showing a steeper decline in OAT-pretreated repertoires relative to PAT (Figure 5D). Thus, OAT pretreatment reduced the expansion of medium- and large-frequency clonotypes in the Pln, resulting in a repertoire enriched for small clonotypes.

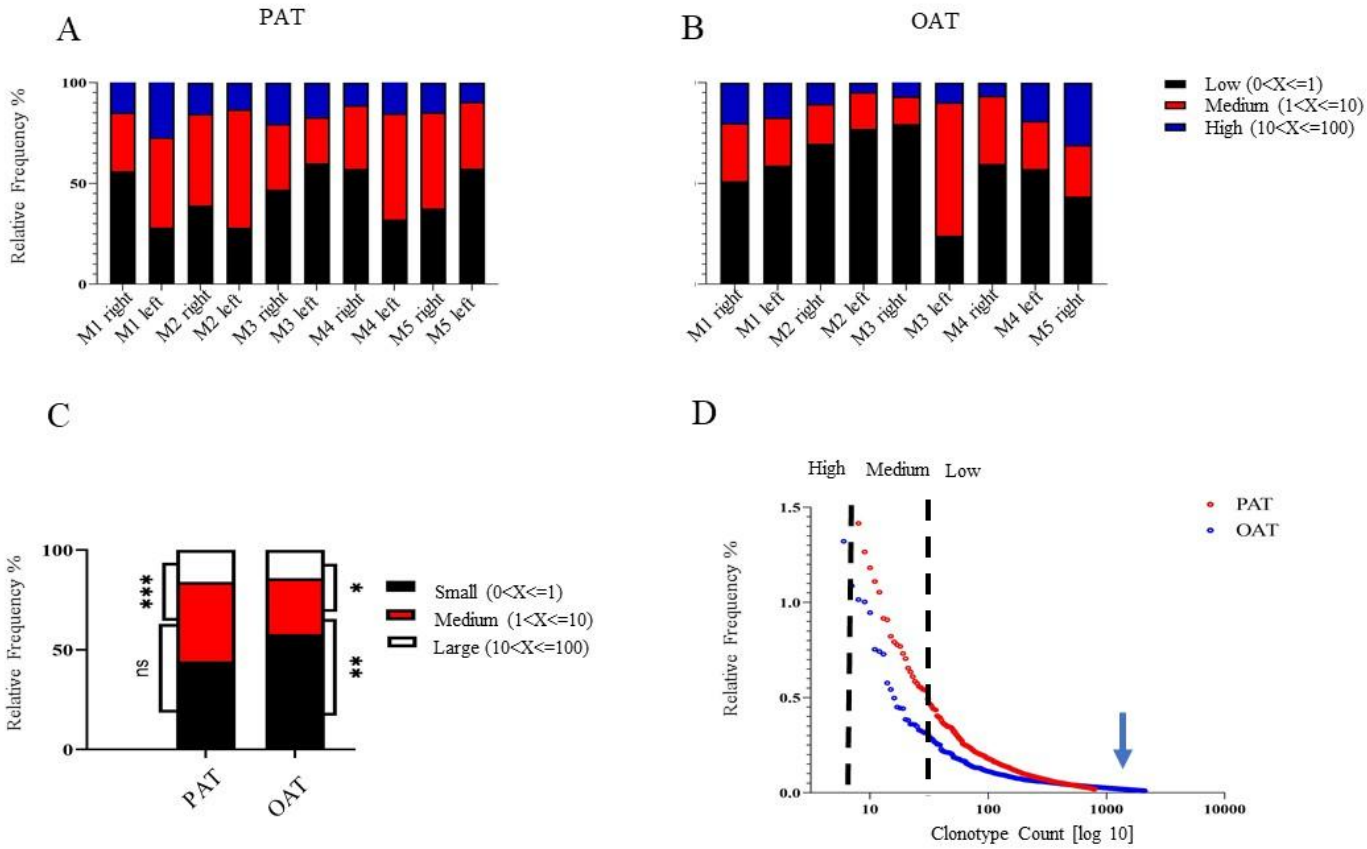

Figure 5. Clonotype abundance analysis of GC–Tfh cells in the Pln of PAT- and OAT-pretreated mice. A–B) Clonotype abundance in individual mice from the PAT (A) and OAT (B) groups (M1–M5), showing the relative frequency (%) of small ($0 < X \leq 1$, black), medium ($1 < X \leq 10$, red), and large ($10 < X \leq 100$, blue) clonotypes. C) Mean clonotype abundance across all mice in the Pln, presented as grouped bar graphs of the relative frequency (%) of small, medium, and large clonotypes in PAT and OAT mice. In PAT mice, the proportion of small and medium clonotypes did not differ significantly, whereas in OAT-pretreated mice small clonotypes became significantly more abundant than medium clonotypes. Significance is indicated as ns (not significant), $p < 0.05$, *$p < 0.01$, **$p < 0.001$. D) Representative cumulative clonotype frequency distribution in the Pln, comparing one PAT (red) and one OAT (blue) mouse, plotted as log10 clonotype count versus relative frequency (%). n=5

In the Ingln, a similar but more pronounced trend was observed. In PAT mice, clonotype frequencies were distributed as ~52% small, ~33% medium, and ~15% large, again showing no significant difference between small and medium (Figure 6A, 6C). Following OAT pretreatment, the proportion of small clonotypes increased significantly to ~57%, while medium clonotypes decreased to ~28% and large clonotypes to ~15% (Figure 6B, 6C). Cumulative distribution analysis confirmed this shift, with OAT-pretreated Ingln repertoires showing a more rapid decline compared to PAT controls (Figure 6D).

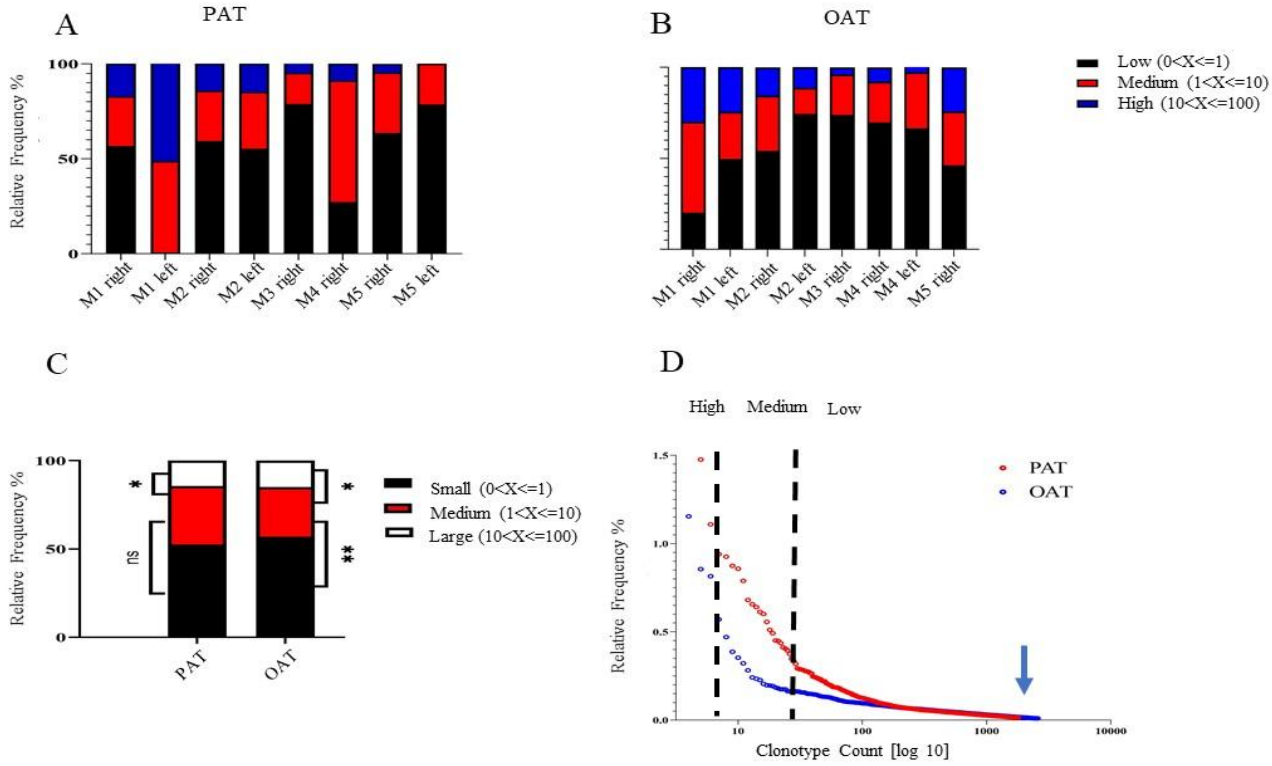

Figure 6. Clonotype abundance analysis of GC–Tfh cells in the inguinal lymph nodes (Ingln) of PAT- and OAT-pretreated mice. A–B) Clonotype abundance in individual mice from the PAT (A) and OAT (B) groups (M1–M5), showing the relative frequency (%) of small ($0 < X \leq 1$, black), medium ($1 < X \leq 10$, red), and large ($10 < X \leq 100$, blue) clonotypes. C) Mean clonotype abundance across all mice in the Ingln, presented as grouped bar graphs of the relative frequency (%) of small, medium, and large clonotypes in PAT and OAT mice. In PAT mice, the proportions of small and medium clonotypes were not significantly different, whereas in OAT-pretreated mice small clonotypes became significantly more abundant than medium clonotypes. Large clonotypes were significantly reduced in OAT compared to PAT. Significance is indicated as ns (not significant), $p < 0.05$, *$p < 0.01$, **$p < 0.001$. D) Representative cumulative clonotype frequency distribution in the Ingln, comparing one PAT (red) and one OAT (blue) mouse, plotted as log10 clonotype count versus relative frequency (%).

Taken together, these results demonstrate that OAT pretreatment alters the frequency distribution of Tfh clonotypes in both the Pln and Ingln, reducing the expansion of medium- and large-sized clones while increasing the proportion of low-abundance clonotypes. This type of analysis is essential because it provides insight beyond the total number of clonotypes (Table 10, Figure 4) by revealing how individual clonotypes contribute to the repertoire. Whereas total clonotype counts showed no differences between groups, abundance analysis uncovers that OAT explicitly prevents the emergence of dominant Tfh clonotypes and instead promotes diversification of the repertoire. Such a shift is consistent with a less autoreactive and potentially more balanced Tfh compartment.

In summary, these data show that pretreatment with OAT increases the percentage of low-abundance Tfh clonotypes in both the Pln and Ingln. This finding suggests that OVA-specific Tfh clonotypes may persist in the GC, even though the last OAT injection occurred six weeks before analysis. Moreover, although both Pln and Ingln displayed similar trends toward an increased proportion of low-abundance clonotypes following OAT pretreatment, the effect appeared more pronounced in the Ingln. One possible explanation is that the final OAT boost at the tail base, which drains directly into the Ingln, provided sustained antigenic stimulation closer to the time of disease induction. This may have allowed OVA-specific Tfh clonotypes to persist longer in Ingln GC, where they could increase clonal competition and thereby limit the expansion of dominant autoreactive clones. While this interpretation remains hypothetical, it offers a plausible mechanism for why the repertoire shift toward low-abundance clonotypes was stronger in the Ingln than in the Pln. Clonotype abundance analysis is a crucial first step because it reveals how OAT pretreatment alters the size distribution of Tfh clonotypes, demonstrating a consistent reduction in medium- and large-frequency clonotypes, accompanied by an enrichment of low-abundance clonotypes. This provides direct evidence that OAT prevents the expansion of dominant clones and promotes diversification within the repertoire. However,

abundance analysis alone is limited, as it only reflects the relative size of clonotype classes within individual repertoires. It does not address whether the same clonotypes are shared between different mice or groups, nor does it capture broader repertoire-level relationships. Therefore, to obtain a more comprehensive understanding of how OAT pretreatment reshapes Tfh repertoires, complementary approaches are required to assess repertoire similarity and diversity across samples and within-sample abundance distributions.

3.1.1.3. Repertoire overlap across mice is not altered by OAT pretreatment

To extend the analysis beyond clonotype abundance, we next evaluated the degree of repertoire similarity across individual mice. For this purpose, we employed an overlap measure that captures the proportion of clonotypes shared between two repertoires relative to the total clonotype pool. This metric, commonly used in repertoire studies, provides an estimate of the degree of convergence or private T cell responses across biological replicates. Values theoretically range from 0 (no shared clonotypes) to 1 (identical repertoires), but in practice, the absolute number is relative and highly dependent on sequencing depth, sample size, and biological variability. Therefore, the index should be interpreted comparatively between groups rather than as an absolute measure of repertoire similarity. In short, the Jaccard index is a similarity measure that quantifies the proportion of clonotypes shared between two repertoires relative to the total number of clonotypes present in both. Applying this approach allowed us to determine whether OAT pretreatment leads to convergence of GC–Tfh clonotypes across mice or whether repertoires remain largely individualized despite pretreatment.

In the Pln, abundance analysis had already shown that OAT pretreatment shifted the repertoire toward a higher proportion of small clonotypes, raising the question of whether such redistribution would also translate into increased repertoire convergence. Since both pretreatment and disease induction were delivered via footpad injections, with drainage into the

respective Plns, one might expect that antigen exposure through this highly standardized route could drive a certain degree of overlap, particularly between the right and left Pln of the same animal. If OAT pretreatment imposed a strong immunoregulatory imprint, it would be expected to not only alter clonotype abundance but also increase repertoire convergence across mice, reflecting a shared tolerogenic Tfh response.

To investigate this possibility, we first examined clonotype overlap across all individual Pln samples. Pairwise similarity heatmaps revealed uniformly low Jaccard values, with no evidence of clustering according to treatment group (Figure 7A). This indicates that despite the marked abundance shifts observed within repertoires, the overall clonotype composition remained largely private to each mouse. In other words, OAT pretreatment did not lead to the emergence of a common set of clonotypes across individuals but instead reshaped the distribution of existing clones within each repertoire.

We then focused on the direct comparison of right and left Pln within the same animal, reasoning that paired draining LNs exposed to identical antigenic stimulation should serve as a more sensitive readout of repertoire convergence. In principle, if OAT induced a shared tolerance pattern, greater similarity between right and left Pln repertoires would be expected. Indeed, within-mouse Jaccard values were consistently higher than between-mouse comparisons, reflecting the biological proximity of paired draining nodes and their shared antigen exposure. However, the magnitude of this similarity did not differ between OAT- and PAT-pretreated mice (Figure 75B). This suggests that even in the context of identical antigenic challenge within the same organism, OAT pretreatment did not enhance repertoire convergence beyond the baseline similarity observed in control animals.

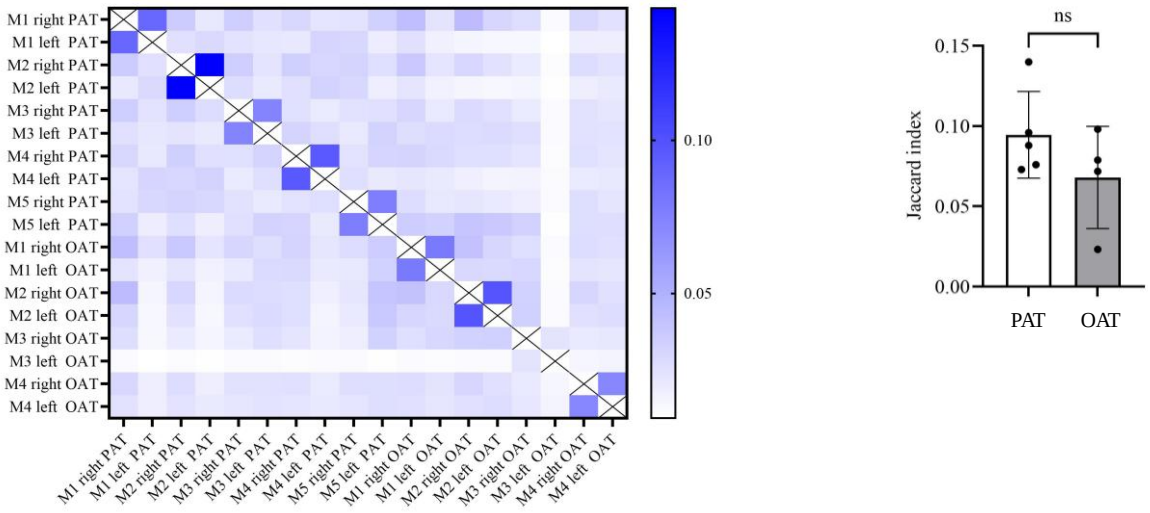

Figure 7. Clonotype overlap of GC–Tfh cells in Pln of PAT- and OAT-pretreated mice. A) Heatmap of pairwise Jaccard similarity indices between right and left Pln repertoires from individual mice in PAT and OAT groups. Each square represents the degree of overlap between two repertoires, with darker blue indicating higher similarity. No clustering by treatment group was observed, and values remained low overall. B) Quantitative comparison of Jaccard indices between right and left Pln within individual mice. Mean similarity values were comparable between OAT- and PAT-pretreated groups, with no significant difference (ns). Data are shown as mean ± SD, with individual mice represented by dots.

Taken together, these findings highlight an important aspect of OAT-mediated modulation: repertoire remodeling in the Pln is primarily driven by internal shifts in clonotype abundance rather than by the emergence of a convergent, shared clonotype pool across mice. The observation that right and left Pln within the same animal did not exhibit greater similarity after OAT pretreatment further supports the view that repertoire reprogramming remains individualized, shaped by local clonal dynamics rather than by a universal, group-wide clonotypic imprint.

In contrast to the Pln, the Ingln represents the draining site of the final OAT boost at the base of the tail, and thus is exposed to antigenic stimulation closer to the time of mCol7c challenge. This injection pattern suggested that Ingln might retain a stronger imprint of OAT pretreatment,

potentially leading to higher clonotype convergence if OVA-specific Tfh clonotypes persisted and limited the expansion of autoreactive clones.

To test this, we analyzed clonotype overlap within Ingln repertoires. Heatmaps of pairwise Jaccard values again revealed low overall similarity across mice, without clustering by treatment group (Figure 8A). This finding indicates that, as in the Pln, repertoires remained largely individualized, and OAT pretreatment did not impose a convergent clonotypic signature across animals.

We then compared the overall similarity of Ingln repertoires within treatment groups. Mean Jaccard indices were slightly higher in OAT than in PAT mice, suggesting a trend toward increased overlap; however, this difference did not reach statistical significance (Figure 8B). Thus, while OAT pretreatment significantly reshaped clonotype abundance distributions in the Ingln, it did not translate into a measurable increase in repertoire similarity.

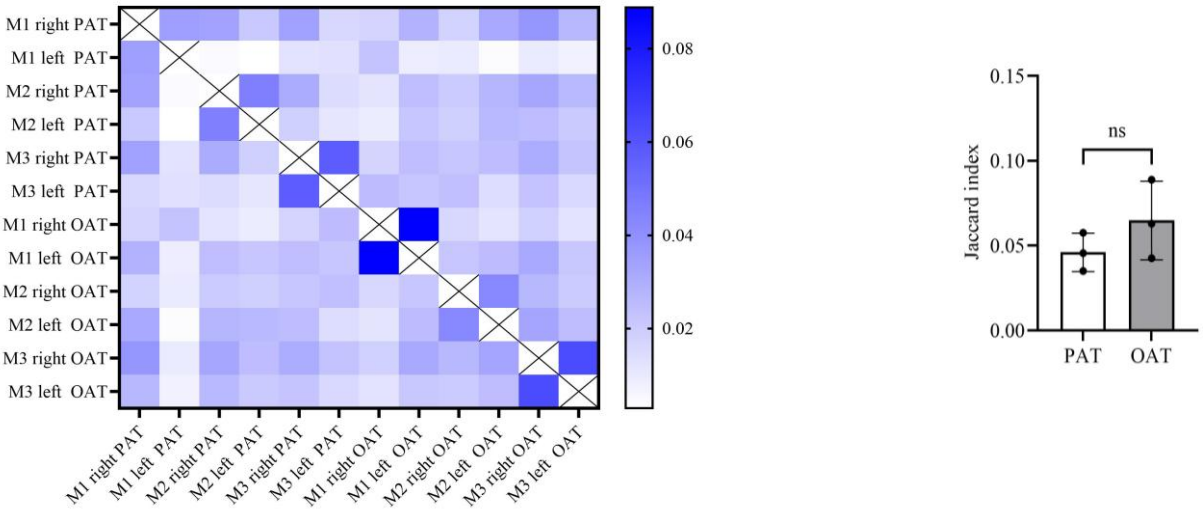

Figure 8. Clonotype overlap of GC–Tfh cells in Ingln of PAT- and OAT-pretreated mice. A) Heatmap of pairwise Jaccard similarity indices between right and left Ingln repertoires from individual mice in PAT and OAT groups. Each square represents the degree of overlap between two repertoires, with darker blue indicating higher similarity. No clustering by treatment group was observed, and values remained low overall. B) Quantitative comparison of Jaccard indices between right and left Ingln within individual mice. Mean similarity values were comparable between OAT- and PAT-pretreated groups, with no significant difference (ns). Data are shown as mean ± SD, with individual mice represented by dots.

Our findings suggest that, despite expected local antigen exposure, OAT pretreatment did not lead to the convergence of clonotypes across individuals in the Ingln. Rather, the Ingln repertoire's remodeling after OAT is primarily driven by internal shifts in clonotype abundance, rather than the emergence of a shared clonotype pool.

In conclusion, the Jaccard analyses show that OAT pretreatment has no impact on the degree of Tfh clonotype overlap between LNs. In the Pln, where pretreatment and disease induction were delivered via footpad injections, repertoires remained largely distinct, and the similarity between right and left nodes was comparable in OAT- and PAT-pretreated mice. Similarly, in the Ingln, which drained the final OAT injection at the base of the tail, repertoires exhibited low overall overlap, with no notable differences between groups. Although redistribution of clonotype frequencies was observed in abundance analyses, OAT pretreatment does not lead to convergence of Tfh repertoires across individuals or between paired draining LNs. Instead, repertoire remodeling under OAT is limited to internal changes in clonotype abundance, without the emergence of a shared clonotype pool.

3.1.1.4. The number of the top 50 overlapping Tfh clonotypes among Pln and Ingln differ between the groups

In the preceding analysis, we assessed clonotype overlap using the Jaccard index, which quantifies the proportion of shared clonotypes between repertoires. Contralateral comparisons (right vs left Pln or Ingln) revealed no significant differences between OAT- and PAT-pretreated groups. These results indicated that OAT pretreatment does not alter repertoire convergence at the global level when comparing paired LNs of the same type. However, the Jaccard index is an aggregate measure that gives equal weight to all clonotypes, regardless of their abundance. It therefore lacks sensitivity to shifts occurring within the most expanded clonotypes, which are most likely to shape GC output and autoimmune responses.

Given that our abundance analysis had already shown the redistribution of clonotype frequencies, with OAT pretreatment favoring smaller clones over medium- and large-sized ones, we next focused on the subset of clonotypes that dominate the repertoire. For this purpose, we restricted the analysis to the top 50 most abundant clonotypes in each LN. These clonotypes represent the expanded populations with the greatest likelihood of contributing to autoreactive B cell help and were therefore chosen as a biologically meaningful subset.

Since contralateral comparisons did not reveal significant differences, we turned to ipsilateral analyses that capture clonal dissemination between LNs draining distinct antigen exposure sites. To avoid potential left–right biases, clonotypes from both left and right nodes of the same type were combined for each mouse. We then asked whether clonotypes dominating the Pln were also detectable in the ipsilateral Ingln (Pln→Ingln analysis) and, conversely, whether Ingln clonotypes were represented in the Pln (Ingln→Pln analysis). This approach provides directional information on clonal sharing between LN compartments, allowing us to determine whether OAT pretreatment alters the balance of repertoire exchange between them.

First, we looked from Pln to Ingln. To assess the dissemination of dominant clonotypes from Pln into Ingln, we selected the 50 most abundant clonotypes in each mouse, pooling left and right Pln to avoid laterality effects. These clonotypes represent the most expanded GC–Tfh populations and are most likely to drive functional B cell help. We then asked whether these clonotypes were also detectable in the ipsilateral Ingln (left and right combined). Overlap was defined as the fraction of top-50 Pln clonotypes present in Ingln, while clonotypes absent from Ingln were considered Pln-restricted.

In representative PAT mice, the majority of top-50 Pln clonotypes were also detected in Ingln, as illustrated by rank–frequency plots in which Pln and Ingln curves largely co-tracked. Only 4/50 clonotypes (8%) were node-restricted, corresponding to 92% overlap (Figure 9A). In contrast, representative OAT mice displayed reduced overlap, with 10/50 clonotypes (20%)

restricted to the Pln and 80% shared with Ingln (Figure 9B). The restricted clonotypes in OAT were not confined to the lowest-frequency ranks but distributed across the lower half of the top-50, indicating that reduced overlap was not solely driven by sampling of rare clonotypes.

Group quantification confirmed this trend: mean Pln to Ingln overlap was significantly lower in OAT- compared to PAT-pretreated mice ($p < 0.05$; Figure 9C). Given that total sequencing output and clonotype numbers were comparable across groups (Table 10, Figure 4), these findings indicate that OAT pretreatment increases the proportion of Pln-restricted clonotypes, thereby limiting the inter-nodal spread of expanded Tfh clonotypes from the Pln to the Ingln. The reduced Pln to Ingln overlap in OAT-pretreated mice needs to be viewed in the context of the injection pattern. The Pln received both the initial OAT priming and the subsequent mCol7c immunization in the footpads, resulting in substantial local expansion of Pln-derived clonotypes. By contrast, the Ingln primarily drained the final OAT boost at the tail base and did not receive direct mCol7c antigen. Accordingly, fewer Pln-derived clonotypes were represented in the Ingln of OAT mice compared to PAT controls. This indicates that OAT pretreatment alters the balance of clonal dissemination between LNs in a manner reflecting both the sequence of OAT injections and the later site of mCol7c challenge.

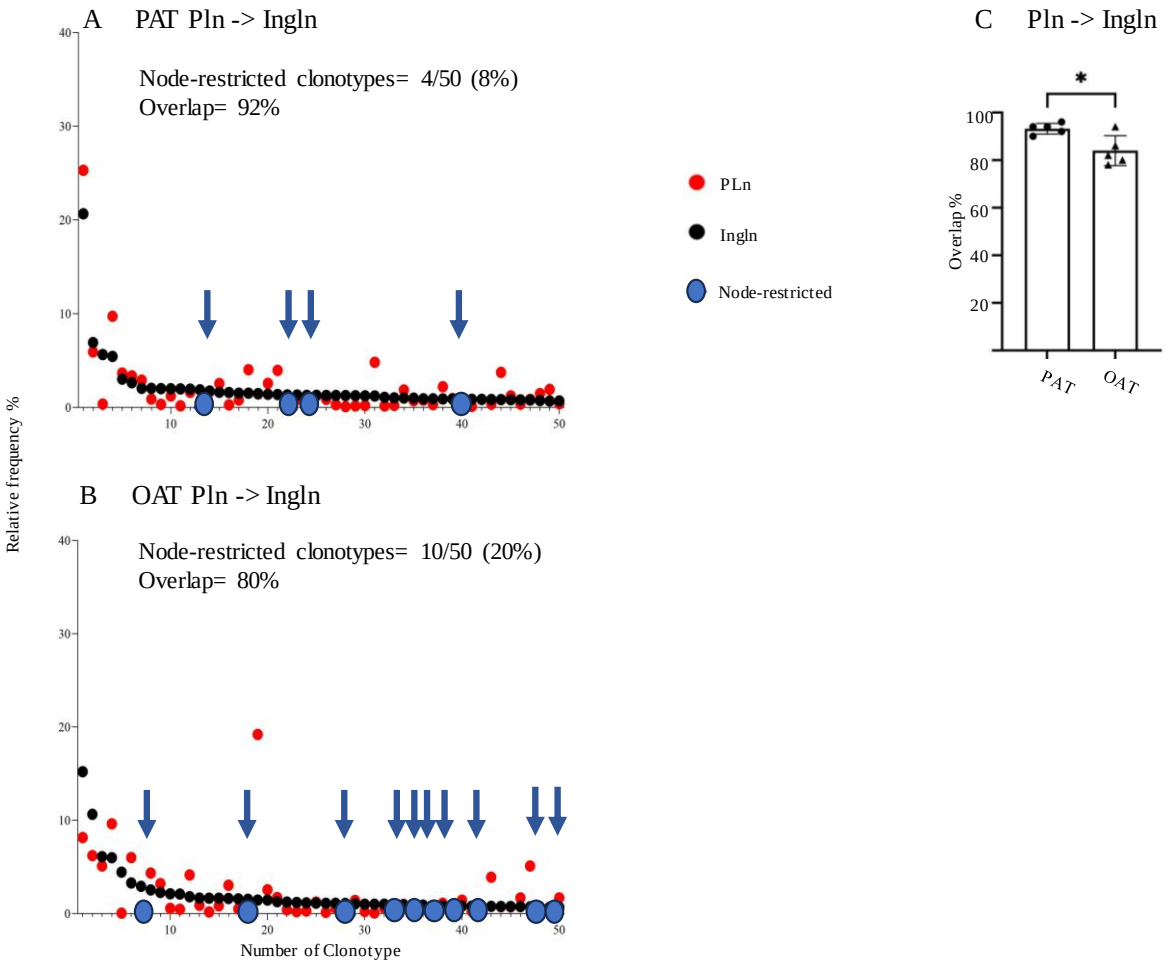

Figure 9. Overlap of the top 50 most abundant Pln clonotypes with ipsilateral Ingln repertoires. A–B) Representative rank–frequency plots showing the top 50 clonotypes from pooled left and right Pln in a PAT (A) and an OAT (B) mouse. Red dots represent Pln clonotypes, black dots indicate corresponding clonotypes detected in the Ingln, and blue dots mark clonotypes restricted to the Pln. C) Group quantification of overlap, defined as the percentage of top-50 Pln clonotypes also detected in the ipsilateral Ingln. OAT-pretreated mice showed significantly reduced Pln→Ingln overlap compared with PAT controls ($p < 0.05$). Data are presented as mean ± SD, with individual mice represented by dots.

Next, we examined the dissemination of clonotypes from Ingln into Pln. To do this, we selected the 50 most abundant clonotypes in each mouse, pooling left and right Ingln to avoid laterality effects. These clonotypes represent the dominant Tfh populations in the Ingln and are expected to reflect the imprint of the final OAT boost at the tail base. We then asked whether each of these clonotypes was also detectable in the ipsilateral Pln (left and right combined). Overlap

was defined as the fraction of top-50 Ingln clonotypes present in Pln, while clonotypes absent from Pln were considered Ingln-restricted.

In representative PAT mice, Ingln clonotypes were only partially represented in Pln, as shown by rank–frequency plots where several Ingln clonotypes failed to appear in Pln. In this example, 37/50 clonotypes (74%) were shared and 13/50 (26%) were Ingln-restricted (Figure 10A). In contrast, representative OAT mice displayed greater overlap, with 44/50 clonotypes (88%) detectable in Pln and only 6/50 (12%) restricted to Ingln (Figure 10B). Importantly, the restricted clonotypes were distributed across different frequency ranks, indicating that the higher overlap in OAT mice was not simply due to shared low-frequency clonotypes.

Group quantification confirmed this difference: mean Ingln to Pln overlap was significantly higher in OAT compared to PAT mice ($p < 0.05$; Figure 8C). Because sequencing depth and clonotype counts were similar across groups (Table 10, Figure 4), this result reflects an actual biological effect rather than a technical artifact. Taken together, these findings demonstrate that OAT pretreatment reduces the proportion of Ingln-restricted clonotypes, thereby increasing the dissemination of Ingln-derived clonotypes into the Pln. This observation is consistent with the injection pattern: the Ingln directly drained the final OAT boost at the tail base, whereas the Pln was the site of mCol7c challenge in the footpads. Thus, Ingln clonotypes primed or reinforced during OAT pretreatment were more likely to persist and be represented in the Pln during disease induction in OAT-pretreated mice compared to PAT controls.

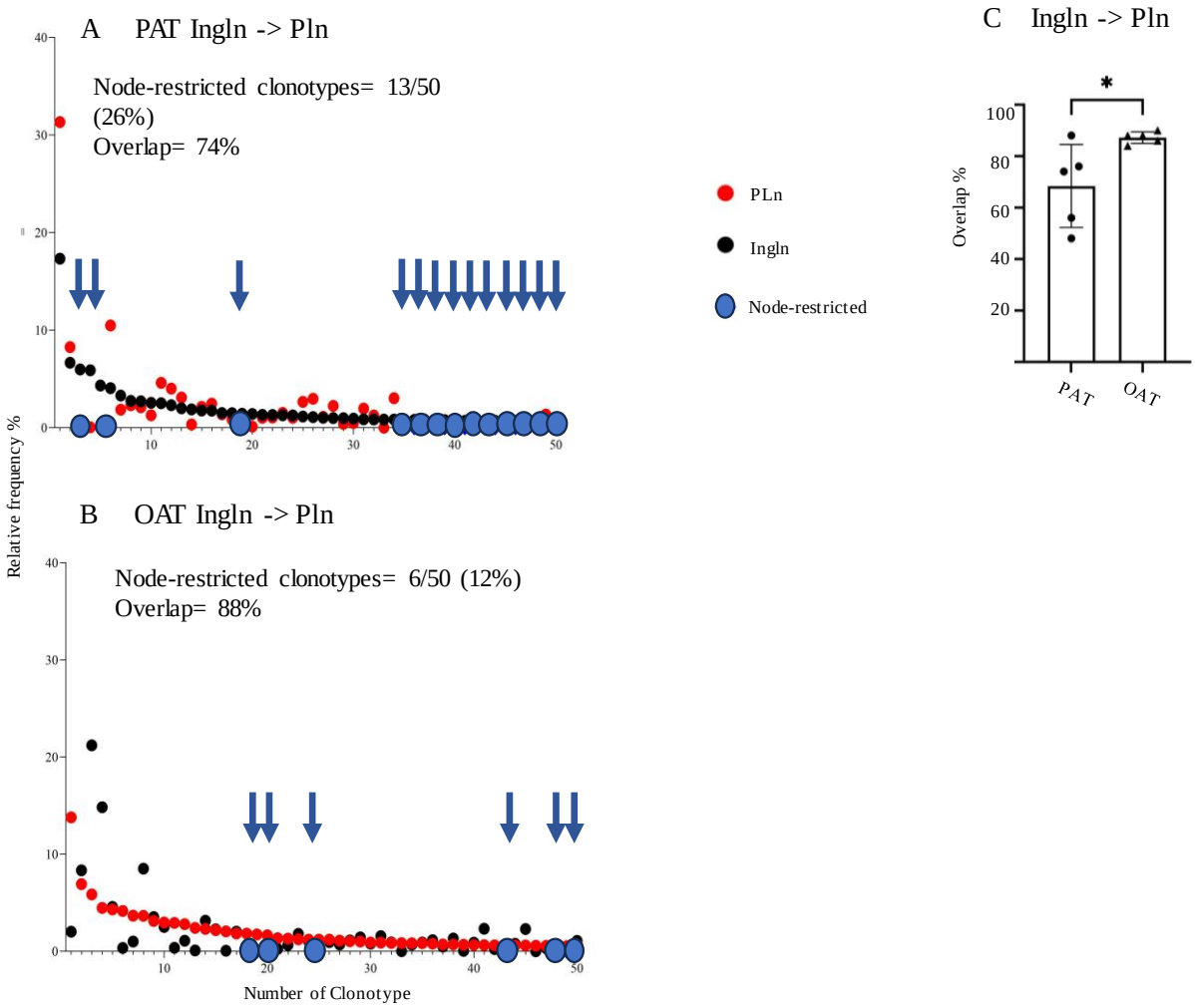

Figure 10. Overlap of the top 50 most abundant Ingln clonotypes with ipsilateral Pln repertoires. A–B) Representative rank–frequency plots showing the top 50 clonotypes from pooled left and right Ingln in a PAT (A) and an OAT (B) mouse. Black dots represent Ingln clonotypes, red dots indicate corresponding clonotypes detected in the Pln, and blue dots mark clonotypes restricted to the Ingln. C) Group quantification of overlap, defined as the percentage of top-50 Ingln clonotypes also detected in the ipsilateral Pln. OAT-pretreated mice showed significantly increased Ingln→Pln overlap compared with PAT controls ($p < 0.05$). Data are presented as mean ± SD, with individual mice represented by dots.

Overall, the directional overlap analyses reveal that OAT pretreatment does not simply increase or decrease clonotype sharing but fundamentally changes the dissemination balance between LN compartments. In PAT-pretreated mice, clonotypes expanded in the Pln disseminated efficiently into the Ingln, with more than 90% of the top-50 Pln clonotypes also detectable in Ingln, whereas only ~74% of Ingln clonotypes were represented in Pln. This asymmetry indicates that, under control conditions, clonotypes arising in the Pln dominate the shared repertoire, while Ingln repertoires remain more restricted. In OAT-pretreated mice, this

relationship was reversed: Pln to Ingln overlap decreased significantly to ~80%, with a higher proportion of Pln-restricted clonotypes, while Ingln to Pln overlap increased significantly to ~88%, reflecting broader dissemination of Ingln-derived clonotypes into the Pln. Thus, OAT pretreatment shifts the directionality of clonotype exchange, favoring Ingln-derived clonotypes over Pln-derived clonotypes.

When considered in the context of the injection pattern, these results suggest a plausible biological explanation. The Pln drained both the early OAT injections and the later mCol7c immunization, whereas the Ingln uniquely drained the final OAT boost delivered at the tail base. The increased representation of Ingln clonotypes in Pln observed only in OAT-pretreated mice is therefore consistent with the persistence of OVA-specific Tfh clonotypes in Ingln, which were maintained for at least six weeks after pretreatment and subsequently disseminated into the Pln during mCol7c challenge. Conversely, the reduced Pln to Ingln overlap under OAT indicates that clonotypes expanded by the later mCol7c immunization in the Pln were less effectively represented in Ingln, further emphasizing that Ingln maintained its imprint from OAT pretreatment. Together, these findings provide evidence that OAT pretreatment directionally reshapes repertoire connectivity between LNs and support the hypothesis that OVA-specific clonotypes persisted in Ingln and contributed to the altered balance of Tfh repertoires during autoimmune induction. In short, because mCol7-specific clonotypes could only arise in the Pln and Pln to Ingln overlap was reduced, whereas Ingln to Pln overlap was increased, the persisting Ingln clonotypes must represent OVA-primed populations that subsequently disseminated into the Pln.

As explained, these data are consistent with the persistence of OVA-specific clonotypes in the Ingln following OAT pretreatment, which subsequently disseminated into the Pln during mCol7c challenge. We next analyzed qualitative repertoire features to further investigate whether these persisting clonotypes also carry distinct molecular signatures. Specifically, we

examined CDR3 length distributions and k-mer composition, as these parameters reflect structural and biochemical properties of the TCRβ repertoire and can reveal antigen-driven selection processes. This approach allows us to test whether OAT pretreatment imprints distinct sequence characteristics on Pln or Ingln clonotypes compared with PAT control.

3.1.1.5 Qualitative features of the Tfh TCRR reveal sequence differences between OAT- and PAT-pretreated draining LNs

Building on our findings that OAT pretreatment reshapes Tfh clonality and alters the ipsilateral dissemination of clonotypes between Ingln and Pln, we next examined whether OAT also imprints qualitative features of the Tfh repertoire. Specifically, we hypothesized that persistent Ingln clonotypes following OAT pretreatment may exhibit distinct sequence characteristics, reflected in altered CDR3 length distributions and k-mer motifs, which could in turn influence peptide–MHC II interactions compared with PAT controls (J. Li et al., 2020).

To test this, we analyzed the CDR3 length distribution and k-mer frequencies within TCR sequences from Tfh cells, focusing on the Ingln where OAT-specific effects were pronounced. The CDR3 region determines TCR specificity for peptide-MHC II complexes, and k-mer motifs can reveal amino acid patterns that affect binding stability. This analysis is crucial for understanding how qualitative TCRR differences in the Ingln influence Tfh cell interactions with peptide-MHC II complexes, potentially impacting the immune response in EBA.

3.1.1.5.1. OAT pretreatment reshapes CDR3 length distributions of Tfh repertoires in draining LNs

First, we analyzed CDR3β length distributions, a parameter that reflects structural diversity of the TCR and is closely linked to antigen specificity. Most clonotypes in both groups fell within the typical 33–48 amino acid range, with clear peaks at 36, 39, and 42 amino acids, indicating conserved structural constraints of GC–Tfh repertoires across conditions (Figure 9). Thus, at a

global level, both OAT- and PAT-pretreated mice shared the canonical architecture of Tfh CDR3 lengths.

In the Pln (Figure 11A), OAT and PAT mice exhibited nearly identical profiles, with dominant peaks at 36–42 amino acids and no major differences between groups. This suggests that in the footpad-draining nodes, which received both OAT priming and the subsequent mCol7c immunization, the selective pressures imposed by antigen exposure converged on a similar distribution of CDR3 lengths.

By contrast, the Ingln (Figure 11B) showed a distinct shift. In PAT mice, shorter CDR3 clonotypes of 33 and 36 amino acids were relatively enriched, accounting for ~4–5% and 12% of the repertoire, respectively. OAT-pretreated mice exhibited lower frequencies at these lengths (~2% and ~10%), but displayed a relative enrichment of longer CDR3s, particularly at 42 and 45 amino acids. These longer CDR3s are of immunological interest: in general, extended CDR3β loops are associated with recognition of more diverse or structurally complex epitopes, including atypical or cross-reactive peptides. While this cannot directly prove OVA specificity, the observed bias is consistent with the unique antigen exposure history of OAT mice, in which the final OVA boost was delivered at the tail base, draining to the Ingln. Thus, the Ingln repertoire of OAT mice may have retained clonotypes originally primed by OVA, whereas PAT mice, exposed only to mCol7c, were dominated by shorter CDR3 clonotypes more typical of antigen-driven selection by a single target.

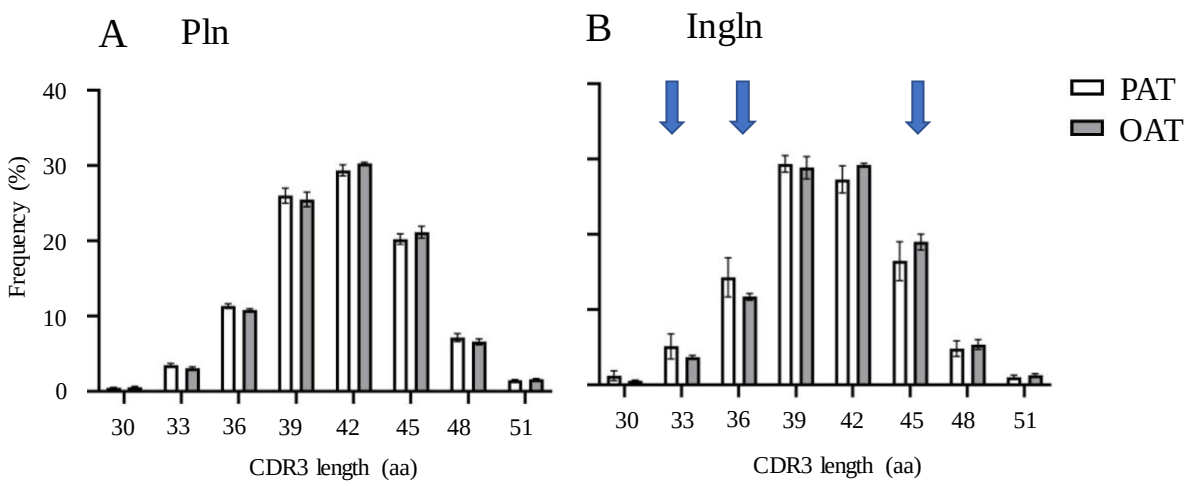

Figure 11. OAT pretreatment modifies the CDR3 length distribution of Tfh clonotypes in Pln and Ingln. CDR3 length distributions (in amino acids, aa) were analyzed in Tfh clonotypes isolated from A) Pln and B) Ingln of mice pretreated with PAT (white bars) or OAT (gray bars). Clonotypes from left and right lymph nodes were combined within each group to avoid laterality effects. The frequency of each CDR3 length is shown as a percentage of total clonotypes. In the Pln (A), both groups exhibited similar distributions with dominant peaks at 36–42 aa, indicating no major effect of OAT pretreatment. In the Ingln (B), however, OAT-pretreated mice showed reduced frequencies of shorter CDR3s (33 and 36 aa) and a relative enrichment of longer clonotypes (42–45 aa, blue arrows). Longer CDR3s are often associated with recognition of more diverse or structurally complex epitopes, suggesting persistence of distinct clonotypes shaped by the OVA boost in the Ingln. Bars represent mean ± SD across mice (n=5).

These findings suggest that OAT pretreatment has a lasting impact on the qualitative structure of the Ingln Tfh repertoire, favoring clonotypes with longer CDR3s. Although the absolute differences in each bin did not reach statistical significance, the consistent pattern supports the persistence of clonotypes shaped by the OVA boost in the Ingln and provides a mechanistic rationale for further probing sequence-level features, such as k-mer composition, in subsequent analyses.

3.1.1.5.2. Distinct k-mer usage patterns emerge in Ingln Tfh clonotypes after OAT pretreatment

To better understand the qualitative aspects of the Tfh repertoire, we used k-mer analysis on CDR3β sequences. This method pinpoints short amino acid patterns within the CDR3 that may contribute to the structural preferences of TCR–peptide–MHC II interactions. To minimize variability caused by laterality, we first combined clonotypes from the left and right Pln or Ingln for each mouse. The ten most abundant clonotypes were selected from these combined repertoires, thereby focusing the analysis on the dominant populations most likely to contribute to functional GC responses.

In the Pln, both OAT- and PAT-pretreated mice displayed repertoires dominated by canonical motifs, such as CAS and ASS, which together accounted for more than half of the sequences (Figures 12A and 12 B). These motifs, enriched in serine, represent germline-associated frameworks that are universally observed across TCRRs and were comparably present in both groups. However, differences became apparent beyond this shared baseline. In PAT-pretreated mice, motifs such as CTC and TCS were detected at higher frequencies, together contributing ~15–20% of the top-10 clonotypes. Both contain cysteine residues, which confer chemical reactivity and structural rigidity, potentially limiting conformational flexibility at the TCR–MHC interface. Their enrichment is consistent with a more restricted, autoreactive repertoire driven by mCol7c immunization. In contrast, OAT-pretreated Pln repertoires exhibited a broader motif distribution with reduced frequencies of cysteine-containing motifs, suggesting attenuation of autoreactive skewing.

The most striking differences, however, were observed in the Ingln, as in the Pln, CAS and ASS remained the dominant motifs in both groups (Figure 12. C, D). Yet, in OAT-pretreated mice, additional motifs, such as NTL and AEQ, were reproducibly identified among the top 10 clonotypes, whereas they were nearly absent in PAT controls. These motifs are biochemically

distinct: NTL combines polar residues (Asn, Thr) with a hydrophobic anchor (Leu), enabling both hydrogen bonding and hydrophobic interactions within the MHC II peptide-binding groove. AEQ incorporates Ala (small hydrophobic), Glu (acidic, negatively charged), and Gln (polar, amide), a combination that supports electrostatic stabilization and polar contacts in addition to structural flexibility. Such mixed polar–hydrophobic chemistries are particularly compatible with MHC II binding, which relies on hydrophobic anchor pockets interspersed with polar and charged surfaces. Their enrichment in the Ingln of OAT-pretreated mice suggests that pretreatment favored persistence of clonotypes with more versatile TCR–peptide–MHC binding potential.

In contrast, Ingln repertoires of PAT-pretreated mice resembled those of the Pln, with a high frequency of CAS/ASS and enrichment for cysteine-containing motifs like CTC and TCS. The biochemical constraints imposed by cysteine residues likely contribute to a more restricted spectrum of peptides recognized, which aligns with the clonotypic narrowing and autoreactive expansion seen in PAT mice.

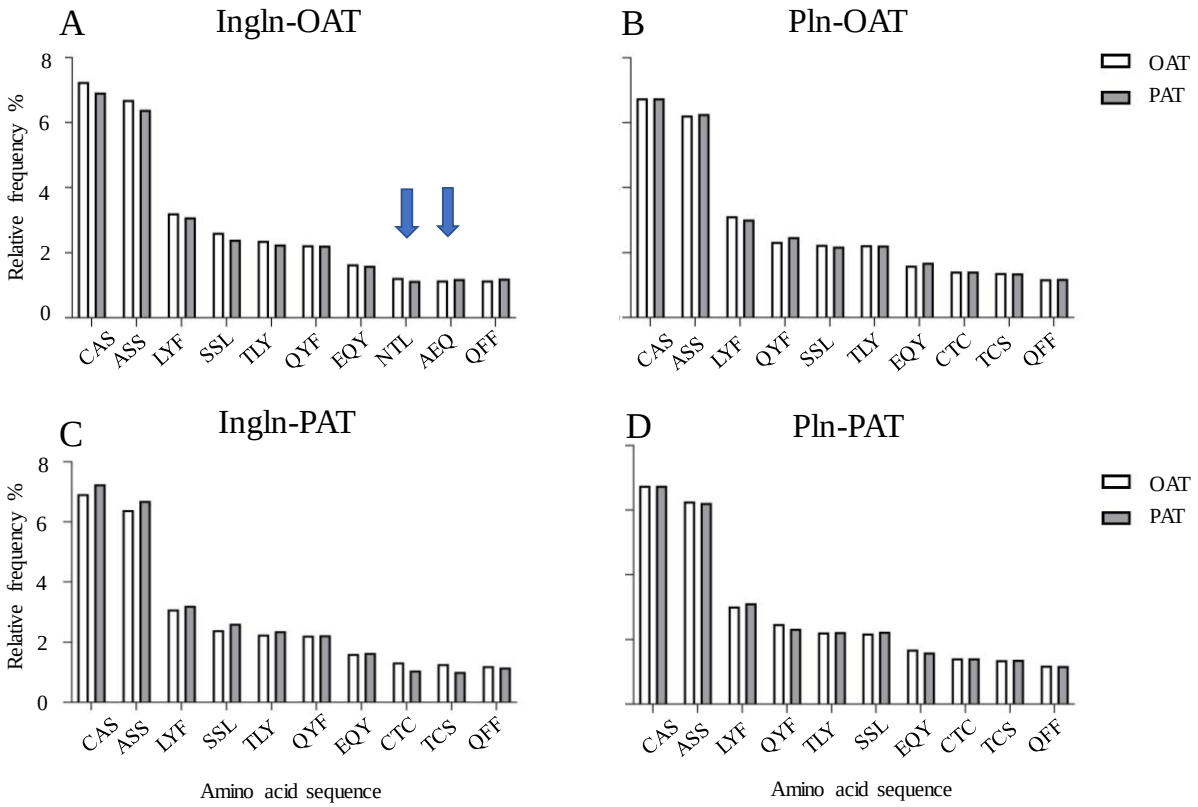

Figure 12. Kmer Distribution in Ingln and Pln Under OAT and PAT Treatment Conditions. The figure shows the relative frequencies of the first 10 Kmers in Ingln and Pln, sorted according to two experimental conditions: OAT and PAT. A) Ingln first 10 Kmers sorted on OAT, showing the distribution of Kmers under OAT treatment. B) The first 10 Kmers were sorted on OAT, displaying the Kmer distribution in the Pln under OAT treatment. C) Ingln's first 10 Kmers were sorted on PAT, showing the distribution of Kmers under the control condition in Ingln. D) The first 10 Kmers were sorted on PAT, illustrating the Kmer distribution in the Pln under the control condition.

In summary, these findings indicate that OAT pretreatment does more than just reduce clonal dominance; it also reshapes the motif landscape of the Tfh repertoire in a way that is specific to the LN. While Pln repertoires in PAT mice were biased toward cysteine-rich motifs, which is consistent with autoreactive selection, OAT-pretreated Ingln repertoires showed new motifs (NTL, AEQ) with a balanced mix of hydrophilic and hydrophobic chemistry that matches MHC II binding preferences. These results build on our previous studies of overlap and CDR3 length, supporting the idea that OVA-induced clonotypes persist in the Ingln and add new sequence features to the local repertoire.

Taken together, the TCRR analyses show that OAT pretreatment reshapes both the quantitative and qualitative architecture of Tfh clonotypes. At the contralateral level, differences were detectable in the distribution of small-abundance clonotypes. However, Jaccard overlap values remained unchanged, indicating limited impact on global repertoire convergence across opposite LNs. In contrast, the most striking findings emerged in ipsilateral comparisons: OAT pretreatment reduced Pln to Ingln but increased Ingln to Pln dissemination of the top 50 most abundant clonotypes, altered CDR3 length distributions by reducing short clonotypes and favoring longer ones in Ingln, and introduced distinct sequence motifs, such as NTL and AEQ. Together, these results indicate that OAT pretreatment promotes the persistence of clonotypes with distinct structural features in the Ingln and alters their dissemination toward the Pln during mCol7c challenge.

Together, these data show that OAT pretreatment does not globally alter Tfh clonotype numbers but instead reshapes their distribution, persistence, and qualitative features in a LN-specific manner. Notably, the most outstanding effects were ipsilateral, with Ingln repertoires displaying biases in CDR3 length and k-mer usage consistent with the persistence of OVA-induced clonotypes. These repertoire-level findings highlight localized immune imprinting by OAT pretreatment and raise the question of how such clonal remodeling integrates into the broader LN transcriptional program.

3.1.2. RNA sequencing reveals regional immune and metabolic shifts in OAT-treated Mice

After confirming that OAT pretreatment alters Tfh clonotype architecture in a specific node, we investigated whether these changes are linked to broader transcriptional reprogramming within the LN microenvironment, which could finally be responsible for the lack of pathology in EBA. We achieved this by performing RNA sequencing on whole Ingln and Pln sections from OAT- and PAT-pretreated mice. This approach provides a comprehensive view of

immune and metabolic pathways, offering insights into how OAT pretreatment promotes localized tolerance and protects against EBA.

3.1.2.1. RNA-seq demonstrates an absence of significant transcriptional reprogramming in OAT versus PAT

To examine whether OAT pretreatment induces global transcriptomic differences in draining LNs, we first applied principal component analysis (PCA) to the RNA-seq data. PCA condenses the expression of thousands of genes into a few principal components (PCs) that represent the major axes of variation across samples. If OAT and PAT pretreatments imposed distinct transcriptional programs, one would expect samples to segregate into non-overlapping clusters along these PCs. Conversely, overlap between groups indicates that the dominant sources of variation are shared and not driven by treatment condition.

In the Pln, the first two principal components accounted for 44% (PC1) and 14% (PC2) of the variance, respectively (Figure 13). OAT- and PAT-pretreated samples occupied overlapping regions of the PCA space and did not resolve into distinct clusters. Although some variability was evident among individual mice, this variation did not correlate with the treatment condition. These results indicate that the major transcriptional axes in Pln are common to both groups, and that OAT pretreatment does not induce broad transcriptome-wide remodeling in this node.

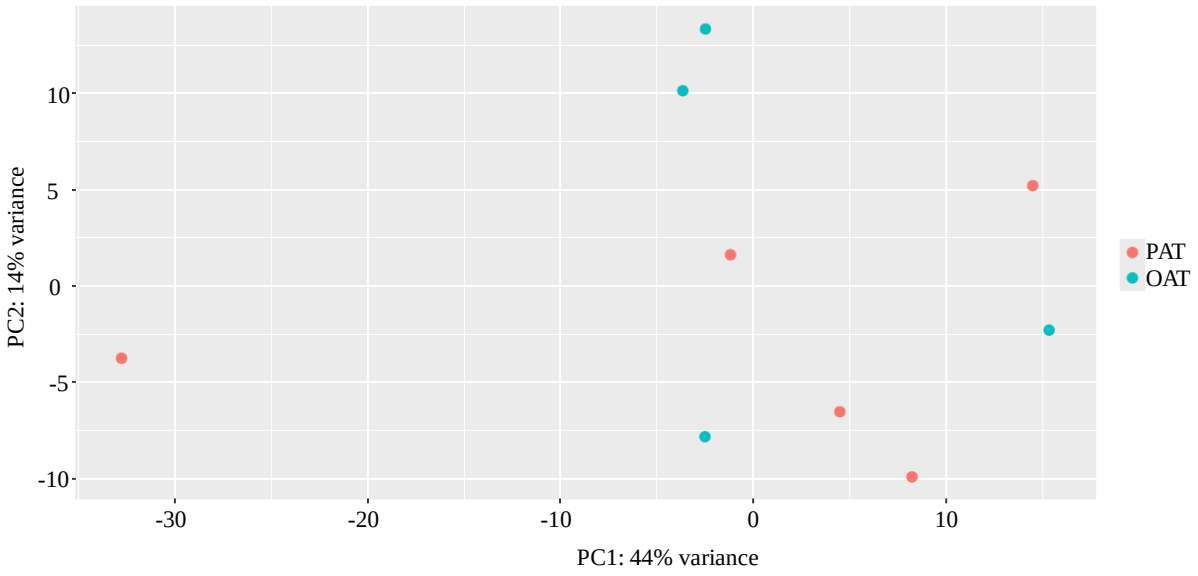

Figure 13. PCA of Pln transcriptomes from OAT- and PAT-pretreated mice. PCA was performed on bulk RNA-seq data from whole Pln sections to visualize global transcriptional variance. The first two principal components explained 44% (PC1) and 14% (PC2) of the variance. Samples from OAT and PAT mice overlapped broadly and did not form distinct clusters, indicating that global transcriptional variation in the Pln is not driven by pretreatment condition.

In the Ingln, principal component analysis yielded a similar outcome. The first two principal components explained 39% (PC1) and 21% (PC2) of the variance, together accounting for a substantial fraction of the total transcriptional variability in the dataset (Figure 14). If OAT pretreatment had imposed a strong and coordinated transcriptional program, the samples would be expected to segregate into two distinct clusters corresponding to OAT and PAT. However, this was not the case: OAT- and PAT-pretreated samples were broadly intermingled in the PCA space, without forming discrete groups. Instead, the spread of points reflected variability between individual mice rather than systematic differences linked to treatment.

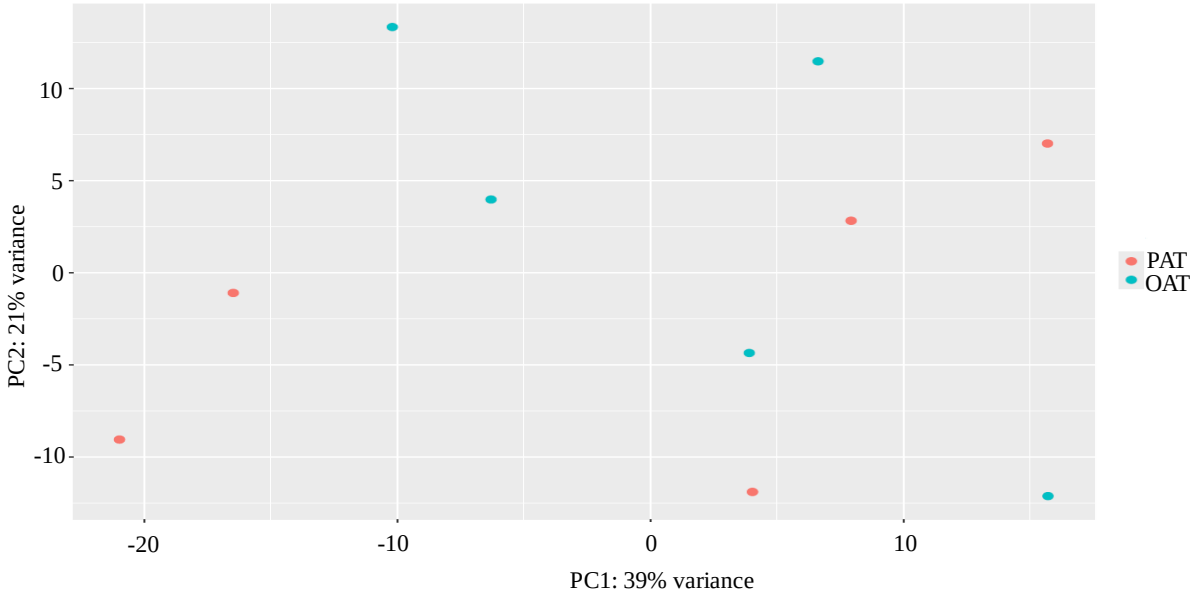

Figure 14. Principal component analysis (PCA) of Ingln transcriptomes from OAT- and PAT-pretreated mice. PCA was performed on bulk RNA-seq data from whole Ingln sections to visualize global transcriptional variance. The first two principal components explained 39% (PC1) and 21% (PC2) of the variance. OAT- and PAT-pretreated samples overlapped substantially and did not resolve into distinct clusters, indicating that the principal transcriptional axes in the Ingln are shared between groups and not determined by pretreatment condition.

Notably, the overlap of OAT and PAT samples indicates that the dominant axes of transcriptional variation in the Ingln are shared between groups and are not driven by OAT pretreatment. While some samples deviated more strongly along PC1 or PC2, this dispersion was observed in both groups, suggesting that biological heterogeneity within the LN microenvironment outweighed any pretreatment-related effect. Taken together, these data indicate that, despite the Ingln being the anatomical site most directly exposed to the final OVA boost, OAT pretreatment does not remodel the global transcriptomic structure of this node at a bulk-tissue level.

To complement the PCA, which already showed that OAT and PAT samples were not clearly separated into distinct groups, we next performed differential expression analysis to identify specific genes that might distinguish the two conditions. The results were visualized using volcano plots (Figure 15), which simultaneously display the magnitude of expression change ($\log_2$ fold change, OAT vs. PAT) and the statistical significance of those changes ($-\log_{10}$

adjusted p-value). In this representation, genes that are both highly differentially expressed and statistically significant appear in the upper corners of the plot, while genes that do not differ substantially between conditions cluster near the center.

In the Pln, 23,129 genes were tested. Strikingly, only two genes passed the statistical thresholds for differential expression: *Igkv4-57-1* and *Iglv3-5*, both immunoglobulin variable region genes, which were significantly upregulated in OAT-pretreated mice compared to PAT controls (Figure 15A). Although these transcripts reached high significance, their isolated appearance highlights that OAT pretreatment does not induce broad transcriptional remodeling in the Pln. Instead, these findings likely reflect stochastic or localized variation in B cell activity rather than a coordinated gene expression program. Importantly, no other immune-related or metabolic pathways were significantly altered, underscoring the absence of systematic reprogramming at the transcriptional level.

In the Ingln, the analysis of 23,737 genes yielded an even clearer picture: no differentially expressed genes (DEGs) were identified (Figure 15B). The volcano plot for Ingln shows an entirely central distribution of genes, with no significant outliers. This indicates that, despite the clonotypic and sequence-level differences revealed by our TCRR analysis in the Ingln, OAT pretreatment did not translate into detectable global transcriptional shifts when considering the whole LN transcriptome.

Taken together, these findings strongly support the conclusion that OAT pretreatment does not trigger broad, node-wide transcriptional reprogramming. Instead, its effects are highly localized to specific clonotype dynamics within GC Tfh cells, as demonstrated by our repertoire analysis. The detection of only two immunoglobulin genes in Pln, and none in Ingln, further emphasizes that any OAT-driven changes at the cellular level are subtle and likely diluted within the complexity of the entire LN microenvironment. These results also highlight the complementary

nature of RNA-seq and TCRR analysis: whereas TCRR is highly sensitive for detecting antigen-specific clonal remodeling, bulk RNA-seq reflects the average state of many cell populations and therefore reveals little evidence of a generalized transcriptional program induced by OAT pretreatment.

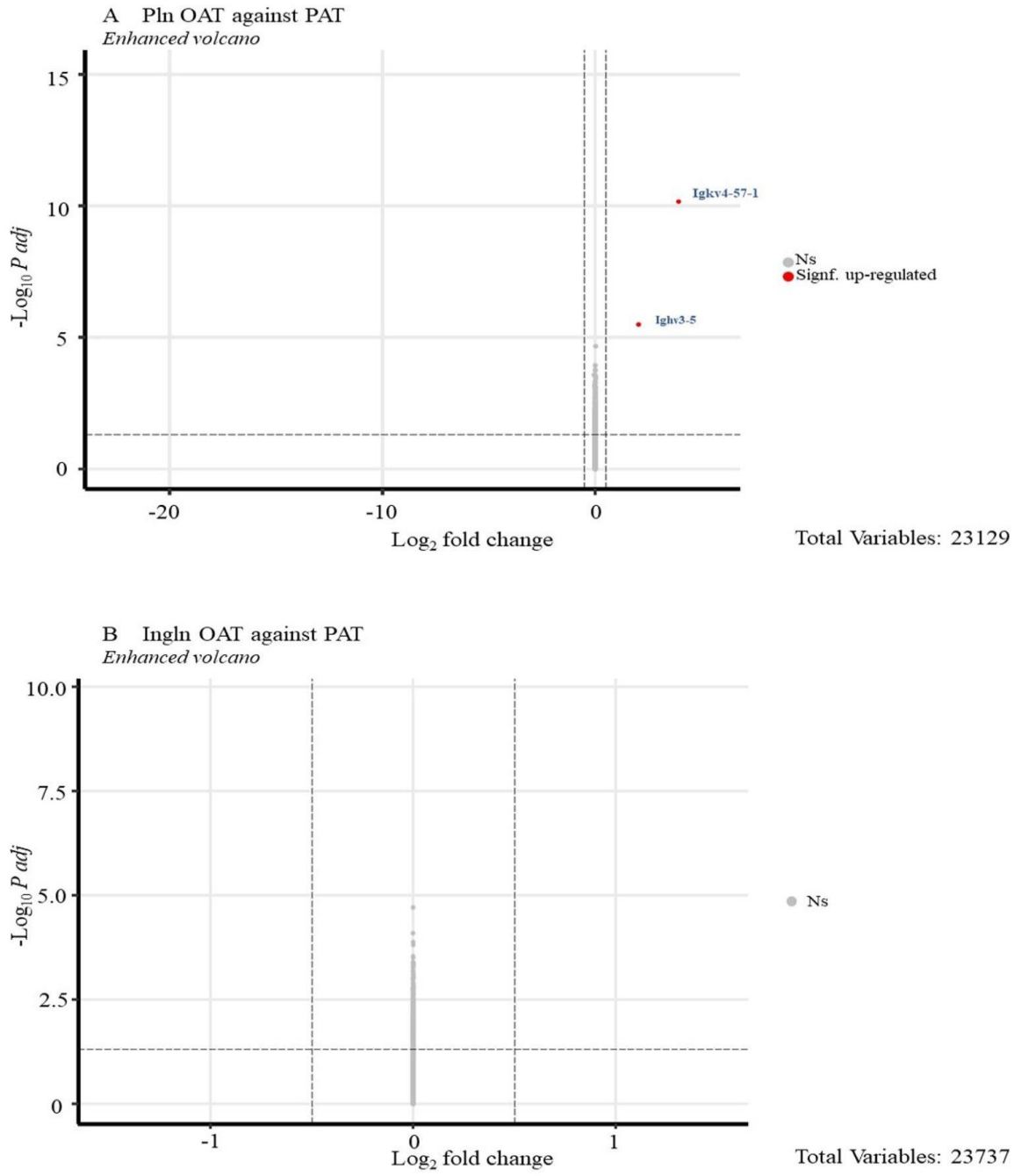

Figure 15. RNA-seq shows minimal transcriptional differences between OAT- and PAT-pretreated mice. Volcano plots display differential expression analysis of whole lymph node transcriptomes from OAT- versus PAT-pretreated mice in A) Pln and B) Ingln. Each dot represents one gene; red indicates significantly upregulated transcripts, gray indicates non-significant transcripts. In the Pln (A), only two immunoglobulin variable region genes (Igkv4-57-1 and Iglv3-5) were significantly upregulated in OAT-pretreated mice, while no genes were downregulated. In the Ingln (B), no differentially expressed genes were identified, and expression profiles of OAT and PAT groups were indistinguishable. Data are shown as $\log_2$ fold change versus $-\log_{10}$ adjusted p-value (FDR < 0.05).

Taken together, PCA and volcano analyses demonstrate that OAT pretreatment does not induce broad transcriptional remodeling in either the Pln or Ingln. Both LNs showed strong overlap of OAT- and PAT-pretreated samples in PCA space, indicating that pretreatment did not drive global transcriptome variance. Consistently, differential expression analysis revealed only two upregulated immunoglobulin variable region genes in the Pln and no significant changes in the Ingln after false discovery rate correction, confirming the absence of large-scale transcriptional shifts. These findings suggest that the major immunological effects of OAT pretreatment are confined to specific cellular subsets, such as GC–Tfh cells, and are not detectable at the bulk transcriptomic level of the whole LN.

Our TCRR analyses showed that OAT effects were most noticeable in comparisons between ipsilateral regions, with Ingln clonotypes persisting and spreading into the Pln. We thought that bulk RNA-seq might also reveal differences in transcription between the Pln and Ingln regions, rather than comparing OAT directly with PAT. We examined transcriptional variation between Pln and Ingln within each group to determine if we could detect node-specific shifts that reflected the localized effects of OAT pretreatment.

3.1.2.2. OAT pretreatment remodels Pln–Ingln transcriptional divergence, shifting immune and metabolic gene expression programs

Since comparisons between OAT and PAT groups within the same LN showed minimal differences, we then examined whether OAT pretreatment affected the transcriptional relationship between Pln and Ingln in each condition. This was inspired by our TCRR results, where the most notable effects of OAT appeared in ipsilateral comparisons rather than contralateral ones. By comparing Ingln and Pln within PAT and OAT mice separately, we aimed to see if OAT influences the inherent transcriptional differences between these two draining LNs, which experience different levels of antigen exposure during immunization.

First, to determine whether PAT/OAT pretreatment causes regional differences in the transcriptional landscape of draining LNs, we compared whole-tissue RNA-seq profiles between Ingln and Pln within each treatment group. Initially, we used PCA to condense the high-dimensional data into principal axes of variation. This method organizes samples with similar overall expression patterns, allowing the separation between groups to indicate meaningful transcriptomic differences.

Focusing on the PAT group, principal component analysis showed that the first two components explain most of the variance in the data: PC1 accounts for 65%, and PC2 accounts for 9% of the total variance (Figure 16). This suggests that the main transcriptional differences between samples are captured along the first component. Notably, samples from Ingln and Pln did not form separate clusters in the PCA plot. Instead, they were widely intermixed, with individual samples spread across the PC1 axis. The absence of clear separation indicates that the regional transcriptional programs in these two LN areas are broadly similar under PAT conditions. Although some spread was observed, mainly along PC1, this variability seems to reflect differences between individual mice rather than systematic differences between compartments. The high variance explained by PC1 underscores that a dominant, shared transcriptional pattern influences both LN types, with only minor contributions from PC2.

Together, these data indicate that in the absence of OAT pretreatment, the transcriptional landscape of Ingln and Pln is not clearly distinct. Instead, both compartments share similar global transcriptomic profiles, with individual variability outweighing location-specific transcriptional divergence.

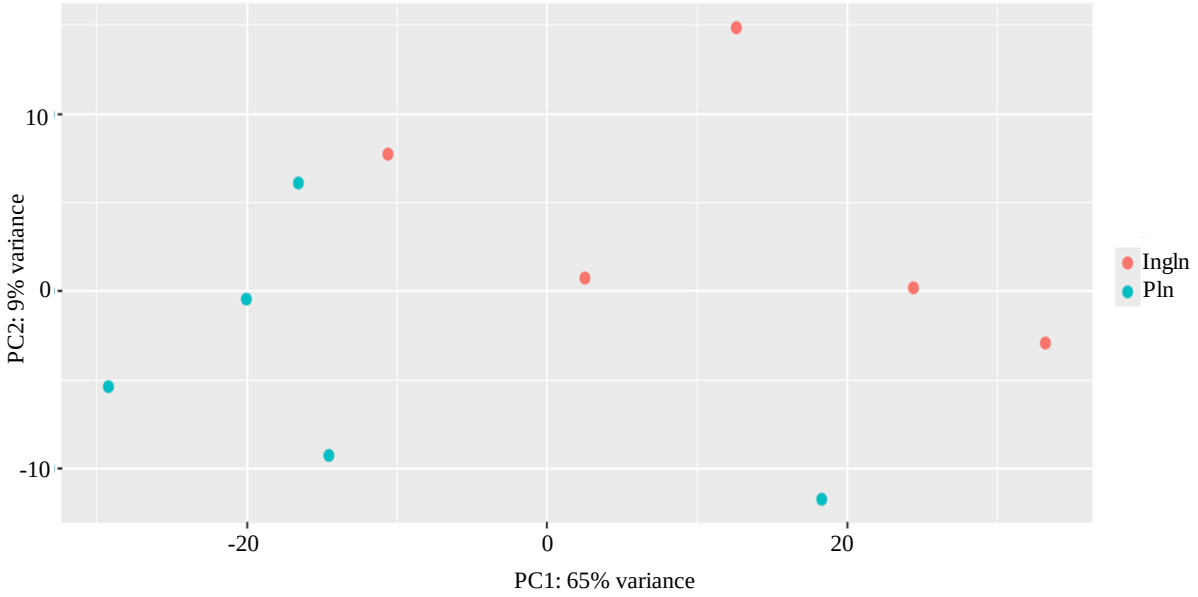

Figure 16. Principal component analysis (PCA) of Ingln and Pln transcriptomes from PAT-pretreated mice. PCA was performed on bulk RNA-seq data from whole Ingln and Pln sections to assess global transcriptional variance. The first two principal components explained 65% (PC1) and 9% (PC2) of the variance. Ingln and Pln samples were broadly intermingled in the PCA space and did not segregate into distinct clusters, indicating that the dominant transcriptional programs are shared between the two lymph node compartments and are not driven by anatomical location under PAT conditions.

In the group pretreated with OAT, the first two principal components accounted for 64% of the variation (PC1: 50%, PC2: 14%) (Figure 17). Samples from Ingln and Pln were distinctly separated along PC1, with no overlap, indicating that LN identity, rather than individual differences, was the main source of variability. While PC2 introduced some variation among biological replicates, it did not blur the clear distinction between Ingln and Pln. These findings suggest that, after OAT pretreatment, Ingln and Pln maintain unique transcriptional profiles, reflecting their different antigen exposures, Ingln draining the OVA boost site at the tail base, and Pln draining the mCol7c challenge site in the footpad. This underscores the role of tissue environment and drainage history in shaping localized transcriptional responses.

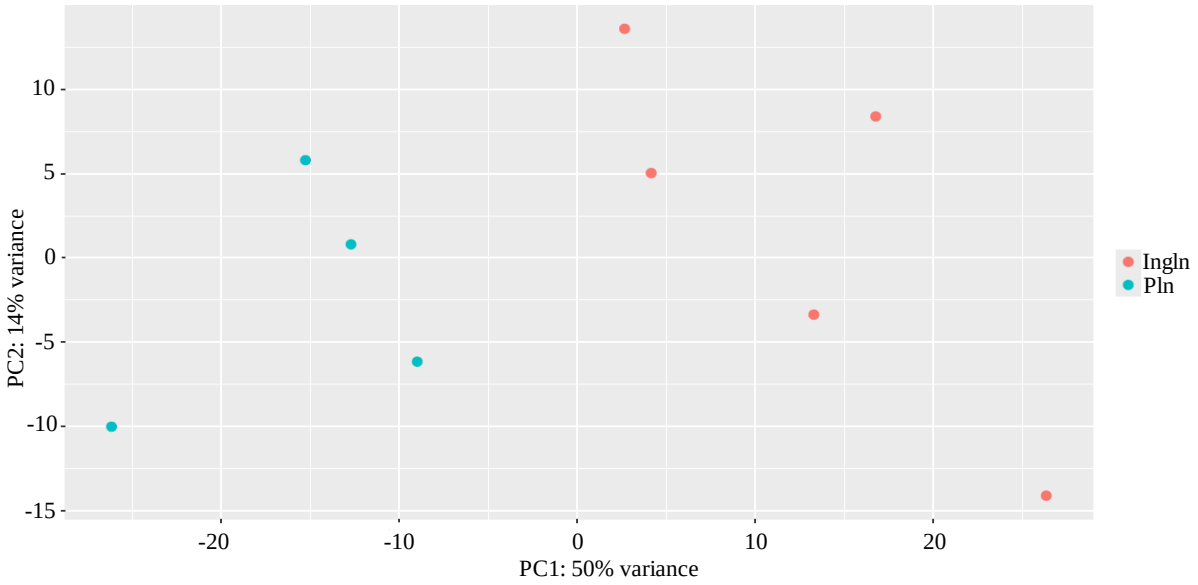

Figure 17. PCA of Ingln and Pln transcriptomes in OAT-pretreated mice.PCA was performed on bulk RNA-seq data from whole Ingln and Pln sections of OAT-pretreated mice to visualize global transcriptional variance. The first two principal components explained 64% of the total variance (PC1: 50%, PC2: 14%). Samples segregated clearly by lymph node identity, with Ingln and Pln forming non-overlapping clusters along PC1. This separation indicates that Ingln and Pln exhibit distinct transcriptional programs under OAT pretreatment, consistent with their differential antigenic exposures and drainage contexts.

Although PCA offered an overall view of the transcriptional differences between Pln and Ingln, it does not pinpoint the specific genes responsible for this variation. To identify the molecular drivers behind this separation, we conducted differential expression analysis, visualized through volcano plots. These plots enable the evaluation of both statistical significance and the magnitude of gene regulation between nodes. As a result, this analysis reveals gene-level details of the transcriptional programs that differentiate Pln from Ingln under PAT and OAT pretreatment conditions.

In the PAT group (Figure 18A), Ingln and Pln exhibited clear transcriptional differences, showing a wide range of significantly altered transcripts, both up- and downregulated. Ingln increased the expression of multiple genes associated with cytokine signaling, tissue remodeling, and immune regulation, such as *Adamdec1*, *Reg3g*, and *Ccl5*, indicating an inflammatory and chemokine-driven environment. Conversely, Pln demonstrated higher levels

of genes like *Lrrfip1* and *Hoxa11*, suggesting distinct developmental or structural programs. Overall, the data reveal that, under PAT pretreatment, Pln and Ingln acquire notably different transcriptional profiles, likely due to their different anatomical locations and mechanisms of antigen exposure; Pln being the direct draining LN of the footpad mCol7c injection, while Ingln is activated indirectly.

In the OAT group (Figure 18B), the transcriptional relationship between Pln and Ingln was notably reprogrammed. Ingln expressed significantly fewer pro-inflammatory mediators compared to PAT controls and showed increased levels of inhibitory and metabolic genes, such as *Lum*, *Cd244a*, and *SiglecE*. These genes are linked to extracellular matrix remodeling, checkpoint inhibition, and immune regulation, indicating that Ingln in OAT-pretreated mice adopts a more tolerogenic or quiescent phenotype. Meanwhile, Pln maintained high expression of immunoglobulin variable region genes (*Ighv1-82*, *Ighv1-66*, *Ighv5-12*), highlighting its role as the main site for B cell activation and antibody production after footpad immunization.

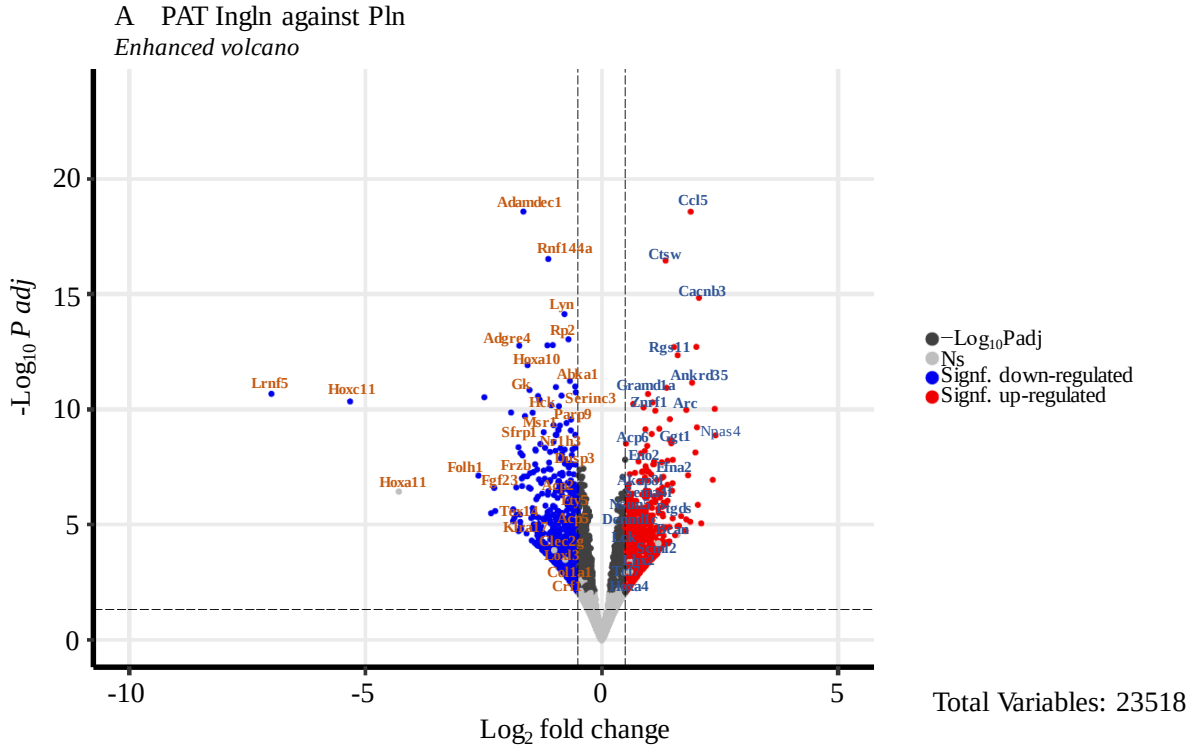

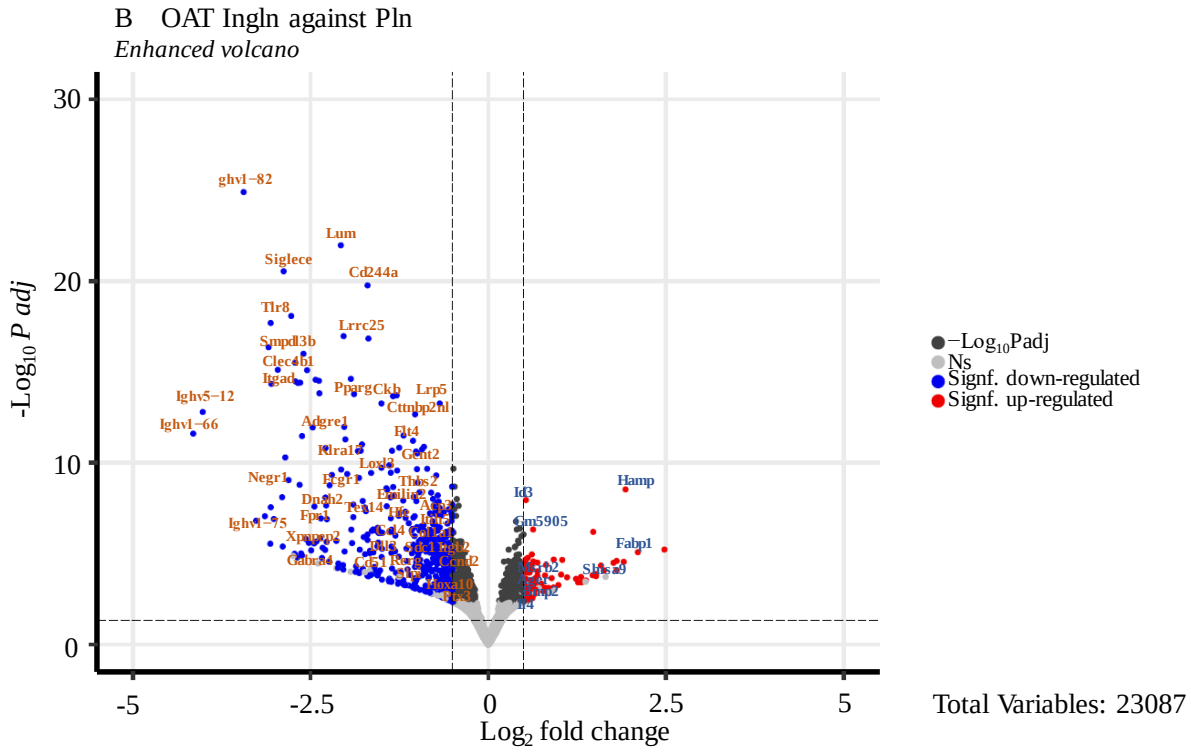

Figure 18. Volcano plots of differential gene expression between Pln and Ingln under PAT and OAT pretreatment. Differential expression analysis was performed on bulk RNA-seq datasets to compare ipsilateral Pln and Ingln transcriptomes. A) In PAT-pretreated mice, Ingln versus Pln comparison revealed a large set of significantly upregulated (red) and downregulated (blue) transcripts among 23,518 genes analyzed. Notable Ingln-enriched genes included *Adamdec1, Reg3g, and Ccl5*, whereas Pln displayed higher expression of *Lrrfip1 and Hoxa11*. B) In OAT-pretreated mice, transcriptional divergence between Ingln and Pln was also evident among 23,087 genes analyzed, but with a distinct molecular signature. Ingln exhibited increased expression of regulatory and metabolic genes such as Lum, Cd244a, and SiglecE, while Pln showed enrichment for immunoglobulin variable region genes (I*ghv1-82, Ighv1-66, Ighv5-12*). Vertical lines indicate $\log_2$ fold-change thresholds, and the horizontal line denotes the adjusted p-value cutoff (FDR < 0.05). These plots illustrate how OAT pretreatment reprograms Ingln toward a tolerogenic and regulatory state, contrasting with the inflammatory divergence observed under PAT pretreatment.

These findings show that although Pln and Ingln stay transcriptionally separate under both pretreatment types, the reasons for this separation are fundamentally different. In PAT pretreatment, Ingln and Pln diverge mainly along a pathway driven by inflammatory and effector genes. Conversely, OAT pretreatment redirects Ingln away from the inflammatory profile toward pathways involved in regulation and tissue stability. This shift aligns with the

tolerogenic effects of OAT and underscores Ingln's role as a central point for systemic immune modulation.

In summary, PCA and volcano analyses reveal that although Pln and Ingln show transcriptional divergence under both pretreatment conditions, their underlying programs are distinct: PAT-pretreated Ingln displays an inflammatory signature, while OAT-pretreated Ingln leans toward regulatory and metabolic pathways, with Pln continuing to show B cell–related activity. These results emphasize that OAT does not eliminate node-specific transcriptional differences but instead shifts them towards a tolerogenic profile. To validate and interpret these expression differences functionally, we conducted gene ontology (GO) enrichment analysis, which identifies biological pathways and processes driving these transcriptional signatures.

GO enrichment analysis comparing Ingln to Pln in PAT-pretreated mice revealed a distinct separation between suppressed and activated transcriptional pathways (Figure 19). Genes downregulated in Ingln relative to Pln (Figure 19A) were closely linked to innate immune processes, including defense against viruses, innate immune signaling pathways, responses to lipopolysaccharide, regulation of inflammation, and cell chemotaxis. This suggests that Ingln in PAT-pretreated mice shows reduced transcriptional activity in innate immune signaling, while Pln maintains a more pro-inflammatory, pathogen-detecting profile.

Genes in Ingln that are activated compared to Pln (Figure 19B) are associated with immune processes related to adaptation and regulation. These processes include lymphocyte proliferation, T cell differentiation, and the positive regulation of T cell activation, lymphocyte activation, and cell–cell adhesion. Collectively, these terms indicate a transcriptional tendency toward the growth and coordination of adaptive immune cells within Ingln. This suggests that Ingln acts as a niche supporting lymphocyte-driven responses, while Pln maintains innate inflammatory activity. Therefore, with PAT pretreatment, LN compartmentalization remains intact, with Ingln supporting adaptive responses and Pln involved in innate responses. Ingln and

Pln in PAT-pretreated mice show distinct transcriptional profiles. Pln is primarily associated with innate immune and inflammatory pathways, whereas Ingln is more involved in adaptive lymphocyte-related activities. This separation likely results from different routes of antigen exposure, highlighting Pln's role as an inflammatory center and Ingln's function in lymphocyte expansion.

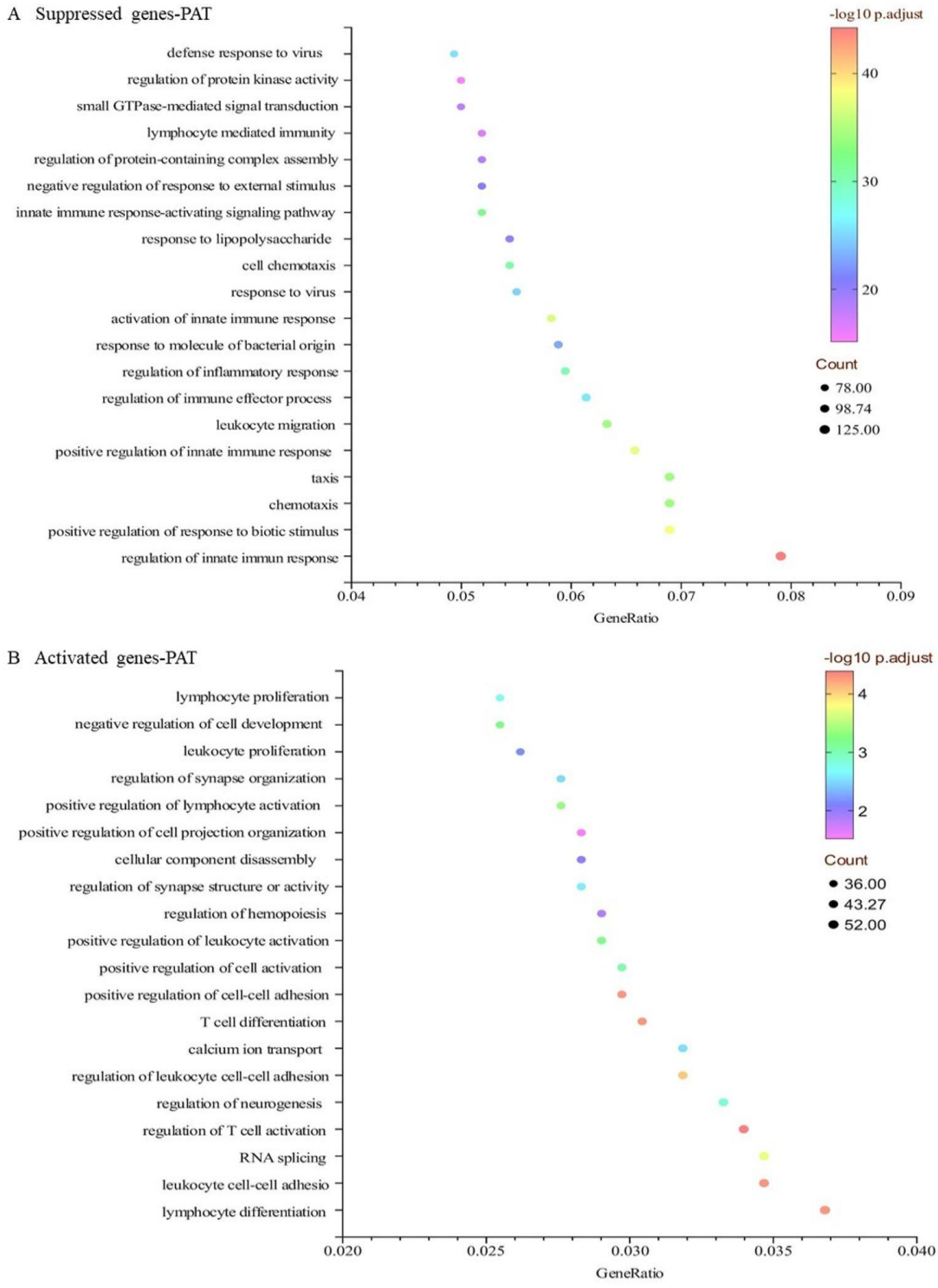

Figure 19. GO enrichment analysis of differentially expressed genes between Ingln and Pln in PAT-pretreated mice. A) Suppressed genes in Ingln compared to Pln were enriched for innate immune and inflammatory pathways, including defense response to virus, regulation of protein kinase activity, small GTPase-mediated signaling, and chemotaxis-related processes. B) Activated genes in Ingln relative to Pln were enriched for adaptive immune functions, such as lymphocyte proliferation, T cell differentiation, and positive regulation of lymphocyte activation. Gene ratio denotes the proportion of DEGs associated with each pathway, dot size indicates gene count, and color intensity reflects statistical significance (–log10 adjusted p value).

Next, we performed GO enrichment analysis on differentially expressed genes to understand the pathways behind the transcriptional differences between Ingln and Pln in OAT-pretreated mice. Pathways related to immune and inflammatory responses, such as regulation of inflammatory response, innate immune activation, phagocytosis, leukocyte migration, and chemotaxis, were strongly suppressed in Ingln compared to Pln (Figure 20A). Additionally, pathways like response to bacterium and immunoglobulin-mediated immune response were downregulated, indicating that Ingln in OAT-pretreated mice is less involved in acute pathogen detection or antibody-mediated effector functions. This suppression suggests a functional reduction of classical immune activation pathways, contrasting with the more inflammatory response seen under PAT pretreatment.

In contrast, pathways upregulated in Ingln mainly involved cellular metabolism, RNA processing, and protein synthesis. Key categories included mitochondrial gene expression, RNA splicing and processing, ribosome biogenesis, and cytoplasmic translation (Figure 20B). The dominance of these biosynthetic programs suggests a shift in transcriptional focus from immune effector functions to maintaining cellular homeostasis, translation, and metabolism. This pattern indicates that the Ingln microenvironment under OAT pretreatment is not transcriptionally inactive but is instead dedicated to supporting metabolic and structural stability.

These findings show that OAT pretreatment significantly alters Ingln's transcriptional profile by downregulating innate immune and inflammatory pathways, while upregulating biosynthetic and metabolic processes. This indicates a tolerogenic shift in Ingln, where the potential for rapid immune response is lowered, but the cellular systems for long-term tissue health and immune regulation are strengthened. These transcriptional patterns are consistent with the TCRR results, which revealed persistent yet modified clonotypic repertoires in Ingln, offering a molecular

basis for how OAT pretreatment redirects the local environment from pro-inflammatory activity to immune regulation.

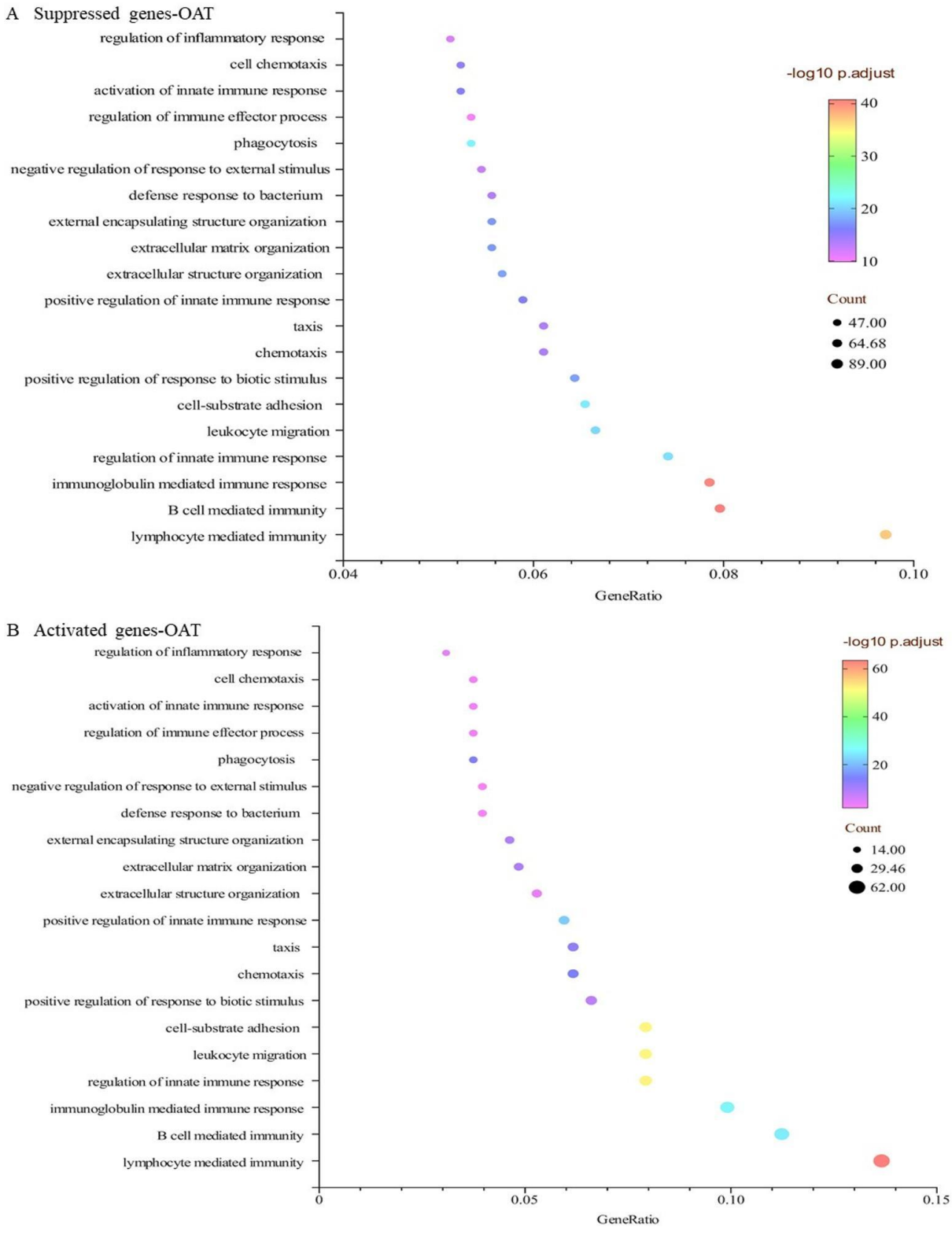

Figure 20. GO enrichment analysis of differentially expressed genes between Ingln and Pln in OAT-pretreated mice. A) Suppressed genes in Ingln compared to Pln were enriched for innate immune and inflammatory pathways, including regulation of inflammatory response, activation of innate immune response, phagocytosis, leukocyte migration, and immunoglobulin-mediated immunity. B) Activated genes in Ingln relative to Pln were enriched for metabolic and biosynthetic programs, including mitochondrial gene expression, RNA splicing, ribosome biogenesis, and cytoplasmic translation. Gene ratio denotes the proportion of DEGs associated with each pathway, dot size indicates gene count, and color intensity reflects statistical significance (–log10 adjusted p value).

Overall, TCRR analysis indicated that OAT pretreatment altered clonotype distribution, with Ingln maintaining and displaying more diverse clonotypes, including changes in CDR3 length and k-mer motifs, whereas Pln clonotypes were more limited. RNA-seq supported this, revealing that OAT did not cause widespread transcriptional changes across nodes, but instead shifted Ingln gene expression away from inflammatory and immune effector pathways toward metabolic and biosynthetic processes. Overall, TCRR analysis indicated that OAT pretreatment altered clonotype distribution, with the Ingln maintaining and displaying more diverse clonotypes, including changes in CDR3 length and k-mer motifs, whereas Pln clonotypes were more limited. RNA-seq supported this, revealing that OAT did not cause widespread transcriptional changes across nodes but instead shifted Ingln gene expression away from inflammatory and immune effector pathways toward metabolic and biosynthetic processes. Collectively, these results suggest that OAT acts in an ipsilateral, Ingln-specific manner, modifying local Tfh clonotype patterns and transcriptomic profiles toward a tolerogenic, non-inflammatory state rather than inducing broad immune suppression.

OAT pretreatments show that the autoimmune process can be stopped before the disease starts: injecting OVA into the left and right footpads, then at the tail base, conditions the nearby Ingln LN, turning it into a tolerogenic environment. This prevents disease development when challenged later with mCol7. This illustrates a key idea: autoimmunity can be prevented through targeted, early immune re-education at the specific site where it begins, rather than through systemic suppression begins.

3.2. Isolation and characterization of CDNPs

Building on our prior findings, we suggest that a multiepitope, protein-based method from intracellular sources, used without adjuvants, could therapeutically adjust the TCR repertoire in a more physiological manner. By exposing the immune system to a wide range of intracellular protein epitopes, this strategy may refine T-cell activation thresholds and promote repertoire

diversity. This targeted approach aims to slow disease progression in T cell–mediated disorders by shifting the immune response from autoreactivity to tolerance and increasing Tfh cell repertoire diversity, as demonstrated by our results in the EBA mouse model. Due to the intricate nature of TCR interactions in immune regulation, we aimed to investigate the potential of immunomodulatory nanoparticles to enhance or redirect these effects. CDNPs, characterized as multiepitope protein aggregates, were isolated with consistent compositions. By utilizing the CDNPs, we aimed to assess their potential impact on the TCRR and their ability to modulate immune responses within the context of T-cell-mediated diseases.

This section outlines the isolation and characterization of CDNPs, providing insight into their physicochemical properties, protein composition, and potential significance in immunomodulation. CDNP isolation was refined to achieve higher yields than previously attained, addressing earlier limitations in production efficiency. Comprehensive characterization confirmed uniform protein compositions across CDNP batches alongside well-characterized physical attributes essential for their application. Endotoxin contamination, initially detected, was effectively reduced to negligible levels, ensuring the suitability of CDNP for subsequent studies. These results collectively advance the preparation of CDNPs for immune-related investigations. The following subsections detail the enhanced yield, protein consistency, particle characteristics, and endotoxin management of CDNPs.

The protein content and purity of CDNP preparations were assessed by SDS-PAGE under reducing conditions. Protein concentration was first determined by BCA assay to ensure comparable loading. For electrophoretic separation, NuPAGE 4–12% Bis-Tris Protein Gels were used in combination with NuPAGE MES SDS Running Buffer and NuPAGE Antioxidant. After electrophoresis, gels were either stained with Coomassie Brilliant Blue R-250 to visualize total protein profiles or transferred onto PVDF membranes for subsequent Western blotting (e.g., detection of Annexin A5 as characteristic CDNP markers).

3.2.1 Medium supplementation with Ribonucleoside enhanced protein yield

Following the optimization goal outlined in the CDNP isolation process, EFN-R cells were cultured in MEM with or without ribonucleoside supplementation. This was followed by cell harvesting, CDNP isolation, and protein quantification via infrared fluorescence scanning. Initial protein yield assessments revealed a marked disparity between the two conditions. CDNPs from ribonucleoside-supplemented cultures yielded an average protein mass of 6000 ± 500 µg (n = 5), a 3-fold increase over the 2000 ± 200 µg (n = 5) obtained from unsupplemented cultures (Figure 21). Further analysis revealed that yields in the supplemented condition ranged from 5,500 to 6,500 µg. In comparison, the unsupplemented condition ranged from 1800 to 2200 µg, with the latter exhibiting lower variability (coefficient of variation: 8.3% vs. 10%). The broader distribution in the supplemented cultures, as indicated by the error bars, suggests greater inter-replicate heterogeneity. Statistical analysis confirmed the yield difference as highly significant ($p < 0.001$, two-tailed t-test), underscoring the efficacy of ribonucleoside in enhancing CDNP production efficiency. This yield enhancement necessitated an evaluation of CDNP protein composition to confirm consistency across culture conditions in the subsequent analysis.

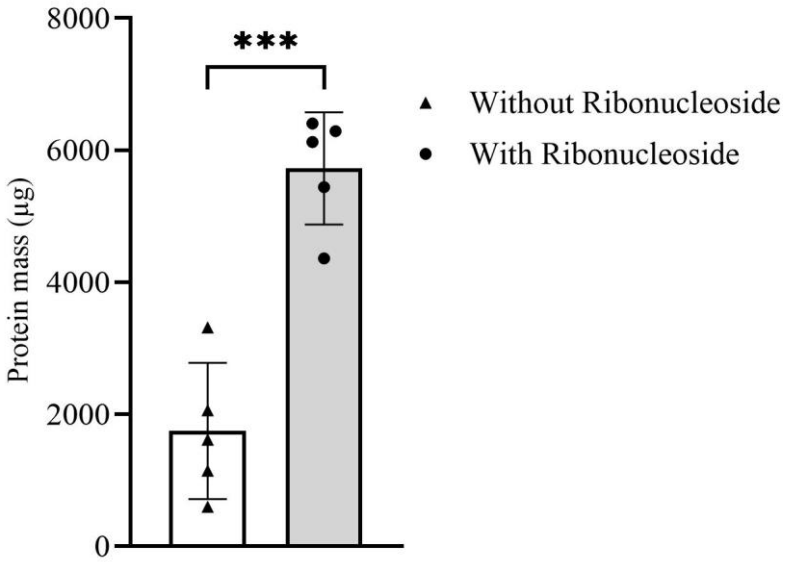

Figure 21. Effect of Ribonucleoside Supplementation on CDNP Protein Yield. Protein yields of CDNPs from EFN-R cells cultured in MEM with (circles) or without (triangles) ribonucleoside supplementation. Data represent protein mass (µg) from five independent replicates (n = 5) per condition, with error bars indicating standard deviation. Statistical significance between conditions is denoted by *** ($p < 0.001$, two-tailed t-test).

3.2.2. Consistent protein composition across culture conditions

To evaluate the protein composition of CDNPs across different culture conditions, we performed SDS-PAGE analysis followed by Western blot. The SDS-PAGE gel (Figure 22A) displays the protein profiles of CDNPs isolated from three independent batches (Batch 1, Batch 2, Batch 3) cultured with and without ribonucleoside supplementation. While the banding patterns across batches are largely similar, with major bands observed at approximately 70 kDa, 55 kDa, and 35 kDa, subtle differences in band intensity and the presence of minor bands were noted, suggesting slight variations in protein expression or aggregation between conditions. As previously published, Annexin A5 is a housekeeping protein of CDNPs and serves as a reliable marker for consistency. To confirm its presence and ensure uniformity, we performed a Western blot targeting Annexin A5 (Figure 22B). The Western blot results revealed the consistent expression of Annexin A5 at approximately 35 kDa across all batches and conditions. These findings confirm that, despite minor differences observed in the SDS-PAGE, the core

composition of CDNPs remains stable, as validated by the consistent presence of Annexin A5. This supports the reliability of our CDNP isolation process for subsequent immunomodulatory studies, with Annexin A5 serving as a stable reference protein.

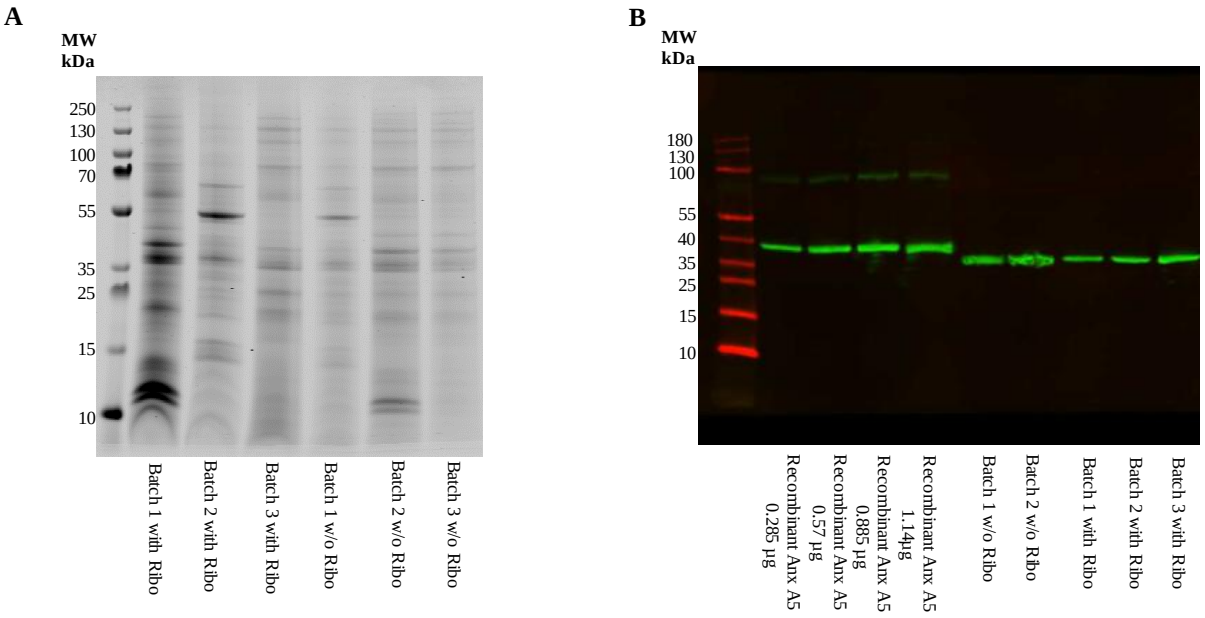

Figure 22. SDS-PAGE and Western Blot Analysis of CDNP Protein Composition Across Culture Conditions. A) SDS-PAGE gel showing protein profiles of CDNPs isolated from three independent batches (Batch 1, Batch 2, Batch 3) cultured with and without ribonucleoside (Ribo) supplementation. Molecular weight markers (MW) in kDa are indicated on the left. Major bands are observed at approximately 70 kDa, 55 kDa, and 35 kDa, with minor variations in band intensity and additional bands between conditions. B) Western blot targeting Annexin A5, a housekeeping protein of CDNPs, confirms its consistent expression at ~35 kDa across all batches and conditions. Recombinant Annexin A5 was included as a control.

3.2.3. Characterization of particle size, distribution, and protein-particle correlation

To further characterize the physicochemical properties of isolated CDNPs, detailed analyses were performed, examining particle size, number, distribution, and their relationship with protein concentration using ZetaView, a nanoparticle tracking analysis (NTA) system. The results showed that CDNPs from four separate batches consistently had an average particle radius of about 150 to 200 nm (Figure 23A). This high level of consistency in particle size across different preparations highlights the robustness, reproducibility, and reliability of our

optimized isolation method, which is crucial for ensuring uniformity in subsequent immunological and therapeutic applications.

Particle number assessment showed variability across batches (Figure 23B). All batches produced particle counts significantly higher than the PBS control, with Batch 2 showing the highest yield, indicating slight differences in isolation or culture conditions. These minor batch-to-batch variations underscore potential sensitivity in the production process, highlighting the need for strict conditions to maximize yields.

Although there was variability in particle number, especially in Batch 2, a strong linear relationship ($R^2 = 0.88$) between particle number and protein concentration was consistently observed across all batches (Figure 23C). This correlation confirms that the amount of protein used during production has a direct impact on particle formation efficiency. It indicates that protein availability is a key factor in nanoparticle aggregation, offering essential insights into the mechanisms of nanoparticle formation and aggregation dynamics. Understanding this relationship is crucial for future research aimed at optimizing production conditions to improve yield and reproducibility.

Further analysis of particle size distribution (Figure 23D) showed a remarkably uniform profile across all batches. Each sample had a clear peak between 150-200 nm, confirming consistent nanoscale particle formation. The tight size range is especially important for clinical use, as uniform particle size can significantly influence biological effectiveness and safety.

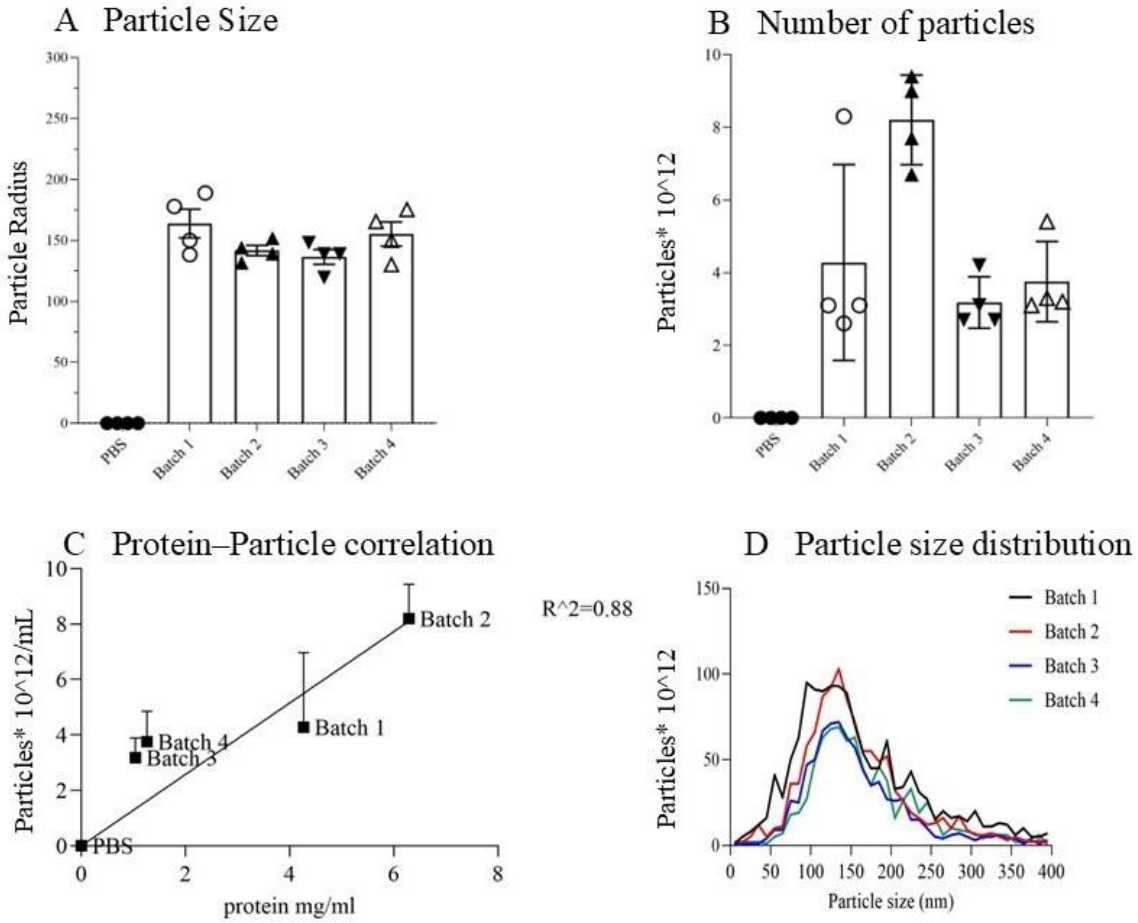

Figure 23. Characterization of CDNP Particle Size, Number, Distribution, and Protein-Particle Correlation. A) Mean particle radius measurements (nm) of CDNPs isolated from four independent batches compared to PBS controls, showing consistent particle sizes across batches. Each symbol represents an individual measurement, and bars indicate the mean ± SEM. B) Quantification of particle numbers (particles $\times 10^{12}$) revealed variability between batches, with Batch 2 showing the highest yield. Data points represent individual measurements, bars indicate mean ± SEM. C) Strong linear correlation ($R^2 = 0.88$) between particle number and protein concentration across batches, demonstrating the dependence of particle formation on protein availability. Data points represent mean ± SEM for each batch. D) Particle size distribution profiles of four independent batches, exhibiting consistent peak sizes between 150–200 nm, indicative of uniform nanoparticle formation and confirming the reproducibility of the isolation process.

Together, these comprehensive characterizations of CDNPs strongly demonstrate their stable and reproducible physicochemical traits, which are crucial for their use in immunomodulatory and therapeutic research. Additionally, these results substantiate the CDNP isolation and analysis methods as dependable, consistent, and scalable, supporting their suitability for future large-scale experiments and clinical applications.

3.2.4. Endotoxin Detection and Removal

To utilize CDNPs in mouse studies, their safety was ensured by assessing endotoxin contamination levels. A standard curve for the LAL assay was first established, demonstrating a linear relationship between endotoxin concentration (0 to 1.0 EU/mL) and OD405 absorbance, with an R^2 value of 0.99, confirming the assay's reliability for accurate quantification (Figure 24A). Endotoxin levels in three CDNP batches were then quantified using the LAL assay, followed by treatment with Triton X-114 (TX-114) to reduce contamination. Initial LAL assay results revealed elevated endotoxin levels in untreated batches: Batch 1 at 1.5 ± 0.1 EU/mL, Batch 2 at 1.2 ± 0.1 EU/mL, and Batch 3 at 2.5 ± 0.2 EU/mL, all exceeding the acceptable threshold of 0.1 EU/mL for immunological studies (Figure 24B). These levels corresponded to 15-fold, 12-fold, and 25-fold above the threshold for Batches 1, 2, and 3, respectively, highlighting significant contamination in the untreated samples. Post-TX114 treatment, endotoxin levels decreased markedly across all batches: Batch 1-TX114 to 0.05 ± 0.01 EU/mL, Batch 2-TX114 to 0.03 ± 0.01 EU/mL, and Batch 3-TX114 to 0.04 ± 0.01 EU/mL, achieving reductions of 96.7%, 97.5%, and 98.4%, respectively. All treated batches fell below the 0.1 EU/mL threshold, with values ranging from 0.03 to 0.05 EU/mL, ensuring compliance with purity standards for in vivo applications. The reduction in endotoxin content was highly consistent across batches, with standard deviations indicating low inter-replicate variability in both untreated and treated samples. Batch 3, which exhibited the highest initial contamination,

showed the most pronounced decrease, dropping from 2.5 EU/mL to 0.04 EU/mL, a 25-fold reduction relative to the threshold. These results confirm the efficacy of TX114 in achieving CDNP purity, rendering them safe for subsequent mouse studies and completing their characterization for immune-related investigations.

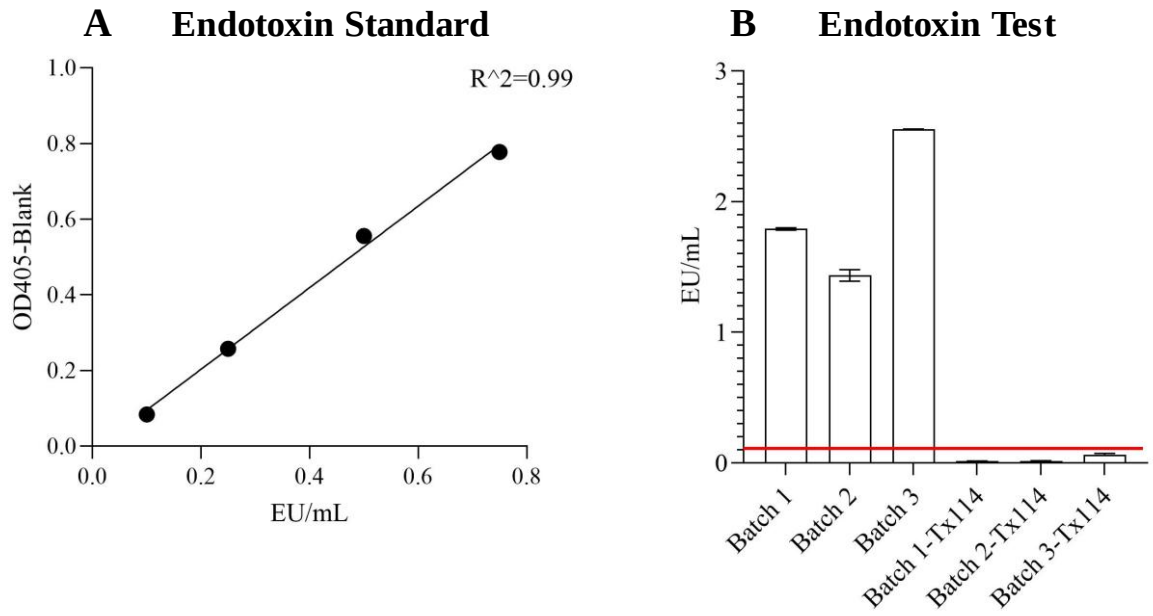

Figure 24. Endotoxin Quantification and Reduction in CDNPs. A) Standard curve for the LAL assay, plotting OD405 absorbance (corrected for blank) against endotoxin concentration (0 to 1.0 EU/mL). Data points represent mean absorbance from triplicate measurements, with a linear fit ($R^2 = 0.99$). B) Endotoxin levels in CDNP batches before and after Triton X-114 (TX114) treatment. Untreated batches (Batch 1, 2, 3) and treated batches (Batch 1-TX114, 2-TX114, 3-TX114) are shown, with endotoxin concentrations (EU/mL) measured by LAL assay. Data represent means ± SD from two independent replicates per batch. The red line indicates the acceptable threshold of 0.1 EU/mL for immunological studies.

3.2.5. CDNPs Suppress IL-6 Production in a Non-Monotonic, Concentration-Dependent Manner in PAM-Activated Macrophages

After effectively removing endotoxin contamination from CDNP preparations with TX-114 treatment (see Section 3.2.4), we aimed to assess the direct immunomodulatory effects of CDNPs in vitro under strictly endotoxin-free conditions. For this, we used the murine macrophage cell line J774.A1, which was stimulated with the TLR2/1 ligand PAM to provoke

a proinflammatory cytokine response. Cells were co-treated with increasing doses of CDNPs (0.5, 1, 2.5, and 5 μg/mL) or OVA as a protein control. After 5 hours of incubation, the supernatants were collected and analyzed for IL-6 secretion via ELISA (Figure 25).

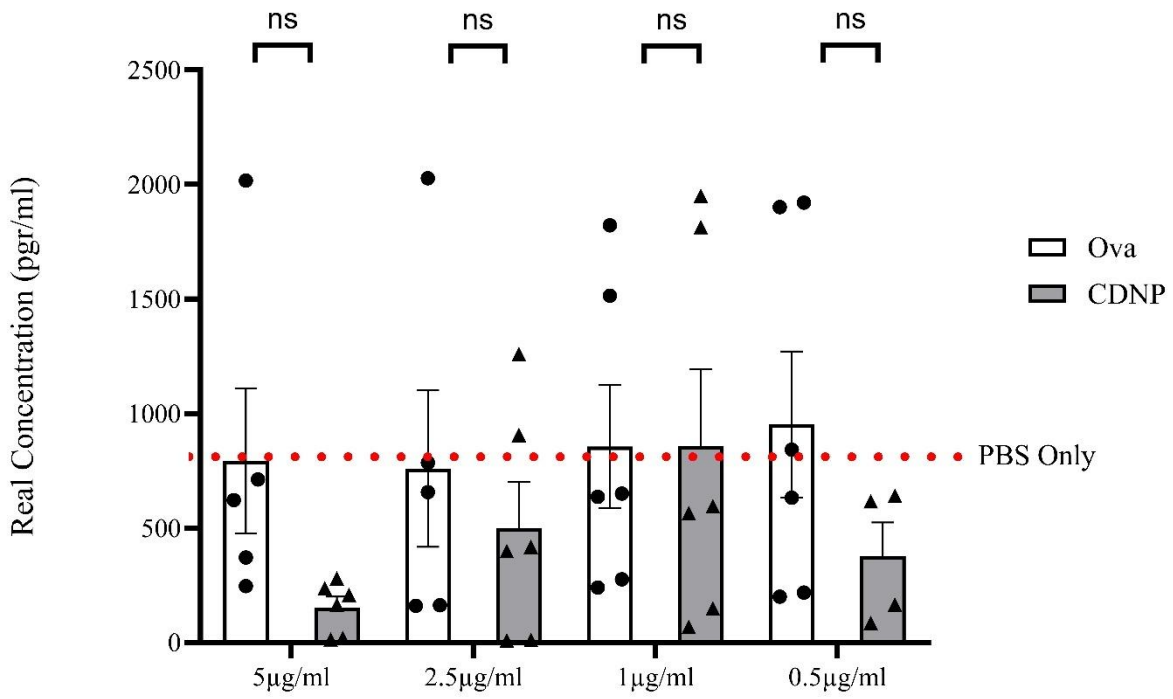

Figure 25. CDNPs modulate IL-6 secretion by macrophages in a concentration-dependent manner. Murine J774.A1 macrophages were stimulated with PAM3CSK4 (PAM) and co-treated with increasing concentrations of CDNPs (0.5, 1, 2.5, and 5 μg/mL) or OVA as a protein control. After 5 hours, IL-6 levels in the supernatants were measured by ELISA. OVA had no measurable effect at any concentration, while CDNPs showed a trend toward reduced IL-6 production, particularly at 5 and 0.5 μg/mL. However, none of the differences reached statistical significance (ns) compared to OVA-treated controls (n=6 per group; unpaired t-test). The red dashed line indicates the IL-6 level in PAM dissolved in PBS (PBS Only) stimulated samples. Data are presented as mean ± SEM.

OVA showed no significant impact on IL-6 production at any concentration tested, with cytokine levels comparable to PAM-only controls. This indicates that OVA does not have immunosuppressive activity in this setting and functions effectively as a negative control for protein-related effects.

CDNPs showed a variable, dose-dependent modulation of IL-6 secretion, although no statistically significant differences from OVA were observed at any concentration (p-values: 5 µg/mL, $p = 0.11$; 2.5 µg/mL, $p = 0.54$; 1 µg/mL, $p = 0.77$; 0.5 µg/mL, $p = 0.31$). The most pronounced reduction in IL-6 levels occurred at 5 µg/mL, while moderate or inconsistent effects were observed at 1 and 2.5 µg/mL. Interestingly, even the lowest concentration (0.5 µg/mL) showed a reduction compared to controls, suggesting residual activity at very low doses.

These findings suggest a biphasic response, with the strongest inhibition of IL-6 at both high and low CDNP concentrations, whereas intermediate doses were less effective. Similar variability in CDNP-mediated cytokine suppression was reported by Vasco-León Köhling (2022), who observed fluctuating inhibition of IL-6 and other cytokines in PAM-activated J774.A1 macrophages (Köhling, 2022). The underlying cause of this non-linear response remains unclear but may involve distinct receptor interactions or signaling thresholds activated at different CDNP levels. Further studies are needed to confirm this trend and elucidate the mechanisms underlying CDNP-mediated immunomodulation in inflammatory and autoimmune contexts.

3.3. CDNPs increase the TCRR in the T cell zones *in-vivo*

To evaluate whether CDNPs can modulate TCRR dynamics *in vivo* in the absence of adjuvants or sensitizing haptens, we designed a modified DTH-like experiment that excluded classical agents such as 2,4,6-trinitrochlorobenzene (TNCB). The aim was to assess whether

repeated exposure to CDNPs alone could influence T-cell activity and repertoire composition under steady-state, non-inflammatory conditions.

Mice received intraperitoneal injections of CDNPs (10 µg in PBS, 200 µL per injection) or PBS alone, administered every other day for a total of 16 injections over a 5-week period, starting on day −28. This extended dosing regimen ensured sustained systemic exposure to CDNPs throughout both the sensitization-like and challenge-like phases of the DTH framework, allowing sufficient time for potential immunomodulatory effects to develop.

To maintain structural similarity to a classical DTH model while avoiding the introduction of exogenous sensitizing antigens, acetone was used as a neutral vehicle control and applied to the abdomen on day 0 and to the ears on day 5. Ear thickness was measured to detect possible contact reactivity (for the injection scheme, refer to Figure 26). No significant difference between CDNP-treated and PBS-control mice was observed, indicating that CDNPs alone did not provoke an inflammatory skin response (data not shown).

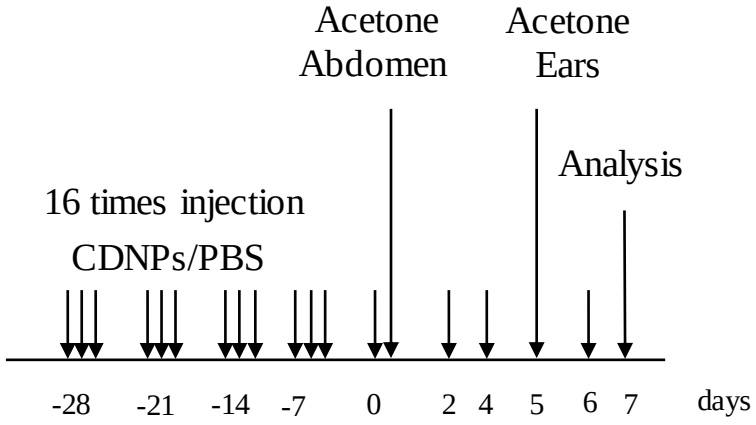

Figure 26. Experimental timeline for evaluating the immunogenic potential of CDNPs in a modified delayed-type hypersensitivity model.
Mice received intraperitoneal injections of CDNPs (10 µg/mL in PBS, 200 µL per injection) or PBS alone, administered 16 times over a period of 5 weeks starting on day -28. Acetone was applied to the abdomen for sensitization (day 0), followed by challenge on the ears (day 5) to assess potential contact reactivity. Mice were sacrificed on day 7 for immunological analysis, including TCRR sequencing of TCZs from the spleen.

On day +7, the mice were euthanized, and organs, including the spleen, were harvested for immunological analysis. Two TCZs per spleen were isolated using laser microdissection for TCRR analysis, employing high-throughput sequencing to evaluate the repertoire diversity and frequency of autoreactive T cell clones within the TCZs. The total number of sequencing reads, along with the counts of total and unique TCRβ clonotypes, is presented in Table 11. As presented, PBS-treated mice yielded a mean of $1.33 \times 10^6 \pm 0.34$ TCRβ sequences and 43,323 ± 14,571 unique clonotypes across TCZs, whereas CDNP-treated mice showed significantly fewer sequencing reads ($0.76 \times 10^6 \pm 0.29$, $p < 0.05$), accompanied by a nonsignificant reduction in clonotype richness (23,050 ± 16,980). Figure 27 illustrates that CDNP treatment results in a noticeable decrease in the total TCRβ sequences, as shown in Panel A. Since identical tissue volumes were used for each sample, this reduction likely indicates decreased T cell activity or proliferation in the spleen, rather than any technical variation. Panel B presents the count of unique clonotypes, showing that CDNP-treated mice are similar to PBS controls, with only a slight downward trend. Overall, these findings imply that CDNPs suppress the expansion of specific T cells but do not significantly alter the TCRβ repertoire's diversity.

Table 11. Comparative Analysis of TCRβ Clonality and Sequencing Output in TCZ1 and TCZ2 Across Treatment Groups

Treatment	Mouse	Position	Total TCRβ sequences (×10⁶)	Unique TCRβ clonotypes
PBS	1	TCZ1	1.92	71874
PBS	1	TCZ2	1.14	34544
PBS	2	TCZ1	1.40	42658
PBS	2	TCZ2	1.34	33965
PBS	3	TCZ1	1.30	42560
PBS	3	TCZ2	0.90	34336
Mean ± SD			1.33 ± 0.34	43322.83 ± 14571.16
CDNP	1	TCZ1	1.18	26841
CDNP	1	TCZ2	0.69	24590
CDNP	2	TCZ1	0.66	7838
CDNP	2	TCZ2	0.37	10070
CDNP	3	TCZ1	1.00	54022
CDNP	3	TCZ2	0.67	14940
Mean ± SD			0.76 ± 0.29	23050.17 ± 16980.37

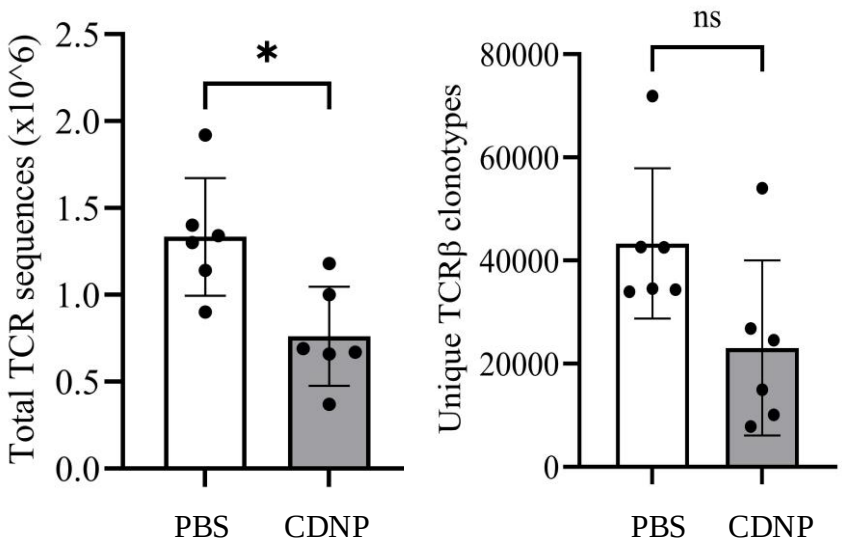

Figure 27. CDNP treatment reduces total TCRβ sequencing output without significantly altering clonotype diversity in splenic T cell zones. TCRR sequencing was performed on laser-microdissected T cell zones (TCZ1 and TCZ2) from spleens of PBS- (white bars) and CDNP-treated (gray bars) mice. A) CDNP-treated mice showed a significant reduction in total TCRβ sequencing reads compared to PBS controls (*$p < 0.05$, unpaired t-test), indicating lower overall transcript abundance. B) The number of unique TCRβ clonotypes trended lower in CDNP-treated mice but did not reach statistical significance (ns). Data are presented as mean ± SD across mice.

This method allowed us to compare two TCZs within each mouse spleen, identifying potential differences in T cell activation and regulation caused by microenvironmental gradients, such as variations in cytokine signaling or antigen-presenting cell distribution. It enabled us to evaluate whether CDNPs differentially influence TCRR dynamics across splenic regions, providing a sensitive measure of their immunological impact without a sensitizing agent. By examining these two zones, we gained insights into the spatial variability of CDNPs' effects on T cell responses, deepening our understanding of their safety and potential immunomodulatory role.

This experimental design provided a controlled framework to evaluate CDNPs' immunological effects without the confounding influence of a DTH sensitizing agent, addressing a key gap in understanding their standalone immunological impact. The TCRR analysis aimed to determine whether CDNPs influence T cell repertoire dynamics in the T cell zones, potentially indicating an immunomodulatory effect that could be leveraged in therapeutic contexts. By extending the experiment to 5 weeks and harvesting organs on day +7, sufficient time was ensured for any delayed immunological effects of CDNPs to manifest, thereby enhancing the reliability of the findings. The following subsection presents the detailed findings from these analyses, elucidating CDNPs' potential to induce contact reactivity and their broader immunological impact in the context of T cell-mediated immunity.

3.3.1. TCRR analysis reveals significant modulation of clonotype diversity by CDNPs using Jaccard and Morisita-Horn indices

To evaluate the effects of CDNP administration on the TCRR's structural organization, we measured inter-zone repertoire similarity using two established indices: the Jaccard index and the Morisita-Horn index. Analyses were performed on paired T cell zones (TCZ1 vs. TCZ2) from individual spleens of CDNP- and PBS-treated mice. We calculated both indices for the entire set of detected clonotypes and within specific abundance categories (top 10%, 10–20%, 20–50%, 50–80%, and the bottom 20%), offering a detailed view of repertoire overlap.

Utilizing the Jaccard index to measure the proportion of shared clonotypes across zones, regardless of their relative frequencies, we found a noticeable decrease in repertoire overlap in mice treated with CDNP compared to those given PBS. Analyzing the entire clonotype pool, the average Jaccard similarity between TCZ1 and TCZ2 was significantly lower in CDNP-treated mice than in the PBS controls, reflecting a general decline in shared clonotype presence among anatomical sites (Figure 28A). A closer look at abundance-based subsets showed that this decline appeared across all frequency categories. Specifically, clonotypes in the top 10%, 10–20%, 20–50%, 50–80%, and bottom 20% frequency bins demonstrated significantly reduced Jaccard similarity in CDNP-treated mice (all $p < 0.05$), underscoring a widespread decrease in inter-zone clonotype sharing (Figure 28B-F). These findings suggest a diversification in clonotype composition between T cell zones after exposure to CDNP.

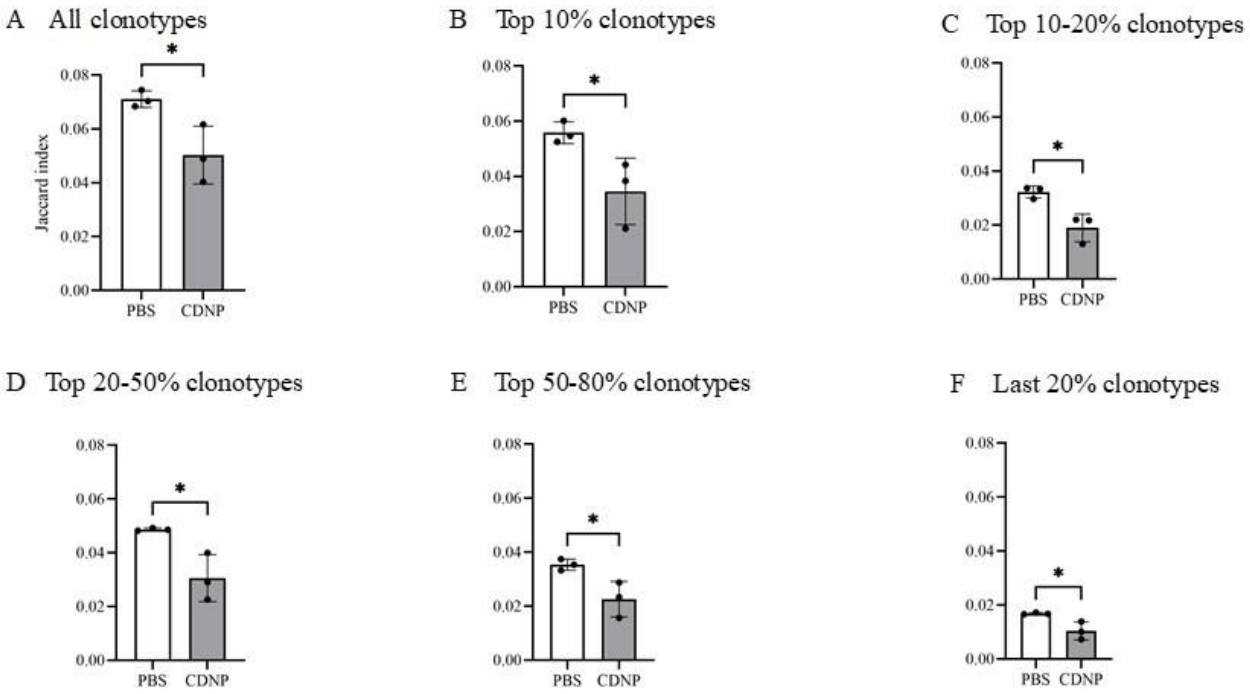

Figure 28. CDNP treatment reduces inter-zone TCRR similarity in a frequency-resolved manner. Jaccard index was calculated between paired splenic T cell zones (TCZ1 vs. TCZ2) from individual mice treated with PBS or CDNP to assess the extent of clonotype sharing. A) Jaccard similarity for all detected clonotypes. (B–F) Similarity was further analyzed within abundance-based subsets: B) top 10%, C) 10–20%, D) 20–50%, E) 50–80%, and F) bottom 20% of clonotypes based on relative frequency. Across all abundance categories, CDNP treatment resulted in significantly lower inter-zone clonotype overlap compared to PBS controls, indicating a broad-scale diversification of the TCRR structure following CDNP exposure. Bars represent mean ± SD. *$p < 0.05$, unpaired t-test.

To complement the presence/absence-based overlap measures, we also applied the Morisita–Horn index, which considers both clonotype identity and abundance. This provided an additional perspective on repertoire similarity between TCZ1 and TCZ2 zones. Consistent with the Jaccard analysis, CDNP treatment was associated with a modest reduction in Morisita–Horn similarity for the complete TCRR ($p < 0.05$) (Figure 29A), indicating slightly greater variation in clonotype abundance between zones.

Stratified analysis by clonotype abundance revealed a similar trend: while the most dominant clonotypes (top 10%) remained largely comparable between zones ($p = 0.12$), lower- and mid-abundance groups (10–20%, 20–50%, 50–80%, and bottom 20%) showed minor decreases in

similarity (Figure 29B–F). These differences were not pronounced but suggest that CDNP exposure may influence the distribution of less frequent T-cell clones. These results indicate subtle repertoire adjustments following CDNP treatment rather than major restructuring between splenic T-cell zones.

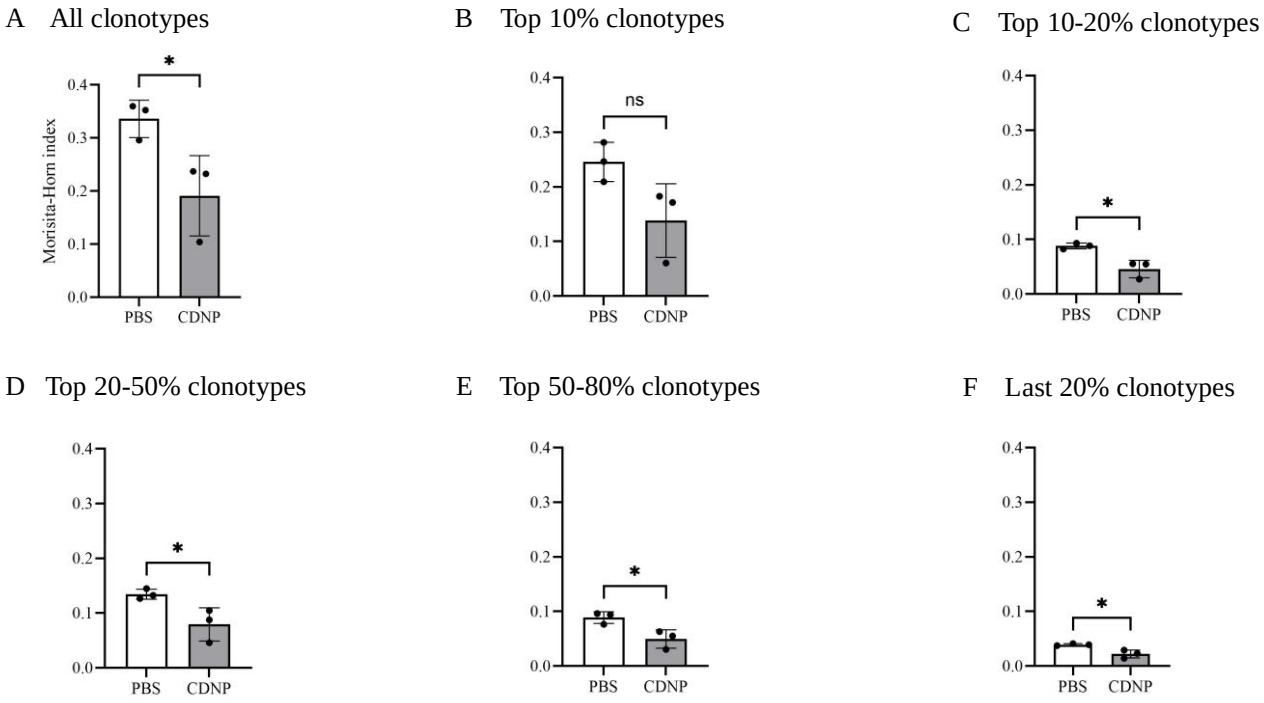

Figure 29. CDNP treatment alters abundance-weighted TCRR similarity across splenic T cell zones. Morisita-Horn index was calculated between paired splenic T cell zones (TCZ1 vs. TCZ2) from individual mice treated with PBS or CDNP to assess abundance-weighted repertoire similarity. A) Morisita-Horn similarity for all detected clonotypes. (B–F) Similarity was further analyzed within abundance-based subsets: B) top 10%, C) 10–20%, D) 20–50%, E) 50–80%, and F) bottom 20% of clonotypes based on relative frequency. While no significant difference was observed for the top 10% clonotypes, CDNP treatment led to significantly lower Morisita-Horn similarity across all other frequency bins, suggesting that divergence primarily affects mid- to low-abundance clones. Bars represent mean ± SD. *$p < 0.05$, unpaired t-test.

Notably, both indices consistently indicated that inter-zone repertoire divergence was more pronounced in CDNP-treated mice, and this effect was not confined to any single clonotype subset. Instead, it encompassed the full range of clonotype frequency. This observation was noted in all individual CDNP-treated animals, indicating a reliable and significant change in the spatial arrangement of T cell clones within the spleen.

Analysis using both similarity indices revealed that CDNP exposure was linked to a decrease in clonotype overlap between splenic T-cell zones. Although the changes were modest, they were consistent across different abundance levels and statistically significant in several cases. The combined use of Jaccard and Morisita–Horn indices offers complementary insights into how CDNP treatment may affect repertoire similarity and clonotype distribution. However, these indices mainly measure shared elements and their relative frequencies and do not account for broader features of the repertoire, such as its overall organization or entropy.

3.3.2. Jensen–Shannon divergence reveals significant regional divergence in TCRRs following CDNP injection

To better understand the structural complexity and spatial variation of the TCRR after CDNP administration, we calculated the Jensen–Shannon divergence (JSD) between paired T cell zones (TCZ1 vs. TCZ2) in individual spleens. JSD, an entropy-based metric derived from Kullback–Leibler divergence, measures the dissimilarity between two probability distributions, in this context, the normalized frequency distributions of TCR clonotypes. In contrast to the Jaccard and Morisita-Horn indices, which focus on clonotype identity and overlap in abundance, JSD examines differences across the complete range of clone frequencies, including shifts in overall distribution shape and entropy.

JSD analysis indicated a significant increase in repertoire divergence between TCZ1 and TCZ2 in mice treated with CDNP compared to PBS controls ($p < 0.05$) (Figure 30). JSD values were consistently higher in the CDNP group throughout all biological replicates, suggesting greater

heterogeneity in TCR distribution across splenic regions. The rise in JSD was apparent when examining the entire repertoire distribution without stratification, indicating that CDNP administration modifies the global architecture of the T cell repertoire across zones.

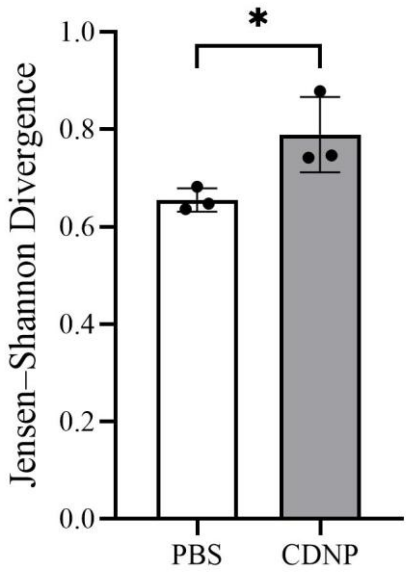

Figure 30. CDNP treatment increases inter-zone TCRR divergence based on Jensen–Shannon entropy. Jensen–Shannon divergence (JSD), an entropy-based metric that quantifies distributional differences between TCRRs, was calculated between paired splenic T cell zones (TCZ1 vs. TCZ2) from individual mice treated with PBS or CDNP. CDNP-treated mice exhibited significantly higher JSD values compared to PBS controls, indicating increased divergence in the distribution of clonotype frequencies between zones. Bars represent mean ± SD. *$p < 0.05$, unpaired t-test.

This increase in JSD was observed across all CDNP-treated mice and was not influenced by outliers, as shown by the low inter-sample variance within treatment groups. Conversely, PBS-treated mice showed relatively low and consistent JSD values between TCZ1 and TCZ2, indicating a more uniform distribution of TCR clonotypes between splenic compartments when CDNP was absent. These results suggest that CDNPs correlate with heightened regional repertoire disparity, reflecting a deviation from the baseline state of inter-zone TCR similarity.

The heightened JSD in the CDNP group signifies broader distributional divergence rather than mere changes in clonotype presence or abundance. It indicates a restructuring of the overall clonal hierarchy, encompassing changes in diversity, dominance, and entropy between compartments. Therefore, JSD introduces an additional and independent dimension to our evaluation of repertoire structure, complementing the pairwise overlap and frequency similarity highlighted by the Jaccard and Morisita-Horn indices, respectively.

Collectively, these entropy-based findings provide quantitative evidence that CDNP treatment enhances intra-splenic repertoire asymmetry, supporting a framework in which CDNPs promote region-specific clonal distributions. The results from JSD analysis correlate with and reinforce the reductions noted in Jaccard and Morisita-Horn metrics, collectively demonstrating a significant alteration in the spatial distribution of T cell repertoires following CDNP exposure. While Jensen–Shannon divergence highlighted global differences in repertoire structure between splenic T cell zones, it does not inform on the specific features within the TCR sequences that may underlie this divergence. As a first step toward identifying such qualitative differences, we next analyzed the length distribution of the CDR3, a critical determinant of TCR specificity and structural diversity.

3.3.3. CDNPs modestly alter CDR3 length distribution within splenic T cell zones

To examine whether CDNP treatment affected the qualitative features of the TCR repertoire, we analyzed the distribution of CDR3β lengths in paired splenic T-cell zones (TCZ1 and TCZ2). Both PBS- and CDNP-treated mice exhibited the typical bell-shaped CDR3β length distribution, with most clonotypes ranging from 12 to 15 amino acids and a peak at 14 amino acids (Figure 31). This pattern indicates a diverse, polyclonal repertoire characteristic of normal T-cell populations.

A slight decrease in the frequency of 14-amino-acid CDR3s was observed in CDNP-treated mice compared with controls, but this difference was not statistically significant ($p > 0.05$) and showed no consistent shifts at other lengths. Thus, CDNP exposure did not cause central repertoire narrowing or dominant clonal expansions, but may have induced minor adjustments within the most common CDR3 length class.

Overall, the analysis confirms that CDNPs do not substantially alter CDR3β length distribution, and any observed differences are subtle. This result supports the conclusion that CDNPs exert mild modulatory effects on TCRR structure under steady-state conditions.

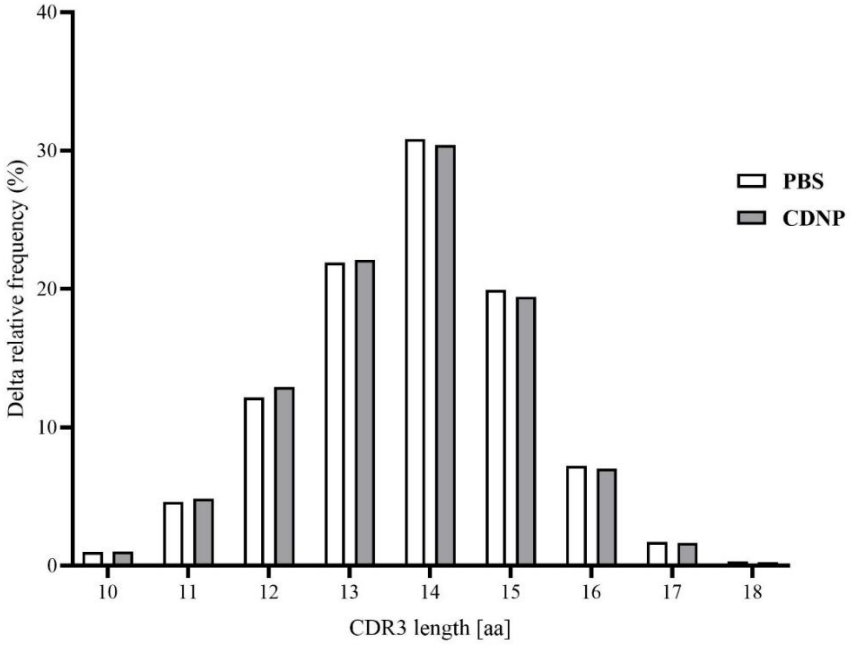

Figure 31. CDNPs modestly influence the CDR3β length distribution in splenic T cell zones. The bar graph shows the delta relative frequency (%) of CDR3β lengths (10–18 amino acids) in paired T cell zones (TCZ1 and TCZ2) from PBS-treated and CDNP-treated mice. Both groups exhibited the expected bell-shaped length distribution, with a dominant peak at 14 amino acids. A modest but consistent decrease in the frequency of 14-aa CDR3s was observed in CDNP-treated mice, while all other lengths remained nearly identical between groups. Although this reduction did not reach statistical significance, it may reflect subtle alterations in clonotype representation at the most frequently used length. Bars represent mean values across zones; error bars indicate SEM.

Although CDR3 length analysis provides valuable information about the structural diversity of TCRs, it fails to capture the sequence-level motifs that directly affect antigen recognition. While minor fluctuations in length can indicate broader repertoire dynamics, they do not uncover the specific sequence patterns that drive these variations. To address this issue, we then conducted a k-mer analysis on the CDR3 region, focusing on conserved amino acid motifs that may explain the observed zonal divergence in T cell responses following CDNP exposure.

3.3.4. CDNPs increase intra-splenic k-mer divergence in the TCRR

To evaluate how CDNP administration impacts the sequence-level structure of the TCRR in splenic compartments, we conducted a k-mer analysis of CDR3 amino acid sequences from paired TCZ (TCZ1 and TCZ2) in individual mice. This method reveals conserved short sequence motifs (k-mers) that indicate shared antigen recognition and clonal selection, offering a detailed perspective on repertoire composition that goes beyond clonotype-level comparisons.

For each mouse, we identified the ten most frequent k-mers in the TCZ1 and TCZ2 repertoires, calculating both the signed difference (Δk-mer) and the absolute difference (| Δk-mer |) in motif frequencies between the zones. This approach enabled us to assess the direction of motif enrichment or depletion as well as the overall extent of divergence in motif use between T cell zones. Figure 32 schematically illustrates the distribution of dominant k-mers across TCZ1 and TCZ2 in PBS- and CDNP-treated mice. In PBS controls, motif usage is largely symmetric between zones, indicating minimal intra-splenic divergence. In contrast, CDNP-treated mice exhibit apparent asymmetry, characterized by zone-specific enrichment of motifs, which reflects increased Δk-mer values and localized repertoire remodeling.

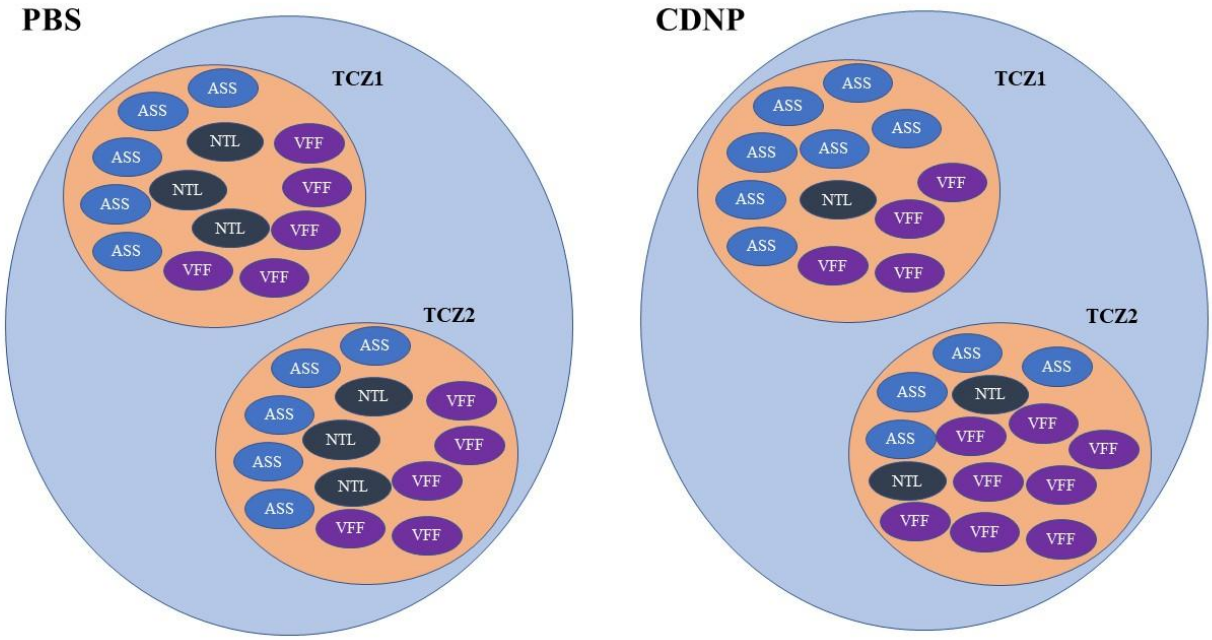

Figure 32. CDNP treatment increases intra-splenic k-mer divergence between T cell zones. The schematic illustrates the distribution of dominant CDR3 k-mers (e.g., ASS, NTL, VFF) across two splenic T cell zones (TCZ1 and TCZ2) in PBS- and CDNP-treated mice. Each colored oval represents a frequently detected motif. In PBS-treated mice (left), motif distribution is largely symmetric between TCZ1 and TCZ2, indicating minimal intra-splenic variation in TCR sequence usage. In contrast, CDNP-treated mice (right) display asymmetric motif distribution, with distinct k-mers enriched in specific zones. This visualizes the increased intra-splenic divergence (Δk-mer and |Δk-mer|) observed in CDNP-treated animals, suggesting localized clonal expansions and compartmentalized remodeling of the TCRR.

To quantify this data, we made comparisons between PBS- and CDNP-treated groups to evaluate the effects of CDNP immunization on intra-splenic motif-level variation. In PBS-treated mice, Δ k-mer and |Δ k-mer| values were typically low, indicating slight variation in k-mer usage between TCZ1 and TCZ2 (Figure 33). The most common motifs, such as ASS, SSL, CAS, and QYF, showed relatively even frequencies across the two zones, implying that without immunogenic stimulation, the TCRR is distributed uniformly throughout the splenic compartments. This aligns with a largely naive or homeostatically maintained T cell pool, with little selective pressure or localized expansions influencing zone-specific motif distributions.

In contrast, mice treated with CDNP showed significant differences in motif usage between TCZ1 and TCZ2. The signed Δ k-mer values indicated both systematic and reproducible shifts, with several motifs (e.g., ASS, SSL, QYF, AEQ, YEQ) consistently enriched in one region while being depleted in the other across various animals. These shifts were not random; instead, they adhered to reproducible patterns maintained across biological replicates, suggesting a structured and compartment-specific remodeling of TCR motif landscapes. For example, the ASS and SSL motifs were notably more prevalent in one region compared to the other in CDNP-treated animals, a trend that was not seen in PBS controls (Figure 33A).

To quantify the overall extent of motif-level divergence, we examined |Δ k-mer| values (Figure 33B). For nearly all of the top ten motifs per mouse, CDNP treatment resulted in significantly larger absolute frequency differences between zones. The mean |Δ k-mer| values for predominant motifs were considerably higher in the CDNP group compared to PBS, indicating increased intra-splenic variability in motif distributions. These differences encompassed more than just a few individual motifs, impacting a broad array of sequences, and were consistent across all mice in the CDNP group.

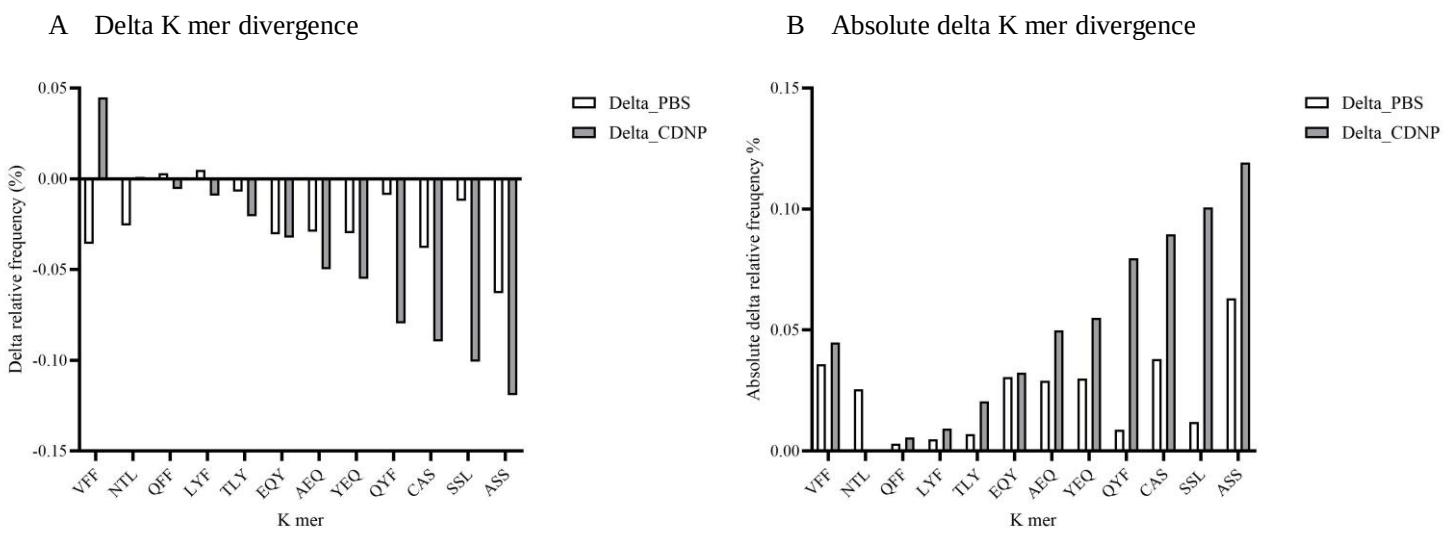

Figure 33. CDNP treatment induces intra-splenic divergence in TCR CDR3 k-mer usage. A) Signed delta (Δ) k-mer values show the directional differences in motif frequencies between paired splenic T cell zones (TCZ1 and TCZ2) within individual mice from PBS- and CDNP-treated groups. CDNP-treated mice exhibit pronounced motif-level asymmetry, with several k-mers (e.g., ASS, SSL, QYF, AEQ, YEQ) enriched in one zone and depleted in the other, indicating localized repertoire remodeling. In contrast, PBS-treated mice show relatively balanced motif distributions between zones. B) Absolute delta (|Δ|) k-mer values quantify the magnitude of motif frequency differences between TCZ1 and TCZ2, regardless of direction. CDNP-treated mice display markedly elevated |Δ| values across a broad range of motifs, reflecting increased intra-splenic repertoire heterogeneity. These results demonstrate that CDNPs induce spatially distinct clonal expansions, leading to structured divergence in CDR3 motif usage between splenic compartments. Bars represent mean delta or absolute delta relative frequency (%) across biological replicates.

The intra-animal, inter-zonal divergence in k-mer frequencies suggests CDNP treatment promotes localized clonal expansions of distinct T cell populations within the spleen. While PBS-treated mice exhibited largely symmetric motif distributions between TCZ1 and TCZ2, CDNP-treated animals showed specific motif enrichments in each region, implying that each area contains a non-overlapping pool of T cells with unique sequence characteristics. This spatial divergence in TCR motif usage indicates a structurally reorganized T cell response, characterized by distinct repertoire signatures localized to different splenic compartments.

Importantly, this difference was not confined to rare or low-abundance motifs; high-frequency motifs exhibited the most significant inter-zonal shifts in CDNP-treated mice. This indicates that the response to CDNPs entails substantial, zone-specific growth of antigen-specific clones, which dominate the local repertoire and produce distinct motif signatures between TCZ1 and TCZ2.

Our findings reveal that CDNP treatment triggers notable spatial reorganization of TCR sequence motifs in the spleen, as shown by increased Δ k-mer and |Δ k-mer| values across conserved CDR3 motifs. This effect is reproducible and consistent across various motifs, and it is markedly different from the pattern observed in PBS-treated controls. These results demonstrate that CDNP immunization not only alters global diversity metrics and clonotype overlap but also reorganizes the motif-level composition of the repertoire in a compartment-specific manner, reflecting localized, motif-driven clonal expansion within the spleen.

3.3.5. CDNPs enhance T cell activation and promote a Th2-skewed transcriptional profile in whole spleen

The observed remodeling of the TCRR in response to CDNP treatment, including increased intra-splenic clonal divergence, motif-level asymmetry, and enhanced repertoire diversity, prompted us to investigate whether these structural changes were accompanied by corresponding shifts in T cell transcriptional activity and polarization. Specifically, we aimed

to determine whether CDNPs, similar to OAT pretreatment described in Section 3.1, modulate the functional profile of T cells by promoting a Th2-biased immune environment. To test this hypothesis, we measured the expression of *Tcrb*, a general marker of T cell abundance and activation, and *Gata3*, the lineage-specifying transcription factor for Th2 cells, in whole spleen tissue collected on day +7. mRNA levels were quantified by qPCR in both CDNP- and PBS-treated mice.

Quantitative analysis revealed a significant increase in *Tcrb* expression in CDNP-treated mice compared to controls, indicating enhanced T cell transcriptional activity or expansion in the spleen (Figure 34A). As *Tcrb* encodes the β-chain of the TCR, this upregulation suggests either a greater number of T cells or increased engagement of TCR signaling machinery. These transcriptional findings align with and reinforce the TCRR results described in Sections 3.3.1–3.3.4, which demonstrated elevated TCRβ sequencing reads, reduced inter-zonal clonotype overlap (Jaccard and Morisita-Horn indices), increased Jensen–Shannon divergence, and a more even CDR3 length distribution in CDNP-treated mice. Together, these data indicate that CDNPs induce systemic T cell activation and clonal diversification, even in the absence of a classical sensitizing agent.

In parallel, expression of *Gata3* was also significantly elevated in CDNP-treated mice (Figure 34B). This upregulation suggests a shift in T cell polarization toward a Th2 phenotype, consistent with a less inflammatory or potentially tolerogenic immune profile. Notably, this transcriptional shift occurred without signs of tissue inflammation, as no increase in ear thickness was observed between CDNP- and PBS-treated groups during the challenge phase. This finding supports the notion that CDNPs engage T cells without triggering overt effector pathology. Notably, this immune deviation mirrors the effect of OVA/A/TM pretreatment, where the suppression of Th1 cytokines, such as IFN-γ, is associated with protection from tissue damage, despite ongoing immune activity.

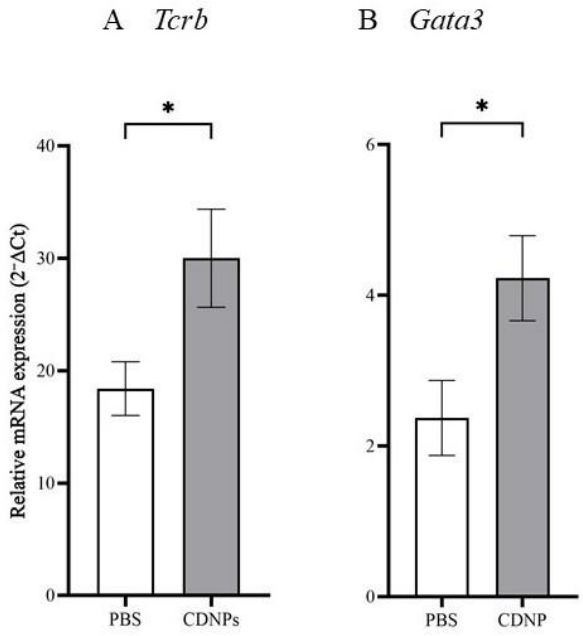

Figure 34. CDNP treatment enhances T cell activation and promotes Th2-associated transcriptional reprogramming. A) Relative expression of *Tcrb*, encoding the TCR β-chain, was significantly increased in spleens from CDNP-treated mice, indicating enhanced T cell abundance or activation. B) Expression of *Gata3*, the lineage-defining transcription factor for Th2 cells, was also significantly elevated following CDNP administration, suggesting a shift toward Th2 polarization. Gene expression was assessed by quantitative PCR on day 28 and normalized to a housekeeping gene using the $2^{-}\Delta Ct$ method. Results are presented as mean ± SEM. *$P < 0.05$, unpaired t-test.

The simultaneous rise of *Tcrb* and *Gata3* indicates that CDNPs affect both the magnitude and quality of the T cell response. Rather than triggering a typical proinflammatory Th1 response, CDNPs appear to promote T cell activation that leans toward Th2 differentiation, thereby reducing downstream inflammation. This gene expression profile corresponds with broader observations of T cell diversity and emphasizes CDNPs' capacity to redirect T cell responses away from harmful pathways. These results suggest that CDNPs could serve as immunomodulators that support compartmentalized, clonally diverse, and functionally reprogrammed T cell responses, traits advantageous for managing T cell–mediated diseases.

4. Discussion

4.1. Overview of key findings

This thesis explores two complementary approaches to modulate T-cell immunity: antigen-specific conditioning with OAT in the EBA model, and multiepitopic modulation using CDNPs under steady-state conditions. OAT pretreatment altered the GC–Tfh TCRβ repertoire in a LN–specific manner, exhibiting increased diversity, reduced clonal dominance, modified clonal sharing between the Ingln and Pln (especially among abundant clonotypes), and unique sequence features, such as NTL/AEQ motifs, along with changes in CDR3 length. RNA-seq analysis did not show significant differences between OAT and PAT within each node (overlapping PCA clusters; only two Ig variable genes in Pln; none in Ingln), suggesting subtle effects at the whole-tissue level. The main transcriptomic distinction was based on LN identity, with Pln and Ingln being strongly separated, exhibiting apparent differences within each pretreatment. Importantly, OAT shifted the Pln–Ingln divergence, from inflammatory signatures in Ingln toward regulatory/metabolic programs, while PAT emphasized inflammatory/effector traits. These repertoire and transcriptional changes occurred in the context of an established EBA model, where OAT pretreatment is known to prevent disease induction, linking our findings to functional protection against autoimmunity.

Regardless of disease status, CDNPs were thoroughly characterized: approximately 150nm in size, as determined by NTA, with a strong correlation between particles and proteins; stable Annexin A5 was confirmed via Western blot; and effective endotoxin removal was achieved using Triton X-114, lowering levels to below 0.1 EU/mL. Functionally, CDNPs modulated cytokine responses mainly in a dose-dependent manner: the secretion of IL-6 by PAM-stimulated macrophages decreased gradually as the CDNP concentration increased, except at the lowest dose, which did not follow this trend. *In vivo*, administering CDNPs expanded the TCRR within the T cell zone, indicating multiepitopic remodeling of baseline clonality.

Additionally, qPCR transcriptional profiling revealed significantly higher Tcrb expression, suggesting increased T cell abundance or activation, and higher *Gata3* levels, indicating a shift toward Th2 polarization. Overall, these findings suggest CDNPs as protein-rich, multiepitopic modulators that influence both T-cell repertoire diversity and functional programming under steady-state conditions, broadening T-cell clonality while promoting Th2-associated transcriptional reprogramming.

4.2. TCRR modulation in autoimmunity

4.2.1. Tfh cells as drivers of autoantibody-mediated disease

T follicular helper (Tfh) cells are a specialized subset of $CD4^+$ T-cells characterized by the expression of CXCR5, PD-1, ICOS, and the transcription factor BCL-6. In GCs, they provide critical signals for B-cell proliferation, class-switch recombination, and affinity maturation through cell-cell interactions and secretion of cytokines, such as IL-21 and IL-4 (Shlomchik & Weisel, 2012). Dysregulated Tfh cell activity is increasingly recognized as a contributor to autoimmunity. In SLE, circulating Tfh-like cells and elevated serum IL-21 levels correlate strongly with disease activity and autoantibody production (Kim et al., 2018). In BP, increased numbers of $CXCR5^+PD\text{-}1^+$ Tfh cells and IL-21 expression are associated with higher anti-BP180 autoantibody levels (Li et al., 2013). Preclinical studies suggest that depleting Tfh cells or neutralizing IL-21 reduces autoantibody production in autoimmune models, indicating that Tfh cells actively drive, rather than merely reflect, autoreactive antibody responses.

4.2.2. Repertoire restriction as a hallmark of autoimmunity

Beyond mere quantitative expansion, qualitative alterations in the TCRR of Tfh cells are increasingly seen as key indicators of autoimmunity. In various autoimmune diseases, including SLE, rheumatoid arthritis, pemphigus vulgaris, and BP-TCRRs, show decreased diversity, oligoclonal expansions, and biased V-gene usage, indicating antigen-driven selection of

autoreactive clones (Thapa et al., 2015; Ye et al., 2020). Similarly, studies of various autoimmune conditions, such as alopecia areata and Stevens-Johnson syndrome, as well as other inflammatory disorders, reveal reduced TCR diversity and the presence of oligoclonal expansion (Liu et al., 2024). In animal models, infiltrating T cells in affected tissues exhibit biased Vβ gene usage, clonally restricted repertoires, and common CDR3 motifs, indicating signs of antigen-driven selection (Moore et al., 2020). These repertoire distortions are not accidental, and they strongly associate with autoreactive immune responses, supporting the idea that Tfh TCRR both reflect and promote breaches in humoral tolerance.

4.2.3. OAT-induced remodeling of the Tfh repertoire

This study found that OAT pretreatment in the EBA model caused significant changes in the Tfh TCRR. Compared to PAT, OAT increased overall diversity and decreased clonal dominance, indicating a shift away from highly expanded clonotypes. Clonal distribution patterns showed altered dissemination between the popliteal and inguinal LNs, with Ingln presenting broader, less restricted repertoires. Sequence analysis revealed new short CDR3 motifs, such as NTL and AEQ, along with shifts in CDR3 length distributions, indicating qualitative repertoire remodeling beyond simple clone expansion or contraction.

RNA-seq transcriptomic profiling added further insights. Principal component analysis showed considerable overlap between OAT and PAT within individual LNs, suggesting OAT did not cause broad transcriptome reprogramming at the tissue level. Only two immunoglobulin variable genes differed in Pln, with none in Ingln. The main distinction was between Pln and Ingln themselves, highlighting the influence of LN identity. OAT seemed to influence this divergence, shifting Ingln transcription toward regulatory and metabolic profiles away from effector and inflammatory pathways.

Overall, these findings demonstrate that OAT pretreatment altered the Tfh repertoire by increasing diversity, decreasing clonal dominance, and adding unique sequence features. RNA-seq showed subtle differences between OAT and PAT but clear transcriptional differences between Pln and Ingln. These results consistently indicate that Ingln is the most affected site by OAT pretreatment, suggesting it may be the key location for tolerogenic reprogramming.

4.2.4. The inguinal lymph node as a tolerogenic hub

RNA-seq showed minimal differences between OAT and PAT within individual nodes, but a substantial divergence between Pln and Ingln. This underscores the role of LN identity in shaping immune responses. Bulk transcriptomics averages the gene expression of diverse cell populations, which dilutes antigen-specific effects in small subsets, such as Tfh cells. Consequently, the most prominent signal was the difference between Pln and Ingln, reflecting factors like drainage patterns, stromal structure, and migratory antigen-presenting cells. The Pln, draining the hind footpad and mCol7c challenge site, tends to favor effector and inflammatory responses, while the Ingln, draining the tail base where the final OAT injection occurred, receives antigen and adjuvant stimulation. Under PAT, this led to an effector-skewed Ingln profile. In OAT-treated mice, however, Ingln shifted toward regulatory and metabolic pathways, showing greater diversity, less clonal dominance, and new CDR3 motifs. These findings suggest that Ingln is key for establishing tolerance through reprogramming. Several factors may drive this bias. Repeated antigen exposure combined with adjuvants likely plays a role. Alum promotes Th2 responses and IL-10 production by antigen-presenting cells, whereas emulsion adjuvants, such as Titermax, create a depot effect that prolongs antigen presence and alters processing (AWATE et al., 2013; Fan et al., 2022; Kool et al., 2008; McKee & Marrack, 2017). Persistent antigen exposure in Ingln, combined with these adjuvants, may encourage dendritic cells to present lower-avidity peptide–MHC complexes. This reduces the competitive edge of high-affinity autoreactive clones and favors a broader Tfh repertoire, as seen in the

increased diversity after OAT. Additionally, Ingln may harbor a cellular niche more supportive of regulatory activity. LNs draining sites of chronic antigen exposure often contain increased populations of regulatory T cells (Tregs) and T follicular regulatory cells (Tfr), a Treg subset specialized for GCs. These cells suppress GC responses by inhibiting Tfh cell activity and B-cell responses, thereby limiting excessive antibody production and maintaining immune tolerance (Huang et al., 2020; Merkenschlager et al., 2023; Miles & Connick, 2018). The enrichment of regulatory and metabolic signatures in Ingln during OAT suggests these cells help restrict effector expansion, allowing for a more diverse clonotypic profile. Metabolic programming also influences immune fate; effector Tfh cells depend on glycolysis, while regulatory subsets rely on oxidative phosphorylation and lipid metabolism (Ray et al., 2015; Shi et al., 2025). By activating regulatory and metabolic pathways, OAT likely fosters a microenvironment that suppresses effector clones and maintains diverse repertoires. Overall, the data support a model where Ingln acts as a tolerogenic center under OAT. Its location, repeated antigen and adjuvant exposure, and microenvironmental features reprogram antigen presentation and metabolism, broadening the Tfh repertoire and preventing autoreactive dominance. OAT does not eliminate LN heterogeneity but redirects it: OAT reprograms a node initially favoring effector responses under PAT into a regulatory environment. This Ingln-focused reprogramming explains how OAT prevents EBA induction and highlights LN specialization as crucial for tolerance induction.

4.2.5. Repertoire broadening as a mechanism of tolerance

The idea that expanding the immune repertoire offers protection against autoimmunity is logically supported by ecological and epidemiological evidence. This principle is reflected in our data, where OAT pretreatment broadens the Tfh repertoire and reduces clonal dominance. The hygiene hypothesis suggests that decreased microbial exposure in industrialized societies has resulted in a loss of immune diversity and a rise in autoimmune and allergic diseases (Bach,

2020). Early exposure to a variety of microbes and parasites in childhood has been shown to prevent autoimmunity in experimental models, partly by expanding regulatory networks and diversifying TCRR. This parallels the effect of OAT, which diversified the Tfh repertoire in Ingln and introduced novel CDR3 motifs. These findings indicate that immune systems activated by a broad range of antigens are less likely to be dominated by autoreactive clones. Similarly, the broadened repertoires we observed under OAT reduced the likelihood of pathogenic clonotypes achieving dominance. In this context, OAT-induced repertoire diversification can be seen as a biomimetic approach that mimics the protective effects of environmental antigen diversity.

Taken together, these findings emphasize the Tfh receptor repertoire as both a marker and a driver of tolerance. Traditional therapies often aim to block Tfh-derived cytokines or co-stimulatory signals. In contrast, OAT shows that reconfiguring the clonal architecture itself offers an alternative approach to immunomodulation. This aligns with the emerging idea of repertoiric tolerance, where tolerance develops not from global suppression but from redistributing clonotypes to reduce autoreactivity. By expanding and qualitatively modifying Tfh repertoires, OAT introduces a new paradigm for preventing harmful GC responses, with potential applications for translational strategies in EBA, pemphigus, BP, and other antibody-mediated diseases.

While OAT pretreatment has clearly shown that remodeling the antigen-specific repertoire can prevent autoimmunity, its use is restricted because it requires a known antigen. Many human autoimmune diseases have unknown, multiple, or highly variable autoantigens. To overcome this limitation, we investigated whether similar immune-modulating effects could be achieved without using an antigen. We focused on CDNPs, protein-rich particles released during stress that are known to modulate immune responses in a versatile manner. The following section

examines how CDNPs alter repertoire structure and T-cell programming in steady-state conditions, offering an alternative approach to OAT.

4.3. CDNPs as multi-epitope protein immune modulators

4.3.1. Composition and characterization of CDNPs

To assess the potential of CDNPs as multi-epitope protein immune modulators, we began by optimizing and characterizing their production. Initially, using the established method where cells are cultured in MEM without ribonucleosides, we achieved only modest protein yields. However, with the protocol adjustments we implemented, CDNP recovery was notably enhanced. This likely results from increased cellular stress responses under the new culture conditions, leading to greater release of protein-rich particles. The increased yield was crucial for conducting downstream functional assays, which would have been impossible with the original method.

Following optimization, NTA revealed that CDNPs consistently fell within a narrow size distribution of ~150nm (Kunz, Xia, et al., 2017). This parameter is crucial not only for characterization but also as an exclusion criterion. Exosomes, for instance, are generally smaller (~30–120 nm) and originate from endosomal compartments, whereas apoptotic bodies are considerably larger (>500 nm) and contain fragmented DNA and organelles. Protein aggregates can also be found in cell culture supernatants, but usually lack a consistent size distribution and do not demonstrate a reliable correlation with protein content. (Dilsiz, 2024). By demonstrating that CDNPs fall within a specific intermediate range, clearly distinct from other nanoparticle types, we establish their unique identity and exclude the possibility that the preparations are merely mixtures of vesicles, apoptotic debris, or random aggregates. The strong correlation between particle numbers measured by NTA and protein concentrations assessed by SDS-

PAGE further reinforces this conclusion. It shows that CDNPs are consistently rich in protein rather than lipids, and their abundance can be reliably measured using either parameter. This correlation is vital for experimental consistency, enabling normalization of biological assays to protein content as a proxy for particle number.

Due to detecting endotoxin contamination in initial preparations and the fact that even trace amounts of lipopolysaccharide can significantly skew immunological results, we employed phase extraction using TX-114 (Teodorowicz et al., 2017). This process successfully lowered endotoxin levels to under 0.1 EU/mL, ensuring that the biological effects seen in later assays were solely due to the CDNPs.

Proteomic analyses reveal that CDNPs encompass a diverse range of intracellular proteins, including annexins, cytoskeletal components, metabolic enzymes, ribosomal proteins, histones, and heat shock proteins. Among these, Annexin A5 is notably the most abundant and consistently detected component. Its stable presence across different preparations makes it a key molecular marker for CDNPs. Our study's Western blot results confirmed the presence of Annexin A5, establishing a dependable criterion for CDNP identification. Therefore, the consistent detection of Annexin A5 is not only supportive but also diagnostic; samples containing Annexin A5 in this specific context can be identified as CDNPs (Solisch et al., 1999).

These findings confirm that CDNPs are non-extracellular vesicular nanoparticles approximately 150 nm in size, containing intracellular proteins and a complex, multi-epitope protein cargo. Their specific size range serves as a key criterion to differentiate them from other nanoparticle types. Additionally, the observed correlation between particle number and protein content, enhanced recovery through optimized conditions, effective endotoxin removal, and consistent detection of Annexin A5 as a molecular marker offer a solid basis for understanding their immunomodulatory roles.

4.3.2. IL-6 output in a macrophage TLR2/1 model with CDNPs versus OVA

To evaluate whether CDNPs influence innate immune activation through their protein-rich, multiepitopic composition, we analyzed IL-6 secretion in the murine macrophage-like cell line J774A.1, a well-established model for studying macrophage-mediated inflammatory responses. This cell line, derived from a reticulum cell sarcoma, is a commonly used model because it retains key macrophage features such as phagocytosis, response to pattern recognition receptor ligands, and high cytokine production (Ralph & Nakoinz, 1975). To stimulate the response, we employed PAM, a synthetic triacylated lipopeptide that resembles bacterial lipoproteins and specifically triggers Toll-like receptor (TLR)2/1 heterodimers (Aliprantis et al., 1999). Activation of this pathway triggers NF–κB–dependent pro-inflammatory cytokine release, making it a standard system for examining effects on innate immune responses.

As expected, PAM stimulation resulted in high IL-6 levels. Notably, OVA treatment did not affect IL-6 secretion compared to PBS controls, indicating that the presence of a soluble protein antigen alone does not influence TLR2/1 signaling in this context. Conversely, CDNPs showed a steady decrease in IL-6 secretion across all tested concentrations relative to OVA and PBS, with the most significant reduction at 5 µg/ml, where IL-6 levels dropped well below baseline. This downward trend was also observed at 2.5 and 1 µg/ml, though with more variability, and disappeared entirely at 0.5 µg/ml, where IL-6 levels matched those of PBS and OVA. Although none of these differences were statistically significant, the pattern suggests a concentration-dependent effect of CDNPs on macrophage cytokine production.

Yet, with the current observed data, important questions arise: Primarily, why do CDNPs show a downward trend but not significance compared to OVA? One can speculate that several factors likely contribute to this. Initially, nanoparticle uptake varies widely and exhibits a threshold-like behavior at the single-cell level. Quantitative and modeling research reveal significant, random differences in the number of particles each cell internalizes, indicating a

minimum per-cell load needed for reliable intracellular responses. This over-dispersion often diminishes the population-level effects at intermediate doses (Åberg et al., 2021; Fedotov & Alexandrov, 2024). Second, normalizing doses based on bulk protein mass can obscure genuine functional differences between a multi-epitope particulate (CDNPs) and a soluble monomeric protein (OVA). Current guidelines recommend using particle number or surface metrics, rather than just protein mass, to prevent this issue. Additionally, macromolecular crowding caused by high levels of extracellular protein (such as OVA matched by mass) is known to influence diffusion and receptor–ligand interactions, which can reduce signaling efficiency and minimize observed differences between groups ("Correction to "Minimal information for studies of extracellular vesicles (MISEV2023): From basic to advanced approaches"," 2024; Ellis, 2001; Tsiapalis & Zeugolis, 2021; Upadhya & Shetty, 2024; Welsh et al., 2024). Third, IL-6 measurements in J774.A1 macrophage-like cells are inconsistent and depend on the model, a fact supported by comparative studies and reviews of immortalized macrophage lines. This biological variability reduces the ability to detect modest yet consistent trends unless larger sample sizes or additional measurements are used (Andreu et al., 2017; Herb et al., 2024; Martin & Dorf, 1990).

A final point is that the suppression pattern did not follow a straightforward monotonic trend. IL-6 reduction was most pronounced at 5 µg/ml, moderate at 2.5 and 0.5 µg/ml, and least at 1 µg/ml. The similarity between 0.5 and 2.5 µg/ml suggests that the CDNP effect is not strictly dose-dependent but is influenced by how particles interact with proteins and receptors in the culture environment. When nanoparticles are placed in a serum-containing environment, serum proteins rapidly adsorb to their surface, forming a coating whose composition changes depending on the nanoparticle-to-protein ratio. This dynamic, dose-dependent adsorption alters how cells interact with the particles (Kim et al., 2023). At very low doses, such as 0.5 µg/ml, the excess of serum proteins compared to the particle surface area may produce a coating that

affects how CDNPs interact with PAM and cellular receptors, resulting in suppression levels similar to those at 2.5 µg/ml. At 1 µg/ml, the balance of surface-bound proteins and particle availability may shift, resulting in less effective reduction of PAM-driven TLR2/1 signaling and explaining the weaker suppression observed.

Additionally, macrophage uptake of particles is variable, with some cells internalizing many particles, while others take up few. This variability can lead to overlapping effective exposure levels at different bulk concentrations, causing cellular responses at 0.5 and 2.5 µg/ml to appear similar. Finally, accessory receptors like CD14 are known to facilitate triacylated lipopeptide signaling via TLR2/1, and their involvement can influence downstream potency. Such co-receptor dynamics may contribute to dose-dependent variations in IL-6 output under PAM stimulation (Raby et al., 2013).

4.3.3. Effects of CDNPs on TCRR and transcriptional programming

This study shows that CDNPs modulate the TCRR through their multiepitopic composition rather than an antigen-(in)dependent mechanism. In contrast to OAT pretreatment, which protects against EBA through antigen-specific immune deviation, CDNPs act more broadly by altering clonotype distribution and shaping T-cell polarization without relying on a defined epitope.

An initial observation revealed that CDNP administration reduced the overall number of TCRβ sequences retrieved from splenic T-cell zones, while the count of unique clonotypes remained similar to that of the controls. This indicates that, despite recovering fewer TCRβ transcripts, the overall diversity of the repertoire was maintained. In biological terms, this pattern may suggest that CDNPs either limit T-cell expansion or activation, decrease TCRβ transcript levels per cell, or change the spleen's cellular composition—such as by encouraging activated T cells to migrate elsewhere or allowing other lymphocyte subsets to occupy the TCZ. Technically,

total read counts can also be affected by RNA yield and sequencing depth; however, richness generally stabilizes once sufficient coverage is achieved (Rosati et al., 2017). Therefore, the observed reduction in total reads most likely reflects biological modulation of T-cell activity or redistribution rather than a loss of repertoire diversity.

Aside from sequencing depth, a major impact of CDNPs was shown by overlap metrics. Both Jaccard and Morisita–Horn indices were consistently lower in CDNP-treated mice compared to PBS controls, across the entire repertoire and at various clonotype frequency levels. Our data demonstrated that CDNPs not only increase the diversity of TCRR at a whole level of the repertoire but also among the top 10%, between 10-20%, 20-50%, 50-80%, and the last 20% of clonotypes, as demonstrated by both the Jaccard and Morisita-Horn indices. This highlights the multi-epitopic nature of the CDNPs, which can cause a range of shifts in the diversity of the TCRR. In other words, this indicates that CDNPs decreased the sharing of clonotypes between splenic T-cell zones, increasing divergence between compartments. Immunologically, this aligns with the idea that CDNPs, by presenting a wide range of epitopes, engage a more diverse set of TCRs and prevent the dominance of specific clonotypes. Biochemically, the multi-epitope protein makeup of CDNPs broadens the range of peptide–MHC ligands in the spleen, leading to the recruitment of diverse T-cell clones and less overlap between anatomical niches. This diversification corresponds with findings from repertoire studies that show polyepitopic or complex antigens promote clonotypic heterogeneity, whereas single, defined antigens often cause convergence and clonal dominance (Greiff et al., 2015; Mortazavi et al., 2024; Vesin et al., 2025). Furthermore, greater divergence between TCZs may indicate local differences in how antigens are taken up and presented, as splenic dendritic cells and macrophages can process multi-protein complexes differently. This increases regional variation in the selection of clonotypes. Therefore, the lower Jaccard and Morisita–Horn indices after CDNP treatment show a shift from clonotype overlap to divergence. This supports the idea that multi-epitope

nanoparticles spread T-cell engagement more evenly across splenic compartments, fostering a tolerogenic yet structurally varied immune environment.

The decrease in Jaccard and Morisita–Horn indices already indicated less clonotype overlap and greater divergence between splenic TCZs following CDNP administration. To gain a more detailed understanding of these differences, we next evaluated repertoire similarity with JSD, which considers both presence/absence and abundance data in a way that is sensitive to distribution. As expected from the overlap analysis, CDNP-treated samples had a significantly higher JSD than controls, reflecting increased divergence in clonotype distributions. Immunologically, this implies that CDNPs reshape the splenic TCRR by promoting zone-specific expansions and decreasing convergence across zones. In this analysis, similar to one with Jaccard and Morisita-Horn indices, comparisons were made between TCZ1 and TCZ2 of each individual mouse, providing a direct measure of intra-splenic divergence. This divergence aligns with the multi-epitope nature of CDNPs, likely presenting different peptide–MHC complexes to local antigen-presenting cells, thereby expanding the repertoire and accentuating regional differences (Greiff et al., 2015; Horn et al., 2021). Similar patterns have been observed in studies where polyepitopic stimulation results in greater repertoire divergence than single-antigen stimulation (Li et al., 2021). Overall, these findings suggest that CDNPs cause a fundamental redistribution of clonotypic usage, increasing diversity between compartments in the spleen.

Having established that CDNPs expand divergence between splenic T-cell zones, we investigated whether this redistribution was linked to structural changes in the TCRR, explicitly focusing on CDR3 length. The results showed no significant differences between CDNP- and PBS-treated mice, although there was a slight shift in the frequency distribution. This indicates that while CDNPs increase clonotypic divergence between compartments, they do so without fundamentally changing the typical structural constraints of the TCRβ chain. The consistent

CDR3 length distribution supports the idea that thymic selection and MHC-binding requirements impose strong biophysical limits on CDR3 size, which peripheral interventions do not easily alter (Lu et al., 2019; Van Laethem et al., 2022). Thus, CDNPs diversify repertoire usage at the clonotype and sequence level without disrupting the structural equilibrium of the CDR3 region.

While CDR3 length distributions remained essentially unchanged after CDNP treatment, this metric only captures broad structural restrictions imposed by thymic selection and peptide–MHC interactions. These constraints tend to maintain a relatively consistent CDR3 length across different immunological states. Nonetheless, more detailed sequence-level differences within the CDR3 region might still develop in response to CDNPs. To explore this, we examined k-mers, which offer a higher-resolution insight into repertoire structure and can detect antigen-driven selection patterns that length alone does not reveal.

This analysis showed that in PBS-treated mice, k-mer usage was mostly symmetrical between TCZ1 and TCZ2, with minimal Δk-mer and |Δk-mer| differences, consistent with a homeostatically maintained repertoire. In contrast, CDNP-treated animals displayed clear asymmetry in motif distributions, with recurring motifs such as ASS, SSL, QYF, AEQ, and YEQ enriched in one zone and exhausted in the other. These shifts were consistent across animals, demonstrating a structured, compartment-specific remodeling of motif usage. Notably, the largest differences between zones appeared among the most common motifs, implying that CDNPs promote the localized expansion of dominant clones rather than affecting only rare sequences. Immunologically, these findings indicate that the multi-epitope composition of CDNPs generates distinct peptide–MHC landscapes in different splenic regions, engaging heterogeneous sets of TCRs and promoting spatially divergent clonal expansions (Meinhardt et al., 2022). Biochemically, the enrichment of conserved motifs, such as ASS and SSL, is a standard feature of murine TCRβ repertoires. This indicates that CDNPs reshape current public

sequence patterns into zone-specific repertoires instead of forming completely new sequence classes. Consequently, Δk-mer and |Δk-mer| analyses show that CDNPs promote motif-driven, compartmentalized remodeling of the splenic TCRR, building on findings from Jaccard, Morisita–Horn, and JSD analyses at the sequence-motif level. In summary, our data indicate that the different k-mer ratios between TCZ1 and TCZ2 reveal that CDNPs enhance intra-splenic repertoire asymmetry, with each zone enriched for unique sequence motifs. Instead of uniformly altering the repertoire, CDNPs facilitate localized clonal expansions, resulting in compartment-specific motif signatures that align with responses to complex antigens. This means that CDNPs broaden the range of TCRs used in the spleen, making each zone less redundant and helping the repertoire stay balanced and more tolerant.

In conclusion, CDNP administration alters the splenic TCR repertoire through its multiepitopic protein composition, reducing overall sequencing output without diminishing clonotype richness, redistributing clonotype usage across compartments, and increasing divergence at both the repertoire and motif levels. Unlike OAT pretreatment, which causes antigen-specific deviation, CDNPs expand the recognition landscape through their multi-epitope composition, resulting in zone-specific clonal expansions while maintaining the structural integrity of the CDR3 region. These findings suggest that CDNPs foster a T-cell repertoire that is structurally stable yet functionally diverse, supporting a more balanced and potentially tolerogenic immune environment.

Moreover, the qPCR analysis of entire spleen samples showed a notable rise in both *Tcrb* and *Gata3* expression after CDNP administration. The increased *Tcrb* transcripts indicate a general boost in the T-cell transcriptional activity within the spleen, possibly due to either an expansion of the overall T-cell population or heightened transcriptional activity in individual cells. At the same time, the increased Gata3, a key transcription factor for Th2 differentiation, suggests that splenic T cells are shifting toward a Th2-like profile. GATA-3 is known to

enhance Th2 cytokine production, such as IL-4, while reducing Th1 lineage commitment (Oakes et al., 2017; Tindemans et al., 2014; Yagi et al., 2011; Zheng & Flavell, 1997). The concomitant increase in both *Tcrb* and *Gata3*, therefore, suggests that CDNPs do not act by suppressing global T-cell activity, but rather by quantitatively enhancing T-cell transcriptional output while qualitatively skewing differentiation toward a Th2 profile.

These findings complement the repertoire-based analyses. Whereas TCRβ sequencing of microdissected splenic TCZs showed reduced sequencing depth but preserved clonotype richness, the qPCR data from whole spleen indicate that the net splenic T-cell compartment remains transcriptionally active, with a bias toward Th2-associated programming. Taken together, this supports a model in which CDNPs induce a redistribution and functional reprogramming of T cells: repertoire divergence is amplified at the local, compartmental level (as reflected by reduced Jaccard and Morisita–Horn indices and elevated Jensen–Shannon divergence), while the global splenic output remains intact and is shifted toward a tolerogenic Th2 phenotype.

In summary, CDNPs influence the splenic TCRR independently of antigen presence. They reduce the overall sequencing output but do not affect clonotype diversity, and they enhance intra-splenic divergence, as determined by Jaccard, Morisita–Horn, JSD, and k-mer analyses. These modifications occur without changing CDR3 length constraints, which suggests structural stability is maintained. qPCR results also show increased expression of *Tcrb* and *Gata3*, indicating heightened T-cell activity with a Th2-biased profile. Overall, CDNPs foster a repertoire that remains structurally intact while becoming functionally more diverse, thereby supporting a tolerogenic immune environment. These findings demonstrate that CDNPs diversify and reprogram the T-cell repertoire without compromising its structural stability, thereby creating a more compartmentalized and Th2-biased immune response.

The data presented here confirm that CDNPs act as a mixture of proteins that contribute to immune modulation, affecting both innate and adaptive immunity. Unlike classical nanoparticles or single antigens, CDNPs are made of aggregated intracellular proteins, presenting a multi-epitopic structure rather than a single epitope. They form stable, distinct nanoparticles measuring approximately 150 nm, with a consistent protein content and Annexin A5 as a signature component. This complex mixture of proteins likely explains their broad interaction with the immune system.

Functionally, CDNPs slightly decreased IL-6 secretion from macrophages under TLR2/1 stimulation, indicating they can reduce innate inflammatory responses. In adaptive immunity, they increased the TCRβ repertoire within TCZs by decreasing clonal dominance while maintaining overall diversity, suggesting a redistribution of the clonal pool rather than contraction. Transcriptionally, they increased *Tcrb* and *Gata3*, which aligns with enhanced T-cell representation and a Th2 bias.

Overall, these findings suggest that CDNPs function as multi-epitopic proteins, reprogramming immune responses by modulating innate cytokines and expanding adaptive clonotype diversity towards a less oligoclonal state. This receptor diversification supports further investigation of CDNPs in autoimmune disease models, where their broad protein composition could complement antigen-specific strategies, such as OAT, by promoting tolerance through a polyclonal balance.

4.4. Concluding remarks, limitations, and future directions

This thesis showcases two related approaches to immune modulation: one targeting specific antigens and the other independent of antigen specificity, both focusing on modifying TCRR to induce tolerance. Pretreatment with OAT in the experimental EBA model, which completely prevented the disease, caused significant changes in the Tfh repertoire. These included greater

clonal diversity, a decrease in the dominance of expanded clones, and the emergence of new sequence features. These changes were also reflected in node-specific transcriptomic shifts, especially a shift in Ingln programs toward regulatory and metabolic pathways. Such alterations support the prevention of autoantibody-driven disease, highlighting the promise of antigen-specific immune deviation as a targeted tolerance approach.

This thesis also describes CDNPs as immune modulators that function independently of antigens. CDNPs are characterized as multi-epitopic protein aggregates approximately 150 nm in size, consistently containing Annexin A5 as a signature component, alongside various other proteins. Their protein yield is optimized through culture modifications, and endotoxin levels are reduced below biologically active thresholds. Functionally, CDNPs slightly decrease IL-6 secretion from macrophages stimulated via TLR2/1 and expand TCRβ repertoires within splenic TCZs in each test model, reducing clonal dominance within a spleen while preserving overall diversity. Transcriptional analysis shows increased *Tcrb* expression, indicating greater T-cell presence, and upregulation of *Gata3*, suggesting a Th2 bias. Overall, these results demonstrate that CDNPs act as broad-spectrum modulators, reprogramming both innate and adaptive immune responses without depending on specific antigen recognition. This thesis suggests two complementary translational strategies. OAT demonstrates how tolerogenic vaccination can be used in autoimmune diseases with known antigens to specifically reshape immune repertoires. In contrast, CDNPs offer a multi-epitopic approach that could broaden the T-cell repertoire in patients with unknown or diverse autoantigens, reducing clonal dominance and autoreactivity.

Several considerations are important. OAT was studied in experimental autoimmunity, while CDNPs were examined under steady-state conditions. This difference highlights their complementary roles: OAT exhibits antigen-specific tolerance and promotes modulation of the multiepitopic repertoire. Future work should include testing CDNPs in autoimmune models,

such as EBA, to determine if their broadening effects provide protection. Although OAT caused repertoire changes, its antigen specificity was not definitively validated using tetramers, database matching, or clustering tools. In particular, the use of $OVA_{323-339}$ would allow direct identification and sequencing of OVA-specific $CD4^+$ T cells, thereby providing definitive evidence of whether OAT-induced repertoire changes reflect true antigen-driven convergence (Pagán et al., 2013). Such an approach, when combined with complementary strategies such as database matching (e.g., VDJdb, McPAS-TCR) and motif clustering algorithms (e.g., GLIPH2, TCRdist), would allow a more rigorous assessment of antigen specificity and the extent of clonal convergence (Musvosvi et al., 2023). Employing these methods in future research will clarify whether OAT leads to true antigen-specific convergence or broader clonal shifts. The study did not utilize single-cell techniques, which could have provided a more detailed understanding of repertoire changes and functional states. Combining single-cell transcriptomics and TCR sequencing will enhance understanding of tolerance mechanisms. The mechanisms behind these effects were not directly explored. For OAT, it's uncertain whether metabolic shifts or stromal and dendritic cell changes drive the results. Further investigation is needed. For CDNPs, proteomic analysis was limited; comprehensive profiling and recombinant protein studies could clarify whether their effects are due to multi-epitopic content or specific proteins. Transcriptional analysis was also restricted; expanding this with RNA-seq and cytokine profiling will offer a fuller picture of immune responses. Overall, future directions include testing CDNPs in autoimmune models, validating OAT specificity with advanced tools, employing single-cell approaches, and expanding biochemical and transcriptional analyses. These steps will build on the foundation here and support the main conclusion that reshaping T-cell receptors, either by targeted or broad mechanisms, is a powerful way to restore immune tolerance.

It is also possible that CDNPs imitate damage-associated molecular patterns (DAMPs) or resolution-associated molecular patterns (RAMPs), since they are all made up of complex protein mixtures with overlapping components. Therefore, CDNPs might serve as multi-epitopic nanoparticles and also act as pattern-like signals that modulate immune responses. To explore this hypothesis, future research should compare the proteomic profiles of CDNPs with known DAMPs and RAMPs, and evaluate their activity in functional assays that assess typical alarmin or resolution responses, such as cytokine production, immune cell recruitment, or the resolution of inflammation *in vivo*.

This thesis shows that immune tolerance can be attained by adjusting the TCRR, either through antigen-specific methods or broad, multiepitopic reprogramming. This dual strategy enhances our understanding of immune control and opens the door for therapies that go beyond broad immunosuppression, focusing on precise and lasting restoration of immune balance in autoantibody-related diseases.

References

Åberg, C., Piattelli, V., Montizaan, D., & Salvati, A. (2021). Sources of variability in nanoparticle uptake by cells. *Nanoscale*, *13*(41), 17530-17546. https://doi.org/10.1039/d1nr04690j

Aliprantis, A. O., Yang, R. B., Mark, M. R., Suggett, S., Devaux, B., Radolf, J. D., Klimpel, G. R., Godowski, P., & Zychlinsky, A. (1999). Cell activation and apoptosis by bacterial lipoproteins through toll-like receptor-2. *Science*, *285*(5428), 736-739. https://doi.org/10.1126/science.285.5428.736

Allen, C. D., Okada, T., & Cyster, J. G. (2007). Germinal-center organization and cellular dynamics. *Immunity*, *27*(2), 190-202.

Allen, S., Turner, S. J., Bourges, D., Gleeson, P. A., & van Driel, I. R. (2011). Shaping the T-cell repertoire in the periphery. *Immunol Cell Biol*, *89*(1), 60-69. https://doi.org/10.1038/icb.2010.133

Andreu, N., Phelan, J., de Sessions, P. F., Cliff, J. M., Clark, T. G., & Hibberd, M. L. (2017). Primary macrophages and J774 cells respond differently to infection with Mycobacterium tuberculosis. *Sci Rep*, *7*, 42225. https://doi.org/10.1038/srep42225

AWATE, S., Babiuk, L. A., & Mutwiri, G. (2013). Mechanisms of Action of Adjuvants [Review]. *Frontiers in Immunology*, *Volume 4 - 2013*. https://doi.org/10.3389/fimmu.2013.00114

Bach, J. F. (2020). Revisiting the Hygiene Hypothesis in the Context of Autoimmunity. *Front Immunol*, *11*, 615192. https://doi.org/10.3389/fimmu.2020.615192

Bahreini, F., Niebuhr, M., Belde, J., Bieber, K., Westermann, J., & Kalies, K. (2022). Protocol to Induce Follicular T Helper Cells, Germinal Centers, and Skin Lesions in Mouse Models for Skin Blistering Diseases. *Bio-protocol*, *12*(10), e4414-e4414.

Bahreini, F., Niebuhr, M., Belde, J., Westermann, J., & Kalies, K. (2022). Protocol to isolate germinal centers by laser microdissection. *Bio-protocol*, *12*(11), e4431-e4431.

Baumjohann, D., Preite, S., Reboldi, A., Ronchi, F., Ansel, K. M., Lanzavecchia, A., & Sallusto, F. (2013). Persistent antigen and germinal center B cells sustain T follicular helper cell responses and phenotype. *Immunity*, *38*(3), 596-605. https://doi.org/10.1016/j.immuni.2012.11.020

Bieber, K., Witte, M., Sun, S., Hundt, J. E., Kalies, K., Dräger, S., Kasprick, A., Twelkmeyer, T., Manz, R. A., & König, P. (2016). T cells mediate autoantibody-induced cutaneous inflammation and blistering in epidermolysis bullosa acquisita. *Scientific reports*, *6*(1), 38357.

Blanco, P., Ueno, H., & Schmitt, N. (2016). T follicular helper (Tfh) cells in lupus: Activation and involvement in SLE pathogenesis. *Eur J Immunol*, *46*(2), 281-290. https://doi.org/10.1002/eji.201545760

Bolotin, D. A., Poslavsky, S., Davydov, A. N., Frenkel, F. E., Fanchi, L., Zolotareva, O. I., Hemmers, S., Putintseva, E. V., Obraztsova, A. S., & Shugay, M. (2017). Antigen receptor repertoire profiling from RNA-seq data. *Nature biotechnology*, *35*(10), 908-911.

Bolotin, D. A., Poslavsky, S., Mitrophanov, I., Shugay, M., Mamedov, I. Z., Putintseva, E. V., & Chudakov, D. M. (2015). MiXCR: software for comprehensive adaptive immunity profiling. *Nature methods*, *12*(5), 380-381.

Braams, M., Pike-Overzet, K., & Staal, F. J. T. (2023). The recombinase activating genes: architects of immune diversity during lymphocyte development [Review]. *Frontiers in Immunology*, *Volume 14 - 2023*. https://doi.org/10.3389/fimmu.2023.1210818

Chiffelle, J., Genolet, R., Perez, M. A., Coukos, G., Zoete, V., & Harari, A. (2020). T-cell repertoire analysis and metrics of diversity and clonality. *Curr Opin Biotechnol*, *65*, 284-295. https://doi.org/10.1016/j.copbio.2020.07.010

Christodoulou, M., Moysidou, E., Lioulios, G., Stai, S., Lazarou, C., Xochelli, A., Fylaktou, A., & Stangou, M. (2025). T-Follicular Helper Cells and Their Role in Autoimmune Diseases. *Life (Basel)*, *15*(4). https://doi.org/10.3390/life15040666

Correction to "Minimal information for studies of extracellular vesicles (MISEV2023): From basic to advanced approaches". (2024). *J Extracell Vesicles*, *13*(5), e12451. https://doi.org/10.1002/jev2.12451

Croce, G., Bobisse, S., Moreno, D. L., Schmidt, J., Guillame, P., Harari, A., & Gfeller, D. (2024). Deep learning predictions of TCR-epitope interactions reveal epitope-specific chains in dual alpha T cells. *Nat Commun*, *15*(1), 3211. https://doi.org/10.1038/s41467-024-47461-8

Crotty, S. (2014). T follicular helper cell differentiation, function, and roles in disease. *Immunity*, *41*(4), 529-542.

Crotty, S. (2019). T follicular helper cell biology: a decade of discovery and diseases. *Immunity*, *50*(5), 1132-1148.

D'agostino, R., & Pearson, E. S. (1973). Tests for departure from normality. Empirical results for the distributions of b 2 andv b. *Biometrika*, *60*(3), 613-622.

Daniel, L., Bhattacharyya, N. D., Counoupas, C., Cai, Y., Chen, X., Triccas, J. A., Britton, W. J., & Feng, C. G. (2022). Stromal structure remodeling by B lymphocytes limits T cell activation in lymph nodes of Mycobacterium tuberculosis–infected mice. *The Journal of Clinical Investigation*, *132*(21).

Dilsiz, N. (2024). A comprehensive review on recent advances in exosome isolation and characterization: Toward clinical applications. *Transl Oncol*, *50*, 102121. https://doi.org/10.1016/j.tranon.2024.102121

Ellis, R. J. (2001). Macromolecular crowding: obvious but underappreciated. *Trends Biochem Sci*, *26*(10), 597-604. https://doi.org/10.1016/s0968-0004(01)01938-7

Emerson, R. O., DeWitt, W. S., Vignali, M., Gravley, J., Hu, J. K., Osborne, E. J., Desmarais, C., Klinger, M., Carlson, C. S., Hansen, J. A., Rieder, M., & Robins, H. S. (2017). Immunosequencing identifies signatures of cytomegalovirus exposure history and HLA-mediated effects on the T cell repertoire. *Nat Genet*, *49*(5), 659-665. https://doi.org/10.1038/ng.3822

Fan, J., Jin, S., Gilmartin, L., Toth, I., Hussein, W. M., & Stephenson, R. J. (2022). Advances in Infectious Disease Vaccine Adjuvants. *Vaccines (Basel)*, *10*(7). https://doi.org/10.3390/vaccines10071120

Fang, H., Li, Q., & Wang, G. (2020). The role of T cells in pemphigus vulgaris and bullous pemphigoid. *Autoimmun Rev*, *19*(11), 102661. https://doi.org/10.1016/j.autrev.2020.102661

Farmanbar, A., Kneller, R., & Firouzi, S. (2019). RNA sequencing identifies clonal structure of T-cell repertoires in patients with adult T-cell leukemia/lymphoma. *NPJ Genom Med*, *4*, 10. https://doi.org/10.1038/s41525-019-0084-9

Fedotov, S., & Alexandrov, D. V. (2024). Model for random internalization of nanoparticles by cells. *Phys Rev E*, *110*(4-1), 044101. https://doi.org/10.1103/PhysRevE.110.044101

Fu, J., Khosravi-Maharlooei, M., & Sykes, M. (2021). High Throughput Human T Cell Receptor Sequencing: A New Window Into Repertoire Establishment and Alloreactivity. *Front Immunol*, *12*, 777756. https://doi.org/10.3389/fimmu.2021.777756

Fugmann, S. D. (2001). RAG1 and RAG2 in V(D)J recombination and transposition. *Immunol Res*, *23*(1), 23-39. https://doi.org/10.1385/ir:23:1:23

Gatto, D., & Brink, R. (2010). The germinal center reaction. *Journal of Allergy and Clinical Immunology*, *126*(5), 898-907.

Giltiay, N. V., Chappell, C. P., & Clark, E. A. (2012). B-cell selection and the development of autoantibodies. *Arthritis research & therapy*, *14*(Suppl 4), S1.

Greiff, V., Miho, E., Menzel, U., & Reddy, S. T. (2015). Bioinformatic and Statistical Analysis of Adaptive Immune Repertoires. *Trends Immunol*, *36*(11), 738-749. https://doi.org/10.1016/j.it.2015.09.006

Gross, N., Marketon, J., Mousavi, S., Kalies, K., Ludwig, R. J., & Bieber, K. (2024). Inhibition of interferon gamma impairs induction of experimental epidermolysis bullosa acquisita. *Frontiers in Immunology*, *15*, 1343299.

Hammers, C. M., Bieber, K., Kalies, K., Banczyk, D., Ellebrecht, C. T., Ibrahim, S. M., Zillikens, D., Ludwig, R. J., & Westermann, J. (2011). Complement-fixing anti-type VII collagen antibodies are induced in Th1-polarized lymph nodes of epidermolysis bullosa acquisita-susceptible mice. *The Journal of Immunology*, *187*(10), 5043-5050.

Hampe, C. S. (2012). B cells in autoimmune diseases. *Scientifica*, *2012*(1), 215308.

Han, J., Swan, D. C., Smith, S. J., Lum, S. H., Sefers, S. E., Unger, E. R., & Tang, Y.-W. (2006). Simultaneous amplification and identification of 25 human papillomavirus types with Templex technology. *Journal of clinical microbiology*, *44*(11), 4157-4162.

Harrell, M. I., Iritani, B. M., & Ruddell, A. (2008). Lymph node mapping in the mouse. *J Immunol Methods*, *332*(1-2), 170-174. https://doi.org/10.1016/j.jim.2007.11.012

Heather, J. M., Ismail, M., Oakes, T., & Chain, B. (2018). High-throughput sequencing of the T-cell receptor repertoire: pitfalls and opportunities. *Brief Bioinform*, *19*(4), 554-565. https://doi.org/10.1093/bib/bbw138

Hennerici, T., Pollmann, R., Schmidt, T., Seipelt, M., Tackenberg, B., Möbs, C., Ghoreschi, K., Hertl, M., & Eming, R. (2016). Increased Frequency of T Follicular Helper Cells and Elevated Interleukin-27 Plasma Levels in Patients with Pemphigus. *PLoS One*, *11*(2), e0148919. https://doi.org/10.1371/journal.pone.0148919

Herb, M., Schatz, V., Hadrian, K., Hos, D., Holoborodko, B., Jantsch, J., & Brigo, N. (2024). Macrophage variants in laboratory research: most are well done, but some are RAW [Review]. *Frontiers in Cellular and Infection Microbiology*, *Volume 14 - 2024*. https://doi.org/10.3389/fcimb.2024.1457323

Hogquist, K. A., Baldwin, T. A., & Jameson, S. C. (2005). Central tolerance: learning self-control in the thymus. *Nature Reviews Immunology*, *5*(10), 772-782.

Holstein, J., Solimani, F., Baum, C., Meier, K., Pollmann, R., Didona, D., Tekath, T., Dugas, M., Casadei, N., Hudemann, C., Polakova, A., Matthes, J., Schäfer, I., Yazdi, A. S., Eming, R., Hertl, M., Pfützner, W., Ghoreschi, K., & Möbs, C. (2021). Immunophenotyping in pemphigus reveals a T(H)17/T(FH)17 cell-dominated immune response promoting desmoglein1/3-specific autoantibody production. *J Allergy Clin Immunol*, *147*(6), 2358-2369. https://doi.org/10.1016/j.jaci.2020.11.008

Horn, H. S. (1966). Measurement of "overlap" in comparative ecological studies. *The American Naturalist*, *100*(914), 419-424. https://doi.org/https://doi.org/10.1086/282436

Horn, L. A., Fousek, K., Hamilton, D. H., Hodge, J. W., Zebala, J. A., Maeda, D. Y., Schlom, J., & Palena, C. (2021). Vaccine Increases the Diversity and Activation of Intratumoral T Cells in the Context of Combination Immunotherapy. *Cancers (Basel)*, *13*(5). https://doi.org/10.3390/cancers13050968

Hou, X., Wei, W., Zhang, J., Liu, Z., Wang, G., Yang, X., & Dai, Y. (2023). Characterisation of T and B cell receptor repertoire in patients with systemic lupus erythematosus. *Clin Exp Rheumatol*, *41*(11), 2216-2223. https://doi.org/10.55563/clinexprheumatol/1rjr4s

Huang, Y., Chen, Z., Wang, H., Ba, X., Shen, P., Lin, W., Wang, Y., Qin, K., Huang, Y., & Tu, S. (2020). Follicular regulatory T cells: a novel target for immunotherapy? *Clin Transl Immunology*, *9*(2), e1106. https://doi.org/10.1002/cti2.1106

Iwata, H., Bieber, K., Tiburzy, B., Chrobok, N., Kalies, K., Shimizu, A., Leineweber, S., Ishiko, A., Vorobyev, A., & Zillikens, D. (2013). B cells, dendritic cells, and macrophages are required to induce an autoreactive CD4 helper T cell response in experimental epidermolysis bullosa acquisita. *The Journal of Immunology*, *191*(6), 2978-2988.

Kang, B. H., Min, H. S., Lee, Y. J., Choi, B., Kim, E. J., Lee, J., Kim, J. R., Cho, K. H., Kim, T. J., Jung, K. C., & Park, S. H. (2015). Analyses of the TCR repertoire of MHC class II-restricted innate $CD4^+$ T cells. *Exp Mol Med*, *47*(3), e154. https://doi.org/10.1038/emm.2015.7

Kent, S. C., Chen, Y., Bregoli, L., Clemmings, S. M., Kenyon, N. S., Ricordi, C., Hering, B. J., & Hafler, D. A. (2005). Expanded T cells from pancreatic lymph nodes of type 1 diabetic subjects recognize an insulin epitope. *Nature*, *435*(7039), 224-228. https://doi.org/10.1038/nature03625

Kim, S., Park, G.-Y., Park, J. S., Park, J., Hong, H., & Lee, Y. (2021). Regulation of positive and negative selection and TCR signaling during thymic T cell development by capicua. *Elife*, *10*, e71769. https://doi.org/10.7554/eLife.71769

Kim, S. J., Lee, K., & Diamond, B. (2018). Follicular Helper T Cells in Systemic Lupus Erythematosus [Review]. *Frontiers in Immunology*, *Volume 9 - 2018*. https://doi.org/10.3389/fimmu.2018.01793

Kim, W., Ly, N. K., He, Y., Li, Y., Yuan, Z., & Yeo, Y. (2023). Protein corona: Friend or foe? Co-opting serum proteins for nanoparticle delivery. *Adv Drug Deliv Rev*, *192*, 114635. https://doi.org/10.1016/j.addr.2022.114635

Kim, Y.-J., Choi, J., & Choi, Y. S. (2024). Transcriptional regulation of Tfh dynamics and the formation of immunological synapses. *Experimental & Molecular Medicine*, *56*(6), 1365-1372.

Klein, L., Kyewski, B., Allen, P. M., & Hogquist, K. A. (2014). Positive and negative selection of the T cell repertoire: what thymocytes see (and don't see). *Nature Reviews Immunology*, *14*(6), 377-391.

Koga, H., Prost-Squarcioni, C., Iwata, H., Jonkman, M. F., Ludwig, R. J., & Bieber, K. (2019). Epidermolysis bullosa acquisita: the 2019 update. *Frontiers in medicine*, *5*, 362.

Köhling, V.-L. (2022). *Immunomodulatory Effects of Cell-Derived Nanoparticles (CDNPs) on Macrophage Cytokine Responses* [Master's thesis, University of Lübeck]. Lübeck, Germany. https://www.zhb.uni-luebeck.de/epubs/ediss2576.pdf

Kool, M., Soullié, T., van Nimwegen, M., Willart, M. A., Muskens, F., Jung, S., Hoogsteden, H. C., Hammad, H., & Lambrecht, B. N. (2008). Alum adjuvant boosts adaptive immunity by inducing uric acid and activating inflammatory dendritic cells. *J Exp Med*, *205*(4), 869-882. https://doi.org/10.1084/jem.20071087

Kovacs, B., Tillmann, J., Freund, L.-C., Nimmerjahn, F., Sadik, C. D., Bieber, K., Ludwig, R. J., Karsten, C. M., & Köhl, J. (2020). Fcγ receptor IIB controls skin inflammation in an active model of epidermolysis bullosa acquisita. *Frontiers in Immunology*, *10*, 3012.

Kridin, K., Kneiber, D., Kowalski, E. H., Valdebran, M., & Amber, K. T. (2019). Epidermolysis bullosa acquisita: A comprehensive review. *Autoimmunity Reviews*, *18*(8), 786-795.

Kunz, N., Hauenschild, E., Maass, S., Kalies, K. U., Klinger, M., Barra, M., Hecht, L., Helbig, F., Soellner, S., & Caldwell, C. C. (2017). Nanoparticles prepared from porcine cells support the healing of cutaneous inflammation in mice and wound re-epithelialization in human skin. *Experimental dermatology*, *26*(12), 1199-1206.

Kunz, N., Xia, B. T., Kalies, K.-U., Klinger, M., Gemoll, T., Habermann, J. K., Whitacre, B. E., Seitz, A. P., Kalies, K., & Caldwell, C. C. (2017). Cell-derived nanoparticles are endogenous modulators of sepsis with therapeutic potential. *Shock*, *48*(3), 346-354.

Laydon, D. J., Bangham, C. R., & Asquith, B. (2015). Estimating T-cell repertoire diversity: limitations of classical estimators and a new approach. *Philos Trans R Soc Lond B Biol Sci*, *370*(1675). https://doi.org/10.1098/rstb.2014.0291

Lee, A. Y., Kim, T., & Kim, J. H. (2023). Understanding CD4+ T cells in autoimmune bullous diseases. *Frontiers in Immunology*, *14*, 1161927.

Li, J., Xue, H., Ma, Q., He, X., Ma, L., Shi, B., Sun, S., & Yao, X. (2020). Heterogeneity of CD4(+)CD25(+)Foxp3(+)Treg TCR β CDR3 Repertoire Based on the Differences of Symbiotic Microorganisms in the Gut of Mice. *Front Cell Dev Biol*, *8*, 576445. https://doi.org/10.3389/fcell.2020.576445

Li, L., Zhang, X., Wang, X., Kim, S. W., Herndon, J. M., Becker-Hapak, M. K., Carreno, B. M., Myers, N. B., Sturmoski, M. A., McLellan, M. D., Miller, C. A., Johanns, T. M., Tan, B. R., Dunn, G. P., Fleming, T. P., Hansen, T. H., Goedegebuure, S. P., & Gillanders, W. E. (2021). Optimized polyepitope neoantigen DNA vaccines elicit neoantigen-specific immune responses in preclinical models and in clinical translation. *Genome Med*, *13*(1), 56. https://doi.org/10.1186/s13073-021-00872-4

Li, N., Yuan, J., Tian, W., Meng, L., & Liu, Y. (2020). T-cell receptor repertoire analysis for the diagnosis and treatment of solid tumor: A methodology and clinical applications. *Cancer Commun (Lond)*, *40*(10), 473-483. https://doi.org/10.1002/cac2.12074

Li, Q., Liu, Z., Dang, E., Jin, L., He, Z., Yang, L., Shi, X., & Wang, G. (2013). Follicular helper T Cells (Tfh) and IL-21 involvement in the pathogenesis of bullous pemphigoid. *PLoS One*, *8*(7), e68145.

Liu, Q., Yang, S., Tan, Y., Feng, W., Wang, Q., Qiao, J., Yang, B., Wang, C., Tao, J., Wang, H., & Cui, L. (2024). Bulk T-cell receptor sequencing confirms clonality in obstetric antiphospholipid syndrome and may as a potential biomarker. *Autoimmunity*, *57*(1), 2360490. https://doi.org/10.1080/08916934.2024.2360490

Lu, J., Van Laethem, F., Bhattacharya, A., Craveiro, M., Saba, I., Chu, J., Love, N. C., Tikhonova, A., Radaev, S., Sun, X., Ko, A., Arnon, T., Shifrut, E., Friedman, N., Weng, N. P., Singer, A., & Sun, P. D. (2019). Molecular constraints on CDR3 for thymic selection of MHC-restricted TCRs from a random pre-selection repertoire. *Nat Commun*, *10*(1), 1019. https://doi.org/10.1038/s41467-019-08906-7

Ludwig, R. J. (2013). Clinical presentation, pathogenesis, diagnosis, and treatment of epidermolysis bullosa acquisita. *International Scholarly Research Notices*, *2013*(1), 812029.

Magurran, A. E. (2013). *Ecological Diversity and Its Measurement*. Springer Science & Business Media. https://books.google.de/books?hl=en&lr=&id=X7b7CAAAQBAJ&oi=fnd&pg=PP7&dq=ecological+diversity+and+its+measurement.&ots=dateSmFtDk&sig=oJgJF-VZc_xj3oLjBqeP4xyE6hE&redir_esc=y#v=onepage&q=ecological%20diversity%20and%20its%20measurement.&f=false

Mahdy, A. K. H., Lokes, E., Schöpfel, V., Kriukova, V., Britanova, O. V., Steiert, T. A., Franke, A., & ElAbd, H. (2024). Bulk T cell repertoire sequencing (TCR-Seq) is a powerful technology for understanding inflammation-mediated diseases. *J Autoimmun*, *149*, 103337. https://doi.org/10.1016/j.jaut.2024.103337

Mark, M., Reich-Zeliger, S., Greenstein, E., Reshef, D., Madi, A., Chain, B., & Friedman, N. (2022). A hierarchy of selection pressures determines the organization of the T cell receptor repertoire [Original Research]. *Frontiers in Immunology*, *Volume 13 - 2022*. https://doi.org/10.3389/fimmu.2022.939394

Martin, C. A., & Dorf, M. E. (1990). Interleukin-6 production by murine macrophage cell lines P388D1 and J774A.1: stimulation requirements and kinetics. *Cell Immunol*, *128*(2), 555-568. https://doi.org/10.1016/0008-8749(90)90048-v

McKee, A. S., & Marrack, P. (2017). Old and new adjuvants [Review]. *Current Opinion in Immunology*, *47*, 44-51. https://doi.org/10.1016/j.coi.2017.06.005

Meinhardt, M., Tune, C., Schierloh, L. K., Schampel, A., Pagel, R., & Westermann, J. (2022). The splenic T cell receptor repertoire during an immune response against a complex antigen: Expanding private clones accumulate in the high and low copy number region. *PLoS One*, *17*(8), e0273264. https://doi.org/10.1371/journal.pone.0273264

Merkenschlager, J., Berz, R. M., Ramos, V., Uhlig, M., MacLean, A. J., Nowosad, C. R., Oliveira, T. Y., & Nussenzweig, M. C. (2023). Continually recruited naïve T cells contribute to the follicular helper and regulatory T cell pools in germinal centers. *Nat Commun*, *14*(1), 6944. https://doi.org/10.1038/s41467-023-41880-9

Merkenschlager, J., Finkin, S., Ramos, V., Kraft, J., Cipolla, M., Nowosad, C. R., Hartweger, H., Zhang, W., Olinares, P. D. B., Gazumyan, A., Oliveira, T. Y., Chait, B. T., & Nussenzweig, M. C. (2021). Dynamic regulation of T(FH) selection during the germinal centre reaction. *Nature*, *591*(7850), 458-463. https://doi.org/10.1038/s41586-021-03187-x

Migalska, M., Sebastian, A., & Radwan, J. (2018). Profiling of the TCRβ repertoire in non-model species using high-throughput sequencing. *Sci Rep*, *8*(1), 11613. https://doi.org/10.1038/s41598-018-30037-0

Miles, B., & Connick, E. (2018). Control of the Germinal Center by Follicular Regulatory T Cells During Infection [Review]. *Frontiers in Immunology*, *Volume 9 - 2018*. https://doi.org/10.3389/fimmu.2018.02704

Mitchell, A. M., & Michels, A. W. (2020). T cell receptor sequencing in autoimmunity. *J Life Sci (Westlake Village)*, *2*(4), 38-58. https://doi.org/10.36069/jols/20201203

Moore, E., Huang, M. W., Jain, S., Chalmers, S. A., Macian, F., & Putterman, C. (2020). The T Cell Receptor Repertoire in Neuropsychiatric Systemic Lupus Erythematosus. *Front Immunol*, *11*, 1476. https://doi.org/10.3389/fimmu.2020.01476

Mortazavi, B., Molaei, A., & Fard, N. A. (2024). Multi-epitopevaccines, from design to expression; an in silico approach. *Human Immunology*, *85*(3), 110804. https://doi.org/https://doi.org/10.1016/j.humimm.2024.110804

Musvosvi, M., Huang, H., Wang, C., Xia, Q., Rozot, V., Krishnan, A., Acs, P., Cheruku, A., Obermoser, G., Leslie, A., Behar, S. M., Hanekom, W. A., Bilek, N., Fisher, M., Kaufmann, S. H. E., Walzl, G., Hatherill, M., Davis, M. M., & Scriba, T. J. (2023). T cell receptor repertoires associated with control and disease progression following Mycobacterium tuberculosis infection. *Nat Med*, *29*(1), 258-269. https://doi.org/10.1038/s41591-022-02110-9

Niebuhr, M., Bahreini, F., Fähnrich, A., Bomholt, C., Bieber, K., Schmidt, E., Ibrahim, S., Hammers, C. M., & Kalies, K. (2022). Analysis of T cell repertoires of CD45RO CD4 T cells in cohorts of patients with bullous pemphigoid: A pilot study. *Frontiers in Immunology*, *13*, 1006941.

Niebuhr, M., Belde, J., Fähnrich, A., Serge, A., Irla, M., Ellebrecht, C. T., Hammers, C. M., Bieber, K., Westermann, J., & Kalies, K. (2021). Receptor repertoires of murine follicular T helper cells reveal a high clonal overlap in separate lymph nodes in autoimmunity. *Elife*, *10*, e70053.

Niebuhr, M., Bieber, K., Banczyk, D., Maass, S., Klein, S., Becker, M., Ludwig, R., Zillikens, D., Westermann, J., & Kalies, K. (2020). Epidermal damage induces Th1 polarization and defines the site of inflammation in murine epidermolysis bullosa acquisita. *Journal of Investigative Dermatology*, *140*(9), 1713-1722. e1719.

Niebuhr, M. A. (2019). *Assessment of the T-lymphocyte Receptor Repertoire in the Experimental Model of Epidermolysis Bullosa Acquisita* [Dissertation, University of Lübeck]. Lübeck, Germany.

Oakes, T., Heather, J. M., Best, K., Byng-Maddick, R., Husovsky, C., Ismail, M., Joshi, K., Maxwell, G., Noursadeghi, M., Riddell, N., Ruehl, T., Turner, C. T., Uddin, I., & Chain, B. (2017). Quantitative Characterization of the T Cell Receptor Repertoire of Naïve and Memory Subsets Using an Integrated Experimental and Computational Pipeline Which Is Robust, Economical, and Versatile [Methods]. *Frontiers in Immunology*, *Volume 8 - 2017*. https://doi.org/10.3389/fimmu.2017.01267

Oksenberg, J. R., Stuart, S., Begovich, A. B., Bell, R. B., Erlich, H. A., Steinman, L., & Bernard, C. C. (1990). Limited heterogeneity of rearranged T-cell receptor V alpha transcripts in brains of multiple sclerosis patients. *Nature*, *345*(6273), 344-346. https://doi.org/10.1038/345344a0

Osteikoetxea, X., Sódar, B., Németh, A., Szabó-Taylor, K., Pálóczi, K., Vukman, K. V., Tamási, V., Balogh, A., Kittel, Á., Pállinger, É., & Buzás, E. I. (2015). Differential detergent sensitivity of extracellular vesicle subpopulations. *Org Biomol Chem*, *13*(38), 9775-9782. https://doi.org/10.1039/c5ob01451d

Pagán, A. J., Peters, N. C., Debrabant, A., Ribeiro-Gomes, F., Pepper, M., Karp, C. L., Jenkins, M. K., & Sacks, D. L. (2013). Tracking antigen-specific CD4+ T cells throughout the course of chronic Leishmania major infection in resistant mice. *Eur J Immunol*, *43*(2), 427-438. https://doi.org/10.1002/eji.201242715

Parish, I. A., & Heath, W. R. (2008). Too dangerous to ignore: self-tolerance and the control of ignorant autoreactive T cells. *Immunol Cell Biol*, *86*(2), 146-152. https://doi.org/10.1038/sj.icb.7100161

Pérals, C., Le Jan, S., Muller, C., Le Naour, R., Bernard, P., Viguier, M., & Fazilleau, N. (2025). Polarization of circulating follicular helper T cells correlates with bullous pemphigoid severity. *British Journal of Dermatology*, *192*(2), 283-292.

Petersone, L., & Walker, L. S. (2024). T-cell help in the germinal center: homing in on the role of IL-21. *International Immunology*, *36*(3), 89-98.

Pisetsky, D. S. (2024). Unique interplay between antinuclear antibodies and nuclear molecules in the pathogenesis of systemic lupus erythematosus. *Arthritis & Rheumatology*, *76*(9), 1334-1343.

Playoust, E., Remark, R., Vivier, E., & Milpied, P. (2023). Germinal center-dependent and-independent immune responses of tumor-infiltrating B cells in human cancers. *Cellular & Molecular Immunology*, *20*(9), 1040-1050.

Podojil, J. R., & Miller, S. D. (2009). Molecular mechanisms of T-cell receptor and costimulatory molecule ligation/blockade in autoimmune disease therapy. *Immunological reviews*, *229*(1), 337-355.

Raby, A. C., Holst, B., Le Bouder, E., Diaz, C., Ferran, E., Conraux, L., Guillemot, J. C., Coles, B., Kift-Morgan, A., Colmont, C. S., Szakmany, T., Ferrara, P., Hall, J. E., Topley, N., & Labéta, M. O. (2013). Targeting the TLR co-receptor CD14 with TLR2-derived peptides modulates immune responses to pathogens. *Sci Transl Med*, *5*(185), 185ra164. https://doi.org/10.1126/scitranslmed.3005544

Ralph, P., & Nakoinz, I. (1975). Phagocytosis and cytolysis by a macrophage tumour and its cloned cell line. *Nature*, *257*(5525), 393-394. https://doi.org/10.1038/257393a0

Raudszus, L., Bahreini, F., Allan, S., Kalies, K.-U., Caldwell, C. C., & Kalies, K. (2025). Nanoparticles containing intracellular proteins modulate neutrophil functional and phenotypic heterogeneity. *Frontiers in Immunology*, *15*, 1494400.

Ray, J. P., Staron, M. M., Shyer, J. A., Ho, P. C., Marshall, H. D., Gray, S. M., Laidlaw, B. J., Araki, K., Ahmed, R., Kaech, S. M., & Craft, J. (2015). The Interleukin-2-mTORc1 Kinase Axis Defines the Signaling, Differentiation, and Metabolism of T Helper 1 and Follicular B Helper T Cells. *Immunity*, *43*(4), 690-702. https://doi.org/10.1016/j.immuni.2015.08.017

Rosati, E., Dowds, C. M., Liaskou, E., Henriksen, E. K. K., Karlsen, T. H., & Franke, A. (2017). Overview of methodologies for T-cell receptor repertoire analysis. *BMC Biotechnol*, *17*(1), 61. https://doi.org/10.1186/s12896-017-0379-9

Sakaguchi, S., Yamaguchi, T., Nomura, T., & Ono, M. (2008). Regulatory T cells and immune tolerance. *cell*, *133*(5), 775-787.

Schwartz, R. H. (2003). T cell anergy. *Annual review of immunology*, *21*(1), 305-334.

Seay, H. R., Yusko, E., Rothweiler, S. J., Zhang, L., Posgai, A. L., Campbell-Thompson, M., Vignali, M., Emerson, R. O., Kaddis, J. S., Ko, D., Nakayama, M., Smith, M. J., Cambier, J. C., Pugliese, A., Atkinson, M. A., Robins, H. S., & Brusko, T. M. (2016). Tissue distribution and clonal diversity of the T and B cell repertoire in type 1 diabetes. *JCI Insight*, *1*(20), e88242. https://doi.org/10.1172/jci.insight.88242

Seo, K., & Choi, J. K. (2025). Comprehensive Analysis of TCR and BCR Repertoires: Insights into Methodologies, Challenges, and Applications. *Genomics Inform*, *23*(1), 6. https://doi.org/10.1186/s44342-024-00034-z

Shi, Y., Zhang, H., & Miao, C. (2025). Metabolic reprogram and T cell differentiation in inflammation: current evidence and future perspectives. *Cell Death Discov*, *11*(1), 123. https://doi.org/10.1038/s41420-025-02403-1

Shirafkan, F., Hensel, L., & Rattay, K. (2024). Immune tolerance and the prevention of autoimmune diseases essentially depend on thymic tissue homeostasis. *Frontiers in Immunology*, *15*, 1339714.

Shlomchik, M. J., & Weisel, F. (2012). Germinal center selection and the development of memory B and plasma cells. *Immunol Rev*, *247*(1), 52-63. https://doi.org/10.1111/j.1600-065X.2012.01124.x

Simpson, E. H. (1949). Measurement of Diversity. *Nature*, *163*(4148), 688-688. https://doi.org/10.1038/163688a0

Smirnova, A. O., Miroshnichenkova, A. M., Olshanskaya, Y. V., Maschan, M. A., Lebedev, Y. B., Chudakov, D. M., Mamedov, I. Z., & Komkov, A. (2023). The use of non-functional clonotypes as a natural calibrator for quantitative bias correction in adaptive immune receptor repertoire profiling. *Elife*, *12*. https://doi.org/10.7554/eLife.69157

Solisch, P., Kalies, K. U., & Bergmann, S. (1999). *BK-RiV preparations for treatment of proliferative cellular disorders* EP 0 889 053 A2).

Song, W., & Craft, J. (2024). T Follicular Helper Cell Heterogeneity. *Annu Rev Immunol*, *42*(1), 127-152. https://doi.org/10.1146/annurev-immunol-090222-102834

Syeda, M. Z., Hong, T., Huang, C., Huang, W., & Mu, Q. (2024). B cell memory: from generation to reactivation: a multipronged defense wall against pathogens. *Cell Death Discovery*, *10*(1), 117.

Takeuchi, A., Ozawa, M., Kanda, Y., Kozai, M., Ohigashi, I., Kurosawa, Y., Rahman, M. A., Kawamura, T., Shichida, Y., & Umemoto, E. (2018). A distinct subset of fibroblastic stromal cells constitutes the cortex-medulla boundary subcompartment of the lymph node. *Frontiers in Immunology*, *9*, 2196.

Team, I. (2019). Immunarch: an R package for painless bioinformatics analysis of T-cell and B-cell immune repertoires. *Zenodo*, *10*, 5281.

Teodorowicz, M., Perdijk, O., Verhoek, I., Govers, C., Savelkoul, H. F., Tang, Y., Wichers, H., & Broersen, K. (2017). Optimized Triton X-114 assisted lipopolysaccharide (LPS) removal method reveals the immunomodulatory effect of food proteins. *PLoS One*, *12*(3), e0173778. https://doi.org/10.1371/journal.pone.0173778

Terhaar, H., Jiminez, V., Grant, E., Collins, C., Khass, M., & Yusuf, N. (2024). Immune Repertoires in Various Dermatologic and Autoimmune Diseases. *Genes*, *15*(12), 1591. https://www.mdpi.com/2073-4425/15/12/1591

Tešanović Perković, D., Bukvić Mokos, Z., & Marinović, B. (2023). Epidermolysis bullosa Acquisita—current and emerging treatments. *Journal of clinical medicine*, *12*(3), 1139.

Thapa, D. R., Tonikian, R., Sun, C., Liu, M., Dearth, A., Petri, M., Pepin, F., Emerson, R. O., & Ranger, A. (2015). Longitudinal analysis of peripheral blood T cell receptor diversity in patients with systemic lupus erythematosus by next-generation sequencing. *Arthritis Res Ther*, *17*(1), 132. https://doi.org/10.1186/s13075-015-0655-9

Tindemans, I., Serafini, N., Di Santo, James P., & Hendriks, Rudi W. (2014). GATA-3 Function in Innate and Adaptive Immunity. *Immunity*, *41*(2), 191-206. https://doi.org/https://doi.org/10.1016/j.immuni.2014.06.006

Tsiapalis, D., & Zeugolis, D. I. (2021). It is time to crowd your cell culture media - Physicochemical considerations with biological consequences. *Biomaterials*, *275*, 120943. https://doi.org/10.1016/j.biomaterials.2021.120943

Tukey, J. W. (1977). Exploratory data analysis. *Reading/Addison-Wesley*.

Tuong, Z. K., van der Merwe, R., Canete, P. F., & Roco, J. A. (2024). Computational estimation of clonal diversity in autoimmunity. *Immunol Cell Biol*, *102*(8), 692-701. https://doi.org/10.1111/imcb.12801

Turner, S. J., Doherty, P. C., McCluskey, J., & Rossjohn, J. (2006). Structural determinants of T-cell receptor bias in immunity. *Nat Rev Immunol*, *6*(12), 883-894. https://doi.org/10.1038/nri1977

Ujiie, H., & Shimizu, H. (2012). Evidence for pathogenicity of autoreactive T cells in autoimmune bullous diseases shown by animal disease models. *Experimental dermatology*, *21*(12), 901-905.

Upadhya, D., & Shetty, A. K. (2024). MISEV2023 provides an updated and key reference for researchers studying the basic biology and applications of extracellular vesicles. *Stem Cells Transl Med*, *13*(9), 848-850. https://doi.org/10.1093/stcltm/szae052

Van Laethem, F., Bhattacharya, A., Craveiro, M., Lu, J., Sun, P. D., & Singer, A. (2022). MHC-independent αβT cells: Lessons learned about thymic selection and MHC-restriction [Review]. *Frontiers in Immunology*, *Volume 13 - 2022*. https://doi.org/10.3389/fimmu.2022.953160

Venturi, V., Kedzierska, K., Tanaka, M. M., Turner, S. J., Doherty, P. C., & Davenport, M. P. (2008). Method for assessing the similarity between subsets of the T cell receptor repertoire. *J Immunol Methods*, *329*(1-2), 67-80. https://doi.org/10.1016/j.jim.2007.09.016

Vesin, B., Fert, I., Noirat, A., Authié, P., Ciret, S., Blanc, C., Vitrenko, Y., Charneau, P., Majlessi, L., & Anna, F. (2025). Optimized lentiviral backbone induces robust and diverse T cell immunity against neoantigens to counteract tumor heterogeneity. *npj Vaccines*, *10*(1), 143. https://doi.org/10.1038/s41541-025-01199-6

Victora, G. D., & Nussenzweig, M. C. (2012). Germinal centers. *Annual review of immunology*, *30*, 429-457. https://doi.org/10.1146/annurev-immunol-020711-075032

Vinuesa, C. G., Linterman, M. A., Yu, D., & MacLennan, I. C. (2016). Follicular helper T cells. *Annual review of immunology*, *34*(1), 335-368.

Vorobyev, A., Ludwig, R. J., & Schmidt, E. (2017). Clinical features and diagnosis of epidermolysis bullosa acquisita. *Expert review of clinical immunology*, *13*(2), 157-169.

Vujovic, M., Degn, K. F., Marin, F. I., Schaap-Johansen, A. L., Chain, B., Andresen, T. L., Kaplinsky, J., & Marcatili, P. (2020). T cell receptor sequence clustering and antigen specificity. *Comput Struct Biotechnol J*, *18*, 2166-2173. https://doi.org/10.1016/j.csbj.2020.06.041

Walker, L. S. (2022). The link between circulating follicular helper T cells and autoimmunity. *Nature Reviews Immunology*, *22*(9), 567-575.

Wang, C., Sanders, C. M., Yang, Q., Schroeder Jr, H. W., Wang, E., Babrzadeh, F., Gharizadeh, B., Myers, R. M., Hudson Jr, J. R., & Davis, R. W. (2010). High throughput sequencing reveals a complex pattern of dynamic interrelationships among human T cell subsets. *Proceedings of the National Academy of Sciences*, *107*(4), 1518-1523.

Wang, L., Zhang, P., Li, J., Lu, H., Peng, L., Ling, J., Zhang, X., Zeng, X., Zhao, Y., & Zhang, W. (2019). High-throughput sequencing of CD4(+) T cell repertoire reveals disease-specific signatures in IgG4-related disease. *Arthritis Res Ther*, *21*(1), 295. https://doi.org/10.1186/s13075-019-2069-6

Wang, Q., Zeng, H., Zhu, Y., Wang, M., Zhang, Y., Yang, X., Tang, H., Li, H., Chen, Y., Ma, C., Lan, C., Liu, B., Yang, W., Yu, X., & Zhang, Z. (2021). Dual UMIs and Dual Barcodes With Minimal PCR Amplification Removes Artifacts and Acquires Accurate Antibody Repertoire [Original Research]. *Frontiers in Immunology*, *Volume 12 - 2021*. https://doi.org/10.3389/fimmu.2021.778298

Welsh, J. A., Goberdhan, D. C. I., O'Driscoll, L., Buzas, E. I., Blenkiron, C., Bussolati, B., Cai, H., Di Vizio, D., Driedonks, T. A. P., Erdbrügger, U., Falcon-Perez, J. M., Fu, Q. L., Hill, A. F., Lenassi, M., Lim, S. K., Mahoney, M. G., Mohanty, S., Möller, A., Nieuwland, R., . . . Witwer, K. W. (2024). Minimal information for studies of extracellular vesicles (MISEV2023): From basic to advanced approaches. *J Extracell Vesicles*, *13*(2), e12404. https://doi.org/10.1002/jev2.12404

Wong, W. K., Leem, J., & Deane, C. M. (2019). Comparative Analysis of the CDR Loops of Antigen Receptors [Original Research]. *Frontiers in Immunology*, *Volume 10 - 2019*. https://doi.org/10.3389/fimmu.2019.02454

Yagi, R., Zhu, J., & Paul, W. E. (2011). An updated view on transcription factor GATA3-mediated regulation of Th1 and Th2 cell differentiation. *Int Immunol*, *23*(7), 415-420. https://doi.org/10.1093/intimm/dxr029

Yang, Q., Zhang, F., Chen, H., Hu, Y., Yang, N., Yang, W., Wang, J., Yang, Y., Xu, R., & Xu, C. (2024). The differentiation courses of the Tfh cells: a new perspective on autoimmune disease pathogenesis and treatment. *Bioscience reports*, *44*(1), BSR20231723.

Yasmeen, F., Pirzada, R. H., Ahmad, B., Choi, B., & Choi, S. (2024). Understanding autoimmunity: mechanisms, predisposing factors, and cytokine therapies. *International journal of molecular sciences*, *25*(14), 7666.

Yates, A. (2014). Theories and Quantification of Thymic Selection [Review]. *Frontiers in Immunology*, *Volume 5 - 2014*. https://doi.org/10.3389/fimmu.2014.00013

Ye, X., Wang, Z., Ye, Q., Zhang, J., Huang, P., Song, J., Li, Y., Zhang, H., Song, F., Xuan, Z., & Wang, K. (2020). High-Throughput Sequencing-Based Analysis of T Cell Repertoire in Lupus Nephritis. *Front Immunol*, *11*, 1618. https://doi.org/10.3389/fimmu.2020.01618

Yohannes, D. A., Kaukinen, K., Kurppa, K., Saavalainen, P., & Greco, D. (2021). Clustering based approach for population level identification of condition-associated T-cell receptor β-chain CDR3 sequences. *BMC Bioinformatics*, *22*(1), 159. https://doi.org/10.1186/s12859-021-04087-7

Yokota, R., Kaminaga, Y., & Kobayashi, T. J. (2017). Quantification of Inter-Sample Differences in T-Cell Receptor Repertoires Using Sequence-Based Information [Methods]. *Frontiers in Immunology*, *Volume 8 - 2017*. https://doi.org/10.3389/fimmu.2017.01500

Zarnitsyna, V., Evavold, B., Schoettle, L., Blattman, J., & Antia, R. (2013). Estimating the Diversity, Completeness, and Cross-Reactivity of the T Cell Repertoire [Hypothesis and Theory]. *Frontiers in Immunology*, *Volume 4 - 2013*. https://doi.org/10.3389/fimmu.2013.00485

Zeng, L., Yang, L., Zhang, Y., Lan, T., An, Y., He, P., Wen, X., Deng, S., Zhang, Z., Liu, J., & Zhou, Q. (2025). Unravelling the TCRβ repertoire: a key to unlocking the immunopathogenesis and precision medicine in SLE. *Lupus Sci Med*, *12*(1). https://doi.org/10.1136/lupus-2024-001384

Zhang, S., Zhou, Y., Liu, Z., Wang, Y., Zhou, X., Chen, H., Zhang, X., Chen, Y., Feng, Q., Ye, X., Xie, S., Zeng, M.-S., Zhai, W., Zeng, Y.-X., Cao, S., Li, G., & Xu, M. (2025). Immunosequencing identifies signatures of T cell responses for early detection of nasopharyngeal carcinoma. *Cancer Cell*, *43*(8), 1423-1441.e1410. https://doi.org/10.1016/j.ccell.2025.04.009

Zheng, W.-p., & Flavell, R. A. (1997). The Transcription Factor GATA-3 Is Necessary and Sufficient for Th2 Cytokine Gene Expression in CD4 T Cells. *cell*, *89*(4), 587-596. https://doi.org/10.1016/S0092-8674(00)80240-8

Zillikens, H., Kasprick, A., Osterloh, C., Gross, N., Radziewitz, M., Hass, C., Hartmann, V., Behnen-Härer, M., Ernst, N., & Boch, K. (2021). Topical application of the PI3Kβ-selective small molecule inhibitor TGX-221 is an effective treatment option for experimental epidermolysis bullosa acquisita. *Frontiers in medicine*, *8*, 713312.

Zou, J., Li, B., Li, D., Bao, H. F., She, C. H., Ye, J. F., Cai, J. F., & Guan, J. L. (2023). Comprehensive analysis of T-cell receptor repertoires reveals antigen-driven T-cell clusters in patients with Behçet's syndrome. *Eur J Immunol*, *53*(4), e2250181. https://doi.org/10.1002/eji.202250181

Supplementary

Supplementary code 1

Mixcr 4.7.0:

#Command Terminal

1- Cd “Your Path”

2- java -jar mixcr.jar analyze generic-amplicon --species mmu --rna --floating-left-alignment-boundary --floating-right-alignment-boundary C --assemble-clonotypes-by CDR3 --append-export-clones-field -nLength CDR3 Name_Forward.fastq Name_Forward_rev.fastq result-Sample1/

R

#TSV to CSV

1- Set a working directory

2- # Load the data from a TSV file located on your path

data <- read.table("Your path/File name.clones_TRB.tsv", header = TRUE, sep = "\t")

3- # Write the data to a CSV file in the same folder

write.csv(data, "Your path/file nsme.clones_TRB.csv", row.names = FALSE)

Preparation of files for immunarch (MiXCR -> Immunarch)

Same flow as your original script; only generic paths/names used.

load packages

library(tidyverse)

library(dplyr)

library(readr)

library(immunarch)

library(VennDiagram)

library(ggvenn)

working directory (generic)

setwd("path/to/working_directory")

```
# data input as tables (generic placeholders; tab-delimited)

X1  <- read_delim("sample01.tsv", "\t")

# remove all clonotypes that exist only once

X1_1  <- subset(X1,  cloneCount > 1)

# filter all clonotypes that have special symbols (ambiguous signs) in aaSeqCDR3

XX1_1  <- X1_1  %>% filter(grepl("[^[:alnum:]]", aaSeqCDR3))

# filtered results (remove those with special symbols)

T1  <- setdiff(X1_1,  XX1_1)

# readjust to 100% (relative abundance) ,  preserve your flow, but use the column name

for(i  in  1:length(T1$cloneCount))  {  T1$cloneFraction[i]  <-  T1$cloneCount[i]  /
sum(T1$cloneCount)  }

# Test that sum is always 100%

sum(T1$cloneFraction)

# write tables as TSV for immunarch (generic, clean filenames)

write.table(T1,  file = "sample01_immunarch.tsv",  row.names = FALSE, sep = "\t", quote =
FALSE)
```

Supplementary code 2

```
# Data loading (Immunarch)

library(immunarch)

library(writexl)


# Load an Immunarch-formatted repertoire folder

immdata <- repLoad("path/to/repertoires_folder")  # e.g., "Koll47_Abovemedian"


# Number of unique clonotypes (per sample)

p1 <- repExplore(immdata$data, .method = "volume")

write_xlsx(p1, "path/to/output/unique_clonotypes.xlsx")

# ==============================

# KEEP ABOVE THE MEDIAN

# ==============================
```

```
library(dplyr)

# Load metadata
metadata <- read.csv("path/to/metadata.txt", sep = "\t")

# Paths
clone_files_path <- "path/to/clone_files/"         # folder with per-sample CSVs
output_path      <- "path/to/output_above_median/" # folder to save filtered CSVs

# Iterate over samples
for (i in 1:nrow(metadata)) {
  sample_name <- metadata$Sample[i]
  file_path   <- paste0(clone_files_path, sample_name, ".csv")

  # Try different separators (keep exact flow)
  repertoire_data <- read.csv(file_path, sep = ",")
  if (ncol(repertoire_data) == 1) repertoire_data <- read.csv(file_path, sep = "\t")
  if (ncol(repertoire_data) == 1) repertoire_data <- read.csv(file_path, sep = " ")

  print(colnames(repertoire_data))

  if ("readCount" %in% colnames(repertoire_data)) {
    print(head(repertoire_data$readCount))

    # Median filter on readCount
    median_read_count <- median(repertoire_data$readCount, na.rm = TRUE)
    print(paste("Median read count for", sample_name, ":", median_read_count))

    filtered_data <- repertoire_data %>%
      filter(readCount > median_read_count)
```

```
   # Save
   write.csv(filtered_data,
             paste0(output_path, sample_name, "_above_median.csv"),
             row.names = FALSE)

   print(paste("Processed and saved filtered data for", sample_name))
  } else {
   print(paste("readCount column not found in", sample_name))
  }
}# ==============================
# Load two files (example)
# ==============================

setwd("path/to/working_dir")

file1 <- read.csv("sampleA_LN1.csv")
file2 <- read.csv("sampleA_LN2.csv")
# ==============================
# Unique clonotypes (above-median set)
# ==============================

# Re-use immdata if already loaded; otherwise repLoad the above-median folder
# immdata <- repLoad("path/to/output_above_median")

p1 <- repExplore(immdata$data, .method = "volume")
write_xlsx(p1, "path/to/output/unique_clonotypes_above.xlsx")
# ==============================
# Relative Clone Count (per sample)
# ==============================

library(dplyr)
```

```
library(writexl)

# Metadata for above-median set
metadata <- read.csv("path/to/output_above_median/metadata.txt", sep = "\t")

# Paths
clone_files_path <- "path/to/output_above_median/"
output_path      <- "path/to/results_folder/"

if (!dir.exists(output_path)) dir.create(output_path, recursive = TRUE)

for (i in 1:nrow(metadata)) {
  sample_name <- metadata$Sample[i]
  file_path   <- paste0(clone_files_path, sample_name, ".csv")

  if (file.exists(file_path)) {
    # Try comma, then tab, then space (same flow)
    repertoire_data <- read.csv(file_path, sep = ",")
    if (ncol(repertoire_data) == 1) repertoire_data <- read.csv(file_path, sep = "\t")
    if (ncol(repertoire_data) == 1) repertoire_data <- read.csv(file_path, sep = " ")

    if ("readCount" %in% colnames(repertoire_data)) {
      total_read_count <- sum(repertoire_data$readCount, na.rm = TRUE)

      result <- repertoire_data %>%
        mutate(RelativeReadCount = (readCount / total_read_count) * 100) %>%
        select(cloneId, readCount, RelativeReadCount)

      write_xlsx(result, paste0(output_path, sample_name, "_relative_read_count.xlsx"))
      print(paste("Processed and saved relative read counts for", sample_name))
    } else {
```

```
    print(paste("readCount column not found in", sample_name))
   }
  } else {
   print(paste("File not found:", file_path))
  }
}
# ==============================
# Relative Clone Count (per sample)
# ==============================

library(dplyr)
library(writexl)

# Metadata for above-median set
metadata <- read.csv("path/to/output_above_median/metadata.txt", sep = "\t")

# Paths
clone_files_path <- "path/to/output_above_median/"
output_path      <- "path/to/results_folder/"

if (!dir.exists(output_path)) dir.create(output_path, recursive = TRUE)

for (i in 1:nrow(metadata)) {
 sample_name <- metadata$Sample[i]
 file_path   <- paste0(clone_files_path, sample_name, ".csv")

 if (file.exists(file_path)) {
  # Try comma, then tab, then space (same flow)
  repertoire_data <- read.csv(file_path, sep = ",")
  if (ncol(repertoire_data) == 1) repertoire_data <- read.csv(file_path, sep = "\t")
  if (ncol(repertoire_data) == 1) repertoire_data <- read.csv(file_path, sep = " ")
```

```
    if ("readCount" %in% colnames(repertoire_data)) {
      total_read_count <- sum(repertoire_data$readCount, na.rm = TRUE)

      result <- repertoire_data %>%
        mutate(RelativeReadCount = (readCount / total_read_count) * 100) %>%
        select(cloneId, readCount, RelativeReadCount)

      write_xlsx(result, paste0(output_path, sample_name, "_relative_read_count.xlsx"))
      print(paste("Processed and saved relative read counts for", sample_name))
    } else {
      print(paste("readCount column not found in", sample_name))
    }
  } else {
    print(paste("File not found:", file_path))
  }
}
# ==============================
# Combine left & right and track top 50 (example with two samples)
# ==============================

library(dplyr)

# Replace with your actual sample files in the above-median folder
sample1_LN1 <- read.csv("path/to/output_above_median/sample1_LN1.csv")
sample1_LN2 <- read.csv("path/to/output_above_median/sample1_LN2.csv")
sample2_LN1 <- read.csv("path/to/output_above_median/sample2_LN1.csv")
sample2_LN2 <- read.csv("path/to/output_above_median/sample2_LN2.csv")

combined_sample1 <- bind_rows(sample1_LN1, sample1_LN2) %>%
  group_by(aaSeqCDR3) %>%
```

```
  summarise(readCount = sum(readCount), .groups = "drop")

combined_sample2 <- bind_rows(sample2_LN1, sample2_LN2) %>%
  group_by(aaSeqCDR3) %>%
  summarise(readCount = sum(readCount), .groups = "drop")

# Top 50 reference from sample1
top50_ref <- combined_sample1 %>%
  arrange(desc(readCount)) %>%
  slice(1:50)

# Track in sample2
tracked_clonotypes <- full_join(
  top50_ref %>% rename(readCount_ref = readCount),
  combined_sample2 %>% rename(readCount_cmp = readCount),
  by = "aaSeqCDR3"
) %>%
  mutate(
    readCount_ref = ifelse(is.na(readCount_ref), 0, readCount_ref),
    readCount_cmp = ifelse(is.na(readCount_cmp), 0, readCount_cmp),
    relative_freq_ref = readCount_ref / sum(readCount_ref),
    relative_freq_cmp = readCount_cmp / sum(readCount_cmp)
  ) %>%
  filter(readCount_ref > 0) %>%
  arrange(desc(readCount_ref)) %>%
  slice(1:50)

write.csv(tracked_clonotypes, "path/to/output/top50_reference_clonotypes.csv", row.names =
FALSE)
print(tracked_clonotypes)
# ==============================
```

```
# K-mer analysis (k = 3, inguinal nodes, OVA vs PBS)
# ==============================

library(immunarch)
library(dplyr)
library(ggplot2)
library(tidyr)  # for replace_na()

# Metadata and selection
metadata_path <- "path/to/output_above_median/metadata.txt"
metadata <- read.delim(metadata_path)

inguinal_samples <- metadata %>% filter(Position == "Inguinal")
ova_samples <- inguinal_samples %>% filter(Treatment == "Ova") %>% pull(Sample)
pbs_samples <- inguinal_samples %>% filter(Treatment == "PBS") %>% pull(Sample)

ova_repertoires <- immdata$data[names(immdata$data) %in% ova_samples]
pbs_repertoires <- immdata$data[names(immdata$data) %in% pbs_samples]

# k = 3 (same as your code)
ova_kmers <- do.call(rbind, lapply(ova_repertoires, function(x) getKmers(x, 3, .col = "aa")))
pbs_kmers <- do.call(rbind, lapply(pbs_repertoires, function(x) getKmers(x, 3, .col = "aa")))

ova_kmers_summary <- ova_kmers %>%
  group_by(Kmer) %>%
  summarise(Count_OVA = sum(Count, na.rm = TRUE), .groups = "drop") %>%
  mutate(Group = "OVA")

pbs_kmers_summary <- pbs_kmers %>%
  group_by(Kmer) %>%
  summarise(Count_PBS = sum(Count, na.rm = TRUE), .groups = "drop") %>%
```

```
  mutate(Group = "PBS")

combined_kmers <- full_join(ova_kmers_summary, pbs_kmers_summary, by = "Kmer")
%>%
  mutate(
    Count_OVA = replace_na(Count_OVA, 0),
    Count_PBS = replace_na(Count_PBS, 0),
    Rel_Freq_OVA = Count_OVA / sum(Count_OVA) * 100,
    Rel_Freq_PBS = Count_PBS / sum(Count_PBS) * 100,
    Enrichment_Score = Rel_Freq_OVA - Rel_Freq_PBS
  )

write.csv(combined_kmers, "path/to/output/inguinal_all_3mers.csv", row.names = FALSE)
# ==============================
# Merged (paired) for Morisita–Horn
# ==============================

library(immunarch)
library(dplyr)
library(readr)
library(openxlsx)
library(Biostrings)
library(tidyr)

metadata_path <- "path/to/output_above_median/metadata.txt"
data_dir      <- "path/to/output_above_median"
output_path   <- "path/to/output/morisita_horn_results.xlsx"

metadata <- read_delim(metadata_path, delim = "\t")

# Split Sample into Mouse and LN (keeps your flow)
```

```
metadata <- metadata %>%
  separate(Sample, into = c("Mouse", "LN"), sep = "_")

paired_samples <- metadata %>%
  group_by(Mouse) %>%
  filter(n() == 2) %>%  # mice with two sides
  ungroup()

merge_clonotypes <- function(mouse_id) {
  samples <- paired_samples %>% filter(Mouse == mouse_id)
  file1 <- file.path(data_dir, paste0(samples$Mouse[1], "_", samples$LN[1], ".csv"))
  file2 <- file.path(data_dir, paste0(samples$Mouse[2], "_", samples$LN[2], ".csv"))

  if (file.exists(file1) & file.exists(file2)) {
    df1 <- read_csv(file1, show_col_types = FALSE)
    df2 <- read_csv(file2, show_col_types = FALSE)

    colnames(df1) <- tolower(colnames(df1))
    colnames(df2) <- tolower(colnames(df2))

    print("Columns in file1:"); print(colnames(df1))
    print("Columns in file2:"); print(colnames(df2))

    if ("aaseqcdr3" %in% colnames(df1)) {
      sequence_col <- "aaseqcdr3"
      merged <- bind_rows(df1, df2) %>%
        group_by(.data[[sequence_col]]) %>%
        summarise(Clones = sum(readcount, na.rm = TRUE), .groups = "drop") %>%
        mutate(CDR3.aa = .data[[sequence_col]])
    } else if ("nseqcdr3" %in% colnames(df1)) {
      sequence_col <- "nseqcdr3"
```

```
      merged <- bind_rows(df1, df2) %>%
        group_by(.data[[sequence_col]]) %>%
        summarise(Clones = sum(readcount, na.rm = TRUE), .groups = "drop") %>%
        mutate(CDR3.aa = as.character(translate(DNAStringSet(.data[[sequence_col]]))))
    } else if ("targetsequences" %in% colnames(df1)) {
      sequence_col <- "targetsequences"
      merged <- bind_rows(df1, df2) %>%
        group_by(.data[[sequence_col]]) %>%
        summarise(Clones = sum(readcount, na.rm = TRUE), .groups = "drop") %>%
        mutate(CDR3.aa = as.character(translate(DNAStringSet(.data[[sequence_col]]))))
    } else {
      stop("No valid CDR3 sequence column found in CSV files.")
    }

    return(merged)
  }
  return(NULL)
}

merged_data <- lapply(unique(paired_samples$Mouse), merge_clonotypes)
names(merged_data) <- unique(paired_samples$Mouse)
merged_data <- merged_data[!sapply(merged_data, is.null)]

# Immunarch-like list
immdata_paired <- list(data = merged_data)

# Morisita–Horn overlap
imm_ov2 <- repOverlap(immdata_paired$data, .method = "morisita", .verbose = FALSE)
write.xlsx(as.data.frame(imm_ov2), output_path)

print("Analysis complete. Results saved.")
```

Supplementary code 3

```
# RNA-seq DE analysis pipeline
library(readr)
library(DESeq2)
library(dplyr)
library(ashr)
library(org.Mm.eg.db)
library(clusterProfiler)
library(tibble)
library(readxl)
library(EnhancedVolcano)
library(biomaRt)
library(ggplot2)
library(pathview)
library(tidyr)   # for later PCA code (returnData)

# -------- Import counts & metadata --------
counts <- read_delim("path/to/Kathrin_hisat2_out.txt",
                     delim = "\t",
                     escape_double = FALSE,
                     trim_ws = TRUE,
                     skip = 1)

# drop non-count columns (Chr, Start, End, Strand, Length from featureCounts)
counts <- counts[ , -c(2:6)]

# clean column names: strip full paths and "_sorted.bam"
colnames(counts) <- gsub(".*/", "", colnames(counts))
colnames(counts) <- gsub("_sorted\\.bam$", "", colnames(counts))
```

```
# rownames = Gene IDs
counts <- column_to_rownames(counts, var = "Geneid")

# metadata: rows named by sample ID; group = tissue_adjuvant
metadata <- read_excel("path/to/sample_sheet.xlsx")
metadata <- column_to_rownames(metadata, var = "sample")
metadata$group <- factor(paste0(metadata$tissue, "_", metadata$adjuvant))

stopifnot(all(rownames(metadata) %in% colnames(counts)))
stopifnot(all(rownames(metadata) == colnames(counts)))

# -------- Subset example (adjuvant == Alum_Titermax; tissue contrast) --------
metadata_subset <- subset(metadata, adjuvant == "Alum_Titermax")
counts_subset   <- counts[ , rownames(metadata_subset)]

stopifnot(all(rownames(metadata_subset) == colnames(counts_subset)))

dds_subset <- DESeqDataSetFromMatrix(countData = counts_subset,
                                     colData   = metadata_subset,
                                     design    = ~ tissue)

# prefilter low counts
keep <- rowSums(counts(dds_subset)) >= 10
dds_subset <- dds_subset[keep,]

# DESeq2 and LFC shrink (ingLK vs plk)
dds_subset  <- DESeq(dds_subset)
res_subset  <- results(dds_subset, contrast = c("tissue", "ingLK", "plk"))
res_subset  <- lfcShrink(dds_subset,
                         contrast = c("tissue", "ingLK", "plk"),
```

```
                type = "ashr",
                res  = res_subset)

plotMA(res_subset)

# PCA (variance stabilizing transform)
vsd_subset <- vst(dds_subset, blind = TRUE)
plotPCA(vsd_subset, intgroup = "tissue")

#  Full design using combined group factor
dds <- DESeqDataSetFromMatrix(countData = counts,
                      colData   = metadata,
                      design    = ~ group)

# prefilter
keep <- rowSums(counts(dds)) >= 10
dds  <- dds[keep,]

# set reference level (adjust to your control)
dds$group <- relevel(dds$group, ref = "plk_OVA_Alum_TM")

# DE (example: ingLK_OVA_Alum_TM vs plk_OVA_Alum_TM)
dds <- DESeq(dds)
res <- results(dds, contrast = c("group", "ingLK_OVA_Alum_TM", "plk_OVA_Alum_TM"))
res <- lfcShrink(dds,
            contrast = c("group", "ingLK_OVA_Alum_TM", "plk_OVA_Alum_TM"),
            type = "ashr",
            res  = res)

plotMA(res)
```

```
#  Gene annotation (Ensembl → symbol/description)
mart <- useMart("ensembl")
mart <- useDataset("mmusculus_gene_ensembl", mart = mart)
gene_list <- getBM(filters = "ensembl_gene_id",
                   attributes = c("ensembl_gene_id","external_gene_name","description"),
                   values = rownames(res), mart = mart)

res$ensembl <- rownames(res)
res_annot   <- merge.data.frame(as.data.frame(res), gene_list,
                                by.x = "ensembl", by.y = "ensembl_gene_id")

#PCA
vsd <- vst(dds, blind = TRUE)
plotPCA(vsd, intgroup = "group")

# ggplot PCA with labels
pcaData   <- plotPCA(vsd, intgroup = "adjuvant", returnData = TRUE)
percentVar <- round(100 * attr(pcaData, "percentVar"))
ggplot(pcaData, aes(PC1, PC2, color = group)) +
  geom_point(size = 5) +
  xlab(paste0("PC1: ", percentVar[1], "% variance")) +
  ylab(paste0("PC2: ", percentVar[2], "% variance")) +
  geom_text(label = pcaData$name, nudge_x = 3, nudge_y = 3, check_overlap = FALSE) +
  coord_fixed() + theme_bw()

#Significant genes & volcano
resSig <- res[which(res$padj < 0.1), ]
write.csv2(resSig, file = "path/to/output/significant_genes_padj_lt0.1.csv")

FC <- 0.5; p <- 0.05
keyvals <- rep("grey75", nrow(res)); names(keyvals) <- rep("NS", nrow(res))
```

```
keyvals[which(abs(res$log2FoldChange) > FC & res$padj > p)] <- "grey50";
names(keyvals)[which(abs(res$log2FoldChange) > FC & res$padj > p)] <- "log2FoldChange"

keyvals[which(abs(res$log2FoldChange) < FC & res$padj < p)] <- "grey25";
names(keyvals)[which(abs(res$log2FoldChange) < FC & res$padj < p)] <- "-Log10Padj"

keyvals[which(res$log2FoldChange < -FC & res$padj < p)]     <- "blue2";
names(keyvals)[which(res$log2FoldChange < -FC & res$padj < p)]     <- "Signif. down-regulated"

keyvals[which(res$log2FoldChange >  FC & res$padj < p)]     <- "red2";
names(keyvals)[which(res$log2FoldChange >  FC & res$padj < p)]     <- "Signif. up-regulated"


EnhancedVolcano(res,
  lab = rownames(res),
  x = "log2FoldChange", y = "padj",
  xlim = c(-5, 5),
  xlab = bquote(~Log[2]~"fold change"),
  ylab = bquote(~-Log[10] ~ italic(Padj)),
  title = "plk vs ingLK",
  pCutoff = p, FCcutoff = FC,
  pointSize = 1.5, labSize = 4,
  colCustom = keyvals, colAlpha = 1,
  legendPosition = "right",
  legendLabSize = 12, legendIconSize = 4.0,
  drawConnectors = FALSE, widthConnectors = 0.75,
  colConnectors = "grey50",
  gridlines.major = TRUE, gridlines.minor = FALSE,
  border = "partial", borderWidth = 1.5, borderColour = "black"
)


# Functional enrichment (mouse)


# Prepare ranked list (symbols) from significant set
df <- resSig
```

```
orig_gene_list <- df$log2FoldChange
names(orig_gene_list) <- rownames(df)
gene_list <- sort(na.omit(orig_gene_list), decreasing = TRUE)

# GO GSEA (mouse)
gse <- gseGO(geneList = gene_list,
             ont = "ALL",
             keyType = "SYMBOL",
             minGSSize = 3, maxGSSize = 1000,
             pvalueCutoff = 0.05,
             pAdjustMethod = "fdr",
             verbose = TRUE,
             OrgDb = org.Mm.eg.db)

# KEGG prep: map SYMBOL -> ENTREZ (mouse)
ids <- bitr(names(gene_list), fromType = "SYMBOL", toType = "ENTREZID", OrgDb =
org.Mm.eg.db)
dedup_ids <- ids[!duplicated(ids[ , "ENTREZID"]), ]

df2 <- df[rownames(df) %in% dedup_ids$SYMBOL, ]
df2$ENTREZID <- dedup_ids$ENTREZID[match(rownames(df2), dedup_ids$SYMBOL)]

kegg_gene_list <- df2$log2FoldChange
names(kegg_gene_list) <- df2$ENTREZID
kegg_gene_list <- sort(na.omit(kegg_gene_list), decreasing = TRUE)
kegg_genes <- names(kegg_gene_list)

# KEGG (mouse)
kk  <- enrichKEGG(gene = kegg_genes, organism = "mmu",
                  pvalueCutoff = 0.1, qvalueCutoff = 1)
kk2 <- gseKEGG(geneList = kegg_gene_list,
```

```
        organism = "mmu", keyType = "kegg",
        minGSSize = 3, maxGSSize = 500,
        pvalueCutoff = 0.5, pAdjustMethod = "BH")

# Example plots
# library(DOSE)  # if needed for dotplot methods
dotplot(kk, showCategory = 10, font.size = 5)

# Pathway view (mouse NF-κB signaling example: mmu04064; adjust as needed)
pathview(gene.data = gene_list,
      pathway.id = "mmu04064",
      species = "mmu",
      gene.idtype = "SYMBOL",
      limit = list(gene = 10, cpd = 10),
      bins  = list(gene = 10, cpd = 10))
```

Supplementary code 4

```
# TCRβ repertoire analysis pipeline (CDNP vs PBS, TCZ1 vs TCZ2)
# - Uses Immunarch-ready repertoires + metadata.txt

# Libraries =
suppressPackageStartupMessages({
  library(immunarch)
  library(dplyr)
  library(tidyr)
  library(readr)
  library(writexl)
  library(openxlsx)
  library(ggplot2)
  library(stringr)
```

```
  library(purrr)
})

# Project paths
project_dir <- "<project_root>"                    # e.g., "D:/project" or "/data/project"
data_dir     <- file.path(project_dir, "repertoires") # folder with Immunarch-ready per-sample tables
meta_path   <- file.path(project_dir, "metadata.txt")
out_dir     <- file.path(project_dir, "results")
dir.create(out_dir, showWarnings = FALSE, recursive = TRUE)



# Load data
immdata <- repLoad(data_dir)
metadata <- read.delim(meta_path, header = TRUE, sep = "\t", stringsAsFactors = FALSE)

# Standardize key columns if needed
colnames(metadata) <- tolower(colnames(metadata))
if (!all(c("sample","mouse","zone","position","treatment") %in% colnames(metadata))) {
  stop("metadata.txt must contain columns: Sample, Mouse, Zone, Position, Treatment (case-insensitive).")
}

# Ensure immdata$data names match metadata$sample
if (!all(metadata$sample %in% names(immdata$data))) {
  warning("Some metadata samples not found in immdata$data. They will be skipped where applicable.")
}

#  Pairwise overlap metrics (Jaccard / Morisita-Horn)
# Across all samples (matrix). Also stratified by abundance bins within each mouse TCZ1 vs TCZ2.
```

```
# Global matrices:
jaccard_all  <- repOverlap(imm_above$data, .method = "jaccard", .verbose = FALSE)
morisita_all <- repOverlap(imm_above$data, .method = "morisita", .verbose = FALSE)
write.xlsx(as.data.frame(jaccard_all),  file.path(out_dir, "overlap_jaccard_all.xlsx"))
write.xlsx(as.data.frame(morisita_all), file.path(out_dir, "overlap_morisita_all.xlsx"))

# Helper: get paired TCZ1/TCZ2 names for each mouse
paired_by_mouse <- metadata %>%
  filter(sample %in% names(imm_above$data)) %>%
  select(mouse, sample, zone, treatment, position) %>%
  pivot_wider(id_cols = c(mouse, treatment, position),
              names_from = zone, values_from = sample)

# Abundance-bin function for a single pair
# bins: list of indices to slice; we define as percent ranks by "Clones" (or fallback count col)
get_count_col <- function(df) {
  cols <- intersect(count_cols_priority, colnames(df))
  if (length(cols) == 0) return(NULL)
  cols[1]
}
slice_by_percent_bin <- function(df, from = 0, to = 1) {
  ccol <- get_count_col(df)
  if (is.null(ccol)) return(df[0, ])
  n <- nrow(df)
  if (n == 0) return(df)
  d <- df %>% arrange(desc(.data[[ccol]]))
  i_from <- max(1, floor(n * from) + 1)
  i_to   <- max(i_from, floor(n * to))
  d[i_from:i_to, , drop = FALSE]
}
```

```
# Jaccard & Morisita per bin for each mouse
bin_defs <- list(
  all     = c(0.0, 1.0),
  top10   = c(0.0, 0.10),
  p10_20  = c(0.10, 0.20),
  p20_50  = c(0.20, 0.50),
  p50_80  = c(0.50, 0.80),
  last20  = c(0.80, 1.00)
)

overlap_rows <- list()
for (i in seq_len(nrow(paired_by_mouse))) {
  rowi <- paired_by_mouse[i, ]
  s1 <- rowi$TCZ1; s2 <- rowi$TCZ2
  if (is.na(s1) || is.na(s2)) next
  d1 <- imm_above$data[[s1]]
  d2 <- imm_above$data[[s2]]
  for (bn in names(bin_defs)) {
    rng <- bin_defs[[bn]]
    d1b <- slice_by_percent_bin(d1, rng[1], rng[2])
    d2b <- slice_by_percent_bin(d2, rng[1], rng[2])
    # Build a temporary list for repOverlap
    tmp <- list(d1b, d2b); names(tmp) <- c(s1, s2)
    jv <- tryCatch(repOverlap(tmp, .method = "jaccard", .verbose = FALSE)[1,2], error = function(e) NA)
    mv <- tryCatch(repOverlap(tmp, .method = "morisita", .verbose = FALSE)[1,2], error = function(e) NA)
    overlap_rows[[length(overlap_rows) + 1]] <- data.frame(
      Mouse = rowi$mouse,
      Treatment = rowi$treatment,
      Position = rowi$position,
```

```
    Bin = bn,
    Jaccard = jv,
    Morisita = mv,
    stringsAsFactors = FALSE
  )
}
```